PREDICTION OF TURBULENT DIFFUSER FLOWS

MEAN VELOCITY PREDICTION AND EVALUATION OF k-ε MODELS IN TURBULENT DIFFUSER FLOWS

By

GREGORY ALAN KOPP, B.Sc.M.E.

A Thesis
Submitted to the School of Graduate Studies
in Partial Fulfilment of the Requirements
for the Degree
Master of Engineering

McMaster University

MASTER OF ENGINEERING
(Mechanical)

McMASTER UNIVERSITY
Hamilton, Ontario

TITLE: Mean Velocity Prediction and Evaluation of k-ε Models in Turbulent Diffuser Flows.

AUTHOR: Gregory A. Kopp, B.Sc.M.E. (University of Manitoba)

SUPERVISOR: Dr. Ö.F. Turan

NUMBER OF PAGES: xxii, 218

ABSTRACT

Eight decreasing adverse pressure gradient flows, and the similar regions of an initially increasing adverse pressure gradient flow, are examined in terms of the two experimentally observed half-power regions. The existing semi-empirical and analytical mean velocity profiles are examined and their range of applicability is determined in terms of the ratio of outer to inner half-power slopes.

Three variations of the k-ε model of turbulence are evaluated in terms of how well they predict the turbulence field in an eight degree conical diffuser. The model of Nagano and Tagawa (1990) is seen to be superior to the others. It is possible for Nagano and Tagawa's model to yield reasonable prediction of k and ε because they implemented the Hanjalic and Launder (1980) modification for the irrotational strains. However, the k-ε models prediction of the Reynolds stresses is poor.

ACKNOWLEDGEMENTS

I would like express thanks to Dr. Turan for not only her guidance during this project, but also her friendship.

I would like to thank Shelley for her love and support. I would also like to express my appreciation to all my fellow students who have made my stay here enjoyable.

TABLE OF CONTENTS

NOMENCLATURE

C_i	inner half-power slope (from $U = C_i y^{1/2} + D_i$)
C_o	outer half-power slope (from $U = C_i y^{1/2} + D_i$)
D_i	inner half-power intercept (from $U = C_o y^{1/2} + D_o$)
D_o	outer half-power intercept (from $U = C_o y^{1/2} + D_o$)
k	kinetic energy (m^2/s^2)
ℓ	mixing length (m)
P	mean pressure
p	fluctuating pressure
R_{local}	local radius
r	distance from centreline
U	mean axial velocity (m/s)
$U+$	$=U/u_*$
U_∞	freestream velocity (or centreline velocity for fully-developed flows) (m/s)
u_*	$=(\tau_w/\rho)^{1/2}$, friction velocity (m/s)
$\overline{u^2}$, $\overline{v^2}$, $\overline{w^2}$	Reynolds normal stresses (m^2/s^2)
$\overline{uv}$	Reynolds shear stress (m^2/s^2)
V	mean radial velocity (m/s)
y	normal distance from wall (m)
$y+$	$=yu_*/\nu$

Greek

α	$=1/\rho(dP/dx)$, kinematic pressure gradient
Δ	$=\nu\alpha/u_*^3$
δ	boundary layer thickness, $\delta_{0.995}$ (m)
δ_p	$=u_*^2/\alpha$, pressure length scale (m)
δ_v	$=\nu/u_*$, viscous length scale (m)
δ_{ij}	Kronecher's delta

ε	dissipation rate of k (m^2/s^3)
κ	von Kàrmàn's constant
ρ	density
τ	shear stress
μ	viscosity
ν	$=\mu/\rho$, kinematic viscosity

Subscripts and Superscripts

$\overline{\ \ }$	overbar means time-average
t	turbulent
w	wall
+	non-dimensionalized with u_* and/or ν

All other variables not appearing in this list are either empirical constants or functions which are defined in the text as necessary.

LIST OF FIGURES

Figure Page

Figure Page

Figure Page

Figure Page

LIST OF TABLES

CHAPTER ONE

INTRODUCTION

A large amount of research by different groups has been spent on the development of predictive methods for turbulent flow, both semi-empirically and computationally, in order to get a good representation of the mean velocity field and the Reynolds stresses which appear in the governing Navier-Stokes equations when they are time-averaged. Semi-empirical methods, for the most part, are based on the mixing length hypothesis and/or local energy equilibrium (that is, the rate of production of turbulence kinetic energy (k) equals the dissipation rate of k (ε)). With these semi-empirical methods, usually only the mean velocity profiles are calculated. With the development of faster computers more complex modeling is developing. The transport equation for the turbulence kinetic energy or similar equations for the Reynolds stresses along with one for a characteristic length scale are used to close the time-averaged Navier-Stokes equations.

Both types of modeling have had some successes and some failures, and most lacked complete universality. That is, they worked well in certain classes of flows, but not all. With the dawn of super-computers, full numerical simulation of simple flows has been performed without resorting to the usual Reynolds averaging beforehand. However, it seems likely that the solution of the complex flows often encountered in engineering applications with this method is a long way off. Hence, further refinement of existing models is still necessary both for practical engineering uses and also for understanding of the physics of turbulent flows.

With this in mind, the two aspects of the present work are approached. In the first part of the thesis, the prediction of the mean velocity field in adverse pressure gradient flows by semi-empirical means is studied. The relevant models in the literature are examined and it is determined which models work best in the various locations of the flow. This is done in the context of the two half-power regions which have been experimentally observed (Trupp et al, 1986). This also unifies some of the contradiction in the literature.

In the second part of the work, three variations of the two-equation $k-\epsilon$ model of turbulence are evaluated for use in adverse pressure gradient flows, specifically in the eight degree conical diffuser flow of Turan (1988) and Trupp et al (1986). The $k-\epsilon$ model is not explicitly evaluated in terms of how well it reproduces the experimental mean velocity field, but rather how well it reproduces the turbulence field. The two equations are examined term by term with the experimental data to find the possible problems with the model. Numerical solution of the two equations with a finite-difference method is then performed, given the mean velocity field and Reynolds stresses in order to further evaluate the model. The Reynolds stresses are given because of the documented problems in their usage (Nagano and Tagawa, 1990 and Polak and Turan, 1991). If acceptable results occur with this method of calculation, and a reasonable representation of the Reynolds stresses can be obtained, it is assumed that the model can be used for similar complex flows in its full form by solving the Navier-Stokes equations as well as the $k-\varepsilon$ equations. If poor results occur, it implies that the $k-\varepsilon$ model will not predict the experimental mean velocity and turbulence fields.

In the following then, chapter 2 deals with semi-empirical methods of prediction of the mean velocity field in adverse pressure gradient flows while chapter 3 evaluates the $k-\varepsilon$ model of turbulence in an eight degree conical diffuser flow. Chapter 4 offers a summary of the conclusions that were made from this study.

CHAPTER TWO

MEAN VELOCITY PROFILES IN TURBULENT DECREASING ADVERSE PRESSURE GRADIENT FLOWS

2.1 Introduction

Mean velocity profiles in wall-bounded turbulent flows with adverse pressure gradients is a topic which has generated much research due to the common occurrence of such flows in engineering applications. Although there is a large volume of literature on the topic, no one theory is wholly satisfactory, the reason being the high degree of complexity in these types of flows. Developing a better understanding of mean velocity behaviour in this class of flows will allow engineers to more effectively design plane or conical diffusers. In addition, such an understanding will also help in practical prediction without having to resort to expensive experimentation or complete numerical simulation.

In a perfect plane or conical diffuser the pressure gradient is at its maximum at the diffuser inlet, and from there continually decreases in an exponential type manner. In an actual plane or conical diffuser the pressure gradient reaches its maximum at some point after the inlet and then decreases in a manner similar to that of an ideal diffuser. This is illustrated in Trupp et al's (1986) Figure 1. Part of the complexity of this class of flows is due to the presence of many length scales present. This implies that the mean velocity depends on different variables at different distances from the wall (Kader and Yaglom, 1978). That is, there are composite mean velocity profiles. For turbulent boundary layers with adverse pressure gradients, Kader and Yaglom argue from dimensional analysis that there should be three distinct length scales. These are $\delta_v << \delta_p << \delta$ where δ_v is the viscous length scale, ν/u_*, δ_p is the pressure length scale, u_*^2/α. These different length scales imply that the velocity profile is dependent on only local flow parameters and history effects are negligible. Whereas according to Perry et al (1966), adverse pressure gradient flows contain both a wall region which is dependent on local flow parameters such as the pressure gradient and freestream velocity, and a historical region which depends on upstream conditions (Perry et al, 1966) as the pressure gradient starts to decrease, the mean velocity in the wall region varies with the square root of the distance from the wall. Further downstream, a long linear region appears, similar to the half-power region. Following this region the velocity will start to vary with the 3/2-power of the distance from the wall.

With the intention of developing a deeper understanding of the mean velocity field, the data from the nine flows listed in Table 2.1 are examined here. Although this is certainly not all of the experimental data available in the literature for this class of flows, it is a representative sample. Only unseparated, incompressible flows which have no swirling are considered. These nine flows include four plane diffuser flows, as well as five conical diffuser flows from six, eight, and ten degree conical diffusers. One of the plane diffusers has an increasing adverse pressure gradient over a long length of the flow. The other eight flows have decreasing adverse pressure gradients (except for the short region at their respective entrances). All of the data came from either the 1968 AFOSR-IFP-Stanford Conference or the 1980-81 AFOSR-HTTM-Stanford Conference on Complex Turbulent Flows, except for the eight degree conical diffuser. Hence, the geometries are described in the proceedings for the two conferences except for the eight degree conical diffuser. The mean velocity profiles for this flow were obtained from Turan (1988) and by digitizing the respective plots from Kassab (1986), Ozimek (1985), and Trupp et al (1986). The digitization error is estimated to be small. The mean velocity profiles for the remaining flows were obtained from the proceedings of the two conferences. All of the diffusers have developing flow at their inlet except for the eight degree conical diffuser which has fully-developed pipe flow at its inlet.

Along with the proposed mean velocity profiles of Perry et al and Kader and Yaglom, several other profiles are examined. Coles (1956) takes an approach different than Perry et al but similar to Kader and Yaglom's flow development. Coles' empirical Law of the Wake takes into account the similarities between adverse pressure gradient flows and wake flows. Once the flow has developed sufficiently and the pressure gradient is small enough, there is a universal mean velocity profile: the Law of the Wall along with Coles' Law of the Wake. But this universal profile is not valid in the entry region of diffuser flows where the pressure gradient is severe and the flow has been disturbed by the change in geometry (or when the flow is separated or close to it). This, of course, is analogous to wake flow where the universal velocity profile occurs quite far downstream.

Other profiles that are examined here are, those by Townsend (1961), Mellor (1966), McDonald (1969), van Driest

(1956), and Schofield (1981), Nakayama and Koyama (1984), and Granville (1989). In all of the flows examined, an attempt is made to determine the applicability of the these profiles in terms of the two half-power regions.

In section 2 of this chapter the applicable theories that describe the mean velocity in turbulent adverse pressure gradient flows are compared with the experiments listed in Table 2.1. In addition, some modifications are given to represent the experimental data for the eight degree conical diffuser more closely. Section 3 contains an examination of the two half-power regions observed by Trupp et al with the intention of developing a better understanding of this class of flows, and towards the goal of more accurate semi-empirical prediction of the mean velocity in the entry region. Following this, conclusions are given in section 4.

2.2 Comparison of Analytical Mean Velocity Profiles with Experimental Data

In this section the analytical and semi-empirical mean velocity profiles for the different regions of the nine flows examined are compared with the experimental data, both in the entry region and in the universal region. Also, some modifications to these profiles are examined in order to fit the experimental data for the eight degree conical diffuser more closely. The data from the eight degree conical diffuser will be emphasized for three reasons. First, this data is the most recent and has the most up to date corrections for high turbulence intensity. Second, it contains turbulence data for the Reynolds turbulent shear and normal stresses along with values for the dissipation of turbulence kinetic energy. Lastly, the experimentally determined mean velocity field, in conjunction with the k-ϵ model of turbulence, is used to solve for the turbulence field in the eight degree conical diffuser (as discussed further in chapter 3).

One drawback to the eight degree conical diffuser data is that there is some degree of scatter in the mean velocity profiles for the three workers (Turan, Kassab, and Ozimek). This could be due to differences in the cone pressure, inaccuracies in getting the probes to the same axial location, and the fact that Kassab's and Ozimek's data are uncorrected for high turbulence intensity while the data of Turan is corrected.

2.2.1 Moving Equilibrium, Length Scales, and Flow Development

All of the theories examined for the mean velocity in this chapter assume that the flow is in some sort of moving equilibrium. Moving equilibrium is the situation when the flow depends on only local flow parameters and not on upstream or downstream values. This means that the streamwise gradients must be small so that the flow can adjust its structure and, hence, depend on only local parameters. All history effects are ignored. Obviously then, flows which have large streamwise gradients are not in moving equilibrium and the theories are not entirely valid. Specifically, Kader and Yaglom (1978) state that the free stream velocity (or the centreline velocity for fully-developed flows) and the kinematic pressure gradient, should vary slowly in the axial direction. The Kader and Yaglom criterion for moving equilibrium is, then, $U_\infty/(\alpha\delta)^{1/2} >> 1$, where δ is the boundary layer thickness (or the local radius for fully-developed axisymmetric flows). This is a necessary, but not sufficient condition for moving equilibrium, derived from similarity principles. Kader and Yaglom note, however, that $U_\infty/(\alpha\delta)^{1/2}$ does not need to be much larger than unity for the flow to be in moving equilibrium.

Schofield (1981) developed a different criterion for an unseparated adverse pressure gradient "equilibrium" flow which has a maximum shear stress at least one and a half times larger than the wall shear stress. Schofield's equilibrium flow is defined as a specific bounded region on a plot of U_∞/U_h versus m, where U_h is the velocity that the (inner) half-power region would have if it were extended to the wall, that is, the intercept or "slip velocity", and m is defined by $U_\infty = a(x-x_o)^m$ where $m < 0$ (see Schofield's Figure 4). One drawback to this type of criterion is that it is dependent on only the freestream velocity, as opposed to the criterion of Kader and Yaglom which is dependent on the pressure gradient and boundary layer thickness as well.

Townsend's (1961) criterion for equilibrium is that advection is negligible and the shear layer is thin. In the diffuser, advection is significant, even near the wall. The flow, also, has both accelerating and decelerating regions: in the core region the flow is decelerating, while near the wall it is accelerating. This is the cause of the important advection terms. Also, conical diffuser flows are more complex than equilibrium boundary layers or plane diffuser flows because of the added strain terms caused by the geometry. Hence, Townsend's criterion for "equilibrium" flow is more stringent then the previous two. This is because Townsend's equilibrium condition is for the turbulence field while the other two are for the mean field.

In order to examine the Kader and Yaglom criterion for moving equilibrium, the variation of the local flow variables must be known. The variation of $U_\infty/U_{\infty,inlet}$, $u_*/u_{*,inlet}$, $\delta_{0.995}/\delta_{inlet}$, $\alpha\delta/u_*^2$, and $\alpha\nu/u_*^3$ with x/δ_{inlet} for the eight decreasing adverse pressure gradient diffuser flows are shown in Figures 2.1 - 2.5. Table 2.2 shows the actual experimental values for Kader and Yaglom's criterion for moving equilibrium. Since Kader and Yaglom note that $U_\infty/(\alpha\delta)^{1/2}$ does not need to be much larger than unity for the flow to be in moving equilibrium, it appears that all of the flows examined are in moving equilibrium, except for possibly the inlet region of the eight degree conical diffuser.

Because the flows examined here are, thus, considered to be in moving equilibrium, the mean flow should depend on local flow variables and historical effects can be ignored. As seen from Table 2.2, Kader and Yaglom's length scales each differ by at least one order of magnitude, and hence, these three length scales are present in the flows. Therefore, one would expect there to be at least three different functional forms of the mean velocity at each particular axial location. This is indeed the case, as shown in the remainder of the chapter.

The difference between Kader and Yaglom's and Perry et al's flow development theories should be emphasized. Kader and Yaglom's composite mean velocity profile has the same form at each axial station. Perry et al's flow development, however, shows that the mean velocity varies in the streamwise direction and the forms of the composite profiles change. Figures 2.6, 2.7, and 2.8 show Perry et al's flow development for Fraser's flow B (flow # 5100). Figure 2.6 shows the mean axial velocity non-dimensionalized with the local freestream velocity versus the square root of the distance from wall non-dimensionalized with the local boundary layer thickness. One can see that early into the flow (station 4) a long half-power region is present, represented by the straight line. Figure 2.7 shows, on linear coordinates, a long linear region occurs further into the flow (station 6). Figure 2.8 shows, on 3/2 power coordinates, the long 3/2 power regions near the exit of the flow (specifically, station 12). All nine of the flows examined show this development.

Of course, the same data can be plotted on other coordinates as well, such as U+ versus Log y+ coordinates. Although Perry's flow development provides insight into understanding these flows, the idea of a universal mean velocity profile is more ideally suited to the composite mean velocity profiles of Kader and Yaglom. Therefore, Kader and Yaglom's composite mean velocity profile, along with the other profiles found in the literature, are examined in the remainder of this section. Perry's half-power velocity profile is also re-examined in this context.

2.2.2 Inner Wall Layer

The viscous sublayer is the very thin layer right adjacent to a smooth, non-porous wall. This is the region of the Law of the Wall. The Law of the Wall, simply stated, is $U^+ = y^+$ in the region from $0 < y^+ < \approx 5$ in zero or small pressure gradient flows. Outside of the viscous sublayer is the buffer region, which extends to approximately $y^+ = 30$ in zero or small pressure gradient flows. In the viscous sublayer, viscosity dominates the flow; while in the buffer region, inertial forces start to play a more important role. This Linear Law of the Wall can be derived by dimensional analysis, as in Hinze (1975) or Kader and Yaglom (1978).

The first theoretical development for the mean velocity profile in the viscous sublayer and buffer region was by van Driest (1956). He developed this theory for zero pressure gradient flows. Using the mixing length concept, the total shear stress, τ is

$$\tau = \mu \frac{\partial \overline{U}}{\partial y} + \rho\, \ell^2 \left(\frac{\partial \overline{U}}{\partial y}\right)^2 . \qquad (1)$$

In order to use the mixing length concept to calculate the mean velocity, the turbulent shear stress and the mixing length must be known. Van Driest used the mixing length $\ell = \kappa y$ far from the wall, where κ is called the universal mixing constant, or more commonly, the von Kàrmàn constant. Since near the wall the eddies are damped by the presence of the wall, he concluded that

$$\ell = \kappa y\ [1 - \exp(-y/A)] . \qquad (2)$$

where A is a dimensional empirical constant. For a boundary layer with zero pressure gradient, the shear stress gradient at the wall equals zero, hence, near the wall $\tau \approx \tau_w$. Van Driest's non-dimensional velocity profile is then, from equation (1),

$$U^+ = \int_0^{y^+} \frac{2dy^+}{\{1 + [1 + 4\kappa^2 y^{+2}(1 - \exp(-y^+/A^+))^2]^{1/2}\}} , \qquad (3)$$

where $A^+ = 26$. Near the wall, equation (3) yields $U+ = y+$, up to $y+ \approx 5$. Equation (3) also approaches the Logarithmic

Law of the Wall[1] asymptotically for y+ approximately equal to 30. The Log Law is given by

$$U^{+} = \frac{1}{\varkappa} \ln(y^{+}) + b \ , \tag{4}$$

with $\varkappa \approx 0.41$, and $b \approx 5.0$, although there is a wide degree of scatter in these constants. Between the Law of the Wall and the Log Law is the buffer region. Van Driest's velocity profile provides a smooth blending region between the Law of the Wall and the Log Law.

Mellor (1966) and McDonald (1969) have shown theoretically that the mean velocity can change drastically from the usual Law of the Wall in the presence of an adverse pressure gradient, and that the sublayer and buffer region can be shortened substantially. To account for this there have been many modifications to van Driest's mixing length equation. Granville (1989) summarizes these, and makes his own modification as well. In his modification, it is assumed that near the wall

$$\tau^{+} = 1 + \gamma \Delta y^{+} \ , \tag{5}$$

where $\tau^{+} = \tau/\tau_{w}$, $\gamma = 0.9$ is an empirical constant, and $\Delta = \nu\alpha/(u_{*}^{3})$. This leads to a mixing length

---

[1] The Logarithmic Law of the Wall will be called the Log Law throughout the rest of this thesis. The Linear Law of the Wall (U+ = y+) will simply be called the Law of the Wall in order to differentiate it from the Log Law and the other linear region in these flows.

$$\ell^+ = xy^+(\tau^+)^{1/2}\,\{1 - \exp[-y^+(1 + \gamma b\Delta/A^+)^{1/2}]\}\ , \qquad (6)$$

where b = 14.0 for an adverse pressure gradient while b = 16.4 for a favourable pressure gradient. Granville's non-dimensional velocity profile is then

$$U^+ = \int_0^{y^+} \frac{2\tau^+\ dy^+}{\{1 + [1 + (2\ell^+)^2\tau^+]^{1/2}\}}\ . \qquad (7)$$

Kader and Yaglom (1978) take a different approach to obtain an equation for the mean velocity profile in the viscous sublayer and the buffer region. After examining many experimental profiles and doing a similarity analysis, they determine that a reasonable fit for the mean velocity is given by Rannie's equation (see Hinze, 1975)

$$U^+ = D\,\tanh(y^+/D)\ , \qquad (8)$$

with D=14.0. Kader and Yaglom suggest that D=14.5.

Mellor (1966) and McDonald (1969), as stated above, have also developed formulations for the mean velocity profile in the viscous sublayer and buffer region for adverse pressure gradient flows. Mellor uses a similarity analysis with the Boussinesq definition of the eddy viscosity along with a linear shear stress distribution, (with the stress gradient equal to the pressure gradient) and obtains

$$U = \lim_{\varepsilon \to 0} \left(\int_{\varepsilon} \frac{\nu\psi(\chi)}{\chi^2 y^2} dy - \frac{u_*}{x} \ln\left(\frac{\varepsilon u_*}{\nu}\right) \right) + \frac{2}{x}[(u_*^2 + \alpha y)^{1/2} - u_*] + \frac{u_*}{x} \ln\left(\frac{4}{\Delta} \frac{(u_*^2 + \alpha y)^{1/2} - u_*}{(u_*^2 + \alpha y)^{1/2} + u_*} \right) , \qquad (9)$$

where $\psi(\chi)$ is an empirical function obtained from using Laufer's (1954) experimental data and the Law of the Wall. Outside of the sublayer and buffer region the first term becomes constant, and is called the slip velocity or additive constant, which Mellor tabulates.

McDonald objected to Mellor's assumption of the stress gradient and pressure gradient being equal, since this equality holds only right at the wall. In actuality, they quickly become unequal, with the stress gradient becoming smaller than the pressure gradient. McDonald, taking this into account, obtained a similar velocity profile. He shows that in the sublayer or buffer region, it is the pressure gradient which causes the mean velocity to deviate from the Law of the Wall, not the actual value of the stress gradient. He also showed that the stress gradient plays an important role outside of the buffer region and in determining the value of the slip velocity.

As Δ increases, both McDonald and Mellor's models yield mean velocity gradients increasingly larger than the usual gradient in the viscous sublayer. This causes the velocity gradient dU+/dy+ to become greater than unity as Δ becomes large. Also, as the severity of the adverse pressure gradient increases, the end of the buffer region moves closer and closer to the wall.

The profiles of van Driest, Granville, and Rannie (along with the Log Law and the Law of the Wall for reference) are compared with representative experimental data for the conical diffusers in Figures 2.9 and 2.10, and the plane diffusers in Figures 2.11 and 2.12 McDonald's and Mellor's profiles are not shown here because they are nearly identical to the Law of the Wall for the values of Δ in the nine flows examined. Both the van Driest and Rannie profiles do not change with the pressure gradient and are similar to each other. Although the Granville profile is a function of the pressure gradient, the variation is small for this particular range of adverse pressure gradient flows. All three models agree with the Law of the Wall to y+ ≈ 5, but become different following this.

It is difficult to say which model works the best. Both Rannie's and van Driest's mean velocity profiles work at some stations, but certainly not at all stations. Granville's model shows no agreement with the data, as shown in the figures. The Law of the Wall also correlates the data better than van Driest or Rannie at some stations, notably at those where the logarithmic region extends closer to the wall.

For the data sets examined, it is observed that the shortening of the buffer region (or the penetration of the logarithmic region into the sublayer) is related to $\Delta = \alpha\nu/u_*^3$ increasing, as suggested by McDonald. Trupp et al (1986) shows that the Logarithmic Law might well extend to y+ ≈ 3, but hot-wire anemometry is not accurate in this region due to the close proximity to the wall (Turan et al, 1987). Nevertheless, it does appear that the logarithmic region moves closer to the wall than in zero pressure gradient boundary layers or fully-developed pipe flows.

Schofield (1981) suggests that the usual Law of the Wall (U+ = y+) be used for y+ < 10, followed directly by the Log Law. This, however, leads to a discontinuous velocity profile and gradient. Given the above discussion though (and the difficulties with McDonald's and Mellor's models in the logarithmic region, to be discussed later), this seems to be reasonable. Because the experimental data seems to indicate that the Log Law penetrates the buffer region, approaching quite close to the wall, it seems likely that dU+/dy+ is greater than unity. This is precisely what McDonald shows. However, because of problems in measuring the mean velocity and the turbulent shear stress, $\overline{uv}$ close to the wall, along with the fact that Mellor's and McDonald's models are similar to the Law of the Wall for the pressure gradients considered here, Schofield's proposal seems to be the most reasonable at this time.

The logarithmic layer of a flow is the region just outside of the buffer region, as discussed above. The mean velocity profile is usually described by equation (4) in zero and small pressure gradient flows, but there is wide scatter in the experimentally obtained constants. Hinze (1975, § 7.6) discusses this in detail and notes that the Log Law constants should be universal, and only u_* should vary with Reynolds number.

The Log Law can be derived from mixing length theory (van Driest, 1956) as well as dimensional analysis (Hinze, 1975 and Kader and Yaglom, 1978). In this region, inertial forces dominate the viscous forces, and the shear stress is once again assumed to be approximately constant because of the assumed small pressure gradient.

In the presence of an adverse pressure gradient, the logarithmic region often tends to become shorter or can even be destroyed entirely if the pressure gradient is severe enough. This is because in a small pressure gradient flow, the shear stress is nearly constant; while in an adverse pressure gradient flow, the shear stress increases monotonically from the wall out to some maximum point. As the pressure gradient decreases the shear stress gradient decreases as well, until the pressure gradient becomes small enough and the Log Law returns or lengthens (although it may still be shorter than a zero pressure gradient boundary layer). This is verified in the paragraphs that follow.

There are three mean velocity formulations for the Log Law region under adverse pressure gradient conditions. These are the formulations of Townsend (1961), Nakayama and Koyama (1984), and Mellor (1966). There is also two modifications to Townsend's formulation. Townsend (1962) makes a modification to his formulation, as does McDonald (1969).

All five of these formulations asymptotically approach the Log Law under zero pressure gradient conditions. In addition, in the presence of a severe adverse pressure gradient or when the skin friction is small, these mean velocity profiles vary with the square root of distance from the wall. In fact for all adverse pressure gradients, these models vary with the half-power of distance from the wall for large y+. Basically then, these models provide a short logarithmic region (or none at all if Δ is large enough), a blending region, and then a half-power region.

Townsend developed a formulation for the mean velocity profile in the fully turbulent wall region of flows with strong pressure gradients, adverse or favourable. Townsend's theory is for "equilibrium layers". Townsend's equilibrium layers, as discussed earlier, are those where the local rates of turbulent production equal the dissipation, with negligible advection of turbulence kinetic energy. That is, these two terms in the turbulence kinetic energy equation are much larger than the others. Hence, the shear stress plays an important role. Using the above assumptions along with the mixing length concept, his mean velocity profile for a linearly varying turbulent shear stress and a linearly varying mixing length , is developed.

With the stress distribution approximated by

$$\frac{\tau}{\rho} = \frac{\tau_w}{\rho} + \alpha y = u_*^2 + \alpha y \ , \qquad (10)$$

and the same mixing length as used by van Driest, $\ell = xy$. Townsend's mean velocity is then

$$U = \frac{u_*}{x}\left(\ln \frac{(a + \alpha y)^{1/2} - a^{1/2}}{(a + \alpha y)^{1/2} + a^{1/2}}\right) + \frac{2(1 - B\ \mathrm{sgn}(\alpha))}{x}(a + \alpha y)^{1/2} + U_s \ , \qquad (11)$$

where $a = u_*^2$. Using the Log Law, the slip velocity or additive constant, U_s can be obtained, and is

$$U_s = \frac{u}{x}* \left(\ln(\frac{4}{\Delta}) - 2[1 - B\ \mathrm{sgn}(\alpha)]\right) + A, \qquad (12)$$

where A is the intercept of the Log Law and B ≈ 0.2 is a constant representative of the rate of turbulent kinetic energy diffusion.

Nakayama and Koyama also start their derivation with the turbulence kinetic energy balance. They assume that the convection of kinetic energy is negligible near the wall and that the flow is in moving equilibrium. The conservation equation for the turbulent kinetic energy , k is then

$$-\frac{dJ}{dy} + \tau \frac{d\bar{U}}{dy} - \rho\epsilon = 0 \ , \qquad (13)$$

where ϵ is the viscous dissipation and J is called the diffusional flux of turbulent kinetic energy. The middle term in the equation is the production term. The diffusional flux is given by

$$J = -\frac{1}{\sigma} \frac{\tau}{d\bar{U}/dy} \frac{dk}{dy} \ , \qquad (14)$$

where σ is the effective Prandtl number for k. They obtain an equation for the first derivative of the velocity with respect to the shear stress. Upon integration, they obtain the velocity profile

$$U^+ = \frac{1}{x^*} \left(B_1(t - t_s) + \ln\left(\frac{t_s + 1}{t_s - 1} \frac{t - 1}{t + 1}\right)\right) \ , \qquad (15a)$$

where $t = \left(\frac{1 + 2\tau^+}{3}\right)^{1/2}$, $t_s \approx (1 + 0.074\Delta)^{1/2}$,

$$x^* = \frac{0.4 + 0.6\Delta}{1 + \Delta}, \qquad (15b)$$

and the value of the constant B_1 is 3.0, and τ is determined by equation (10). Since the mean velocity here is only a function of the shear stress, Nakayama and Koyama state that the velocity profile is valid for any monotonically increasing shear stress.

Mellor's analysis, discussed in the previous section, is similar to the other two models. Outside of the viscous sublayer and buffer region, the first term in equation (9) becomes constant. Nakayama and Koyama show that Mellor's model is identical to Townsend's, when B = 0 in Townsend's model.

McDonald objects to the assumption of the stress gradient being equal to the pressure gradient, stating that the stress gradient should be less than the pressure gradient in this region of the flow. Townsend (1962) also acknowledges this fact, saying that the average stress gradient in the wall region should be about one-third less than the pressure gradient. McDonald states in his paper that there are difficulties in Townsend's model, specifically that a running calculation of the flow away from the wall has to be performed in order to evaluate the shear stress gradient, and that this may not work in all flows (McDonald, 1969). McDonald assumes a stress distribution of

$$\tau/\rho = a + \gamma\alpha y \qquad (16a)$$

where a can be either positive or negative, and $\gamma < 1$ is empirically determined. McDonald's model is then, for positive a,

$$U = \frac{2}{x}[(a^2 + \gamma\alpha y)^{1/2} - a^{1/2}] + \frac{a^{1/2}}{x} \ln\left(\frac{4}{\Delta} \frac{(a^2 + \gamma\alpha y)^{1/2} - a^{1/2}}{(a^2 + \gamma\alpha y)^{1/2} + a^{1/2}} \right)$$

$$+ U_s \qquad (16b)$$

with the slip velocity matched to the velocity at the end of the buffer region. The resulting expression is similar to equation (11) with B = 0 and the linear shear stress gradient empirically or experimentally determined.

Figures 2.13, 2.14, and 2.15 show McDonald, Townsend, and the Log Law compared with the eight degree conical diffuser data. The models of Mellor and Nakayama and Koyama are not shown because they are very similar to Townsend's model (see Nakayama and Koyama's Figure 2, (1984)).

From examining these figures it appears that the slope of the Log Law, that is, the inverse of von Kármán's constant ($x=0.41$) is reasonable. However, the Log Law intercept decreases as the flow develops. In the flows where Clauser's method is used, the Log Law constants ($x=0.41$, $b=5.0$) work well at every station that was examined. This is expected because Clauser's method assumes the existence of a Log Law with the usual constants (see Perry, 1966 for example). In the more recent experiments (the six and eight degree conical diffusers) where the friction velocity is determined from a Preston Tube, the Log Law intercept decreases as the flows develop.

In the literature there is a wide degree of scatter in the constants used in the Log Law. This could be partially due to experimental inaccuracies, especially those in determining the wall shear stress. From the data used at the Stanford Conferences however, it seems that if Clauser's Method is used to determine the friction velocity, at least some of this scatter disappears. Figures 2.16 and 2.17 illustrate this. Figure 2.16 shows $U+$ versus Log $y+$ for all of the stations from the six degree conical diffuser (flow # 0142) with the friction velocity calculated from Preston Tube data along with the Log Law ($x = 0.41$ and $b = 5.0$). Figure 2.17 shows the same data with the friction velocity calculated from Clauser's method. Most of the scatter is eliminated because of the definition of Clauser's friction velocity. Although it seems quite likely that Clauser's method does not yield the most accurate wall shear stress, it does lead to the velocity scale necessary to correlate the experimental data to the Log Law, assuming that the Log Law is present. This also eliminates the need to assume a variation in the slope of the Log Law (i.e. von Kármán's constant, such as in Nakayama and Koyama's model) and possibly even the Log Law intercept with pressure gradient. Correlation of the Log Law intercept with the pressure gradient or stress gradient is not attempted here for this reason. Of course, it should be noted that the Preston Tube method for determining the wall shear stress also assumes the existence of the Log Law.

Townsend's model, in general, agrees with the measured profiles at only the first few axial stations in all of the flows (and is quantified in Table 2.3 and discussed in section 3). In these locations Townsend's model provides a moderately better approximation to the data then the Log Law. After that, however, his model does not work, for two reasons. First, the model assumes that the slope of the stress curve is equal to the pressure gradient. This condition is not fulfilled in the diffuser flows. Second, there are significant amounts of advection of turbulence kinetic energy which were not accounted for in the model. The amount of advection increases downstream from the inlet.

In order to evaluate McDonald's velocity profile outside the sublayer, the experimental turbulent shear stress needs to be known. For the eight degree conical diffuser the $\overline{uv}$ distributions of Kassab (1986) and Turan (1988) were examined. For the six degree conical diffuser the $\overline{uv}$ distributions were given with the Stanford Conference data. Once the most reasonable straight line regions on $\overline{uv}$ versus y plots for the data sets was determined by eye, the slope and intercept for equation (16a) were obtained graphically. γ was determined to increase from 0.35 to 0.67 for the eight degree conical diffuser as the flow developed. In flow # 0142 γ was between approximately 0.5 and 0.6 and in flow # 0143 γ decreased from approximately 0.8 to 0.15. The a and γ values, plus the slip velocity matched to the end of the buffer region, were used with McDonald's velocity profile in Figures 2.13 - 15. Note that the values of the slip velocity were matched to the end of the sublayer rather than calculated by McDonald's method. This was done in order to more effectively evaluate McDonald's formulation in this region of the flow without the inaccuracies of his sublayer formulation coming into play. Specifically the slip velocity appears to be too large as shown by the values for U_s shown in the captions for Figures 2.13 - 15 (relative to Townsend's slip velocity, equation 12). Figures for McDonald's model in the two six degree conical diffuser flows are shown in Appendix A. McDonald's model is not evaluated in the remaining five decreasing adverse pressure gradient flows because no $\overline{uv}$ data is available for them.

McDonald's formulation is in good agreement with the six and eight degree conical diffuser data sets over a larger region then the Log Law at all the axial stations in the entry region. Basically, McDonald's model works at the beginning and middle regions of the six and eight degree diffusers, but not in the exit region. This is a substantially larger range of axial stations than the range where Townsend's model worked. Far from the wall, the models of McDonald, Townsend, Mellor, and Nakayama and Koyama mathematically asymptote to the half-power law, but none of the four models predict the half-power region data, except for McDonald at a few stations in the entrance regions. The range of validity of McDonald's model is quantified in Table 2.3, as discussed in the following section.

There is, however, a difficulty with using McDonald's mean velocity profile for prediction. His formulation is seen to be a function of Δ as shown in his Figures 2 or 4

(McDonald, 1969). Figure 2.5 shows that Δ increases in the eight decreasing adverse pressure gradient flows as they develop. However, the Log Law returns as the flow develops and the pressure gradient decreases. This directly contradicts what happens with McDonald's velocity profile. Therefore, Δ should not be used as a non-dimensionalization of the pressure gradient. However, McDonald's model can be used in the entry region of these flows. A reasonable approximation for the stress gradient in this region is two-thirds of the pressure gradient (Townsend, 1962).

Because the models of Townsend, Nakayama and Koyama, Mellor, and McDonald did not work in the half-power regions of the flows considered, the principle assumption of these models was examined. At all the stations, the experimental $\overline{uv}$ curve exhibits a slight degree of curvature. In order to determine if the discrepancy in the predicted mean velocity profiles near the diffuser outlet is caused by the curvature in the stress distribution, equation (10) was modified to

$$\frac{\tau}{\rho} = a + \gamma \alpha y^{n} \tag{17}$$

where n, γ, and a are empirical constants, with n in the range $0 < n < 2$. This new stress distribution was used to modify Townsend's original velocity profile in a manner similar to McDonald.

To obtain the modified Townsend velocity profile, a binomial expansion was used. To a reasonable approximation, the mean velocity is

$$U \cong \frac{2b^{1/2}y^{n/2}}{x}\left(\frac{1}{n} - B\right) - \frac{b^{-1/2}y^{-n/2}a}{x}\left(\frac{1}{n} + B\right) \tag{18}$$

$$+ \frac{b^{-3/2}y^{-3n/2}a^2}{x}\left(\frac{1}{3n} + B\right) - \frac{b^{-5/2}y^{-5n/2}a^3}{x}\left(\frac{1}{5n} - + B\right) + U_s$$

where $y^n > u_*^2/(\gamma\alpha)$ is necessary for convergence of the binomial expansion, $b = \gamma\alpha$, and U_s is the slip velocity.

Assuming several different values for n, including n equal to unity, least squares curve-fitting was performed on Kassab's experimental $\overline{uv}$ distributions to obtain the empirical constants of equation (17) to use in equation (18). It was determined that although equation (18) is sensitive to values of n itself, when the curve-fitted constants for equation (17) are used, nearly identical velocity profiles to McDonald's mean velocity are obtained. Hence, it can be concluded that the linear shear stress approximation is not the cause of the disagreement between McDonald's model and the measured mean velocities in the exit regions of these flows.

One further modification was attempted for this region of the flow in order to obtain smoother fitting curves to be used in a program code to solve for the k-ε model of turbulence, as will be discussed in chapter 3.

This was done by modifying the Nakayama and Koyama model. This model was chosen to be modified because it most closely approximated the velocity gradients over the entire diffuser flow.

Using the nomenclature previously given for the Nakayama and Koyama equation, B_1 was modified to an empirical function of the form $(b_1)t^{(b_2)}$, and t_s was determined empirically. This form of the equation allows for an accurate prediction of the mean velocity field in the logarithmic and half-power regions, as shown in Figure 2.18, although there is no physical basis for this modification.

2.2.3 Outer Layer

The final regions that will be discussed here are the half-power and velocity defect regions. As the theories in the previous section show, the mean velocity at the end of the logarithmic region varies with the half-power of the distance from the wall in an adverse pressure gradient flow. Schofield (1981) calls the half-power layer the inner portion of the velocity defect region. Coles' (1956) empirical Law of the Wake begins at the end of the logarithmic region and extends to the edge of the boundary layer. Other researchers, such as Perry (1966) and Kader and Yaglom (1978), include the half-power layer as a distinct region of an adverse pressure gradient flow, between the logarithmic region and the velocity defect layer. The mean velocity profiles of Townsend and McDonald (and the other similar profiles discussed in the previous section) show the half-power region as the replacement for the logarithmic region under a severe adverse pressure gradient, and as the region following the logarithmic region when the pressure gradient is smaller. In this thesis, the half-power region formulations are included with the defect formulations and Coles' Law of the Wake because together, these regions make up the outer portion of the flow for the pressure gradients considered here.

Coles shows that the mean velocity profile in this region is similar to that for a wake flow. He obtains a velocity profile of the form

$$U+ = f(y+) + g(\Pi, y/\delta) \ , \qquad (19)$$

where $f(y+)$ is the Log Law and $g(\Pi, y/\delta)$ is the departure from the Log Law in the outer region. Coles determined that $g(\Pi, y/\delta) = \Pi(x)w(y/\delta)/\kappa$ where $w(y/\delta)$ is called the Law of the Wake, which was determined empirically. $\Pi(x)$ is then determined from

$$\frac{U_\infty}{u_*} = \frac{1}{\kappa} \ln\left(\frac{u_*\delta}{\nu}\right) + b + \frac{\Pi}{\kappa} w(1) \ , \qquad (20)$$

where $w(1)=2$. Hinze (1975) approximates $w(y/\delta)$ with

$$w(\zeta)=1+\sin[(2\zeta-1)\pi/2] \tag{21}$$

where $\zeta = y/\delta$. There is a small error in this approximation at $\zeta \approx 0.1$ and $\zeta \approx 0.8$ to 0.9. In the outer region of the boundary layer, Coles' Law of the Wake should be valid if a logarithmic velocity profile exists and the adverse pressure gradient is not severe.

Figures 2.19, 2.20, and 2.21 compare Coles' Law of the Wake with the velocity profiles from different flows. Figure 2.19 shows Coles' profile applied to three representative stations from the plane flows (# 2900, # 1100, and # 1200). His mean velocity profile fits every station of the plane data examined. There are only a few exceptions where the agreement is not as good. These minor inaccuracies seem to be due to inaccuracies in calculating the boundary layer thickness. If small adjustments are made to the boundary layer thickness, the Law of the Wake fits the data well.

Figure 2.20 shows data for the six and ten degree conical diffusers. In this figure the Log Law intercept is unmodified, so that the Coles profile does not fit the data for flows # 0142 and # 0143. Here u_* was calculated from the Preston Tube method, as opposed to Clauser's method. This figure shows that Coles' formulation still predicts the data reasonably in the outer layer although the fit is much better when the Log Law intercept is modified or the Clauser friction velocity is used.

In the entry region of these flows Coles' Law of the Wake does not work as shown in Figure 2.21a from the eight degree conical diffuser. Eventually though, it works reasonably well, after an entry length, if the Log Law intercept is modified to fit the data as shown in Figures 2.21b and 2.21c. Because Coles' Law of the Wake reasonably fits all of the data sets after some sort of an "entry length", it is considered here to be a universal mean velocity profile.

However, because Coles profile depends on two parameters (u_* and $\Pi(x)$), it does not collapse onto one line for all flows. This can be seen on Figure 2.22 which shows the data for the eight degree and two six degree conical diffuser flows on the usual U+ versus log y+ coordinates. For these three flows the outer layer occurs at varying distances from the wall.

The entry region is defined to end at the point were Coles Law of the Wake starts to accurately predict the data. The idea of an entry length is consistent with other flows such as pipes, wakes, and jets. In the universal region the local flow parameters such as the friction velocity, freestream velocity, and kinematic pressure gradient do not change very rapidly relative to the entry region where the gradients are large. The entry length also appears to be dependent on initial conditions. At this point it is difficult to say whether the entry length is Reynolds number dependent, but it seems likely.

Perry (1966) states that in the half-power layer, the flow is dependent primarily on the kinematic pressure gradient, and of course, the distance from the wall. Perry shows that the half-power velocity gradient, obtained from dimensional analysis, is of the form

$$\frac{\partial \overline{U}}{\partial y} = \frac{1}{2} K_1 \frac{\alpha^{1/2}}{y^{1/2}} , \qquad (22)$$

which upon integration yields the half-power velocity profile. Perry also points out that the universal constant, K_1, shows reasonable agreement with experimental results when the major portion of the velocity profile at a particular station varies with the square-root of y. Of special interest is the way that Perry defines the constant of integration or the "slip velocity". Perry's half-power equation is

$$U^+ = K_1 \left(\frac{\alpha y}{u_*^2} \right)^{1/2} + \frac{K_2}{u_*} \qquad (23)$$

where K_1 is a universal constant and K_2 is a function of Δ. The slip velocity is equal to

$$\frac{K_2}{u_*} = \frac{1}{\kappa}\ \ln(\ C/\Delta) + A \qquad (24)$$

where κ and A are the Log Law constants, $K_1 = 4.16$ and $C = 0.19$ are universal constants. Because of Perry's definition of the slip velocity, the half-power region is designed to follow immediately after the logarithmic region. Perry, thus, assumes that there is a logarithmic region in all unseparated adverse pressure gradient flows.

Kader and Yaglom's half-power law, after performing a similarity analysis and obtaining the constants empirically, is

$$U^+ = K\ \frac{(\alpha\delta)^{1/2}}{u_*}\left(\frac{y}{\delta}\right)^{1/2} + \frac{K_2}{u_*}\ , \qquad (25a)$$

where

$$K = (200u_*^2/\alpha\delta + 20)^{1/2}\ ,\quad \frac{K_2}{u_*} = 2.44\ \ln(\Gamma) - \frac{15}{\Gamma^{1/2}} - \frac{6}{\Gamma}\ ,$$

$$\text{and}\quad \Gamma = \frac{6u_*^3/\alpha\nu}{5 + 50u_*^2/\alpha\delta}\ . \qquad (25b)$$

Kader and Yaglom's half-power slope is, thus, seen to be a function of $\alpha\delta/u_*^2$, while the intercept is a function of $\alpha\delta/u_*^2$ and $\alpha\nu/u_*^3$.

Following the half-power region (and possibly a small blending region) is the velocity defect region. Kader and Yaglom use dimensional analysis and empirical results from a wide range of experiments to obtain their defect law

$$U^+ = \frac{U_\infty}{u_*} - C\left(1 + \frac{\alpha\delta}{u_*^2}\right)^{1/2}\left(1 - \frac{y}{\delta}\right)^2 , \tag{26}$$

where C = 9.6 is an empirical constant. Referring to Kader and Yaglom's (1978) Figure 6 it appears that there a is wide degree of scatter in the experimental data around C = 9.6.

Shown in Figures 2.23, 2.24, and 2.25 are Perry's half-power law, Kader and Yaglom's half-power law and defect formulation, and the Log Law, along with the experimental data for the eight degree conical diffuser (Figures for the other flows are included in Appendix B). It is observed that Perry's and Kader and Yaglom's half-power laws work reasonably well in the middle region of this flow. Kader and Yaglom's defect works quite well towards the exit region of this flow. These models work moderately well in the in the inlet and middle regions of the eight degree conical diffuser.

What was shown in the eight degree conical diffuser is representative of the other flows as well, as shown in Appendix B. Kader and Yaglom's and Perry's half-power laws both appear to work reasonably well over a short axial range, usually in the middle stations of the flows. Kader and Yaglom's half-power law was moderately better over a wider range of axial stations in most of the flows then

Perry's half-power law. It should be noted, however, that Perry's defect law is designed to predict the half-power region only when the half-power region is the dominant region of the flow, as described in the introduction of this chapter. Kader and Yaglom's defect was reasonable and worked much better in the plane diffusers than in the conical ones. These results are summarized in Table 2.3, and discussed in more detail in the following section.

Part of the difficulty with Kader and Yaglom's half-power and defect formulations is shown in Figures 2.4 and 2.5. Figure 2.4 shows the variation of $\alpha\delta/u_*^2$ with respect to the axial distance from the inlet, x/δ_{inlet}, while Figure 2.5 shows the variation of $\alpha\nu/u_*^3$ versus x/δ_{inlet}. It is observed that the different flows behave in different ways, with respect to these parameters. The majority of the flows have $\alpha\delta/u_*^2$ and $\alpha\nu/u_*^3$ increasing in an exponential manner while a couple of the flows have nearly linear variations. The eight degree conical diffuser, however, exhibits a concave down curvature on these plots (or see Trupp et al's (1986) Figure 3), with their respective maxima occurring near the exit.

Kader and Yaglom's velocity defect law constant, C (from equation 26) was modified to fit the experimental data of the eight degree conical diffuser, and a good fit was obtained, as shown in Figure 2.18. The constant increased continuously from the diffuser inlet as did the velocity gradient. The variation of C for this flow is shown in Figure 2.26 and tabulated in Appendix D.

Perry et al (1966), Perry (1966), Kader and Yaglom (1978), and Trupp et al (1986) all acknowledge that there are also other regions in adverse pressure gradient flows, specifically long linear and 3/2-power regions. Trupp et al experimentally correlate the slopes and intercepts of the linear region at each axial location in the conical diffuser. There is apparently no correlation in the literature of the experimental 3/2-power region for any flows.

Only Perry (1966) has developed a semi-empirical correlation for the linear region of the Perry et al (1966) flow development theory. He uses a method similar to his half-power region to obtain the form of, and the constants for, the linear mean velocity profile. However, it is assumed that there are historical effects present in the flow at this point, which are represented analytically by the axial gradient of the kinematic pressure gradient. As with his half-power law, the linear region is assumed to follow the logarithmic region. Perry's linear velocity profile is not examined further.

2.3 Examination of the Two Half-Power Regions

It is observed that in adverse pressure gradient flows there are two regions at each axial station where the mean velocity varies with the square root of the distance from the wall. These regions exist in all of the data examined, although this phenomenon is mentioned only in Trupp et al (1986) with regards to the eight degree conical diffuser.

Although all of the flows progress as described by Perry et al (1966), when the mean velocity is looked at on only half-power coordinates there is definitely a development of two half-power regions. Early in the entry region of these flows the outer half-power slope, C_0 is less than the inner half-power slope, C_i. But as the flows develop, the inner slope decreases while the outer slope increases until they become approximately the same. This is the half-power region discussed by Perry (1966), Samuel and Joubert (1974), and is also (approximately) Kader and Yaglom's (1978) half-power law. As the flow continues to develop, the inner half-power slope becomes very small relative to the outer slope. This progression is exhibited in Figure 2.27, for Fraser's flow A (flow # 5000). This is representative of all the data sets examined as shown in Appendix C.

In the entry region, where $C_i > C_o$, there is some uncertainty about C_i in some of the plane diffuser data because there are few data points at each axial station. Also, there is no entry length data available for these flows. However, in the conical geometries there is no problem observing the inner half-power law in the entry region since there is a multitude of entry length data for these flows, and hence, there is less uncertainty.

The ratio of the inner to outer half-power slopes seems to be quite important. The entry length may well be related to C_o/C_i becoming large enough. Figure 2.28 shows how the ratio of C_o/C_i changes with u_*/U_∞. The degree of correlation is high. The flows develop as u_*/U_∞ decreases (right to left on this plot), with C_o/C_i increasing in this direction. The mean velocity becomes universal for the flows examined here in the range $1.1 < C_o/C_i < 1.4$ for the plane diffusers and $1.2 < C_o/C_i < 4$ for the conical geometries. This criterion is dependent on initial conditions as shown by the six degree conical diffuser of Pozzorini. Flow # 0142 develops a universal profile at $C_o/C_i = 3.2$ while in flow # 0143, it is universal at $C_o/C_i = 1.2$.

It is observed that the inner half-power region overlaps with the Log Law, especially when the Log Law is long. It, therefore, seems reasonable to expect C_i to be a function of the friction velocity, just as the Log Law is. Figure 2.29 shows the plot of the inner slope versus the friction velocity. C_i is definitely a function of u_* as seen on this dimensional plot. However, the best non-dimensional correlation of the inner half-power slope is shown in Figures 2.30. The correlation with this particular non-dimensionalization $(C_i/(U_\infty \ \delta^{1/2})$ versus $x/\delta_{inlet} * \alpha\delta/u_*^2)$ may well be fortuitous, but it at least shows the trend, and offers a first approximation in prediction of the slope. This is most useful in the entry length region where Coles' profile does not work and the Log Law region is small. A moderately better correlation for C_o/C_i is shown in Figure 2.31. The scatter here is less than in Figure 2.28, the only exception on this plot is the ten degree conical diffuser of Fraser where the shape of the curve is the same and it only appears to be "out of phase" with the other data.

There was great difficulty correlating the intercepts (or "slip velocities") of the half-power laws. This is probably because of its sensitivity to the half-power slope. Another possible cause of this difficulty could be because of the data shown in Figure 2.22. This figure shows all of the stations in the eight degree and the two six degree conical diffuser flows. This figure shows that the Law of the Wake occurs at different distances from the wall for different flows, as discussed previously. This causes real difficulty in correlating the intercepts of the half-power regions, especially the outer region. The best correlation for D_i is D_i/U_∞ versus $\alpha\nu/u_*^3$ as shown on Figure 2.32. The agreement is adequate and it does show the trend. Again, good correlation occurs for the ratio of intercepts , D_o/D_i as a function of u_*/U_∞ as shown in Figure 2.33.

Trupp et al (1986) state that there are linear blending regions between the two half-power regions in the eight degree conical diffuser. The data examined in that paper is only near wall data, so that towards the exit there is no data for the outer half-power region. Upon further examination of the experimental data of Turan (1988), Kassab (1986), and Ozimek (1985) from the same conical diffuser, it has been observed that there are two half-power regions present throughout the flow, as already mentioned. Early into all of the diffusers (when $C_i > C_o$) the blending region is small, indeed almost non-existent on half-power coordinates. At this point there are no substantial linear regions present in any of the flows examined. As the flows develop, the slopes of the two half-power regions become equal and one long half-power region is present in the flows. This is the half-power region described by Perry (1966). As the flows develop further, the two half-power regions begin to separate and the blending region becomes linear. Further downstream, the blending region becomes large and has a 3/2-power velocity distribution. This development can be seen in Figures 2.34 - 35. Figure 2.34 shows the linear blending region at station 5 in flow #0142 while Figure 2.35 shows the 3/2-power blending region at station 11. It is observed that the region of overlap can be quite large, especially at the locations where the linear and the 3/2-power regions become dominant.

The only exception to the above discussion is flow # 0143. This flow has a very long entry length caused by the "backward facing step" arrangement just upstream of the diffuser entrance (which was used to generate high core turbulence). Indeed, Coles' profile only works at the last measurement station in this flow. This flow has a much longer entry length than any of the other flows examined. In this flow C_o becomes greater than C_i at the last station, hence the flow flow development is much slower.

Flows 1100 and 1200 developed in much less extreme adverse pressure gradients. Hence, flow 1100 never develops a 3/2 power region and flow 1200 only barely develops a 3/2 power region. All of the other flows have more severe adverse pressure gradients and the 3/2-power region develops readily.

The development of the linear regions of this class of flows appears to be related to the decreasing adverse pressure gradient. Upon examining Samuel and Joubert's (1974) increasing adverse pressure gradient flow (Stanford Conference flow # 0141) it appears that the linear regions are delayed until the adverse pressure gradient starts to decrease. This also appears to be the case in the other flows examined where the pressure gradient increases for only a short distance from the inlet. Once the pressure gradient starts to decrease the ratio of outer half-power slope to the inner slope starts to increase and the long linear blending region between the two 1/2-power regions occurs.

The development of the two half-power regions ties together the flow development theories of Kader and Yaglom (1978) and Perry et al (1966). For the pressure gradients of the flows examined here, a logarithmic region exists at each station, overlapping at least partially with the inner half-power region. Kader and Yaglom's similarity analysis, which shows that there should be a half-power region following the logarithmic region, verifies this. Perry's (1966) linear profile supposedly follows the Log Law but the experimental data shows that a half-power region precedes it. Kader and Yaglom, also, acknowledge that there are linear regions in this class of flows but make no attempt to correlate them. This of course, does not explain the presence of the second (outer) half-power region.

The two half-power regions can also be used to examine where exactly the mean velocity formulations from the previous section correlate the experimental data. Table 2.3 compiles these results, showing exactly where the models of Townsend, McDonald, Kader and Yaglom's half-power and defect regions, Perry's half-power region, and Coles' Law of the Wake work. Generally, Townsend's model works for $C_o/C_i < 1.2$ and McDonald's when $C_o/C_i < 2.5$. Kader and Yaglom's half-power law correlates the data over a wider range than Perry's, while Kader and Yaglom's defect works over an even wider range. Coles profile was discussed previously as the universal profile.

Many of the theories for the half-power region are based on the idea that there is an approximately linear turbulent shear stress distribution (Townsend (1961), Mellor (1966), and McDonald (1969)). It has been observed for the three flows with turbulence measurements (flow #'s 0142, 0143, and the eight degree conical diffuser) that the second half-power region occurs after the peak of $\overline{uv}$, when it decreases in an approximately linear manner. The outer half-power region may be related to this linear stress layer, just as the inner half-power law is.

2.4 Conclusions

The criterion for moving equilibrium of Kader and Yaglom has been found to be of general use because it shows that the flow is dependent on the local flow variables (U_∞, u_*, α, and δ). These local flow variables give rise to distinct length scales which, in turn, imply that a composite velocity profile exists. This is indeed seen to be the case.

It is apparent from the experimental data that there is a universal mean velocity profile in wall-bounded adverse pressure gradient flows. This universal profile, the Log Law with Coles' Law of the Wake, occurs after a certain entry length and before separation possibly occurs. This could be related to the mean field coming to a type of moving equilibrium. Indeed, the universal mean velocity profile starts to fit the experimental data only after the pressure gradient has decreased significantly.

It is difficult to say whether or not there is a universal mean velocity profile in the viscous sublayer and buffer region. The mean velocity is dependent on the pressure gradient and could vary substantially from the usual Law of the Wall as shown by McDonald (1969). It was also observed that the Log Law could penetrate the sublayer and buffer to distances quite close to the wall, verifying the theory of McDonald (1969) and the experimental observation of Trupp et al (1986) for the eight degree conical diffuser.

The Log Law was seen to exist for all of the flows examined, although it was severely shortened at some stations. The Log Law constants could be used without modification if Clauser's method had been used to determine the friction velocity. Much of the scatter around the Log Law was eliminated when Clauser's method was used instead of a Preston Tube. It is doubtful, however, that Clauser's method is more accurate then the Preston Tube in determining the wall shear stress because it assumes a Log Law at a certain location.

McDonald's model works reasonably well as a replacement for the Log Law in the entry region, but it requires the pre-knowledge of the turbulent shear stress $\overline{uv}$. The shear stress gradient can be approximated by 0.67 times the pressure gradient in the entry region.

The existing models for the outer layer in general do only an adequate (at best) job in predicting the mean velocity profiles, especially as a means for predicting the majority of the entry region. Kader and Yaglom's half-power law does a better job than Perry's half-power law overall.

It was observed that there are two half-power regions present in the eight decreasing adverse pressure gradient flows examined. The ratios of the inner and outer half-power slopes and intercepts correlate well with the ratio of the friction velocity and the freestream velocity. A reasonable correlation was obtained for the inner half-power slope and intercept in terms of $C_i/(U_\infty \delta^{1/2})$ versus $x/\delta_{inlet}(\alpha\delta/u_*^2)$ and D_i/U_∞ versus $\alpha\nu/u_*^3$.

The entry length was seen to be possibly related to the ratio of the inner and outer half-power slopes. The entry length was observed to be initial conditions dependent. The analytical and semi-empirical mean velocity profiles in the literature were examined as to where they correlate the experimental data in terms of the two half-power regions.

The blending region between the two 1/2-power regions was small when the inner half-power slope was larger then the outer half-power slope. As the flows develop, the outer half-power slope grows larger than the inner half-power slope and the blending region becomes longer and is linear. Further into the flows, the blending region varies with the 3/2-power of the distance from the wall.

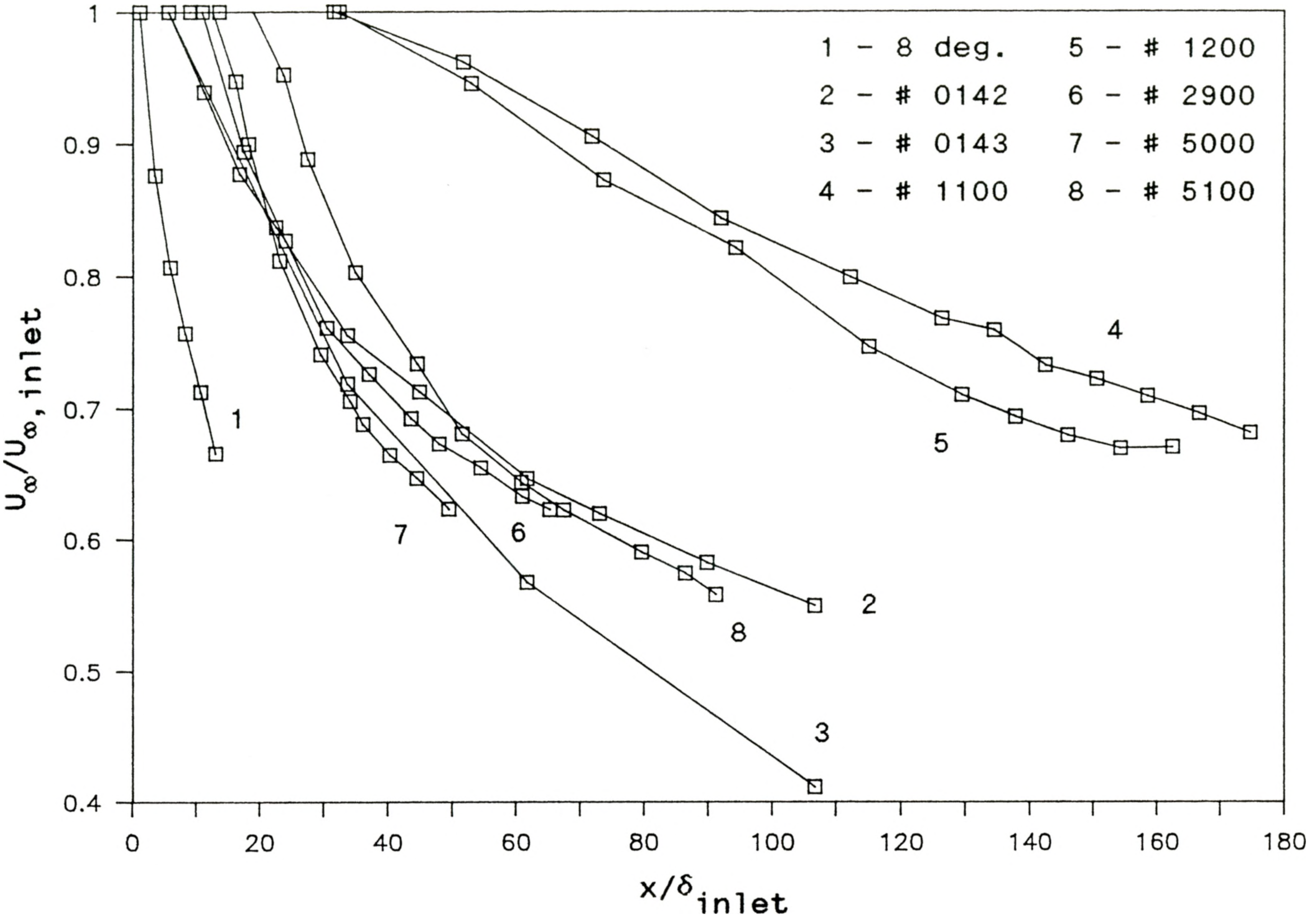

2.1 $U_\infty/U_{\infty,\text{inlet}}$ versus x/δ_{inlet} for the eight decreasing adverse pressure gradient flows examined.

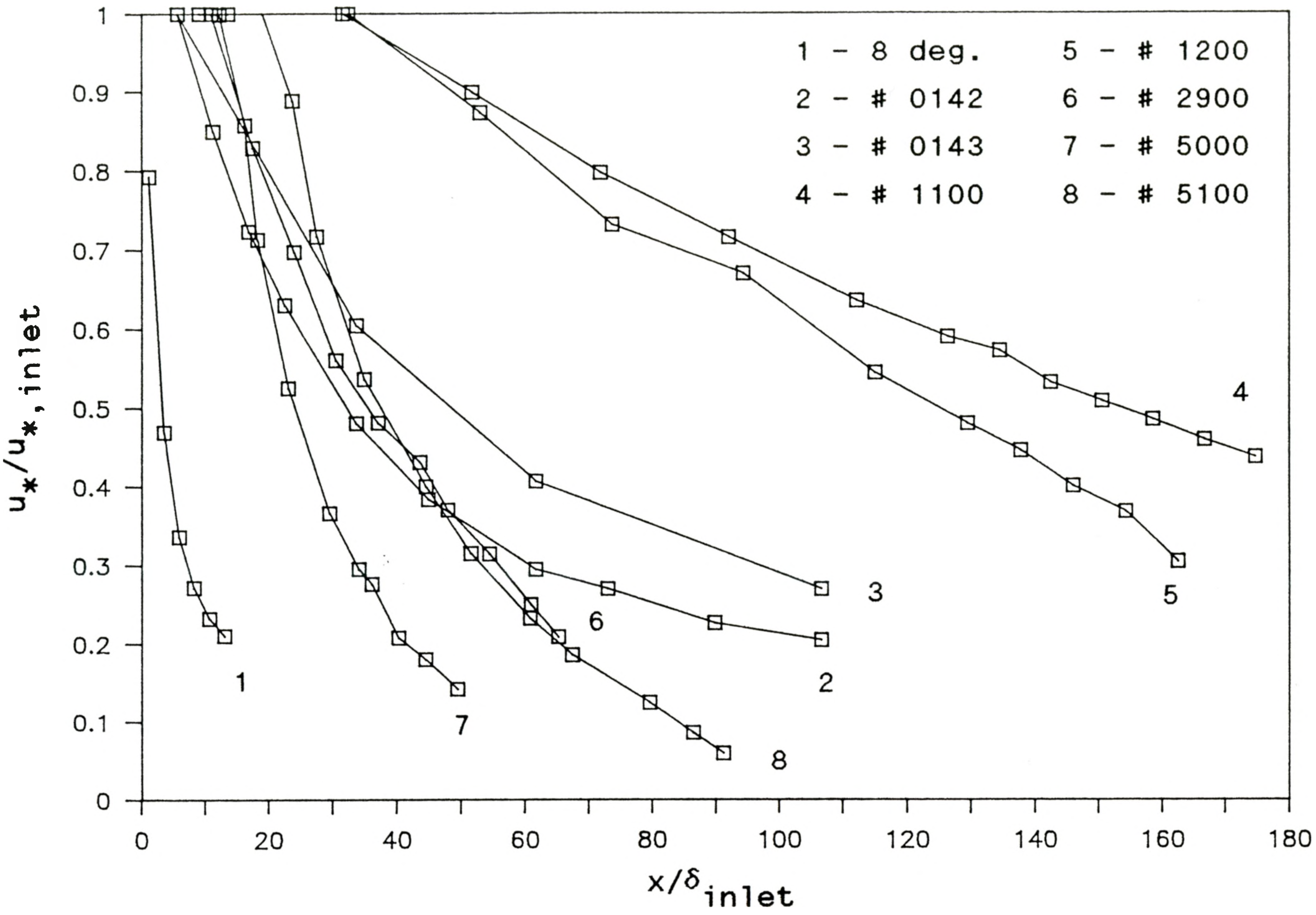

2.2 $u_*/u_{*,inlet}$ versus x/δ_{inlet} for the eight decreasing adverse pressure gradient flows examined.

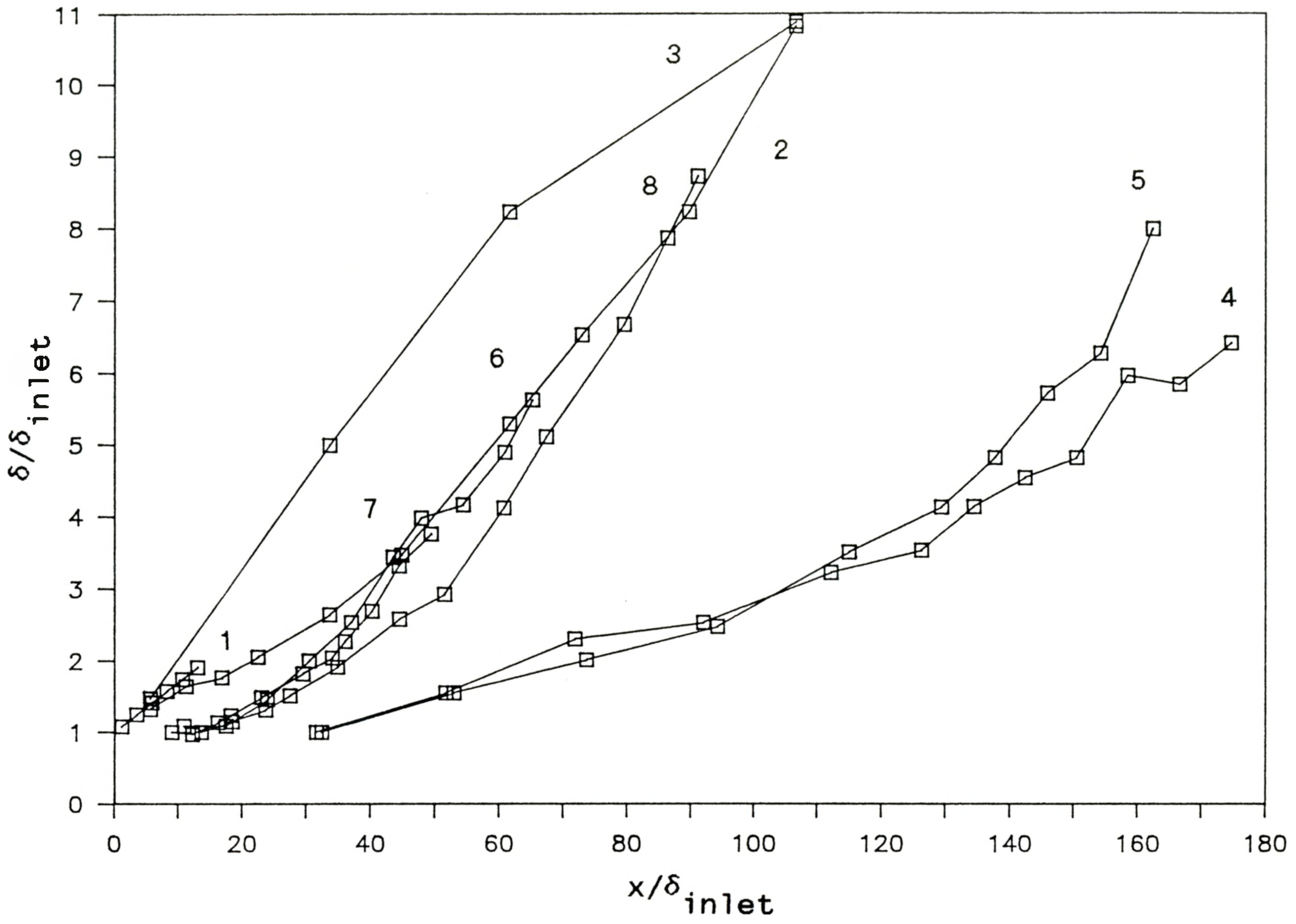

2.3 δ/δ_{inlet} versus x/δ_{inlet} for the eight decreasing adverse pressure gradient flows examined (see legend for Figure 2.1).

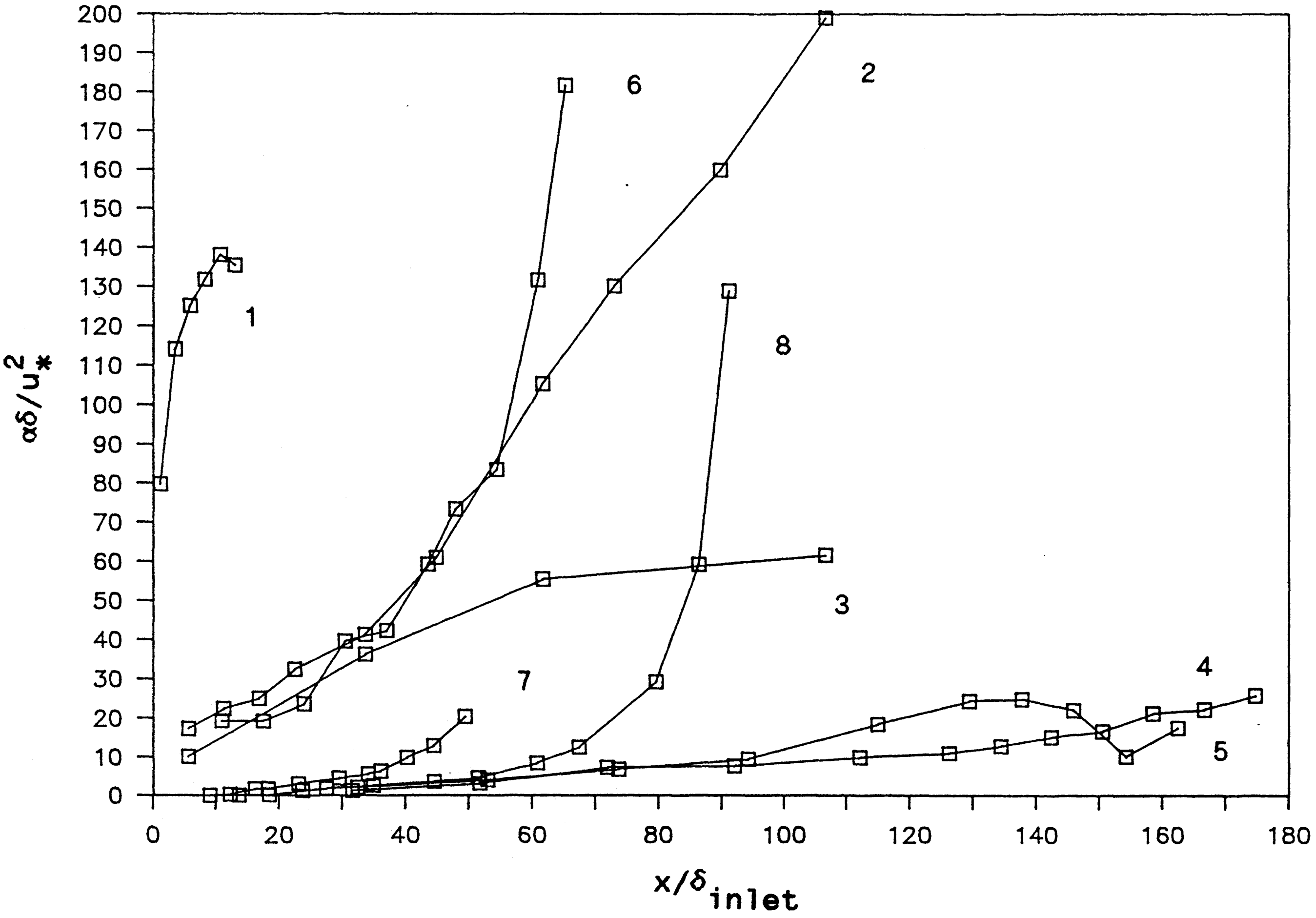

2.4 $\alpha\delta/u_*^2$ versus x/δ_{inlet} for the eight decreasing adverse pressure gradient flows examined (see legend for Figure 2.1).

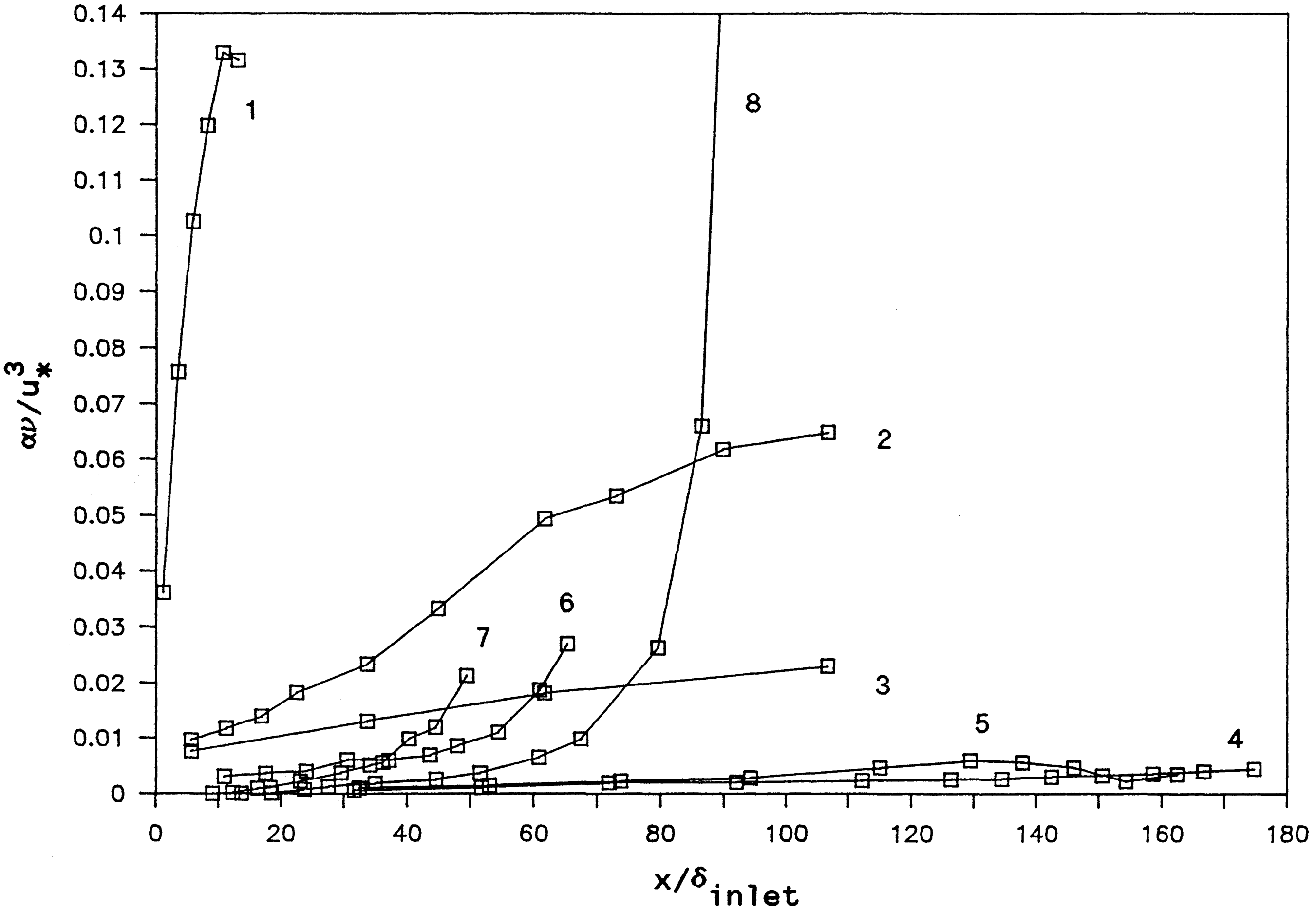

2.5 $\alpha\nu/u_*^3$ versus x/δ_{inlet} for the eight decreasing adverse pressure gradient flows examined (see legend for Figure 2.1).

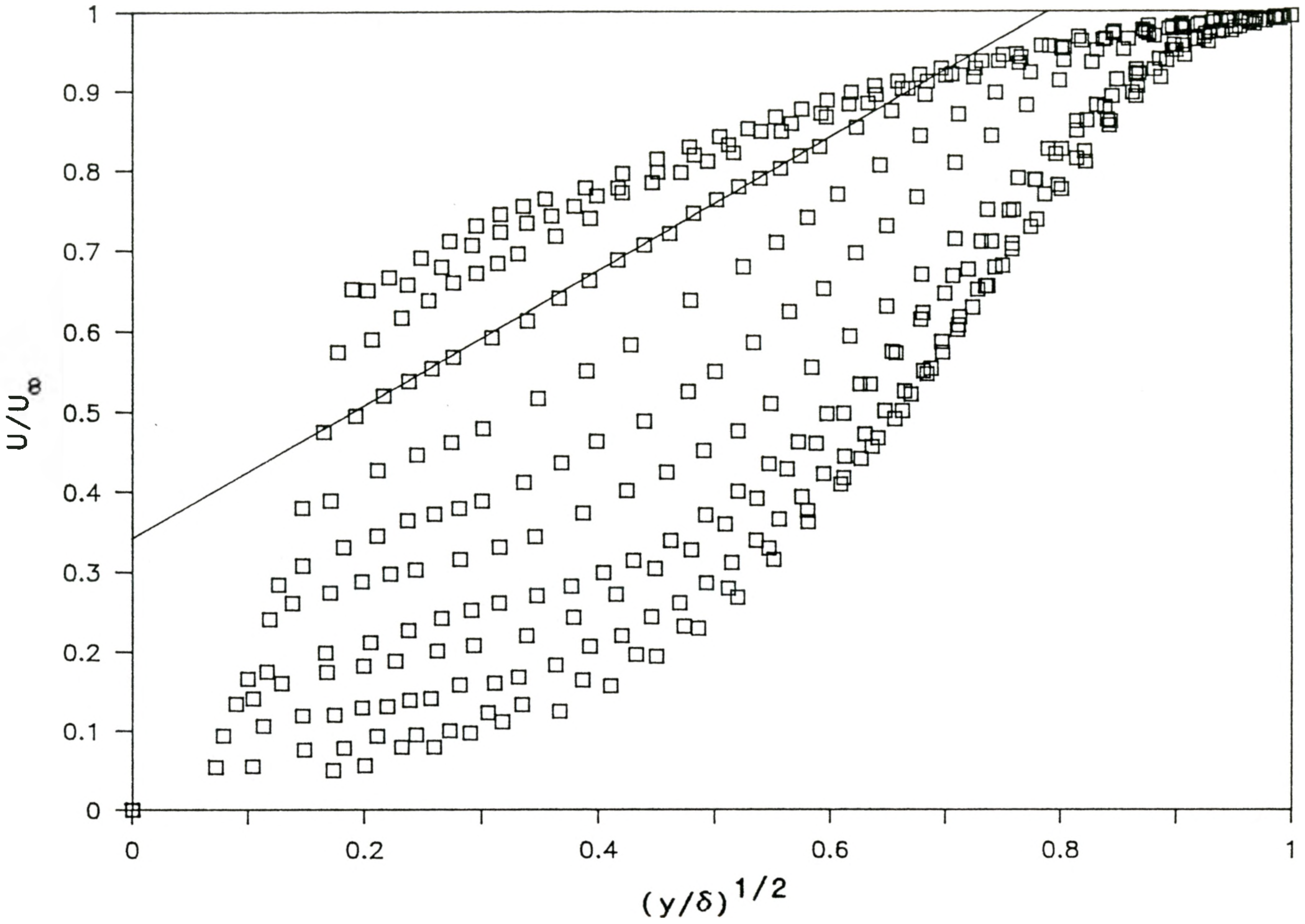

2.6 The experimental mean velocity profiles in Fraser's flow #5100. The solid line shown is through the half-power region at station 4.

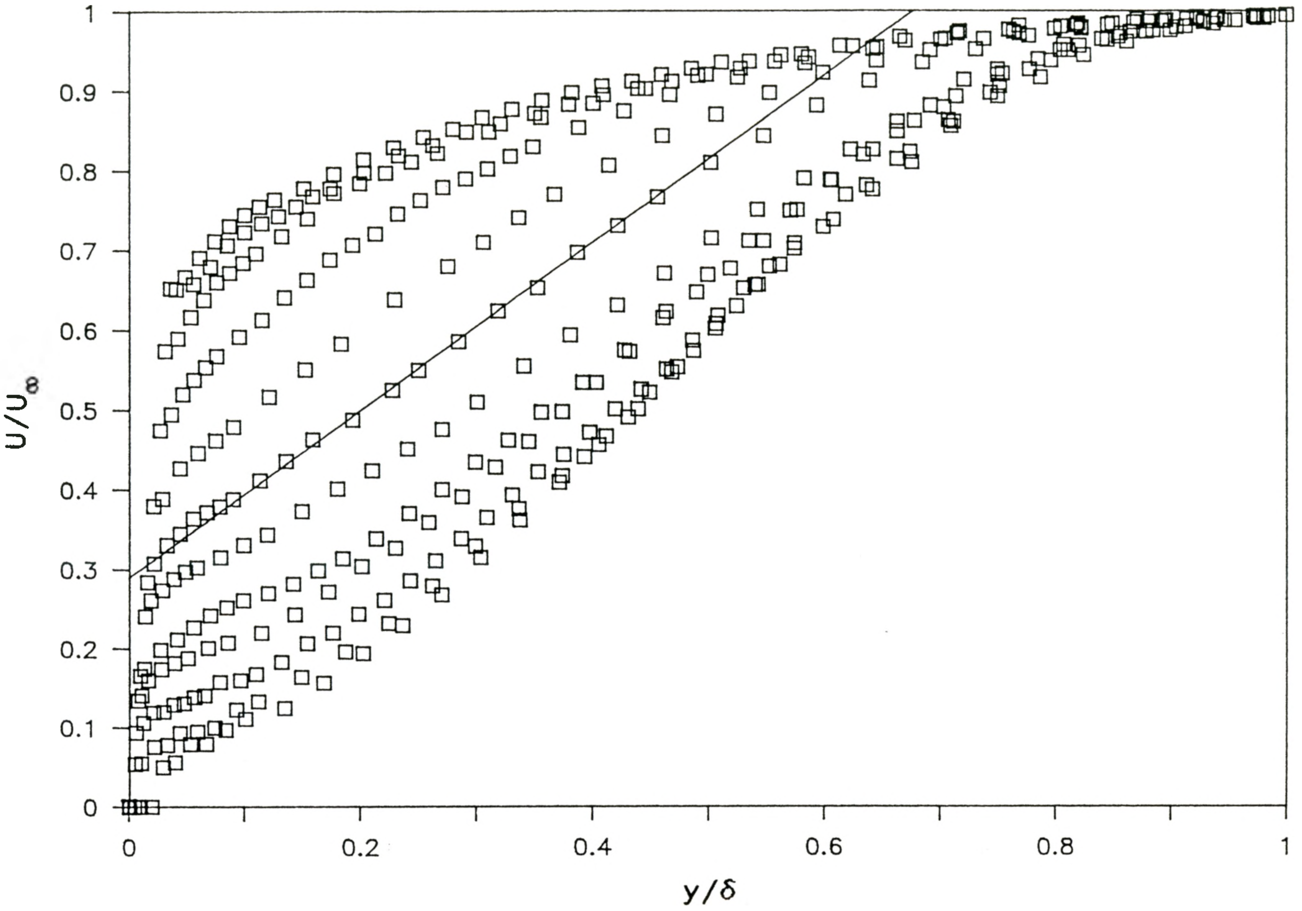

2.7 The experimental mean velocity profiles in Fraser's flow #5100. The solid line shown is through the half-power region at station 6.

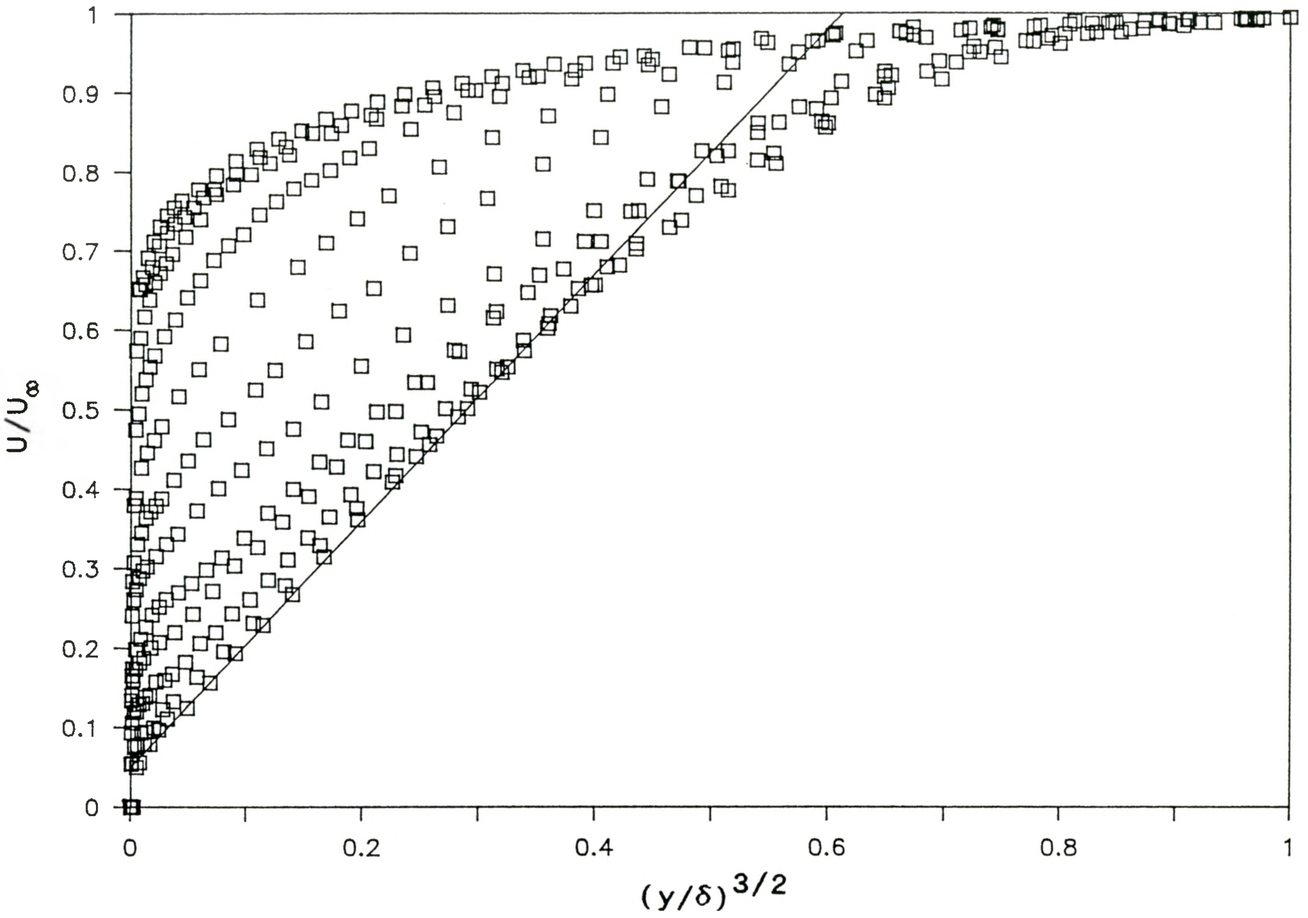

2.8 The experimental mean velocity profiles in Fraser's flow #5100. The solid line shown is through the half-power region at station 12.

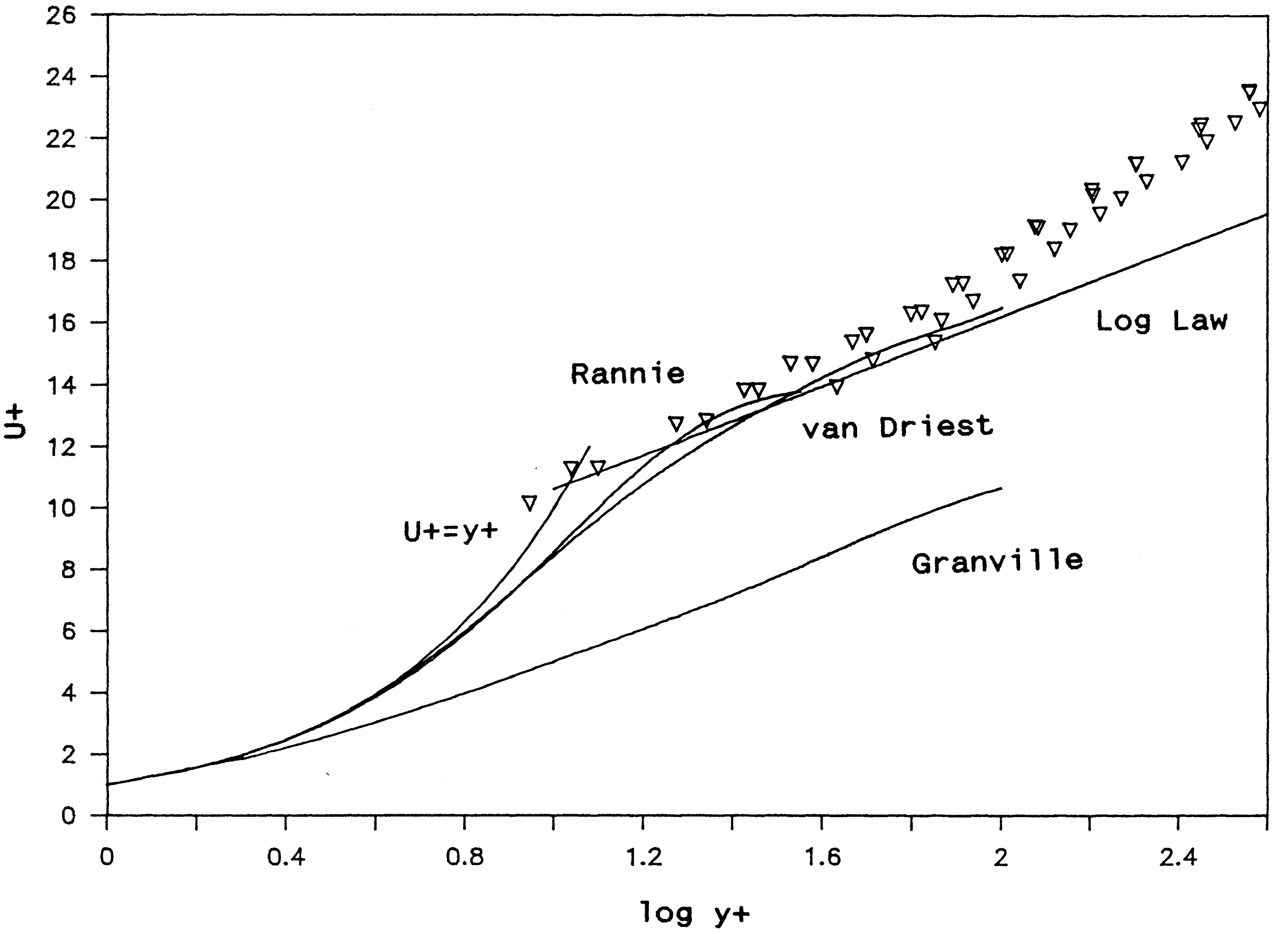

2.9 The experimental data of Ozimek (1985) and Kassab (1986) from the eight degree conical diffuser at x=6cm along with the Log Law (x=0.41, b=5.0), and from left to right, U+ = y+, Rannie, van Driest, and Granville.

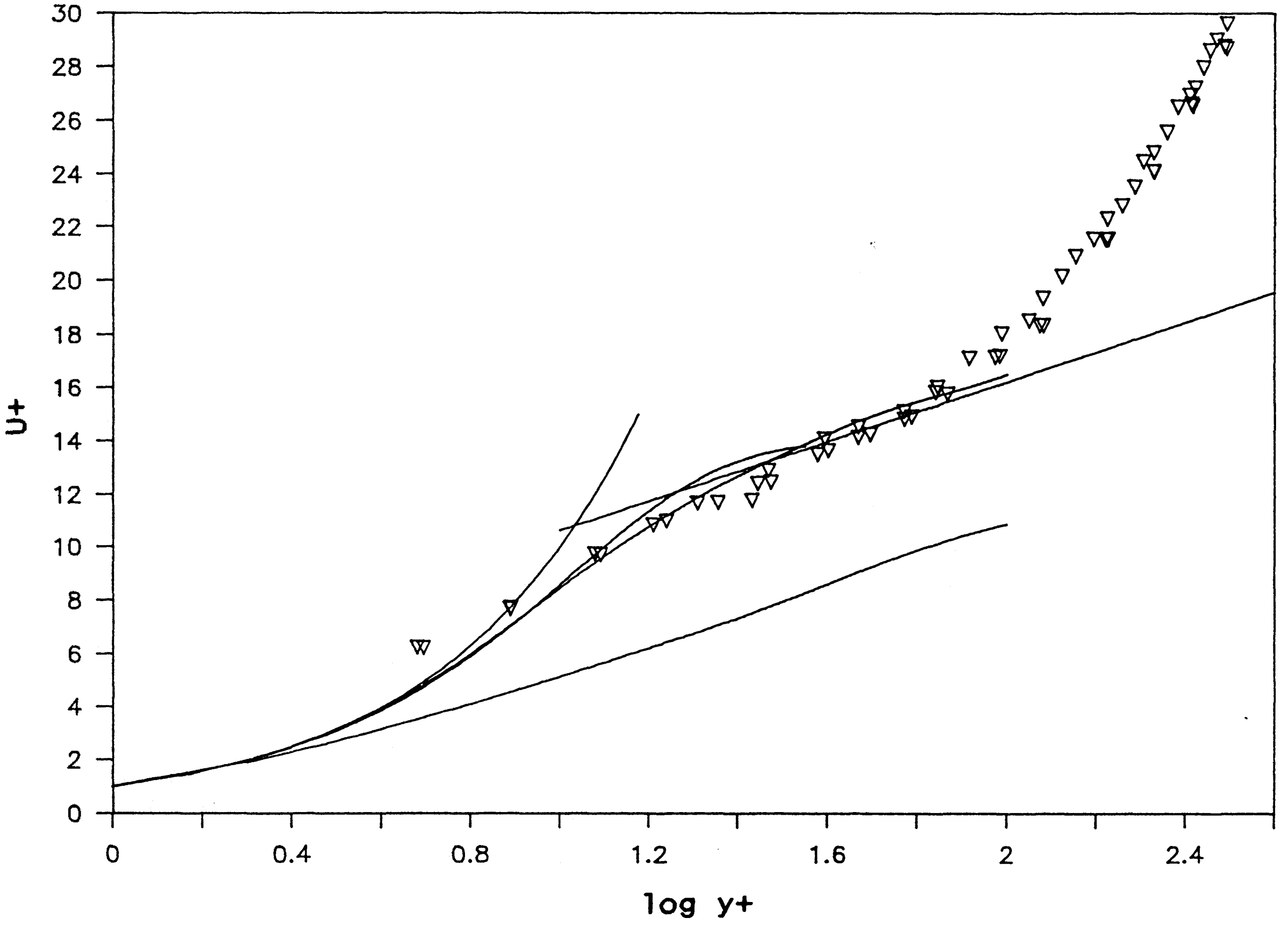

2.10 The experimental data of Ozimek (1985) and Kassab (1986) from the eight degree conical diffuser at x=18cm along with the Log Law (x=0.41, b=5.0), and from left to right, U+ = y+, Rannie, van Driest, and Granville, similar to Figure 2.9.

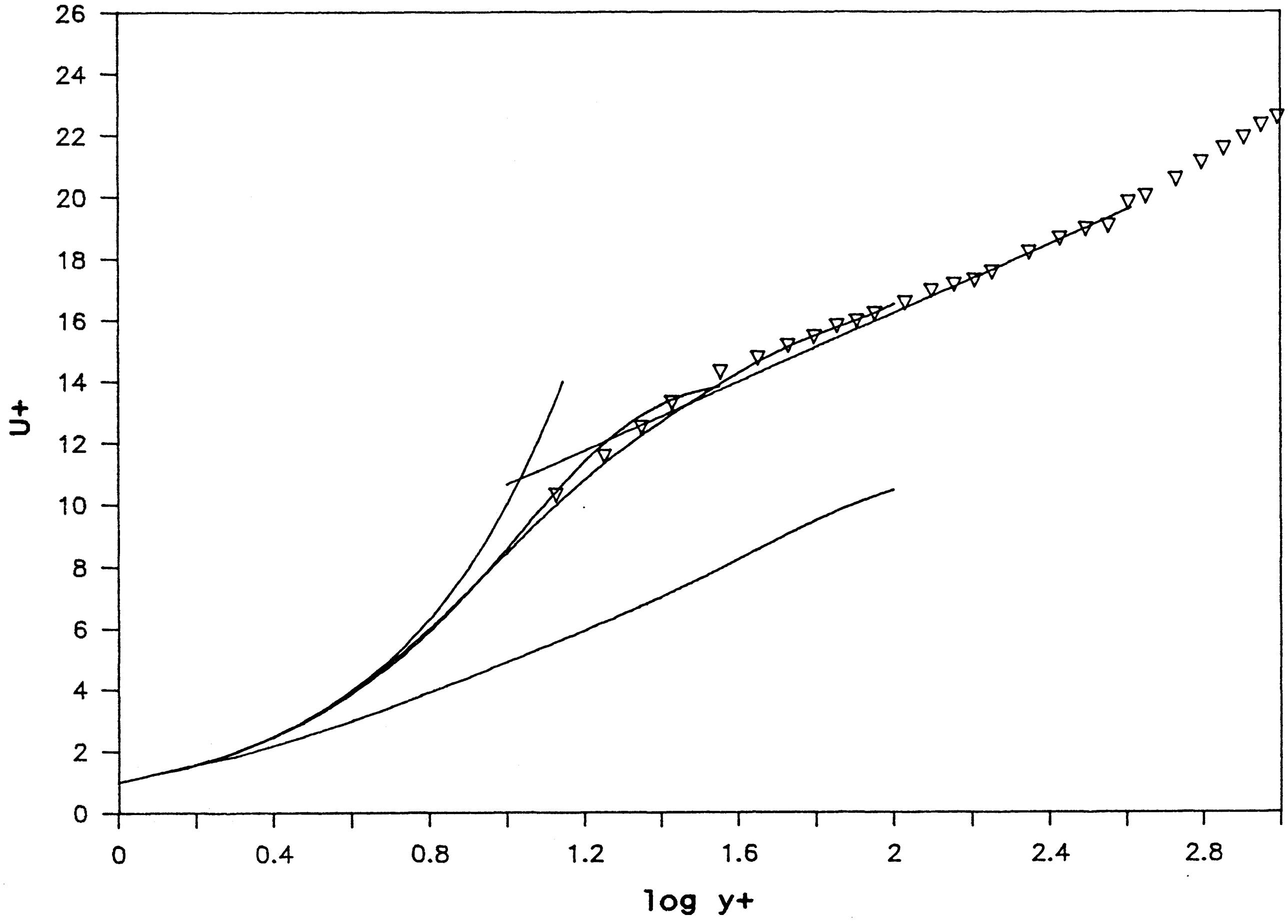

2.11 The experimental data from Perry's flow #2900 at x=3.048m along with the Log Law (x=0.41, b=5.0), and from left to right, U+ = y+, Rannie, van Driest, and Granville, similar to Figure 2.9.

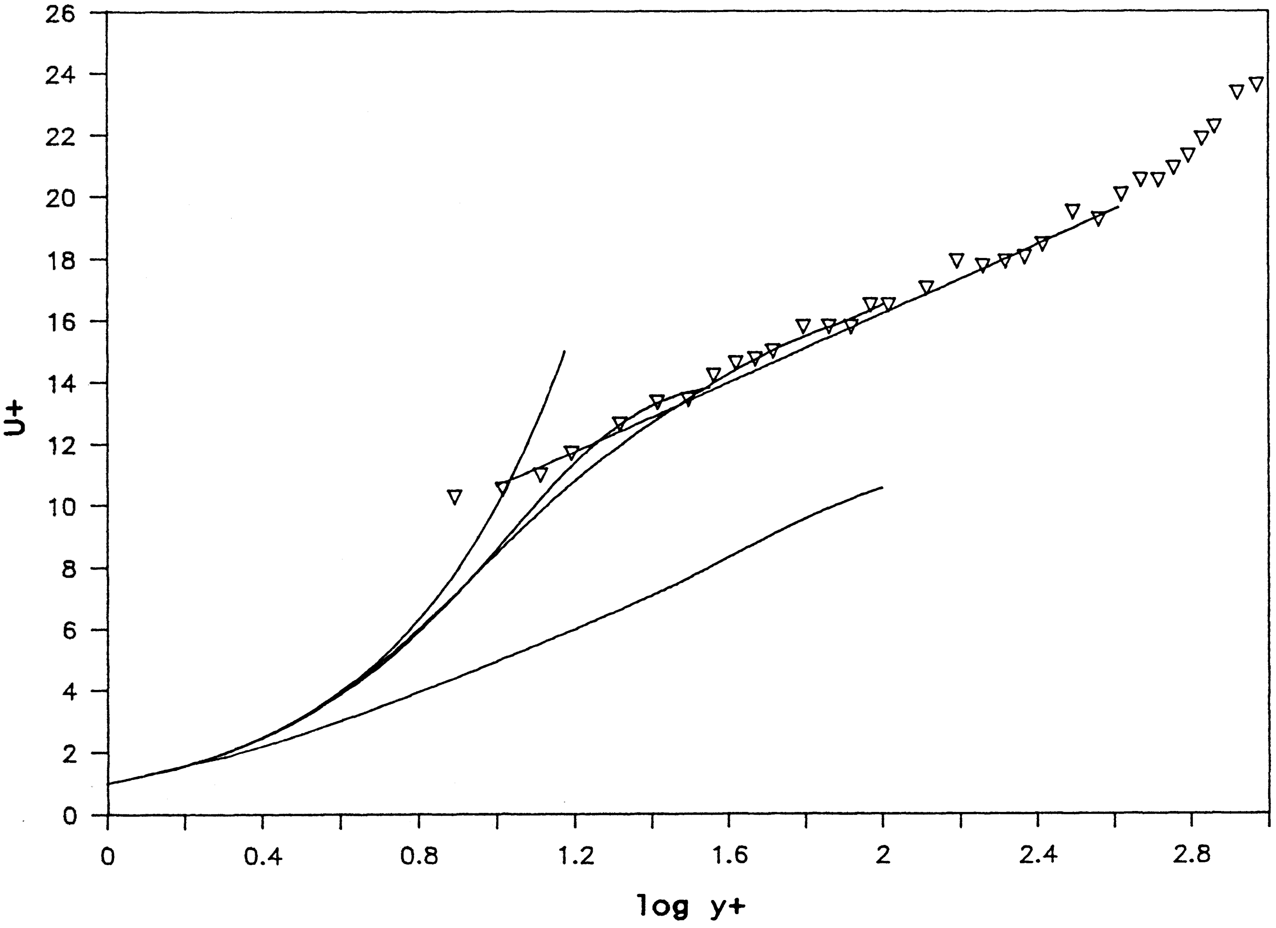

2.12 The experimental data from Perry's flow #2900 at x=4.267m along with the Log Law (x=0.41, b=5.0), and from left to right, U+ = y+, Rannie, van Driest, and Granville, similar to Figure 2.9.

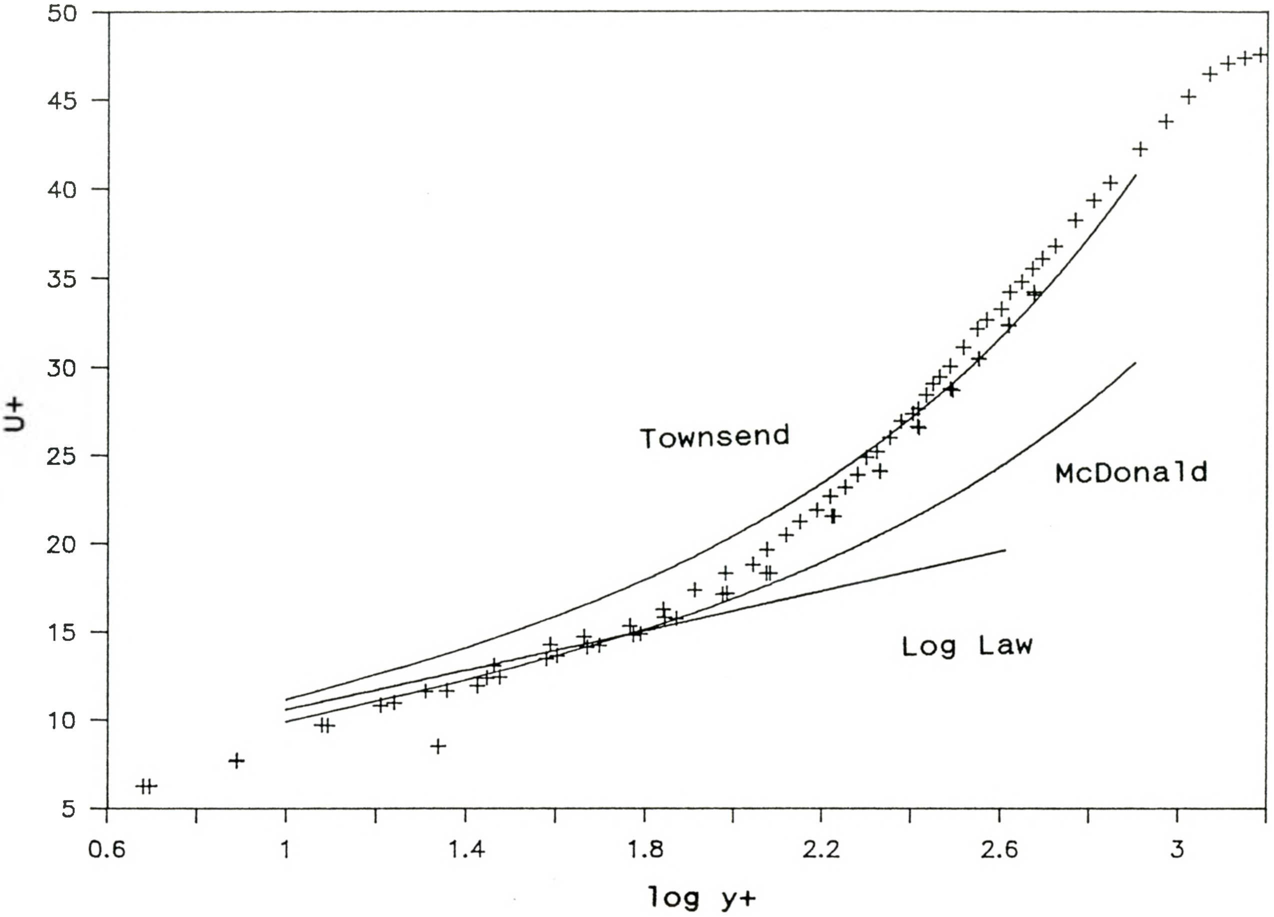

2.13 The experimental data of Ozimek (1985) and Kassab (1986) from the eight degree conical diffuser along with the Log Law, Townsend, and McDonald at x=18cm. McDonald's profile is below Townsend's: a=0.126, γ=0.40, $U_s=U_s(T)-0.8$. $U_s(T)$ is Townsend's slip velocity (equation 12) non-dimensionalized with u_*.

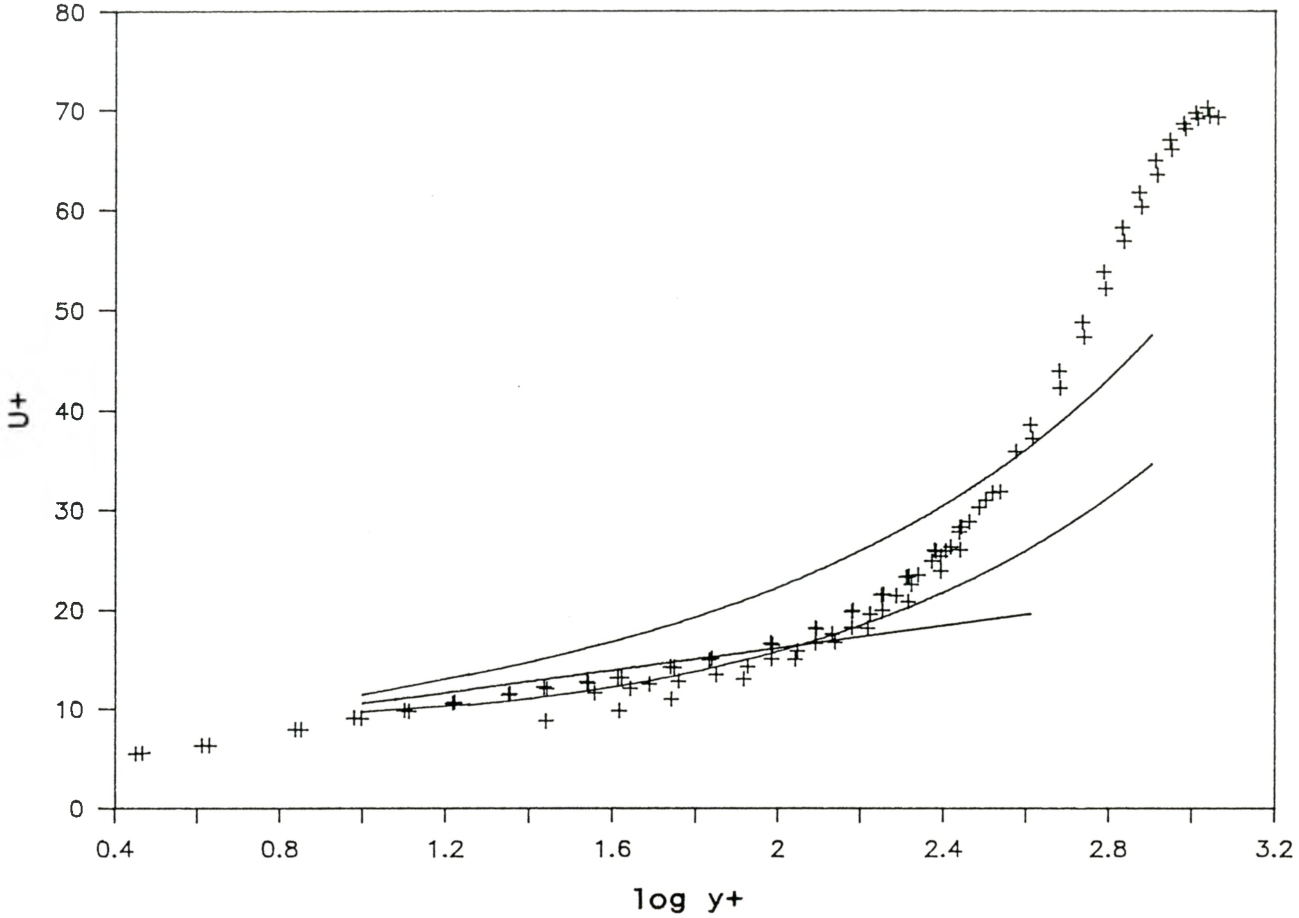

2.14 The experimental data of Turan (1988), Ozimek (1985), and Kassab (1986) from the eight degree conical diffuser along with the Log Law, Townsend, and McDonald at x=42cm. McDonald's profile is below Townsend's: a=-0.017, γ=0.585, $U_s = U_s(T) - 3.6$. $U_s(T)$ is Townsend's slip velocity (equation 12) non-dimensionalized with u_*.

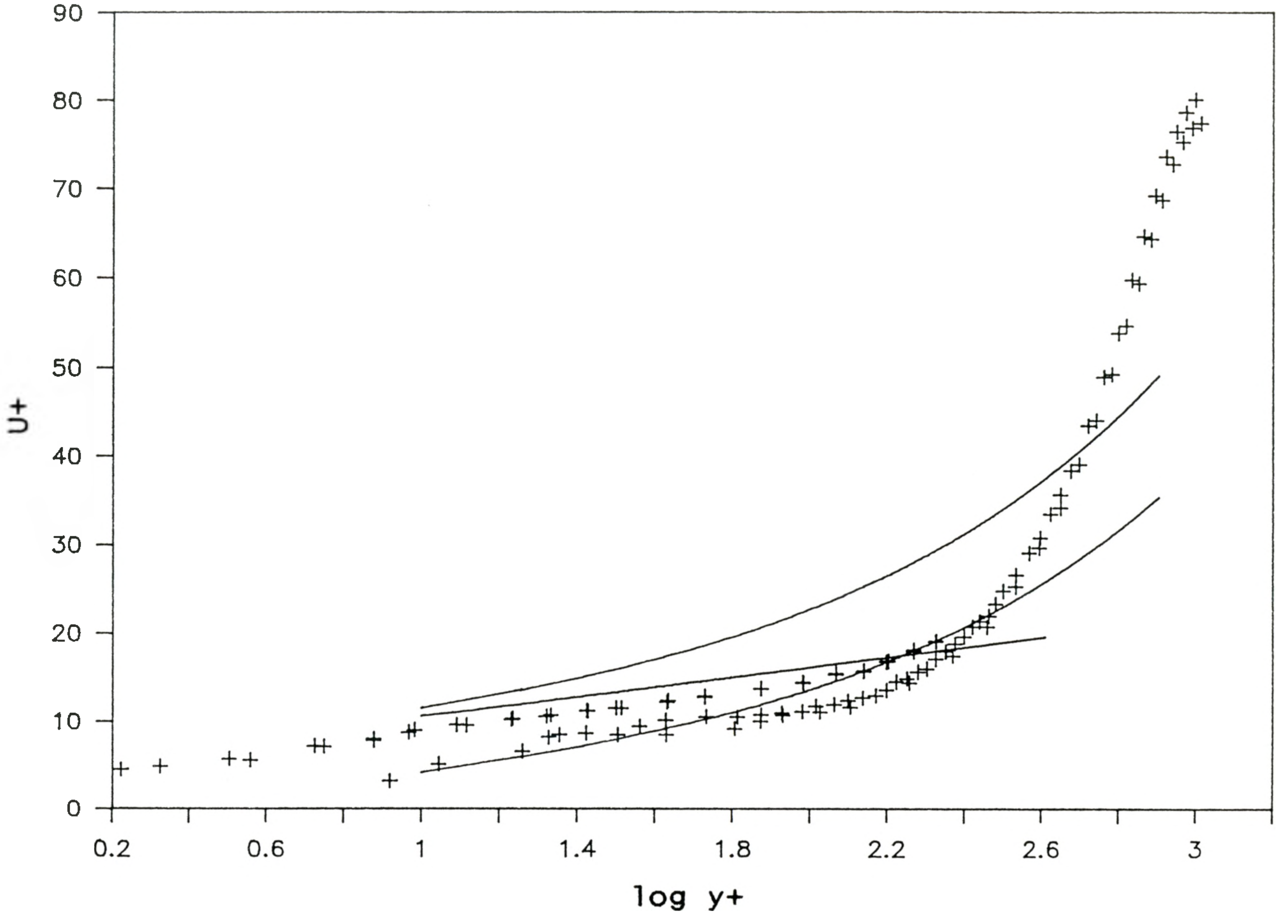

2.15 The experimental data of Turan (1988), Ozimek (1985), and Kassab (1986) from the eight degree conical diffuser along with the Log Law, Townsend, and McDonald at x=66cm. McDonald's profile is below Townsend's: a=0.025, γ=0.673, $U_s=U_s(T)-7.3$. $U_s(T)$ is Townsend's slip velocity (equation 12) non-dimensionalized with u_*.

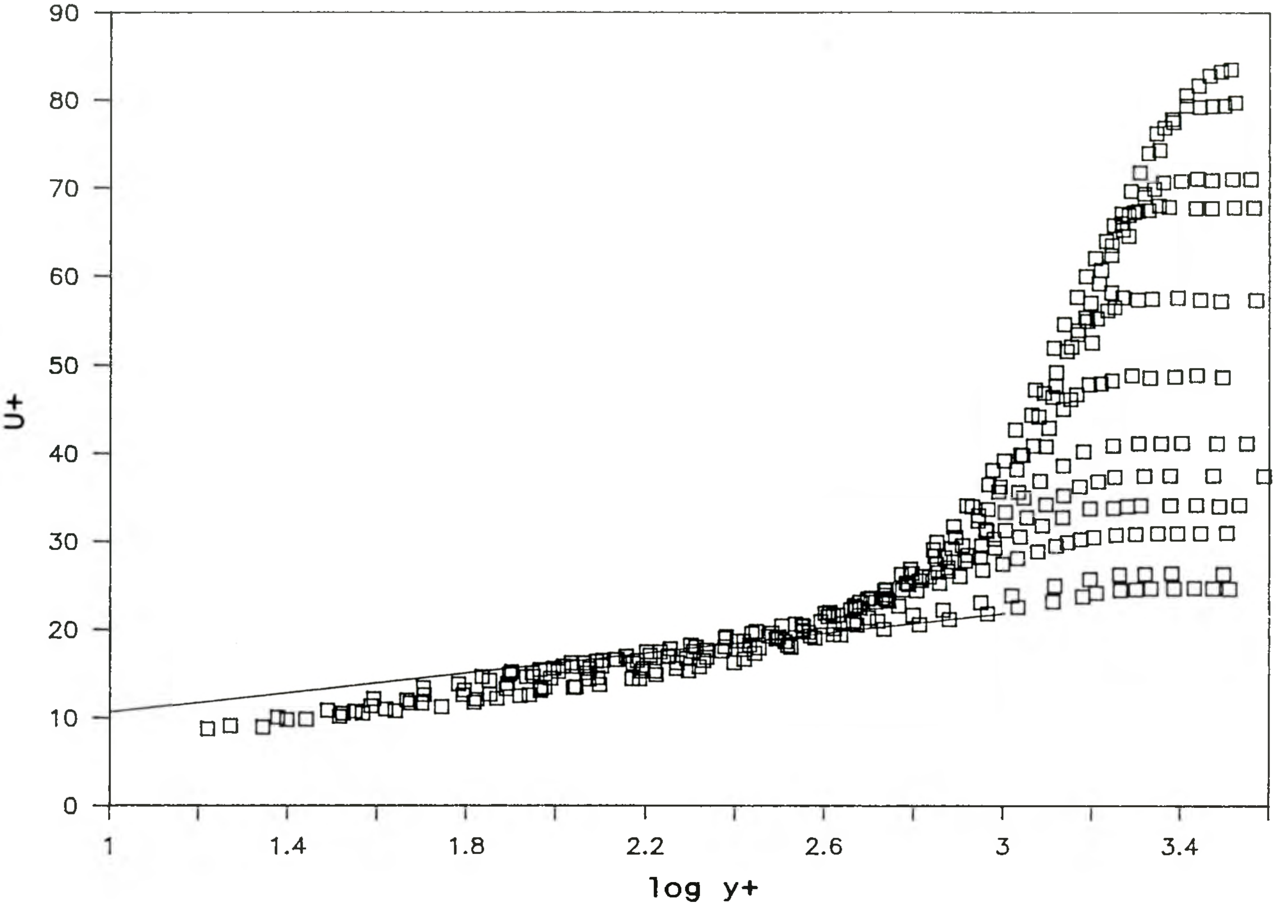

2.16 Data from all of the stations of flow #0142 with u_* from the Preston Tube method.

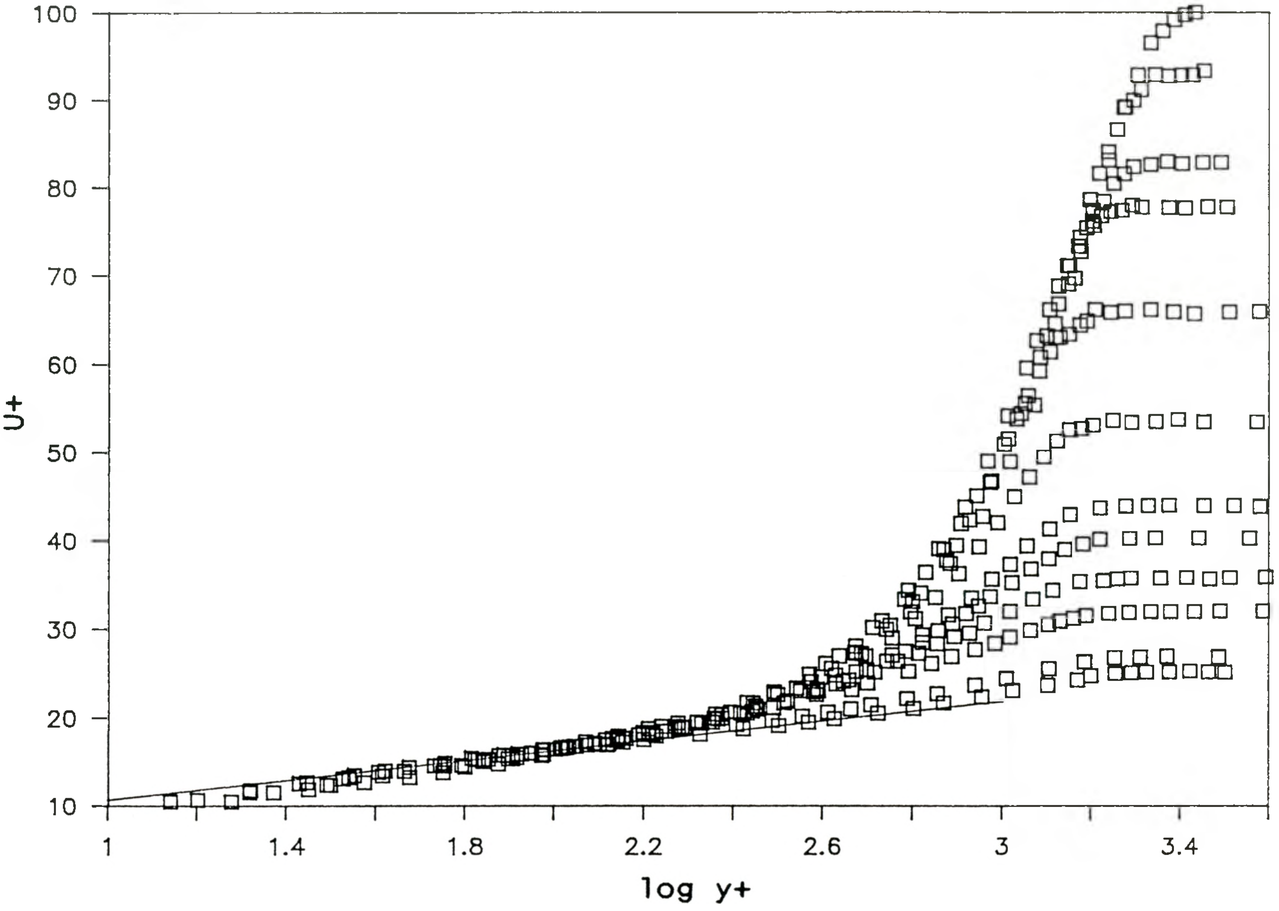

2.17 Data from all of the stations of flow #0142 with u_* from Clauser's method.

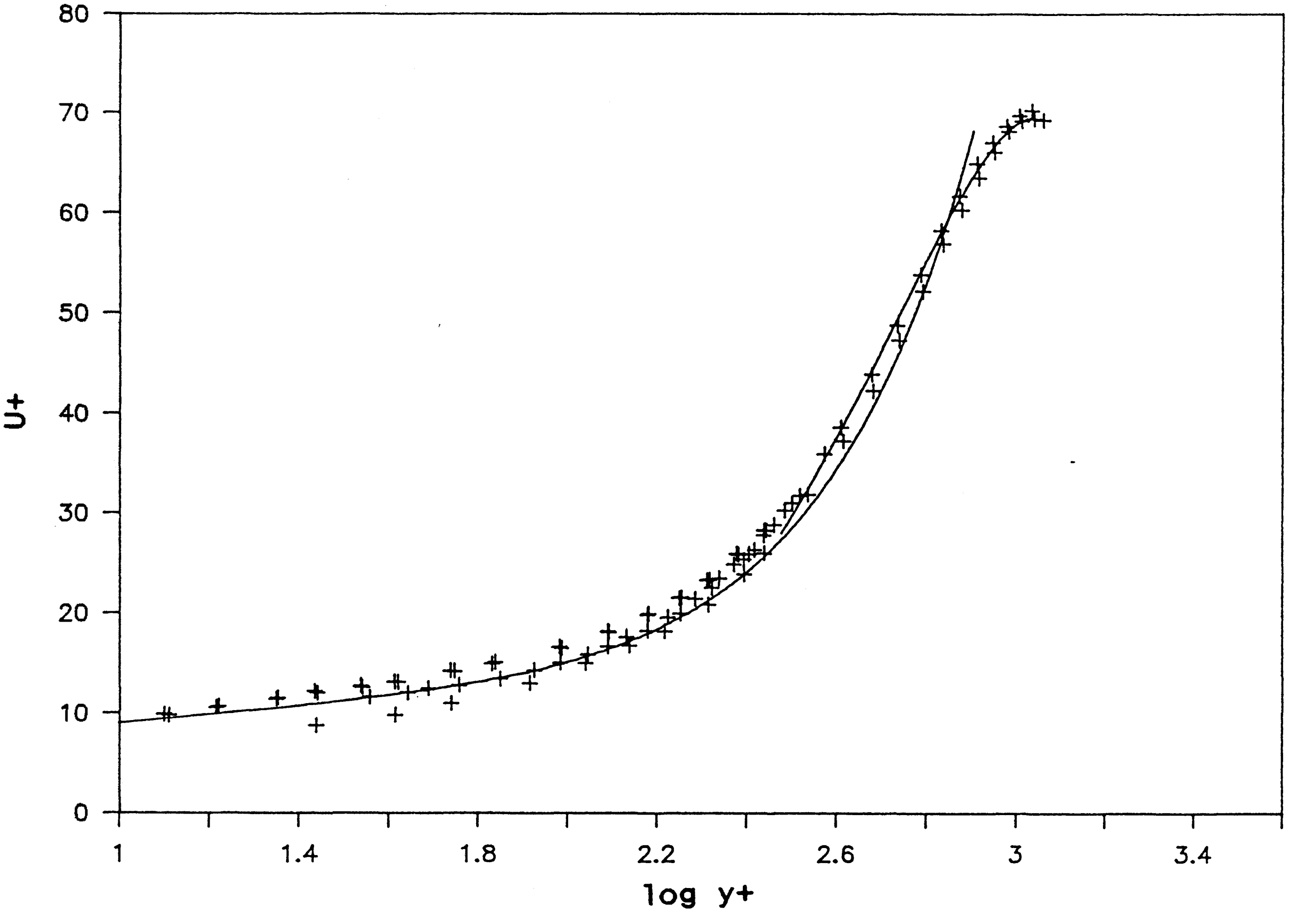

2.18 Data from the eight degree conical diffuser at x=42cm along with the modified Nakayama and Koyama formulation and the modified Kader and Yaglom velocity defect.

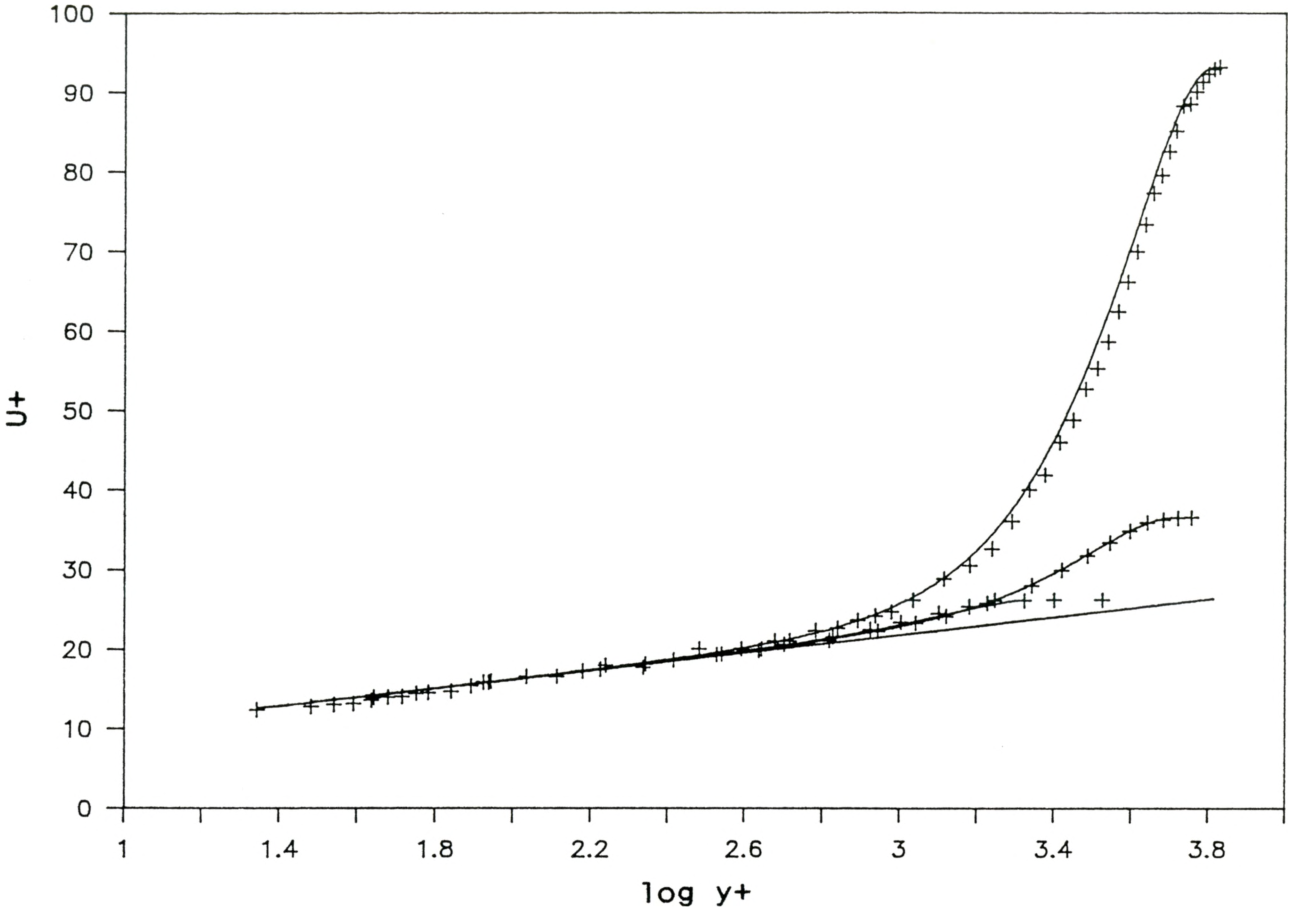

2.19 Coles' Law of the Wake compared with the experimental data, from top to bottom: flow #2900 station 10, flow #1100 station 8, and flow #1200 station 1.

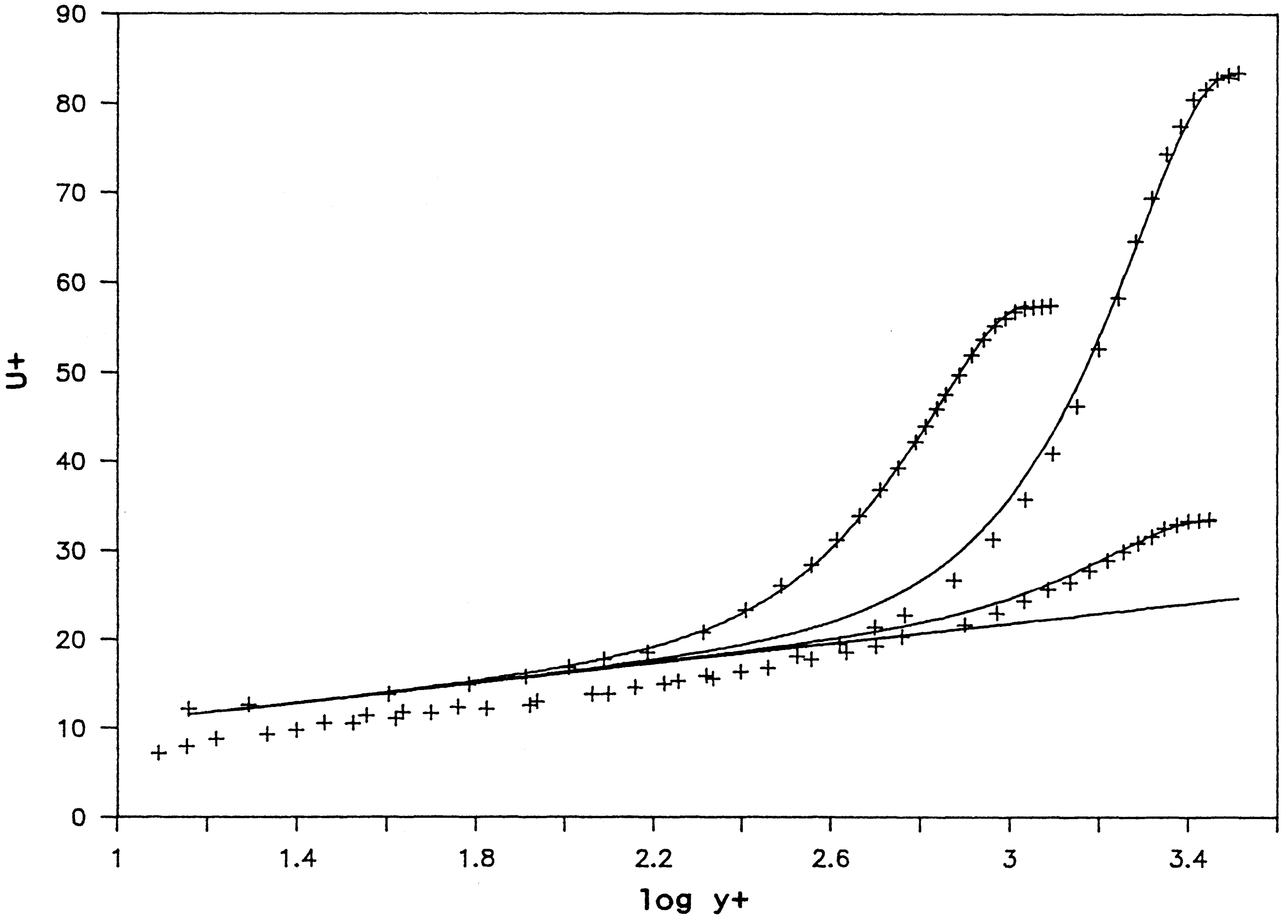

2.20 Coles' Law of the Wake compared with the experimental data, from top to bottom: flow #5000 station 7, flow #0142 x=0.572m, and flow #0143 x=1.813m.

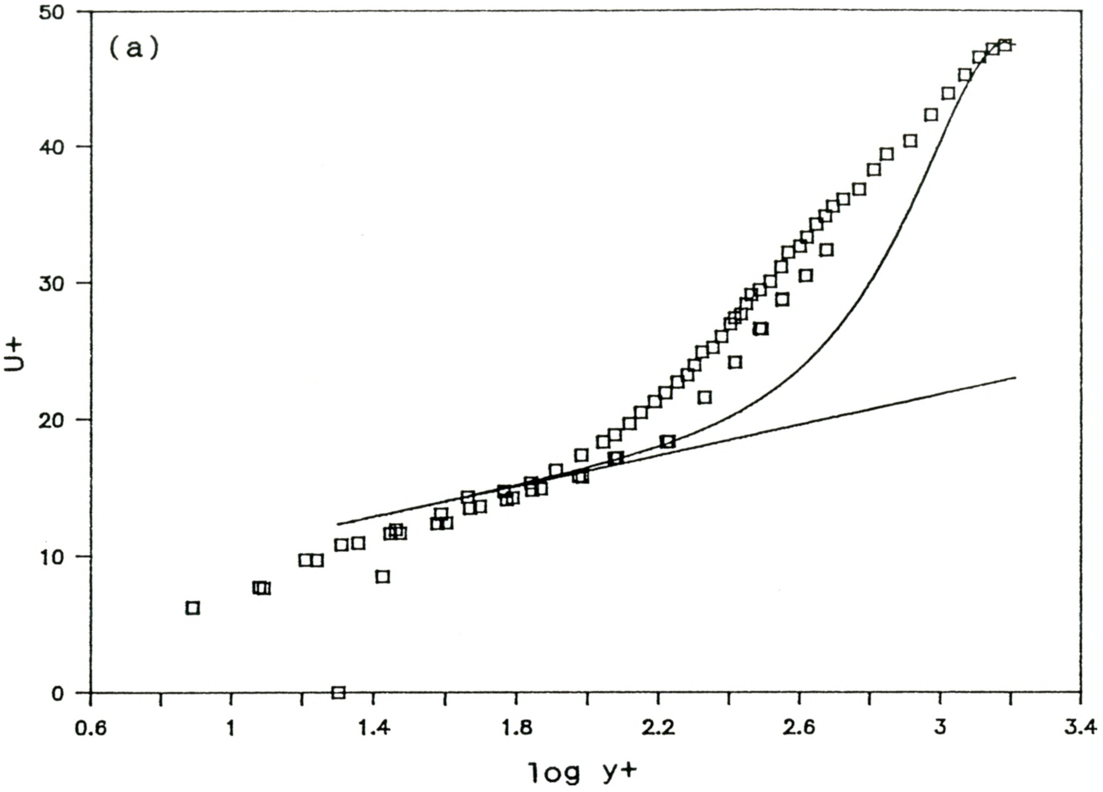
(a)
50
40
30
20
10
0
U+
0.6
1
1.4
1.8
2.2
2.6
3
3.4
log y+

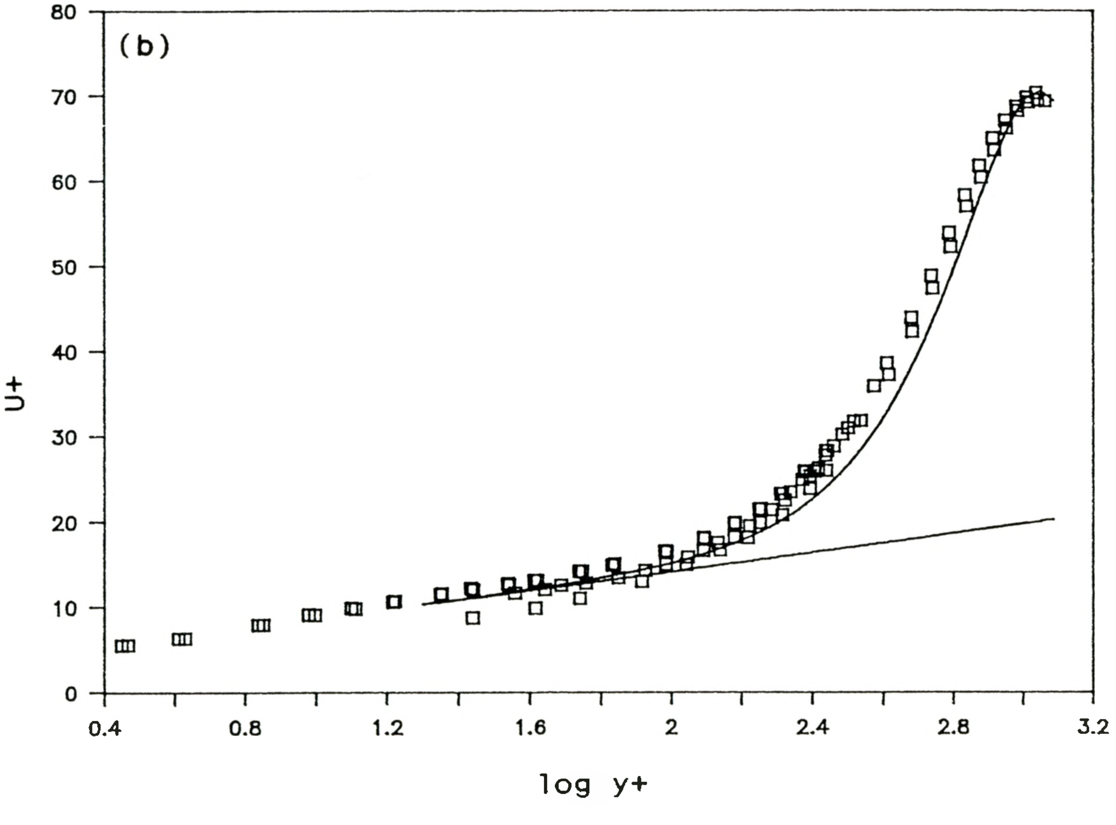
(b)
80
70
60
50
40
30
20
10
0
U+
0.4
0.8
1.2
1.6
2
2.4
2.8
3.2
log y+

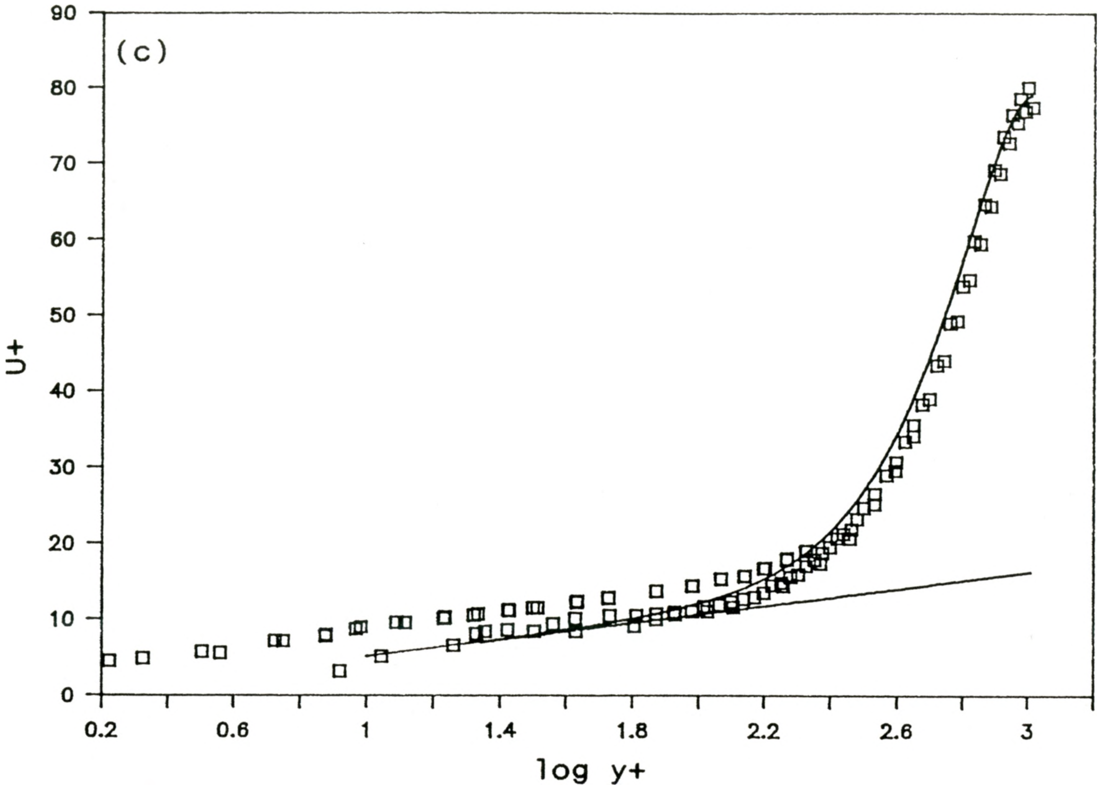

2.21 Coles' Law of the Wake compared with the experimental data of Turan (1988), Ozimek (1985), and Kassab (1986) from the eight degree conical diffuser: (a) x=18cm, (b) x=42cm, (c) x=66cm.

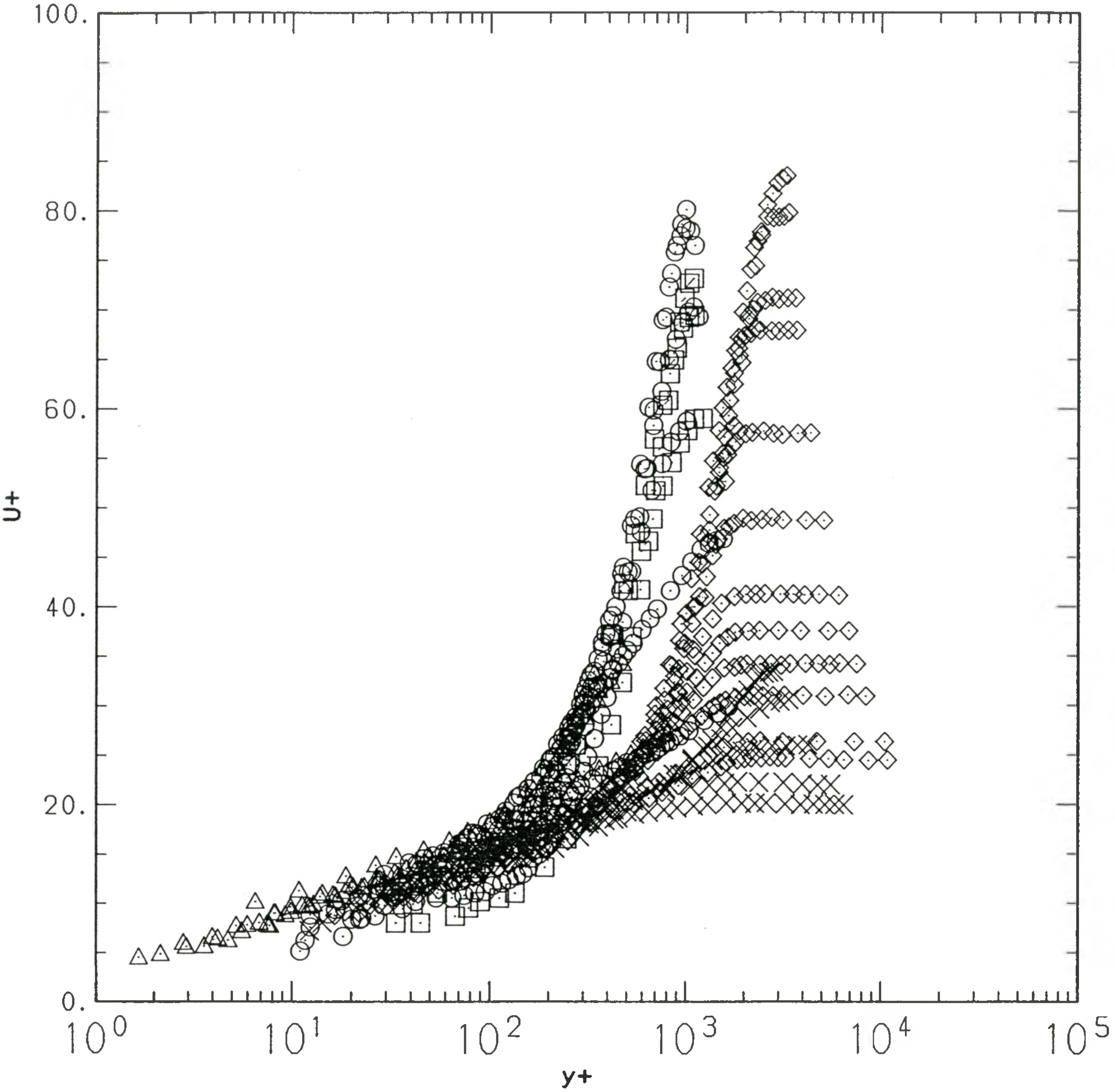

2.22 The experimental data from the following flows; △ , ⊙ , ⊡ , the eight degree conical diffuser; ◇ , flow #0142; ╳ , flow #0143.

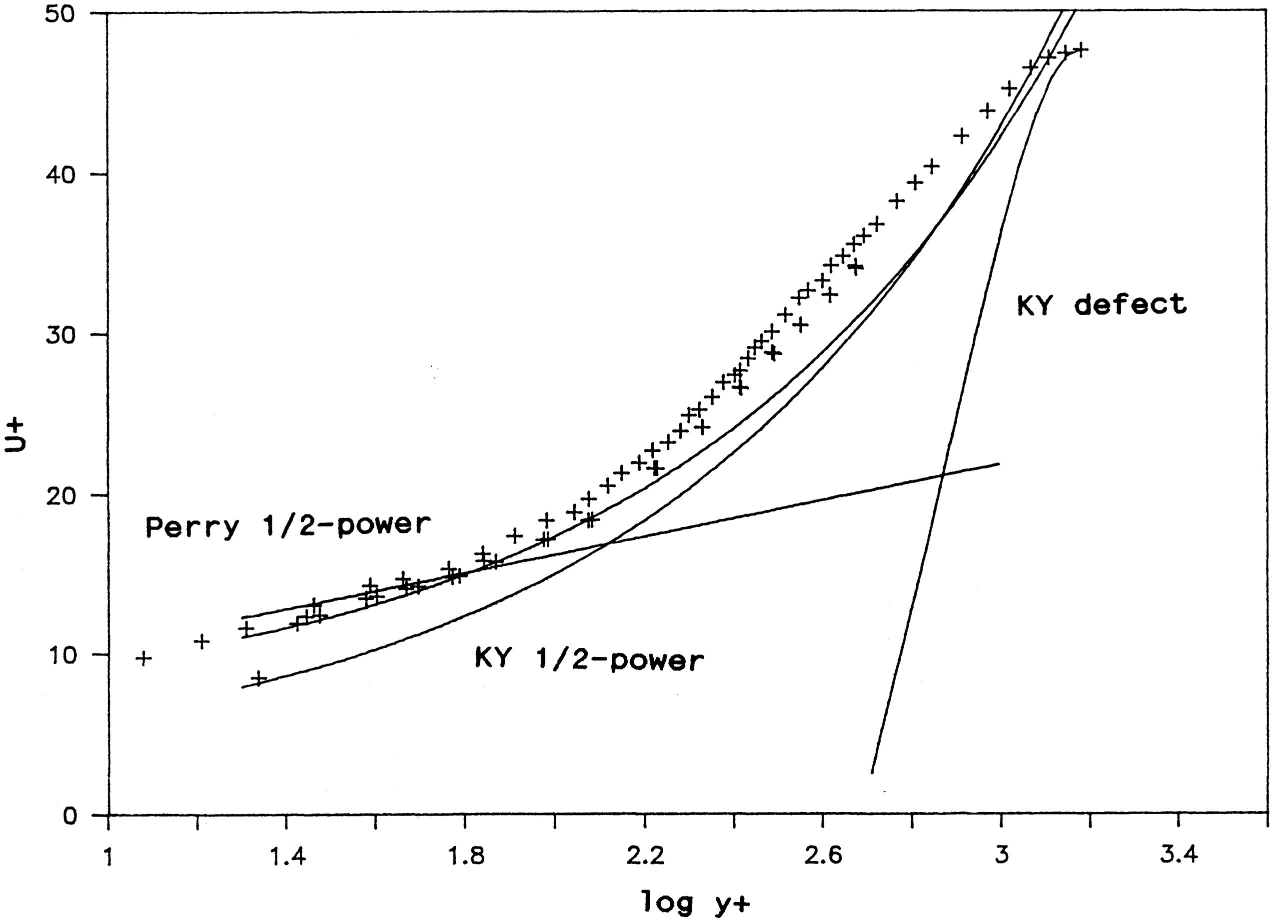

2.23 The experimental data from the eight degree conical diffuser at x=18cm along with the Log Law, Perry's and Kader and Yaglom's half-power formulations, and Kader and Yaglom's velocity defect. Perry's slip velocity is larger than Kader and Yaglom's.

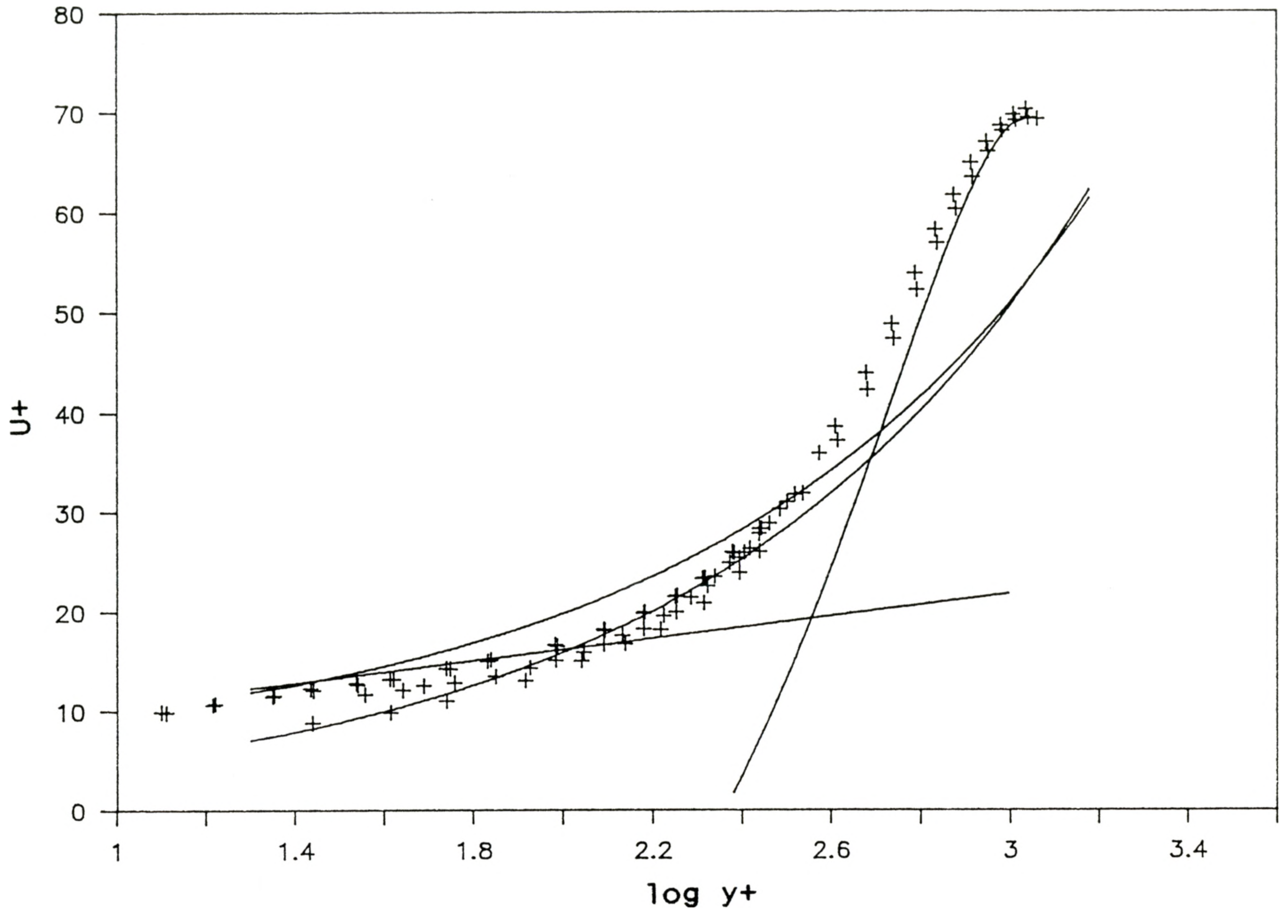

2.24 The experimental data from the eight degree conical diffuser at x=42cm along with the Log Law, Perry's and Kader and Yaglom's half-power formulations, and Kader and Yaglom's velocity defect. Perry's slip velocity is larger than Kader and Yaglom's.

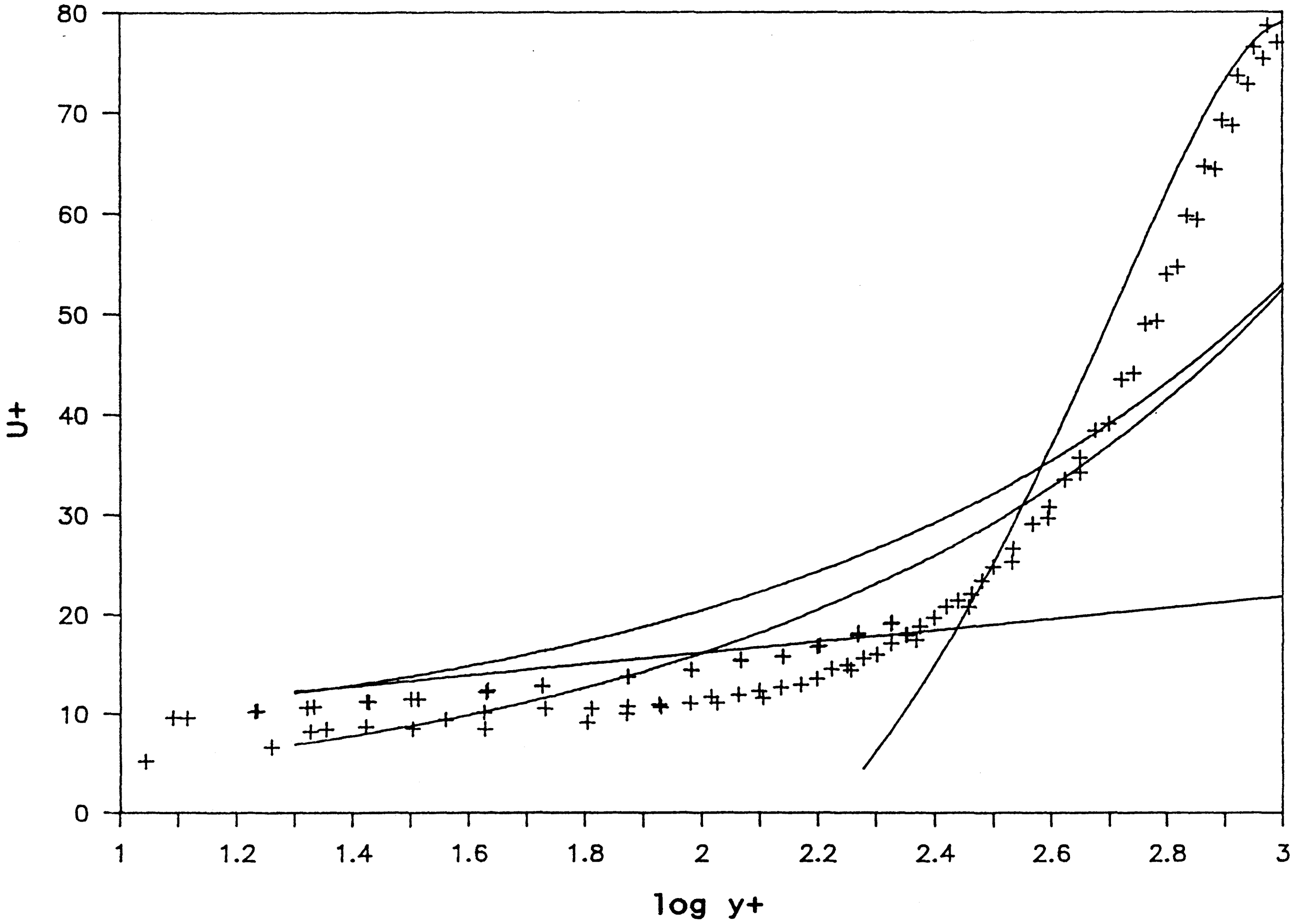

2.25 The experimental data from the eight degree conical diffuser at x=66cm along with the Log Law, Perry's and Kader and Yaglom's half-power formulations, and Kader and Yaglom's velocity defect. Perry's slip velocity is larger than Kader and Yaglom's.

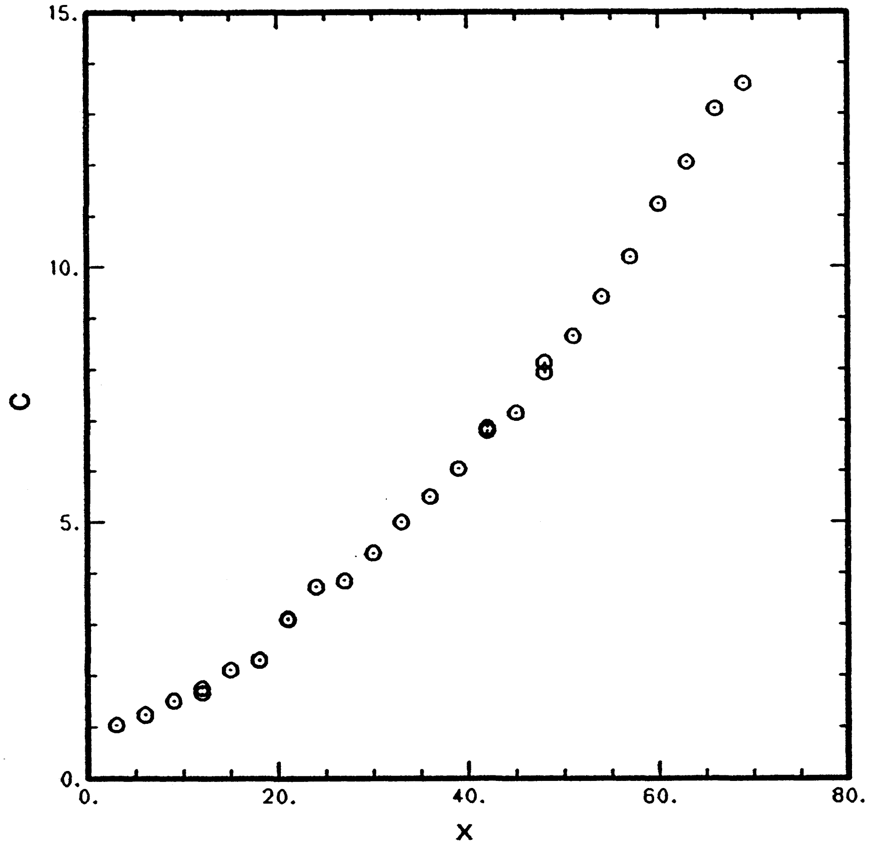

2.26 The modified Kader and Yaglom defect constant C in the eight degree conical diffuser.

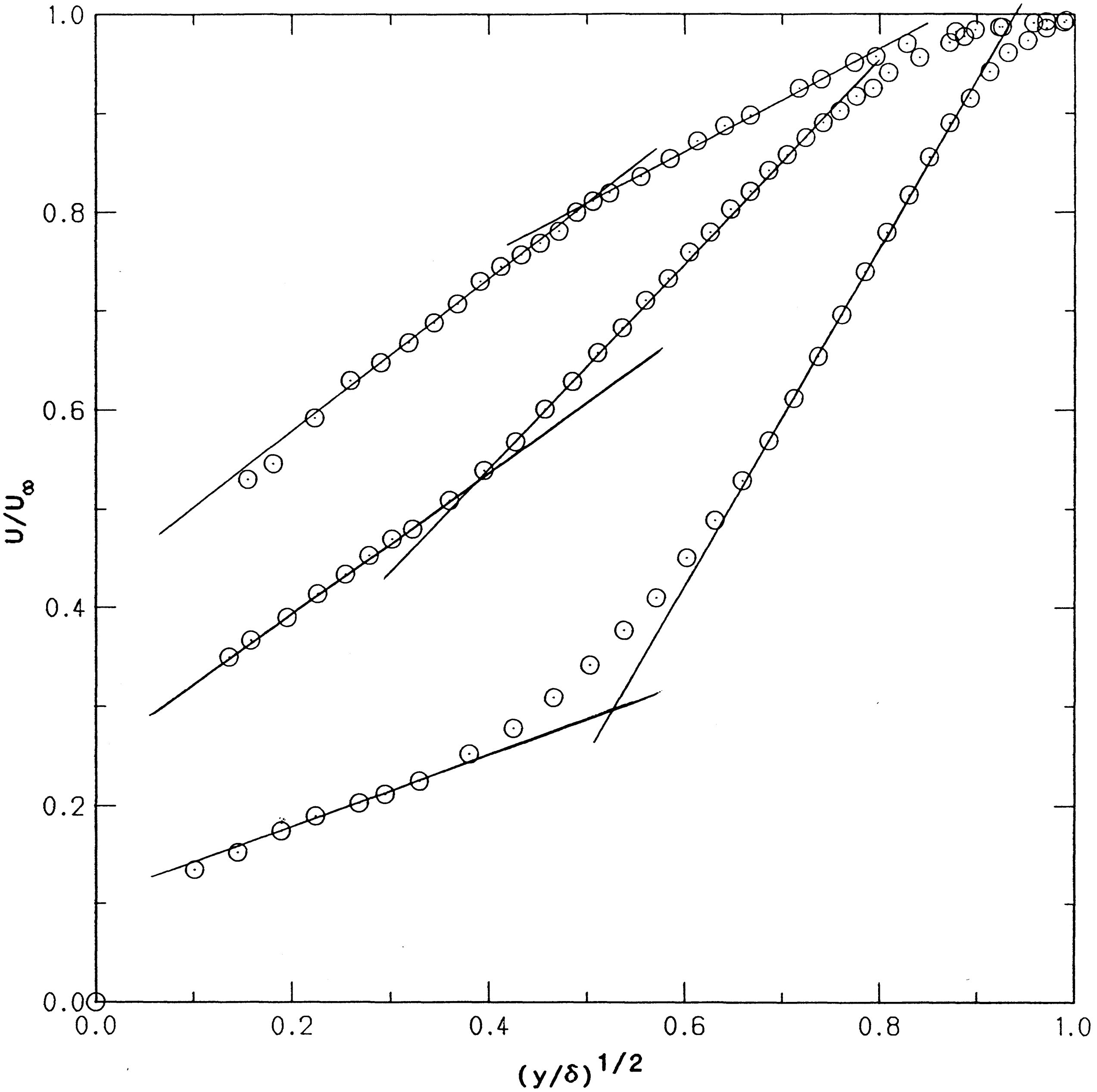

2.27 The half-power development of Fraser's flow #5000 at stations 3, 6, and 9 (from top to bottom).

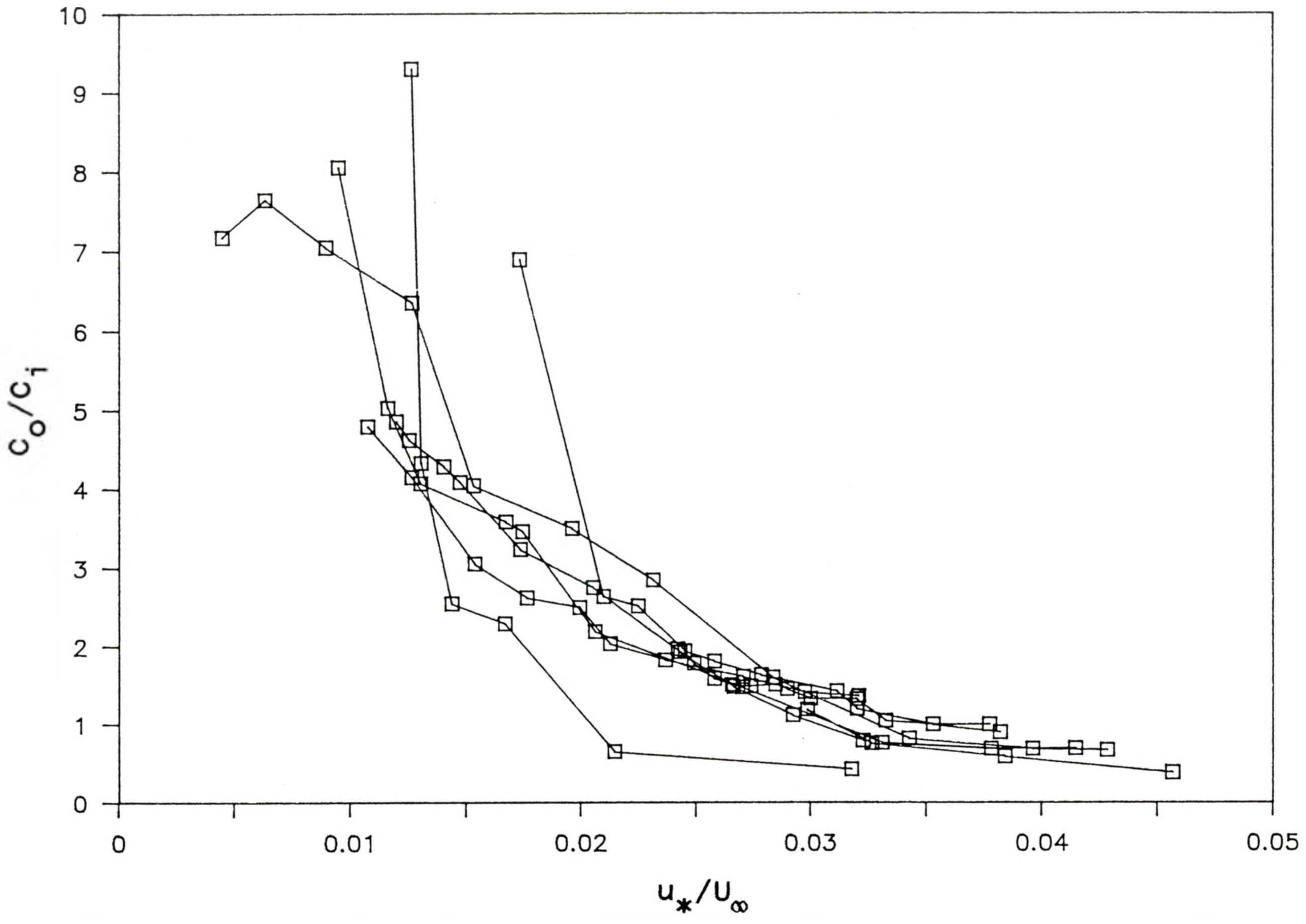

2.28 The ratio of the two half-power slopes for all eight decreasing adverse pressure gradient flows.

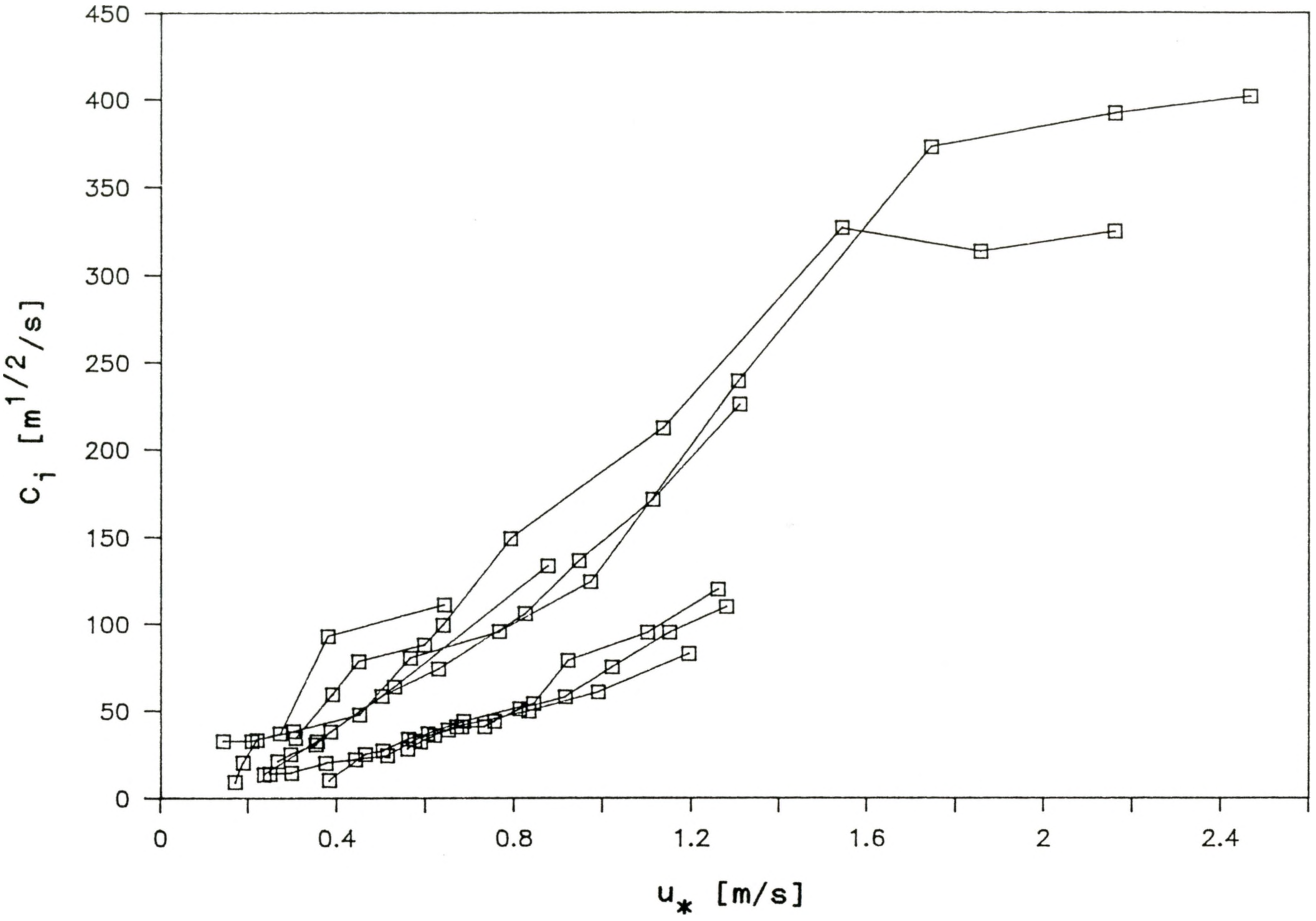

2.29 The inner half-power slope as a function of the friction velocity with the data from the eight decreasing adverse pressure gradient flows.

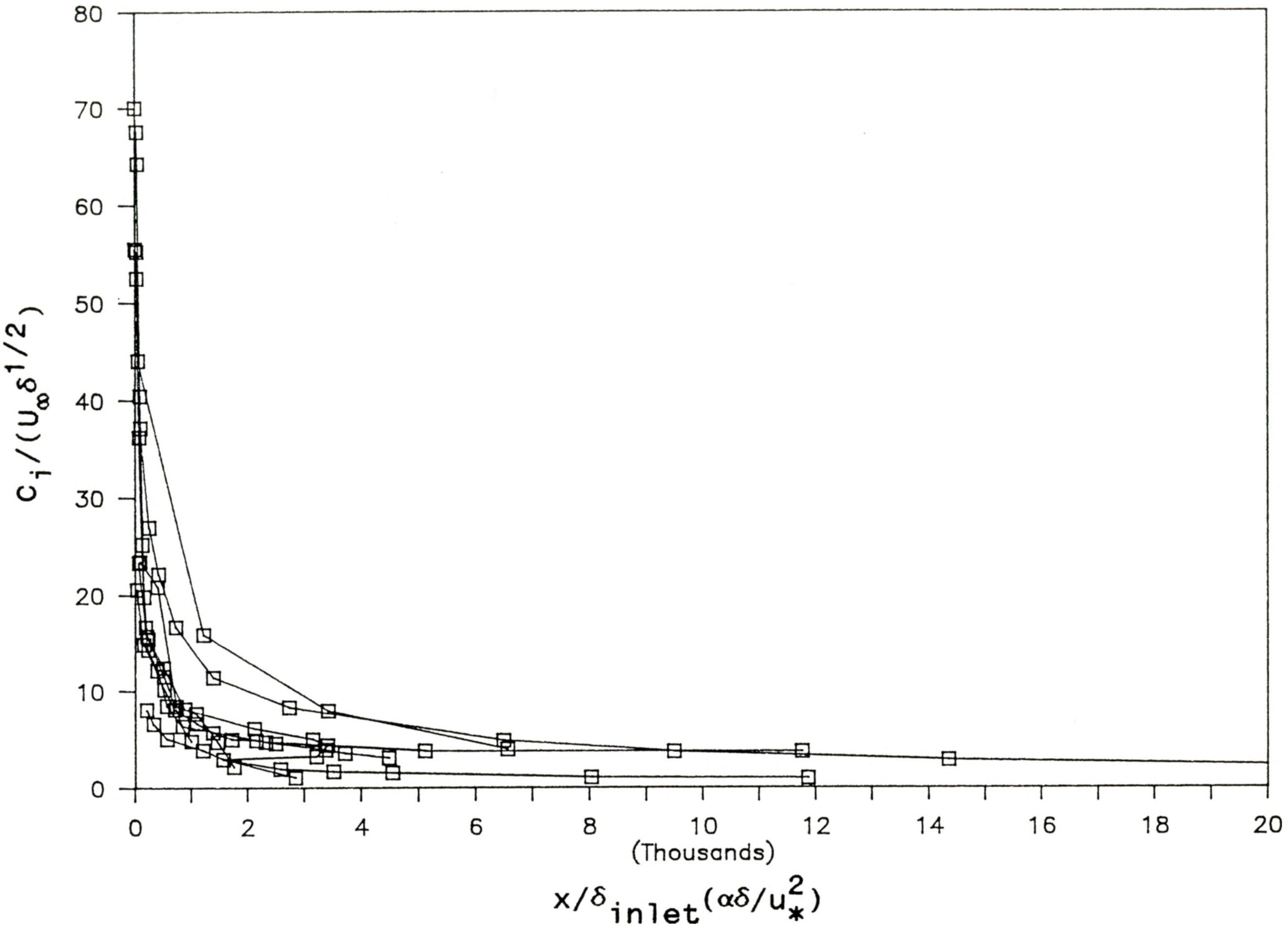

2.30 The non-dimensionalized inner half-power slope with the data from the eight decreasing adverse pressure gradient flows.

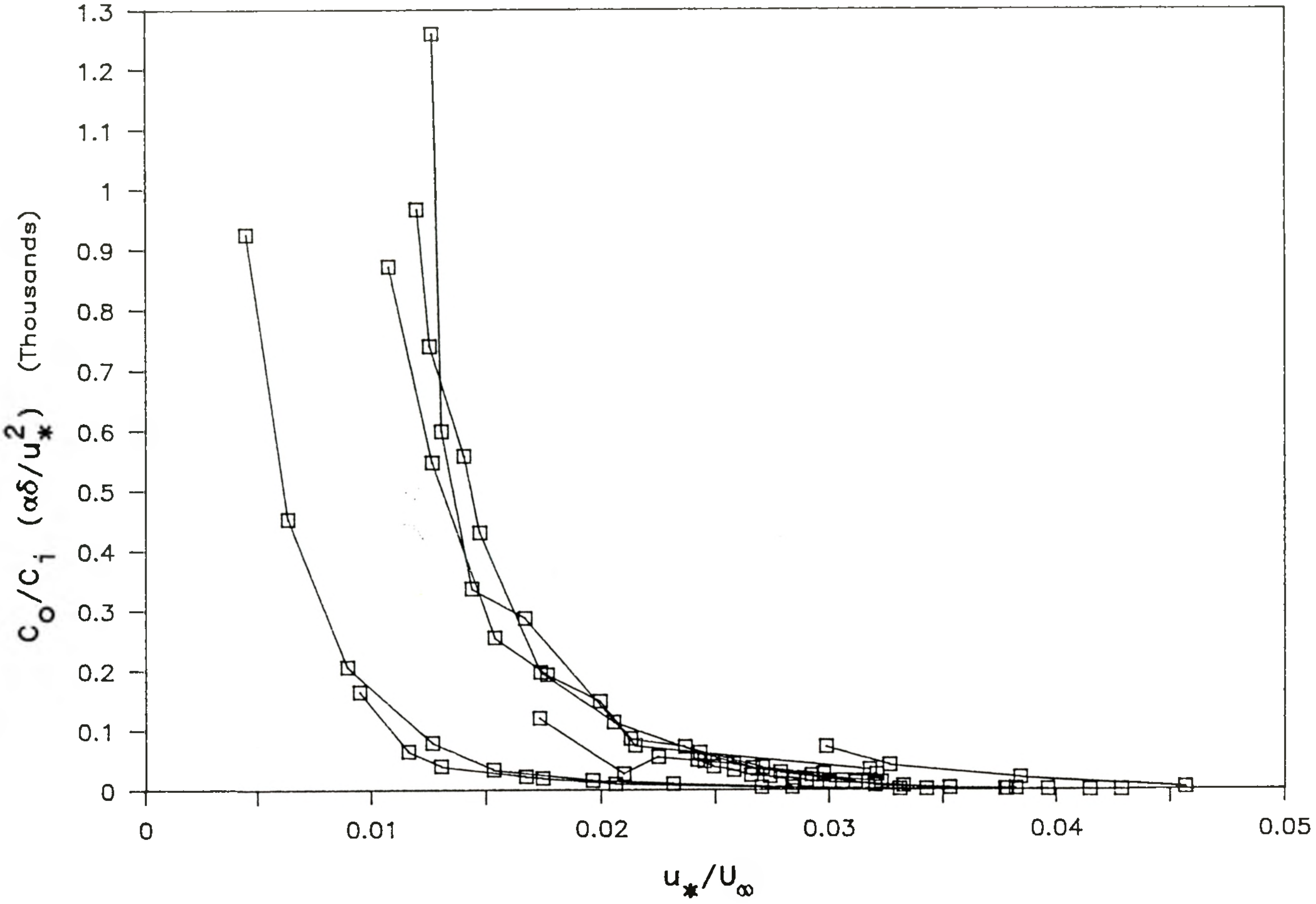

2.31 The ratio of the two half-power slopes for all eight decreasing adverse pressure gradient flows.

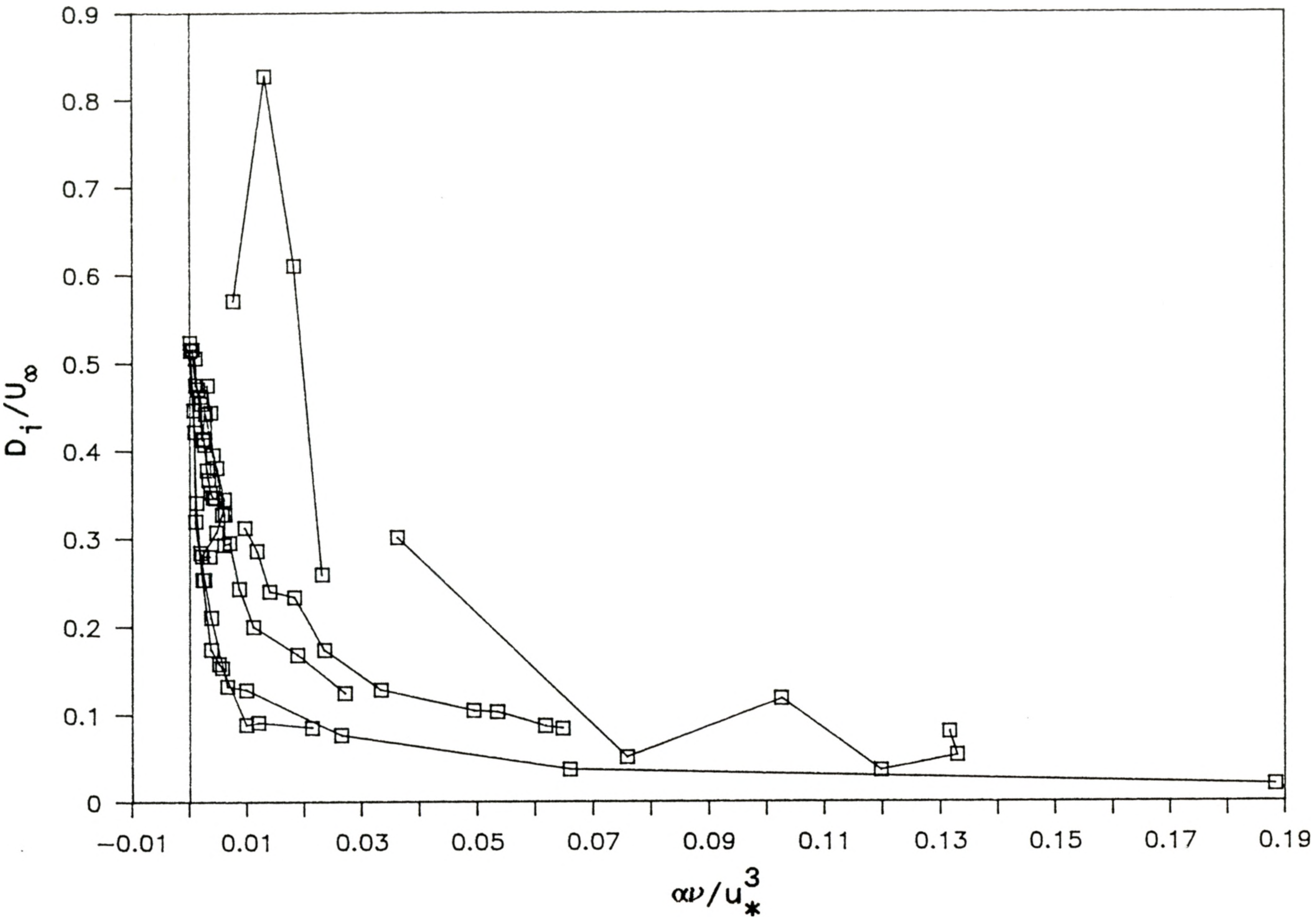

2.32 The non-dimensionalized inner half-power intercept with the data from the eight decreasing adverse pressure gradient flows.

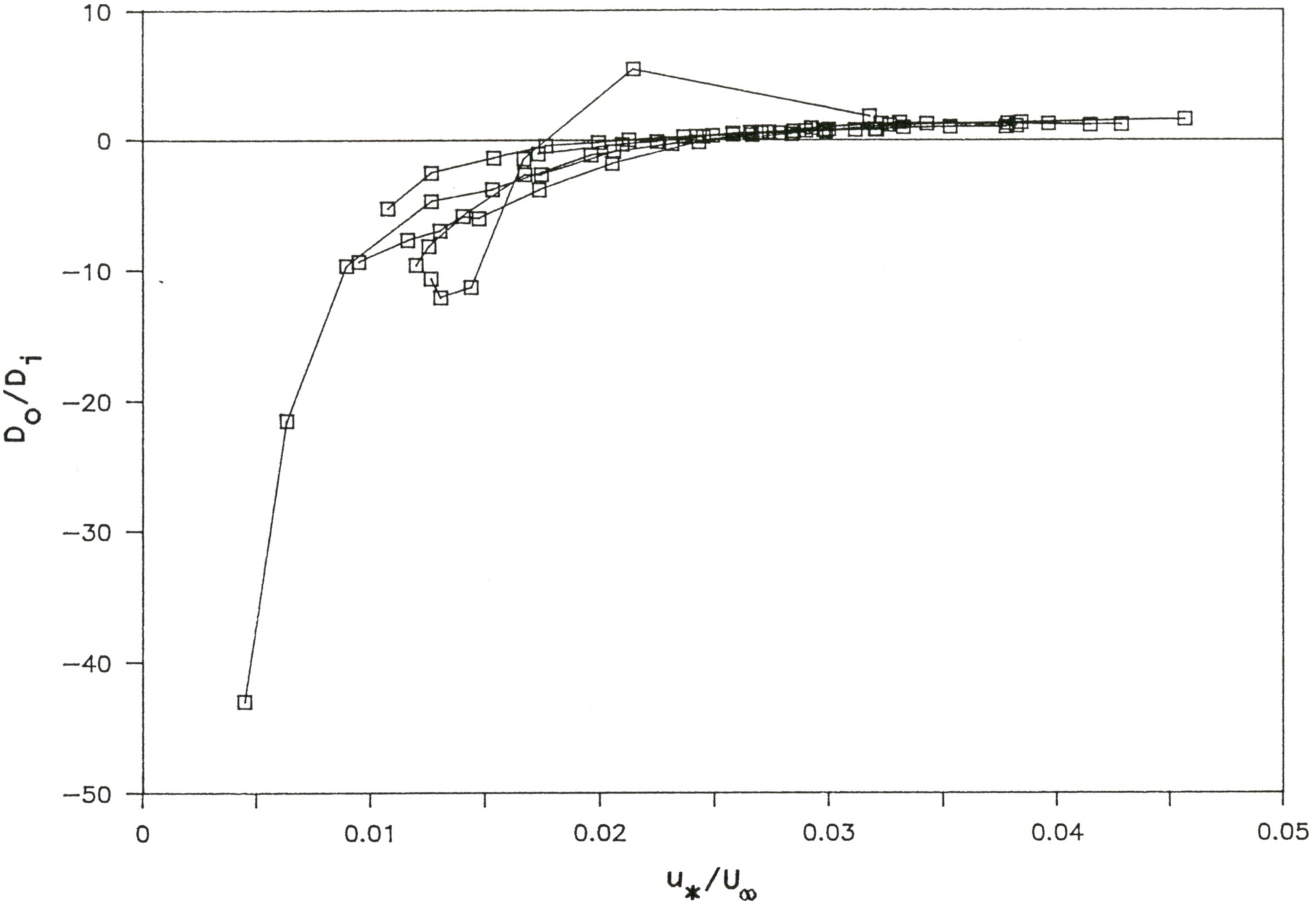

2.33 The ratio of the two half-power intercepts for all eight decreasing adverse pressure gradient flows.

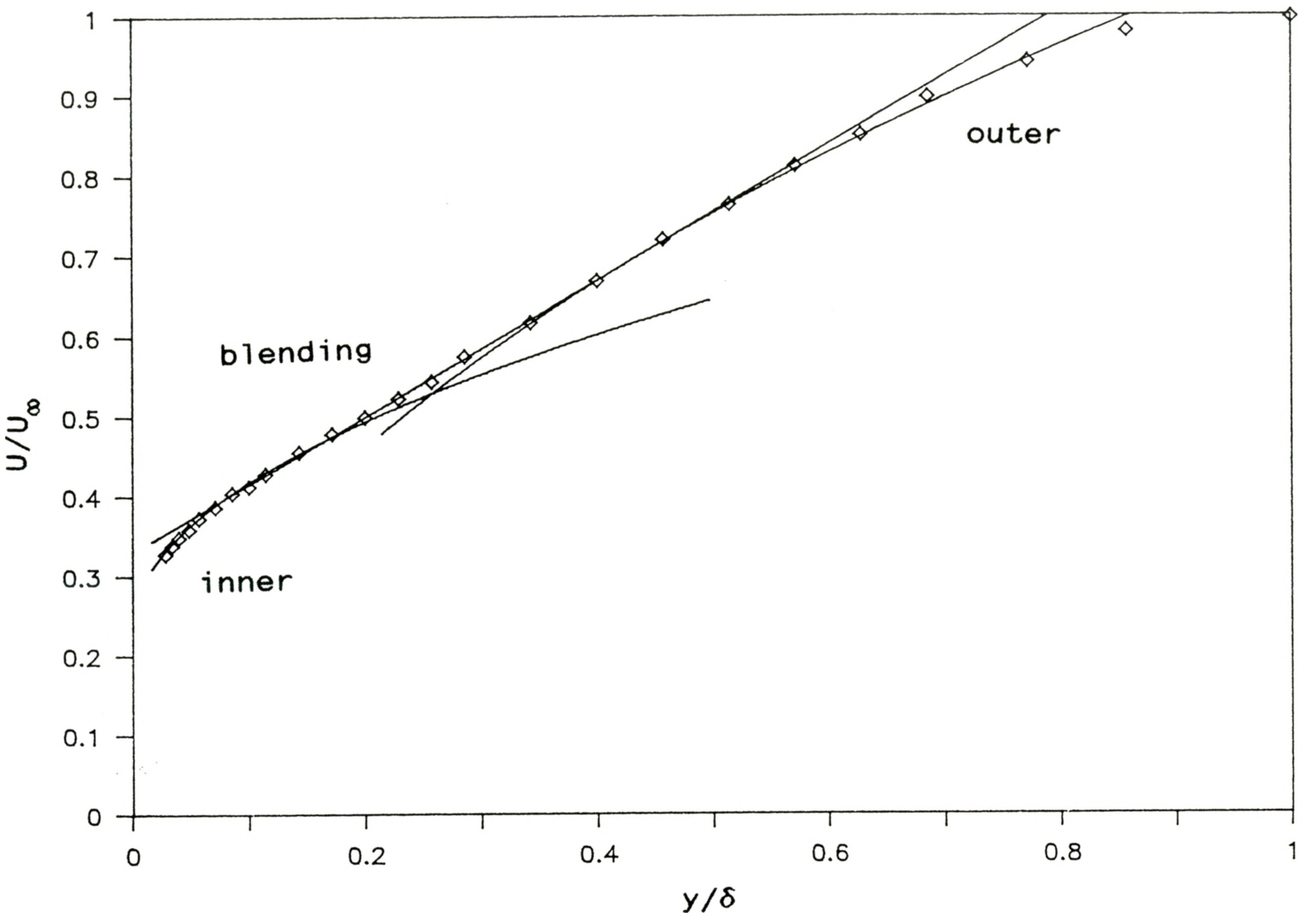

2.34 The linear blending region in flow #0142 at x=0.382m.

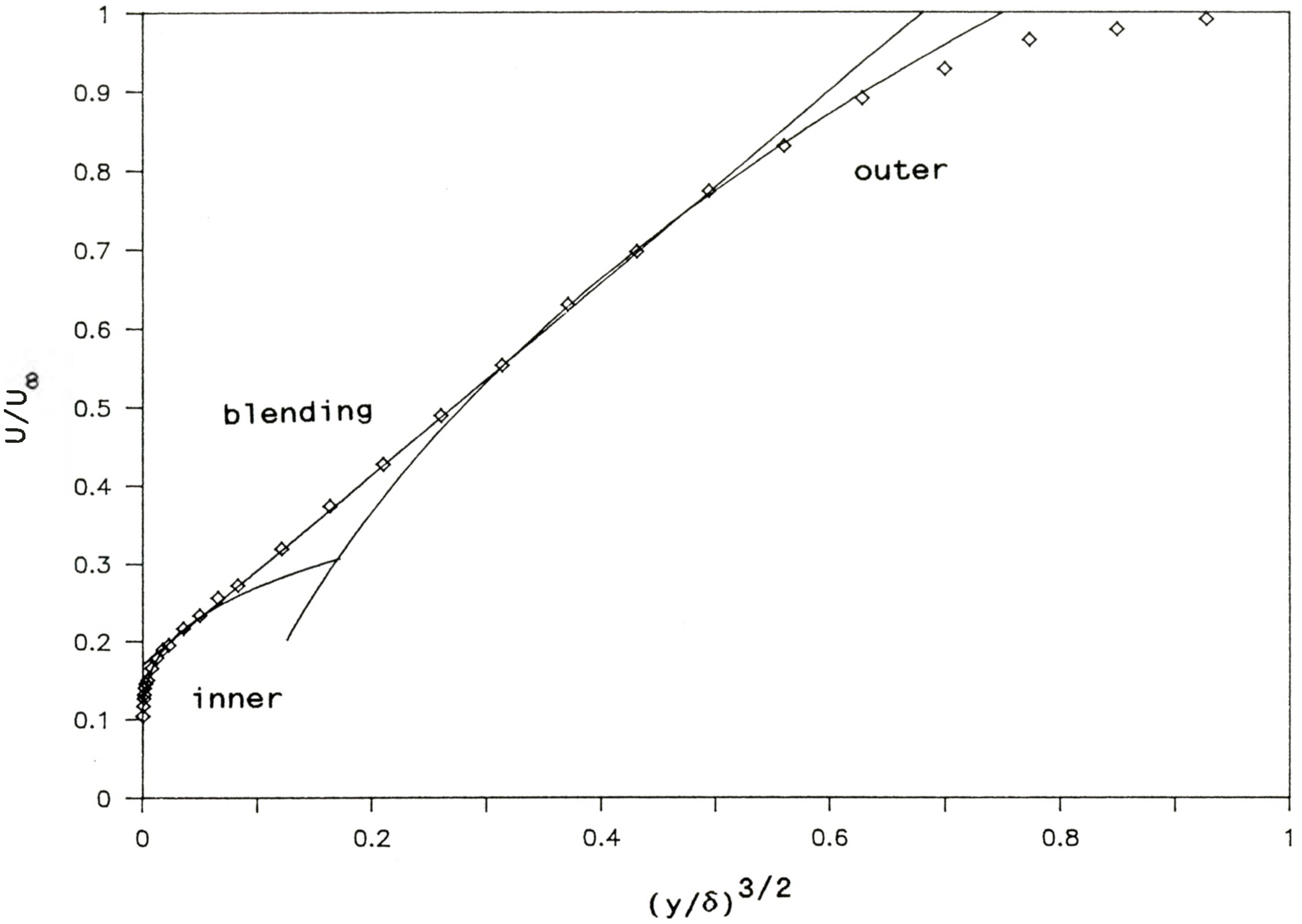

2.35 The 3/2-power blending region in flow #0142 at x=1.813m.

Table 2.1 List of Adverse Pressure Gradient Flows Examined

experimenters	flow #	classification	U/ν [1/m]
Ludwieg & Tillmann	1100*	plane, developing	2.2 E+06
	1200*		2.2 E+06
Perry	2900*	plane, developing	2.5 E+06
Samuel & Joubert	0141+	plane, developing, increasing dP/dx	1.7 E+06
Fraser	5000*	10 deg. conical, dev.	3.3 E+06
	5100*		3.6 E+06
Pozzorini	0142+	6 deg. conical, dev.	2.7 E+06
	0143+		1.2 E+06
Turan, Ozimek, & Kassab#	-	8 degree conical, fully developed inlet	1.4 E+06

*, 1968 Stanford Conference; +, 1980-81 Stanford Conference

#, see also Trupp et al (1986)

Table 2.2 Experimental Values of the Length Scales and Kader and Yaglom's Moving Equilibrium Criterion

flow	distance from inlet	$U_\infty/(\alpha\delta)^{1/2}$	δ_v	δ_p	δ
8 degree conical diffuser	0.06	3.52	2.49E-05	6.89E-04	0.0560
	0.18	4.36	4.21E-05	5.55E-04	0.0634
	0.30	5.36	5.88E-05	5.74E-04	0.0718
	0.42	6.05	7.27E-05	6.07E-04	0.0801
	0.54	6.52	8.51E-05	6.40E-04	0.0885
	0.66	6.80	9.41E-05	7.15E-04	0.0969
0142	0.000	13.40	9.24E-06	4.79E-03	0.016
	0.095	7.43	1.25E-05	1.30E-03	0.023
	0.191	7.21	1.46E-05	1.24E-03	0.028
	0.286	7.51	1.68E-05	1.20E-03	0.030
	0.382	7.22	1.98E-05	1.08E-03	0.035
	0.572	7.57	2.56E-05	1.09E-03	0.045
	0.763	7.37	3.23E-05	9.68E-04	0.059
	1.049	6.62	4.22E-05	8.65E-04	0.090
	1.240	6.24	4.56E-05	8.53E-04	0.111
	1.526	6.31	5.41E-05	8.76E-04	0.140
	1.813	5.92	5.99E-05	9.25E-04	0.184
0143	0.095	6.89	1.88E-05	2.48E-03	0.025
	0.573	4.32	3.08E-05	2.34E-03	0.085
	1.049	4.11	4.61E-05	2.52E-03	0.140
	1.813	4.27	6.95E-05	3.01E-03	0.185
2900	0.762	7.09	1.22E-05	3.94E-03	0.076
	1.219	7.68	1.47E-05	3.97E-03	0.076
	1.676	7.58	1.75E-05	4.29E-03	0.102
	2.134	6.72	2.18E-05	3.53E-03	0.140
	2.591	7.22	2.54E-05	4.20E-03	0.178
	3.048	6.51	2.84E-05	4.06E-03	0.241
	3.353	6.61	3.30E-05	3.80E-03	0.279
	3.810	7.11	3.89E-05	3.50E-03	0.292
	4.267	6.89	4.90E-05	2.60E-03	0.343
	4.572	6.90	5.86E-05	2.17E-03	0.394

flow	distance from inlet	$U_\infty/(\alpha\delta)^{1/2}$	δ_v	δ_p	δ
5000	0.117		7.25E-06		0.013
	0.158	52.44	7.26E-06	5.96E-02	0.013
	0.211	20.48	8.46E-06	8.88E-03	0.015
	0.237	23.06	1.02E-05	9.38E-03	0.016
	0.300	20.73	1.38E-05	6.08E-03	0.019
	0.383	22.76	1.98E-05	5.22E-03	0.024
	0.443	24.20	2.46E-05	4.75E-03	0.027
	0.469	23.61	2.63E-05	4.62E-03	0.030
	0.523	24.35	3.50E-05	3.53E-03	0.035
	0.578	23.97	4.03E-05	3.35E-03	0.043
	0.642	23.34	5.12E-05	2.40E-03	0.049
5100	0.117		6.45E-06		0.009
	0.158	63.16	6.36E-06	7.25E-02	0.010
	0.204	22.72	7.26E-06	9.16E-03	0.011
	0.237	21.82	9.00E-06	7.27E-03	0.013
	0.300	21.86	1.20E-05	6.35E-03	0.017
	0.383	22.78	1.61E-05	6.16E-03	0.022
	0.443	23.60	2.05E-05	5.40E-03	0.025
	0.523	22.41	2.78E-05	4.19E-03	0.036
	0.580	22.33	3.48E-05	3.51E-03	0.044
	0.684	20.67	5.19E-05	1.96E-03	0.057
	0.743	20.54	7.54E-05	1.14E-03	0.068
	0.784	19.69	1.10E-04	5.82E-04	0.075
1100	0.782	24.37	1.21E-05	2.10E-02	0.025
	1.282	15.92	1.35E-05	1.21E-02	0.038
	1.782	11.15	1.52E-05	7.85E-03	0.057
	2.282	11.27	1.69E-05	8.19E-03	0.063
	2.782	10.63	1.91E-05	8.13E-03	0.080
	3.132	10.41	2.05E-05	7.99E-03	0.088
	3.332	9.82	2.12E-05	8.02E-03	0.103
	3.532	9.39	2.28E-05	7.45E-03	0.113
	3.732	9.24	2.38E-05	7.20E-03	0.120
	3.932	8.41	2.50E-05	6.95E-03	0.148
	4.132	8.51	2.64E-05	6.50E-03	0.145
	4.332	8.16	2.77E-05	6.20E-03	0.159
1200	0.782	18.13	1.19E-05	1.16E-02	0.024
	1.282	14.16	1.36E-05	9.36E-03	0.038
	1.782	11.94	1.63E-05	7.11E-03	0.049
	2.282	10.43	1.78E-05	6.33E-03	0.060
	2.782	8.36	2.19E-05	4.60E-03	0.085
	3.132	7.86	2.48E-05	4.10E-03	0.100
	3.332	8.20	2.67E-05	4.71E-03	0.117
	3.532	9.49	2.98E-05	6.29E-03	0.139
	3.732	14.96	3.24E-05	1.50E-02	0.152
	3.932	13.80	3.91E-05	1.11E-02	0.194

Table 2.3 Range of C_o/C_i where mean velocity models predict the data

Flow	Townsend$^+$	KY 1/2	Perry 1/2	KY defect	Coles
1100	$r < 1.0$	$1 < r < 2$	$1.5 < r < 2$	$1 < r < 2$	$r > 1.0$
1200	$r < 1.2$	$1.4 < r < 2.5$	$1.6 < r < 2.5$	$1.4 < r < 6$	$r > 1.0$
2900	$r < 1.4$	$1.4 < r < 2$	$1.4 < r < 2$	$1.6 < r < 3$	$r > 1.4$
5000	Marginally better than Log Law at all of the stations.	not at any	not at any	$0.8 < r < 1.5$	$r > 3.5$
5100		not at any	not at any	$0.8 < r < 1.6$	$r > 3.5$
0142	$r < 1.9$ $\{ r < 3.2 \}$	$1.5 < r < 2.8$	$1.2 < r < 1.5$	$1.1 < r < 4.1$	$r > 3.2$
0143	$r < 0.6$ $\{ r < 1.2 \}$	$r = 0.6$	not at any	not at any	$r > 1.2$
8 deg. conical	$r < 1.5$ $\{ r < 2.5 \}$	$2.3 < r < 2.6$	$0.7 < r < 2.3$	$2.5 < r < 6$	$r > 4$

+ The valid range for McDonald is shown in brackets {}.

In this table, $r = C_o/C_i$

Chapter Three
Calculation of the Turbulence Quantities in a Conical Diffuser Flow

3.1 Introduction

Almost all engineering flows of practical importance are turbulent, hence turbulence modeling is critical for efficient design. Turbulence modeling is required because in the momentum equations for the mean (time-averaged) flow field, the so-called Reynolds stresses appear. For a stationary and axisymmetric flow, the mean momentum equation in the axial direction is

$$V\,\frac{\partial U}{\partial r} + U\,\frac{\partial U}{\partial x} = -\,\frac{1}{\rho}\,\frac{\partial P}{\partial x} + \nu\left(\frac{1}{r}\,\frac{\partial U}{\partial r} + \frac{\partial^2 U}{\partial r^2} + \frac{\partial^2 U}{\partial x^2}\right)$$
$$-\,\frac{1}{r}\,\frac{\partial}{\partial r}(r\overline{uv}) - \frac{\partial}{\partial x}(\overline{u^2}), \qquad (1)$$

and the radial momentum equation is

$$V\,\frac{\partial V}{\partial r} + U\,\frac{\partial V}{\partial x} = -\,\frac{1}{\rho}\,\frac{\partial P}{\partial r} + \nu\left(\frac{1}{r}\,\frac{\partial V}{\partial r} + \frac{\partial^2 V}{\partial r^2} + \frac{\partial^2 V}{\partial x^2} - \frac{V}{r^2}\right) -$$
$$-\left(\frac{\partial}{\partial x}(\overline{uv}) - \frac{\partial}{\partial r}(\overline{v^2}) + \frac{(v^2 - w^2)}{r}\right), \qquad (2)$$

while the continuity equation is

$$\frac{\partial U}{\partial x} + \frac{\partial V}{\partial r} + \frac{V}{r} = 0. \qquad (3)$$

The turbulent shear stress $\overline{uv}$ and normal stresses $\overline{u^2}$, $\overline{v^2}$, and $\overline{w^2}$ require modeling. Transport equations for these terms can be derived from the momentum equation for the turbulence fluctuations, but this in turn leads to third order correlations and the well known closure problem of turbulence. Because the turbulence structure of a given flow varies greatly with such factors as the pressure gradient, geometry, or the streamline curvature (Azad and Kassab, 1989) modeling is difficult.

In order to effectively design fluid mechanical devices an engineer needs to efficiently calculate the turbulence shear and normal stresses, specifically $\overline{uv}$, $\overline{u^2}$, $\overline{v^2}$, and $\overline{w^2}$ along with the mean velocities $\overline{U}$, $\overline{V}$, and $\overline{W}$. Presently, many methods are available, the most common being algebraic stress models, one equation (k) models, two equation (k-ε) models, and multiple equation (Reynolds stress) models. There are also integral methods which are used to evaluate $\overline{uv}$.

Boussinesq was the first to state that the turbulence stresses should be proportional to the mean velocity gradients in a manner similar to the laminar stresses. The laminar stresses are described by Newton's Law of Viscosity

$$\frac{\tau_{ij}}{\rho} = \nu \left(\frac{\partial U_i}{\partial x_j}. + \frac{\partial U_j}{\partial x_i}\right) \tag{4}$$

Similarly, the Boussinesq definition of the eddy viscosity is

$$\frac{\tau_t}{\rho} = -\overline{u_i u_j} = \nu_t \left(\frac{\partial U_i}{\partial x_j} + \frac{\partial U_j}{\partial U_i}\right) - \frac{2}{3} k \, \delta_{ij} \tag{5}$$

where ν_t is the eddy viscosity or turbulence viscosity. The eddy viscosity is thus, flow dependent, not fluid dependent like the laminar viscosity.

Algebraic stress models are just simple equations for $\overline{uv}$. The first zero equation model was Prandtl's mixing length concept, where

$$-\rho\overline{uv} = \ell^2 \left(\frac{\partial U}{\partial y}\right)^2 \tag{6}$$

for a boundary layer or fully-developed pipe flow. Then from Boussinesq, the eddy viscosity is

$$\nu_t = \ell^2 \frac{\partial U}{\partial y} \tag{7}$$

with the mixing length, ℓ specified algebraically. This type of model is well established in relatively simple flows such as boundary layers or fully-developed pipe flow. Because advection, diffusion, and history effects are neglected, it is unlikely that this type of model would work well in complex flows such as conical diffusers.

One equation models have a transport equation for the turbulence kinetic energy, k. The exact kinetic energy equation for stationary and axisymmetric flows is

$$\begin{aligned} &\overset{\text{I}}{U\frac{\partial k}{\partial x} + V\frac{\partial k}{\partial r}} = - \overset{\text{II}}{\left(\frac{\partial}{\partial x}(\overline{uk}) + \frac{1}{r}\frac{\partial}{\partial r}(r\overline{vk})\right)} - \Big(\overline{uv}\left[\frac{\partial U}{\partial r} + \frac{\partial V}{\partial x}\right] + \\ &\underset{\text{III}}{(\overline{u^2} - \overline{v^2})\frac{\partial U}{\partial x} + (\overline{w^2} - \overline{v^2})\frac{V}{r}\Big)} + \nu\underset{\text{IV}}{\left(\frac{1}{r}\frac{\partial k}{\partial r} + \frac{\partial^2 k}{\partial r^2} + \frac{\partial^2 k}{\partial x^2}\right)} - \underset{\text{V}}{\varepsilon} \end{aligned} \tag{8}$$

when the pressure transport term is neglected (Turan, 1988). Term I is the advection of kinetic energy due to the mean flow, term II is the turbulent transport or turbulent diffusion, term III is the turbulent production, term IV is the viscous diffusion, and term V is the dissipation rate of turbulent kinetic energy. The only term that is modeled in equation (8) is the turbulent diffusion which is modeled by

$$\frac{\partial}{\partial x}\left[\left(\frac{\nu_t}{\sigma_k}\right)\frac{\partial k}{\partial x}\right] + \frac{1}{r}\frac{\partial}{\partial r}\left[r\left(\frac{\nu_t}{\sigma_k}\right)\frac{\partial k}{\partial r}\right] \tag{9}$$

where σ_k is the Prandtl number for the kinetic energy. Although the other terms in the exact kinetic energy equation are not modeled explicitly, they are modeled implicitly because the Reynolds stresses are modeled with the Boussinesq approximation. The dissipation is determined from

$$\varepsilon = C_D\ k^{3/2}\ L \tag{10}$$

and the eddy viscosity from the Kolmogorov-Prandtl relation

$$\nu_t = C_\mu k^{1/2} L \tag{11}$$

where the mixing length, L is again specified algebraically.

Thus, the eddy viscosity is related to the kinetic energy of turbulence.

Thus, the modeled kinetic energy equation is

$$U \frac{\partial k}{\partial x} + V \frac{\partial k}{\partial r} = \frac{\partial}{\partial x}\left[\left(\frac{\nu_t}{\sigma_k}\right)\frac{\partial k}{\partial x}\right] + \frac{1}{r}\frac{\partial}{\partial r}\left[r\left(\frac{\nu_t}{\sigma_k}\right)\frac{\partial k}{\partial r}\right] \tag{12}$$

$$-\left(\overline{uv}\left[\frac{\partial U}{\partial r} + \frac{\partial V}{\partial x}\right] + (\overline{u^2}-\overline{v^2})\frac{\partial U}{\partial x} + (\overline{w^2}-\overline{v^2})\frac{V}{r}\right) +$$

$$\nu\left(\frac{1}{r}\frac{\partial k}{\partial r} + \frac{\partial^2 k}{\partial r^2} + \frac{\partial^2 k}{\partial x^2}\right) - \varepsilon$$

In the two equation models, a transport equation for the length scale is developed similar to that for the modeled kinetic energy equation. The most popular two equation model is the k-ε model, and is the only one discussed here. In the k-ε model, the length scale is proportional to $k^{3/2}/\varepsilon$ and the transport equation is developed for ε. For a stationary and axisymmetric flow the dissipation rate equation (Nagano and Hishida, 1987) is given by

$$\overset{\text{I}}{U \frac{\partial \varepsilon}{\partial x} + V \frac{\partial \varepsilon}{\partial r}} = \overset{\text{II}}{\frac{\partial}{\partial x}\left((\nu + \frac{\nu_t}{\sigma_\varepsilon})\frac{\partial \varepsilon}{\partial x}\right) + \frac{1}{r}\frac{\partial}{\partial r}\left(r(\nu + \frac{\nu_t}{\sigma_\varepsilon})\frac{\partial \varepsilon}{\partial r}\right)} \tag{13}$$

$$\overset{\text{III}}{- C_{\varepsilon 1} f_1 \frac{\varepsilon}{k}\left(\overline{uv}\left[\frac{\partial U}{\partial x} + \frac{\partial V}{\partial r}\right] + (\overline{u^2} - \overline{v^2})\frac{\partial U}{\partial x} + (\overline{w^2} - \overline{v^2})\frac{V}{r}\right)} \quad \overset{\text{IV}}{- C_{\varepsilon 2} f_2 \frac{\varepsilon^2}{k}}$$

where the f's are damping functions for near wall effects, term I is the advection of the dissipation due to the mean flow, term II is the turbulent diffusion, term III is the production, and term IV is the destruction. The eddy viscosity is again defined by the Kolmogorov-Prandtl relation

$$\nu_t = C_\mu f_\mu \, k^2/\epsilon \tag{14}$$

where C_μ is a constant and f_μ is a damping function for near wall effects. Hence, the eddy viscosity is dependent on both the kinetic energy and the dissipation rate.

In Reynolds stress models (RSM) there is a transport equation for each of the Reynolds stresses, plus an equation for the dissipation rate. Each of the RSM equations is of the same form as the exact kinetic energy equation with the third order correlations modeled as functions of the gradients of the second order correlations (or Reynolds stresses). An eddy viscosity is not required because the Reynolds stresses are modeled in their respective transport equation.

The objective of this chapter is to evaluate some of the current variations of the basic k-ϵ model in comparison with experimental data from Turan (1988) for an eight degree conical diffuser flow. Full numerical simulation will not be done. Instead, experimental data will be used with the k-ϵ closure in order to see how well the model predicts the turbulence quantities. Second, a numerical computation of the two partial differential equations in a conical diffuser flow, given the mean axial and radial velocities, is attempted. Giving the mean velocity and geometry means that only two partial differential equations have to be solved, rather than five. This allows for the possible breakdowns of the model to be evaluated more clearly.

The eight degree conical diffuser of Trupp et al (1986) and Turan (1988) will be the geometry and data used for evaluating the models. This is the most recent data available for this type of flow which includes the dissipation rate of turbulence kinetic energy obtained by an independent method.

In the remainder of this chapter, the finite difference numerical method is described. Following this, three variations of the basic k-ε model will be evaluated with respect to the eight degree conical diffuser flow.

3.2 The Finite-Difference Scheme

Patankar (1980) in his book *Numerical Heat Transfer and Fluid Flow* describes in detail the control-volume formulation. The control-volume formulation is a finite-difference scheme that is obtained by integrating the particular conservation equation (here the equations for k and ε) over a small control volume. This leads to an algebraic equation for the individual control volume. When this is done over the entire domain, a set of algebraic equations which replace the partial differential equation is obtained. These equations are then solved simultaneously to yield the solution.

Referring to Figure 3.1, which shows the control volumes and nodes of the discretized one-dimensional axisymmetric domain, the difference scheme is of the form:

$$a_p\phi_p = a_n\phi_n + a_s\phi_s + b \tag{15}$$

where the a's and b are the difference scheme coefficients and the ϕ's represent either k or ε. In order to more simply evaluate the turbulence model in the complex diffuser flow the two-dimensional, axisymmetric conical diffuser flow is modeled one-dimensionally at each axial station. The rational for this is discussed in more detail in the following section.

Because there are convection terms present in the equations, special precautions have to be taken so that there will not be significant amounts of false diffusion. Patankar (1980) derives what he calls the power law scheme. The power law scheme uses upwinding for highly convective flows and central differencing for low convection flows and a combination of both for intermediate amounts of convection. The partial differential equations are re-written in the form

$$\frac{1}{r}\frac{\partial J_r}{\partial r} = S, \quad \text{where} \quad J_r = r\rho\overline{V}\Phi - r\Gamma\frac{\partial\Phi}{\partial r} \tag{16}$$

where the diffusion coefficient is Γ, Φ represents either k or ε, and S is the source term. Since the axisymmetric conical diffuser flow is being modeled one-dimensionally, the axial convection is included with the source term.

Integrating equation (16) over the control volume shown in Figure 3.1 one obtains:

$$J_n - J_s = (S_C + S_P\Phi_P)\ r'_p\Delta r \tag{17}$$

where $r'_p = 0.5*(r_n - r_s)$ and the source term S (= $S_C + S_p\Phi_p$) is linearized with $S_C > 0$ and $S_P < 0$. This source term linearization assumes that Φ_P prevails over the entire control volume. The flux J_i represent the total flux across the interface i, where i=n,s and are obtained from the integration of $\int J_r dr$. Now, integrating the continuity equation for a one-dimensional incompressible flow, one obtains:

$$F_n - F_s = 0 \tag{18}$$

where $F_n = \rho V_n r_n$ and F_s is similar. Multiplying equation (18) by Φ_P and subtracting it from equation (17) the final discretization is obtained. The coefficients of equation (15) with the power law scheme (Patankar, 1980) are then equal to:

$$a_N = D_n \text{ MAX } [0,1 - 0.1 \text{ ABS}(P_n)^5] + \text{MAX } [-F_n,0]$$
$$a_S = D_s \text{ MAX } [0,1 - 0.5 \text{ ABS}(P_s)^5] + \text{MAX } [F_s,0]$$
$$a_P = a_N + a_S - S_P\ r'_p \Delta r \qquad (19)$$
$$b = S_C\ r'_p \Delta r, \quad D_n = \frac{\Gamma_n r_n}{(\delta r)_n}, \quad D_s = \frac{\Gamma_s r_s}{(\delta r)_s}, \text{ and } P_i = \frac{F_i}{D_i}$$

where P_i is the Peclet number which represents the relative amount of convection to diffusion. The coefficients a_N, and a_S are seen to represent the convection and diffusion across the control volume faces. The power law scheme is used so that false diffusion is minimized in highly convective flows (Patankar, 1980).

The discretization of the partial differential equation leads to a set of algebraic equations over the calculation domain. The method of solution of the set of algebraic equations is important to the speed and accuracy of the numerical solution. The method chosen is the Thomas algorithm, also called the Tri-Diagonal Matrix Algorithm (TDMA). This solver can be used whenever the non-zero elements of the matrix to be solved align themselves on the diagonals of the matrix. The Thomas algorithm is well documented (see Smith (1985) or Patankar (1980) for example) so the details of it will not be given here.

Convergence and stability analysis for the control volume formulation is difficult at best. The difference scheme is nonlinear because of the nonlinear source and sink terms that appear in the turbulence model equations. The convergence of the difference scheme and the stability of the solver will be discussed briefly.

Since the difference scheme is nonlinear, it has to be linearized somehow for a convergence analysis. Equations (12) and (13) are elliptic partial differential equations. Assuming that convection is negligible (for example, there is no convection in a fully-developed pipe flow), the control volume formulation reduces to a central difference approximation of the second derivative. Hence, the convergence analysis is done based on a type of Laplacian equation,

$$\nabla^2\phi = f(\frac{\partial\phi}{\partial r},\phi,r + \text{nonlinear terms})$$

Smith (1985) determined that for Poisson's equation with $f=f(r)$, and a central difference approximation to the second derivative, the maximum error on the domain is

$$\max\ (\mathrm{ABS}(e_i)) \le \frac{1}{24}\ a^2\ h^2\ M_4$$

where $0 \le r \le a$, $h = \Delta r$, and M_4 is the maximum of all fourth partial derivatives of ϕ. This result proves the convergence of the central difference scheme for Poisson's equation because as h approaches zero the truncation error approaches zero. Of course, this result is not entirely valid for the nonlinear turbulence equations with nonlinear coupling.

Smith (1985) proves that the Thomas algorithm is stable with no growth of the rounding errors if:

1. a_P, a_S, and a_N are all greater than zero,
2. $a_P > a_S(i-1) + a_N(i+1)$ for $i=1,2,..,N-1$ with $a_S(0) = a_N(N) = 0$,
3. $a_P > a_S(i) + a_N(i)$ for $i=1,2,..,N-1$ with $a_S(N-1) = a_N(1) = 0$,

where there are N nodes. Conditions 1 and 2 ensure that the forward elimination is stable while conditions 1 and 3 ensure that the back substitutions are stable.

What this means practically is that S_p must be negative and S_c positive when the source term is linearized. This is not, however, a problem because most physical systems behave in this manner (Patankar, 1980).

The convergence criteria is based on the sum of the residuals over the calculation domain becoming small. That is, the left hand side of equation (15) minus the right hand side should sum to a remainder close to zero at each nodal point. The convergence criteria is specifically that the sum of all the remainders for each control volume over the calculation domain is small ($<10^{-8}$).

This finite difference scheme is implemented in the FORTRAN Code listed in Appendix E.

3.3 Evaluation of the k-ε Model of Turbulence with the Experimental Data from a Conical Diffuser Flow

There are several modifications and variations to the k-ε model constants in the literature. A number of these are summarized and evaluated in Nagano and Hishida (1987) or Patel et al (1984) with most of the models giving similar results. Three of the more recent models will be considered here, those being Nagano and Tagawa (1990)[NT], Lai et al (1989) [LSH], and Hoffmann (1975) [HOF]. These three were chosen for the following reasons. The NT model was chosen because it incorporates ideas developed from experimental data along with a significant modification first proposed by Hanjalic and Launder (1980). LSH was chosen because they obtained good results for the mean velocity field in the eight degree conical diffuser flow of Trupp et al (1986). HOF was chosen because the set of constants in this model is quite different from any of the other models. The model constants and damping functions of these three models are summarized in Table 3.1.

Recently, there has been good k-ε prediction of the mean velocity for the eight degree conical diffuser flow (Lai, So, and Hwang, 1989). Lai et al, however, do not show any results for the turbulence field. For this reason, the objective of this chapter is to evaluate the k-ε model of turbulence in terms of how well it can predict the turbulence field in the severe adverse pressure gradient diffuser flow. The approach to this is similar to that of Mansour et al (1989) in that experimental data will be used to evaluate the model. In the case of Mansour et al, the data came from their numerical simulation of a channel flow.

There have been modifications suggested to the basic high Reynolds number k-ε model to take into account the effects of an adverse pressure gradient. The difficulty in these flows seems to be related to relative rates of production and destruction in the ε-equation. In a fully-developed pipe flow the production of kinetic energy is simply $-\overline{uv}(\partial U/\partial r)$ where $\partial U/\partial r$ is the rotational strain. In adverse pressure gradient flows the irrotational strain starts to play an important role in balancing the two equations, specifically in the ε-equation (Patel et al, 1984). Hanjalic and Launder (1980) add a second constant to the ε production, $C'_{\varepsilon 1}$ to help account for this. This leads to their modified ε production of

$$- C_{\varepsilon 1} \frac{\varepsilon}{k} \left[\overline{uv}\left(\frac{\partial U}{\partial r} + \frac{\partial V}{\partial x}\right) + 3.1\ (u^2-v^2)\ \frac{\partial U}{\partial x}\right]$$

where $C'_{\varepsilon 1} = 3.1 C_{\varepsilon 1}$. This added ε production is critical for balancing of the two equations, as will be shown.

The effects of the relative rates of production and destruction of ϵ will be discussed following a brief examination of the kinetic energy equation. The kinetic energy equation (equation 12) has only one modeled term, the kinetic energy diffusion. As a first step in the evaluation of the k-ϵ model, this term is examined. In Figures 3.2, 3.3, and 3.4 at the stations x=30, 42, and 66cm respectively in the conical diffuser, the modeled and experimental radial kinetic energy diffusion are compared, where the modeled diffusion is calculated directly from the experimental data. The modeled term shows general agreement but in the vicinity of the wall the models of NT and Nagano and Hishida (1987) [NH] are too large in absolute value. The modification by NT of $\sigma_k=1.4$ from the Nagano and Hishida (1987) model where $\sigma_k=1.0$ is a significant improvement. The LSH model shows better agreement in the first few stations adjacent to the wall because their f_μ is substantially smaller than that of NT and NH in this region. Away from the wall, f_μ approaches unity for all models and has no direct effect on the calculations. In the region away from the wall, the NT model is superior to the other models because of their using $\sigma_k=1.4$ rather than the usual $\sigma_k=1.0$.

The eddy viscosity also plays an important role in the production of kinetic energy. Since the Reynolds stresses are modeled through the Boussinesq definition of the eddy viscosity, the production is implicitly modeled.

The NT modeled production is calculated directly from the experimental data and is shown with the other terms of the exact kinetic energy budget (equation 8) in Figures 3.5, 3.6, and 3.7 at the same three diffuser stations. It can be seen that the modeled production is much too large at all three stations. Part of the problem may be from the f_μ used in the models. Figures 3.8, 3.9, and 3.10, again for x=30, 42, and 66cm respectively show what the experimental f_μ should be from the equation

$$f_\mu = \frac{-\overline{uv}}{C_\mu[\partial U/\partial r + \partial V/\partial x]} \frac{\varepsilon}{k^2} \qquad (20)$$

The model of LSH is in better agreement with the data than the other models near the wall. All of the models approach unity as the distance from the wall increases while the experimental data goes to values between 0.2 and 0.4. Hence, these models should not show good agreement with the experimental turbulence field if these f_μ damping functions are used. The damping function of NT is similar to that of Nagano and Hishida (1987) while the damping function of HOF is similar to that first proposed by Jones and Launder (1972).

If the dissipation rate is then used as the closing term for the modeled kinetic energy equation, it is necessary for it to be much larger than the experimental dissipation rate. However, if the experimental production is used instead of the modeled production the calculated "closing term dissipation" is much closer to the experimentally measured dissipation rate. This is shown in Figures 3.11, 3.12, and 3.13, again for x=30, 42, and 66cm respectively. In these figures, the experimental dissipation rate is compared with the dissipation rate required to close equation (12) given the different models kinetic energy diffusion rates. This closing term dissipation rate can then be interpreted as the dissipation rate required to keep the kinetic energy at the experimental level. In the wall region at x=30 and 42cm, the dissipation required to close the modeled kinetic energy equation is larger than the experimental dissipation, while at x=66cm the required dissipation is smaller on the average. In the core region, the scatter is around the experimental ϵ so conclusions are difficult to make.

If all of the terms in the modeled kinetic energy equation are moved to the left hand side of the equal sign, the right hand side should sum to zero. Of course, with experimental data some scatter occurs and there will be a remainder. Figures 3.14, 3.15, and 3.16 show the remainder for the kinetic energy equation. Generally, there is quite a large degree of scatter, as in Figures 3.11, 3.12, and 3.13. The most important region, however, is the wall region because poor prediction in this region is likely to cause poor prediction away from the wall. At x=30cm, the remainder in the wall region is on the production side of the balance. This implies that the kinetic energy should become larger if the dissipation remains the same. The same type of remainder occurs at x=42cm except that the remainder is on the order of magnitude of the production term. At x=66cm, the remainder term is on the destruction side in the wall region, meaning that the kinetic energy will become smaller to balance the two equations if the dissipation rate is held at the experimental level.

In order to see what the possible effect the ε-equation could have on the kinetic energy field, the remainder of the ε-equation is also examined with the experimental data. Figures 3.17, 3.18, and 3.19 show the remainder of the NT and LSH models along with the terms of the LSH ε-equation at the same three diffuser stations. In the wall region at x=30cm the remainder is on the production side for $r/R_{local}>0.8$. This implies that if the kinetic energy does not vary from the experimental values, ε should increase. Recalling Figure 3.11, this is exactly what is required of the "closing term dissipation" if the kinetic energy is to remain at the experimental levels. Hence, a reasonable prediction of k at x=30cm is possible when both equations are solved with the experimental production given.

The same is not true for x=42cm. Recalling Figure

3.12, it is necessary for ε to increase over the experimental levels in the wall region. Figure 3.18 shows that the opposite should occur. In the wall region, the remainder term is on the destruction side of the balance. Hence, poor prediction of k at x=42cm is expected when both equations are solved simultaneously and the experimental production is given. At x=66cm, the remainder is also on the destruction side near the wall, as shown in Figure 3.19, but recalling Figure 3.13, this is what is required. Hence reasonable prediction of k at x=66cm should be expected.

In order to examine the above discussion further, both equations are solved simultaneously with the finite-difference method described previously. To do this effectively the equations are solved one-dimensionally with all axial gradients given as input. As well, the experimental production rates are given along with the mean velocity field. Axial diffusion is neglected. The boundary conditions are: $\partial k/\partial r = 0$ and $\partial \varepsilon/\partial r = 0$ at the centreline. At the wall special precautions are taken. In order to avoid errors in interpolating the experimental production and the axial gradients near the wall, k and ε are given at the first experimental point adjacent to the wall.

Figures 3.20, 3.21, 3.22, and 3.23 show the results for the kinetic energy in the fully-developed pipe flow at the inlet of the eight degree diffuser, and at x=30, 42, and

66cm the diffuser flow respectively. Figures 3.24, 3.25, 3.26, and 3.27 show the results for the dissipation rate at the same stations. The Nagano and Tagawa (1990) model shows good agreement with the experimental kinetic energy in Laufer's (1954) fully-developed pipe flow, which is similar to the present flow. They show a slight over-prediction of the kinetic energy and a slight under-prediction of the mean velocity at the centreline of the pipe. Since the mean velocity field and production are invariant in the present calculations, the kinetic energy rises above the experimental values near the centreline because the dissipation rate is moderately small. There is good agreement near the wall, however, for both variables. No conclusions can be made about the near wall region because the first experimental point is not close enough to the wall.

This shows one of the potential problems with this type of calculation. Because of the strong coupling between the equations, small changes in one variable can lead to substantial changes in the other variable (Patel, Rodi, and Scheuerer, 1984). Since the velocity field is invariant in this situation, all of the changes in one variable are amplified in the other variable in order to balance the equations. Even though the equations are over specified with the present method, evaluation of the model is still possible.

At x=30cm the agreement with the experimental data is reasonable with the model of NT, although in the core region the error is high. The models of LSH and HOF show a poor agreement The kinetic energy shows a strong dependence on the value of $C'_{\varepsilon 1}$ used in the ε-equation and this could be why LSH and HOF show poor agreement. When $C'_{\varepsilon 1}$ is changed to $1.0C_{\varepsilon 1}$ in the NT model, the results are similar to those of LSH and HOF. On the other hand, when $C'_{\varepsilon 1} = 3.1C_{\varepsilon 1}$, as recommended by of Hanjalic and Launder (1980) the kinetic energy is in better agreement with the experimental kinetic energy. Increasing this constant increases ε near the wall, while decreasing it in the core region and lowering k in both regions. The solution is quite sensitive to $C'_{\varepsilon 1}$ as shown in Figure 3.21.

At x=42cm the agreement is poor as expected with even $C'_{\varepsilon 1} = 3.1C_{\varepsilon 1}$ having little effect. Figure 3.25 shows the cause of the poorly predicted kinetic energy. Clearly, ε is too small near the wall which causes k to become far too large. The exception to this is HOF where the vastly different constants cause ε to rise above the experimental ε. However, the HOF k values are again similar to LSH. At x=66cm the prediction of k is excellent with NT and good in the wall region with LSH. Clearly, ε decreases enough for k to be predicted well, as shown by the direct calculations from the experimental data. Of note, however, the program code did not converge with HOF or with NT with $C'_{\varepsilon 1} = 3.1C_{\varepsilon 1}$.

In order to examine whether the solution was numerically correct the effect of the various boundary conditions are examined. The effects of varying the specified k and ε values at the first nodal point from the wall was negligible. Increasing the ε value 1000% lead only to a 22% decrease of the centreline value of k and either halving or doubling the k value lead to only a 5% change in the centreline value of k. Hence, using the first experimental measuring station from the wall as the first nodal point with the previously stated boundary conditions was valid.

In order to examine grid independence, a Lagrangian curve fit was applied to the experimental nodal points in order to interpolate the given axial gradients, Reynolds stresses, and mean velocities between the experimental stations. Grid independence was achieved with the experimental number of measurement points, generally about 20 nodes at each axial station. Identical solutions were obtained with twice as many grid points.

For these calculations no under-relaxation was required and convergence was rapid, usually less than 100 iterations. The convergence criterion was that the residual sum of the algebraic equations (equation 15) over the domain for each model equation be less than 10^{-8}. There was generally four significant figures of accuracy when the residual reached 10^{-4}. The program execution time on a 33MHz 80386 computer with an 80387 math co-processor was less than one minute for these one-dimensional calculations.

In order to calculate both k and ϵ with the finite-difference scheme, along with the production, modifications had to be made to the Reynolds stresses. Bradshaw (1967) was the first to note that the structural coefficient $a_1 = -\overline{uv}/k$ was approximately constant for all pressure gradients. Shown in Figure 3.28, 3.29, and 3.30 are plots of $-\overline{uv}$ versus $\overline{q^2}$ (=2k) for the same three diffuser stations. Bradshaw determined a_1=0.30. In order to use this method directly, the functional form of the shear stress is $-\overline{uv} = a_1k+b$ with a_1 and b determined by curve fitting the experimental data. The values at x=30, 42, and 66cm are shown in Table 2 with a_1 generally about 0.28 and b $\approx$ -0.2. With this functional form the shear stress can be closely represented as shown in Figures 3.28, 3.29, and 3.30. Also shown on these figures is $-\overline{uv} = f_\mu(a_1k+b)$ where the LSH damping function is used, as will be mentioned below. With this, unrealistically low shear stresses occur. The reason for using this is shown shortly.

Modeling $(\overline{u^2}-\overline{v^2})$ is also required, as the usual k-ϵ model for this term poorly represents the data (Polak and

Turan, 1991). Hanjalic and Launder (1980) recommend $(\overline{u^2}-\overline{v^2})=0.33k$. Plotted in Figures 3.31, 3.32, and 3.33 are $(\overline{u^2}-\overline{v^2})$ versus $\overline{q^2}$ again for the same three diffuser stations. If the functional form of the difference between the two normal stresses is $(\overline{u^2}-\overline{v^2}) = a_2k+c$, a reasonable representation can be obtained. The results of curve-fitting the experimental data are shown in Table 3.2. It is observed that a_2 decreases from 0.8 to 0.45 in the flow direction with c increasing from -0.45 to -0.17. At x=66cm the data does not fall onto one line but the best average is used. This may be due to the diffuser end effects.

With the above approximations for the turbulence stresses, a better approximation for the production of k and ϵ can be obtained as compared with the usual $k-\epsilon$ models. With $-\overline{uv}$ damped with the LSH f_μ,the production of k using the experimental data is shown in Figures 3.34, 3.35, and 3.36. This yields an under-prediction of the production due to the damping of $-\overline{uv}$.

With a more accurate production thus determined, k, ϵ, $\overline{uv}$, and $(\overline{u^2}-\overline{v^2})$ are calculated with the finite-difference scheme. The boundary conditions are identical to those used in the previous calculations. The results for the three diffuser stations with the NT model are shown in Figures 3.37, 3.38, and 3.39 for k and Figures 3.40, 3.41, and 3.42

for ε. The results are at least an order of magnitude too large with both the modified Reynolds stress and the usual k-ε model Reynolds stress. The modified model yields much better results than the usual model, however.

To possibly rectify this problem $C'_{\varepsilon 1}$ is adjusted. As it was increased the final solution improved, as shown in Figures 3.37-42, but not enough to be even as good as the results shown in Figures 3.20-27. Eventually a value of $C'_{\varepsilon 1}$ was obtained that caused the solution to diverge. The divergence was caused by either k or ε becoming negative. For example, at x=42cm the value of $C'_{\varepsilon 1}$ that caused divergence was $3.88837C_{\varepsilon 1}$ while if $C'_{\varepsilon 1}=3.88836C_{\varepsilon 1}$ the solution converged with the value of k at the centreline equal to 15.22 (This value of $C'_{\varepsilon 1}$ is initial conditions dependent, but the final converged solution is not. All of the calculations and results presented here have experimental k and ε for initial conditions). Table 3.3 shows the various values of the centreline kinetic energy obtained from the different values for $C'_{\varepsilon 1}$, at the three diffuser stations. It is believed that the nonlinearity of the two partial differential equations causes this effect along with possibly that the equations are over-specified. Because of this, an acceptable solution for k and ε cannot be obtained when the Reynolds stresses (or production) are calculated.

Figures 3.43-48 show the k and ε fields just one iteration prior to divergence. Also, included in Figures 3.43, 3.44, 3.46, and 3.47 for x=30 and 42cm, are the partially converged solutions for k and ε with $C'_{\varepsilon 1} = 2.5\ C_{\varepsilon 1}$ at the point where these solutions are at their minimum. It appears that divergence is caused by a local imbalance in the production and destruction of the two equations which in turn causes either variable to become negative.

3.4 Conclusions

It is concluded based on the calculations with the experimental production rates, that the k-ε model of turbulence can yield reasonable predictions for the kinetic energy in the severe adverse pressure gradient flow of an eight degree conical diffuser. The production term in both equations must be modified though. An accurately predicted shear stress is crucial for good prediction. Also, the irrotational portion of the ε-equation production significantly affects the balance between the two equations. The modification by Hanjalic and Launder (1980) incorporated by NT is a significant improvement.

The usual shear stresses and normal stresses calculated by the k-ε model are in poor agreement with the experimental data (Polak and Turan, 1991). Improvements can be made by using Bradshaw's structural coefficient $a_1 = -\overline{uv}/k$ $=0.30$ and by the recommendation of Hanjalic and Launder (1980) that $(\overline{u^2}-\overline{v^2})/k = a_2 = 0.33$. The values for a_2 in the present flow examined do not agree with their a_2, and are approximately twice as large. The reason for the poor representation of $\overline{uv}$ is due to inaccurate damping functions f_μ which do not represent the experimental data. The damping function of LSH represents $\overline{uv}$ reasonably near the wall, which possibly explains why they obtained a reasonable prediction of the mean velocity field. Like the other damping functions, the LSH f_μ is in poor agreement with the data in the core region.

The vastly different model constants of HOF significantly affect the calculation of ε, but do not show an improved prediction of k. The model, in fact, did not converge at the last station, x=66cm. The best model in this evaluation is that of NT because of enhanced irrotational terms in the ε-equation production. The modification of $\sigma_k=1.4$ is also an improvement.

With the poor prediction of the data at x=42cm, it appears that $C'_{\varepsilon 1}$ may need to have a functional form dependent on the pressure gradient rather than being constant. Other constants in the model may need to be dependent on the pressure gradient as well. LSH make an improvement in this regard by including pressure gradient dependence in their f_μ damping function.

With the method used here, the equations may be over-specified causing small imbalances in the model equations to have a significant effect on the solution. These effects are small when the Reynolds stresses are given, but poor results occur when they are calculated. Hence, this type of calculation is only useful for evaluation purposes, but is not of much use for prediction purposes if the a mean velocity field has been assumed.

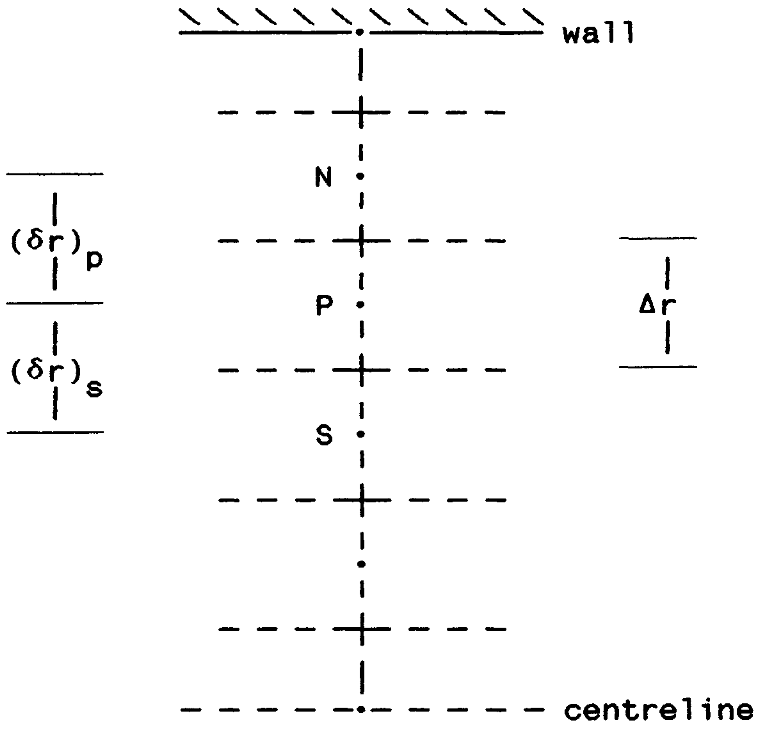

Figure 1. The finite-difference grid (Patankar type A) for the control volume formulation.

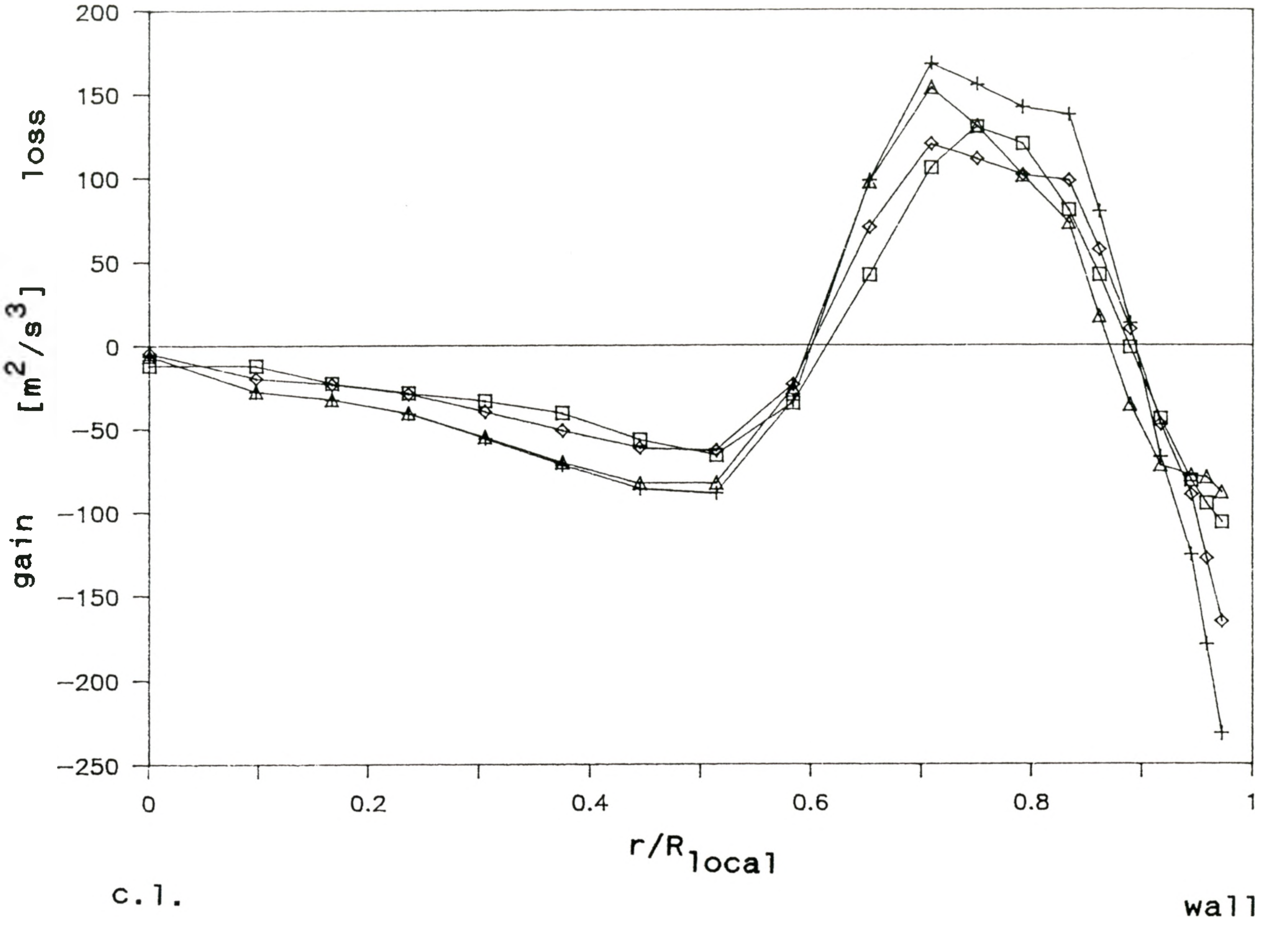

3.2. Comparison of modeled and experimental kinetic energy diffusion rates at x=30cm: □ experimental, ◇ NT, △ LSH, + Nagano and Hishida.

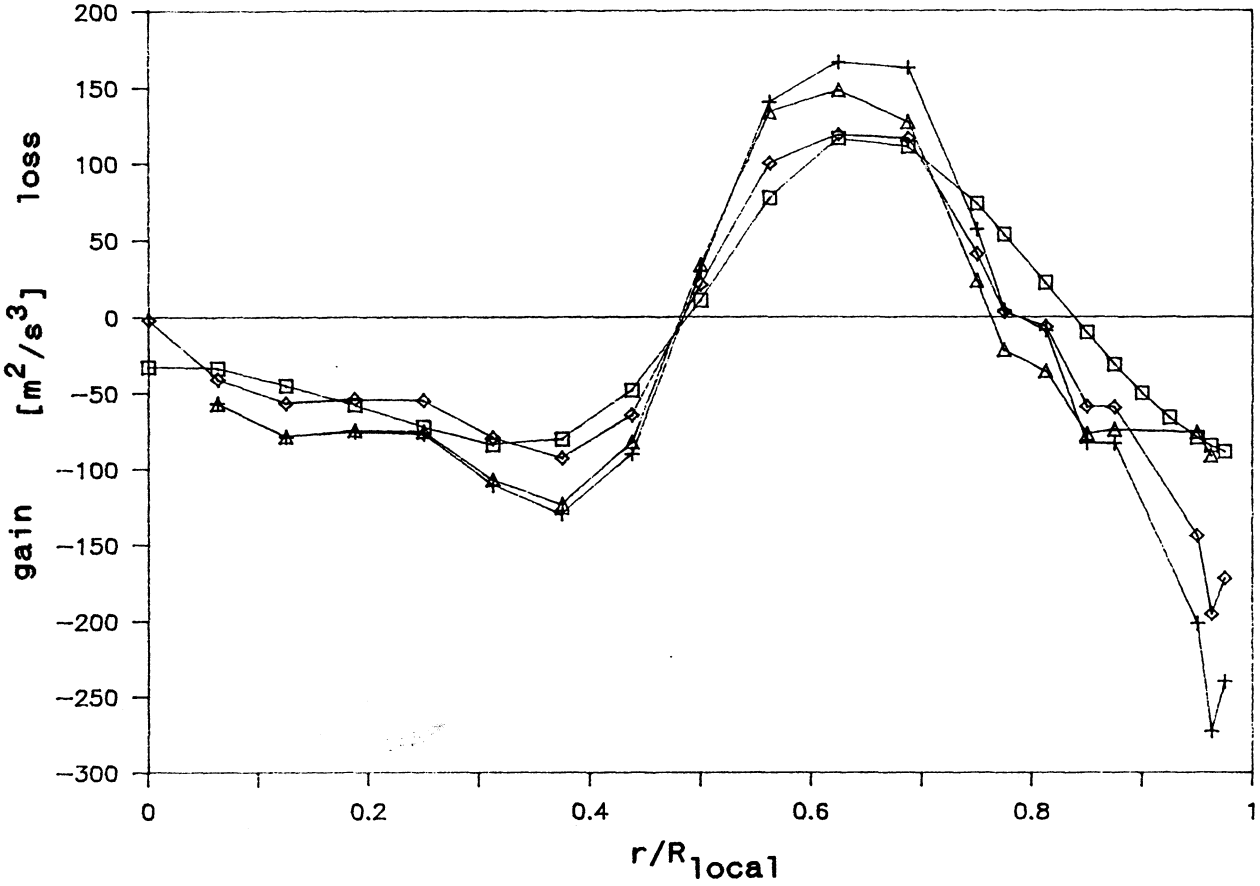

3.3. Comparison of modeled and experimental kinetic energy diffusion rates at x=42cm: □ experimental, ◇ NT, △ LSH, + Nagano and Hishida.

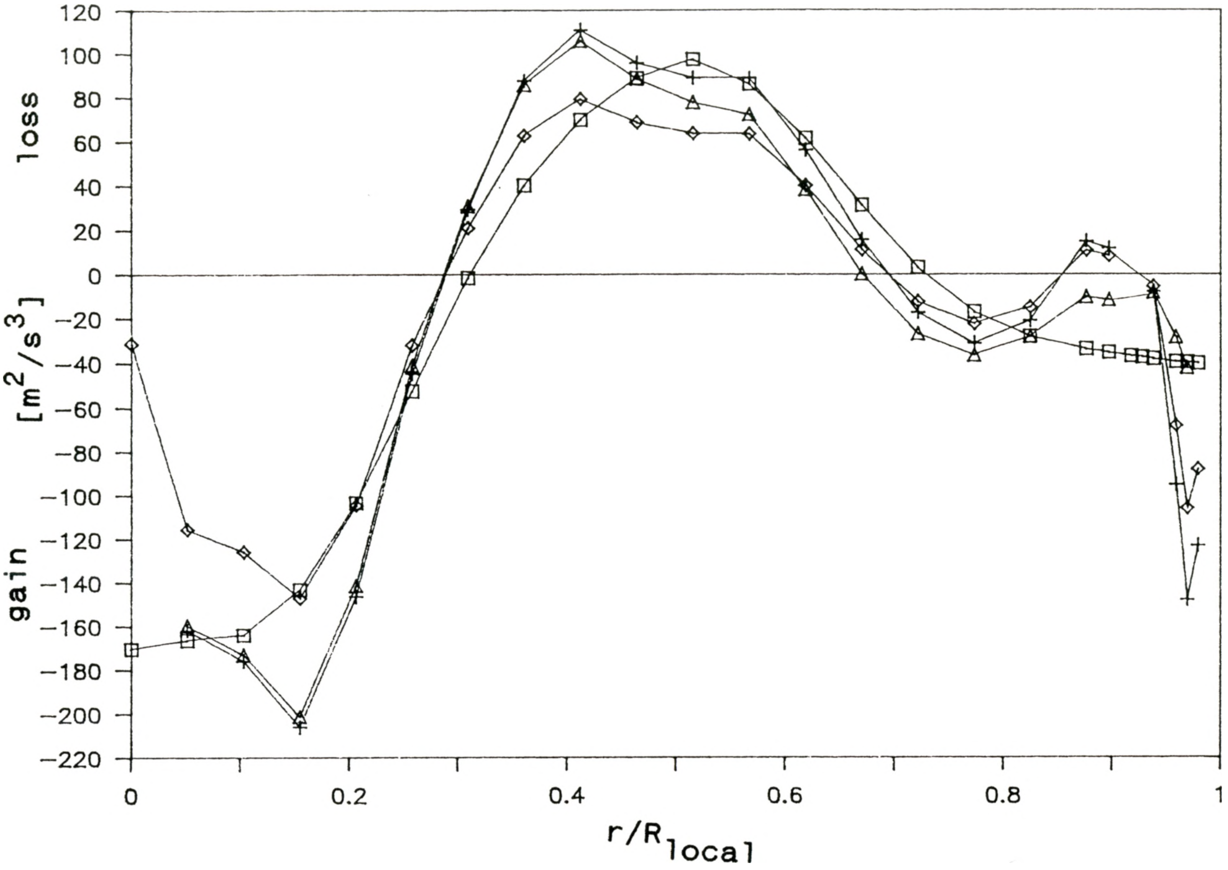

3.4. Comparison of modeled and experimental kinetic energy diffusion rates at x=66cm: □ experimental, ◇ NT, △ LSH, + Nagano and Hishida.

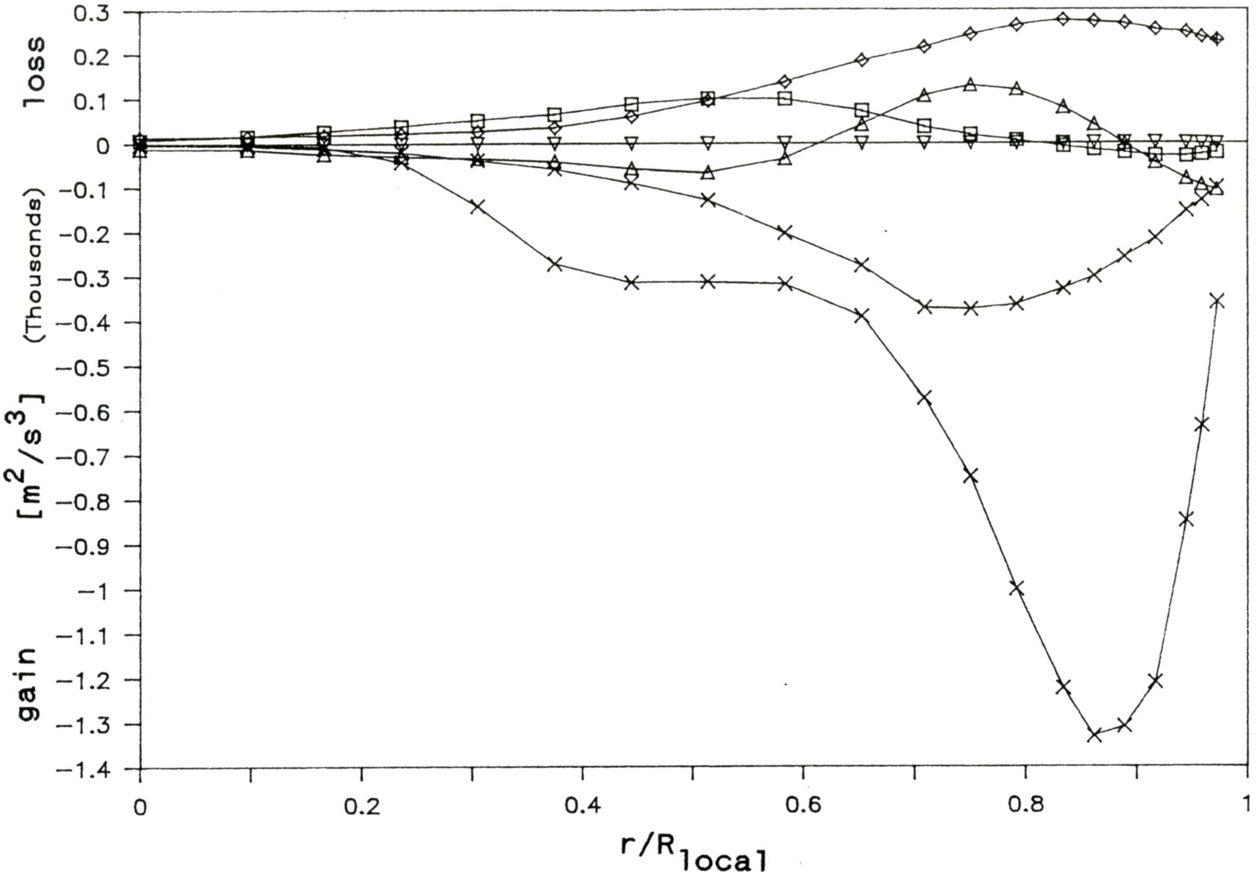

3.5. The terms of the exact kinetic energy equation at x=30cm: □ advection, △ kinetic energy diffusion, ◇ dissipation, × production, ▽ viscous diffusion. The NT modeled production is much larger than the experimental production.

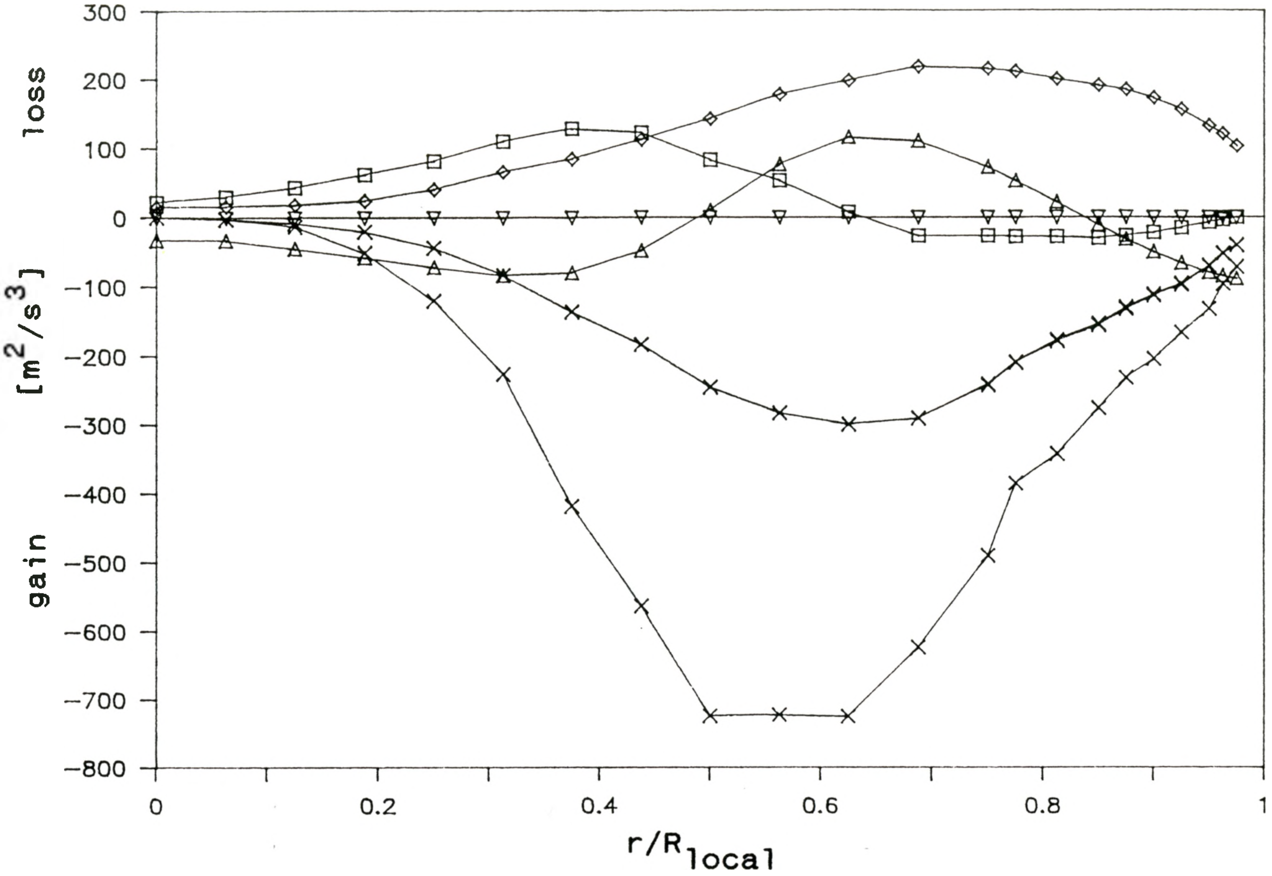

3.6. The terms of the exact kinetic energy equation at x=42cm: □ advection, △ kinetic energy diffusion, ◇ dissipation, × production, ▽ viscous diffusion. The NT modeled production is much larger than the experimental production.

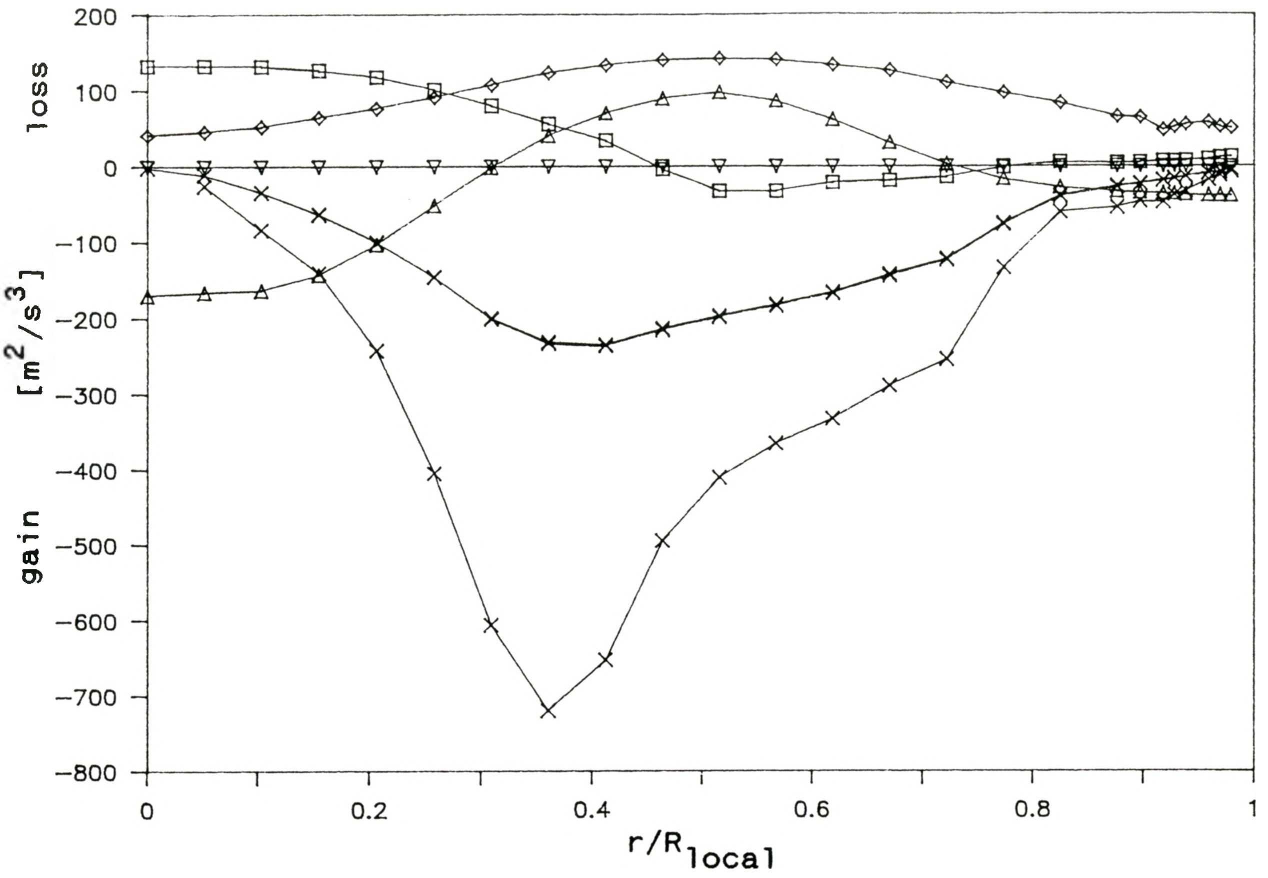

3.7. The terms of the exact kinetic energy equation at x=66cm: □ advection, △ kinetic energy diffusion, ◇ dissipation, × production, ▽ viscous diffusion. The NT modeled production is much larger than the experimental production.

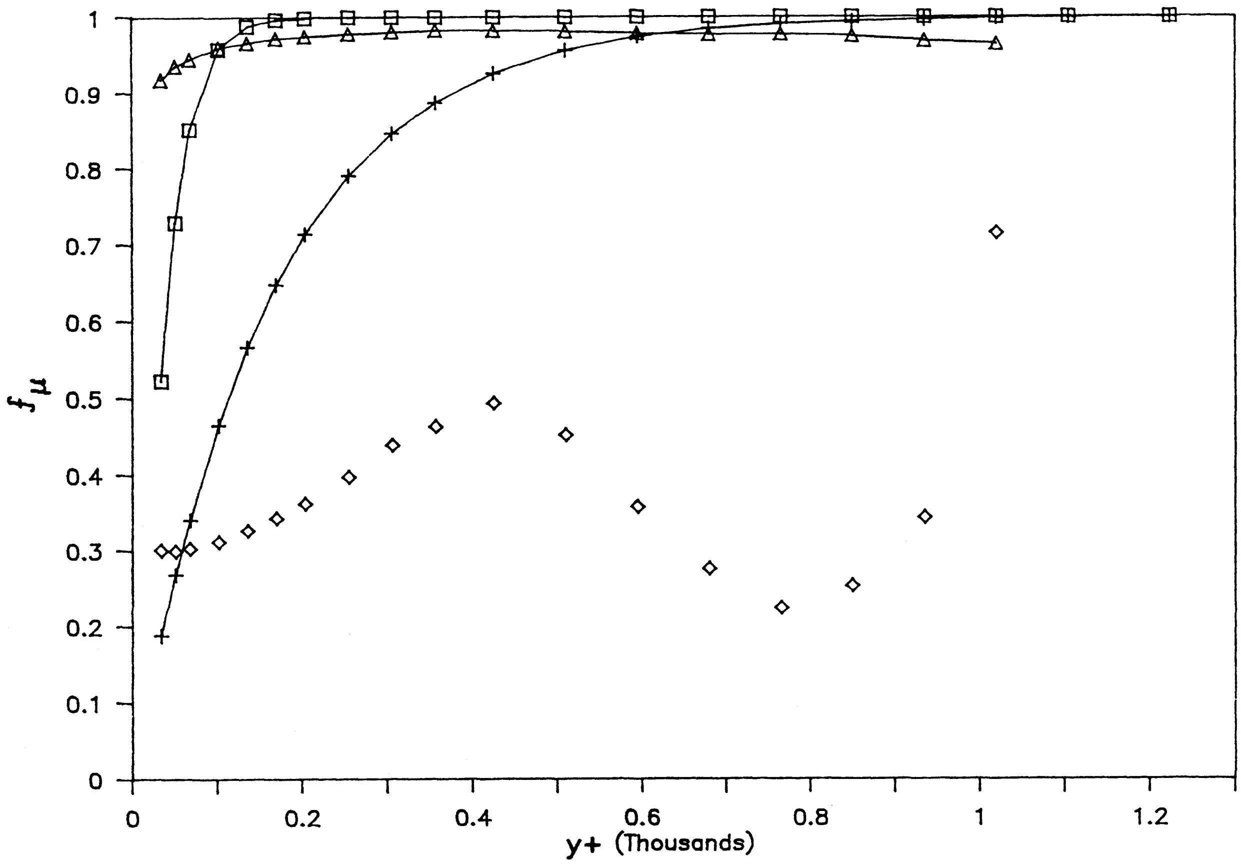

3.8. Comparison with model damping function f_μ with the experimental data at x=30cm: + LSH, □ NT and Nagano and Hishida, △ HOF and Jones and Launder, ◇ experimental (equation (20)).

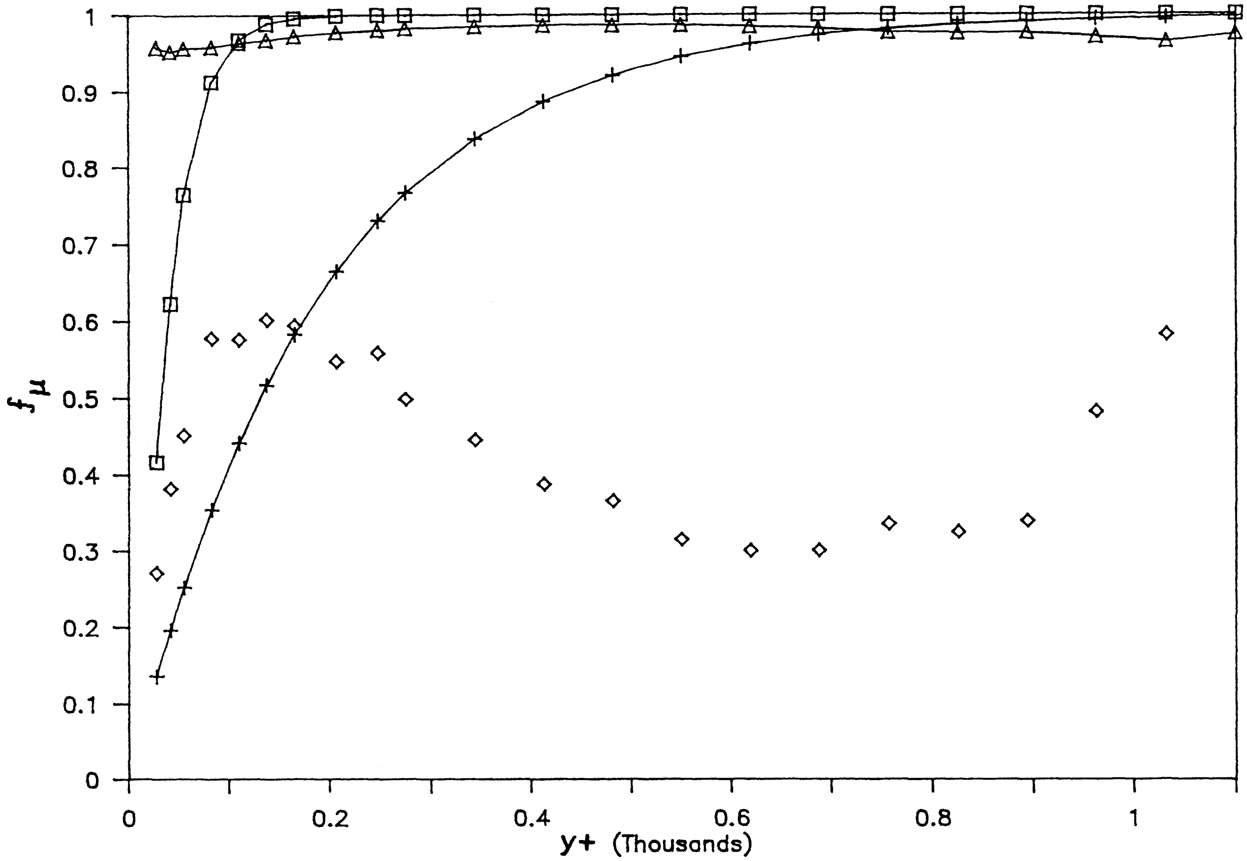

3.9. Comparison with model damping function f_μ with the experimental data at x=42cm: + LSH, □ NT and Nagano and Hishida, △ HOF and Jones and Launder, ◇ experimental (equation (20)).

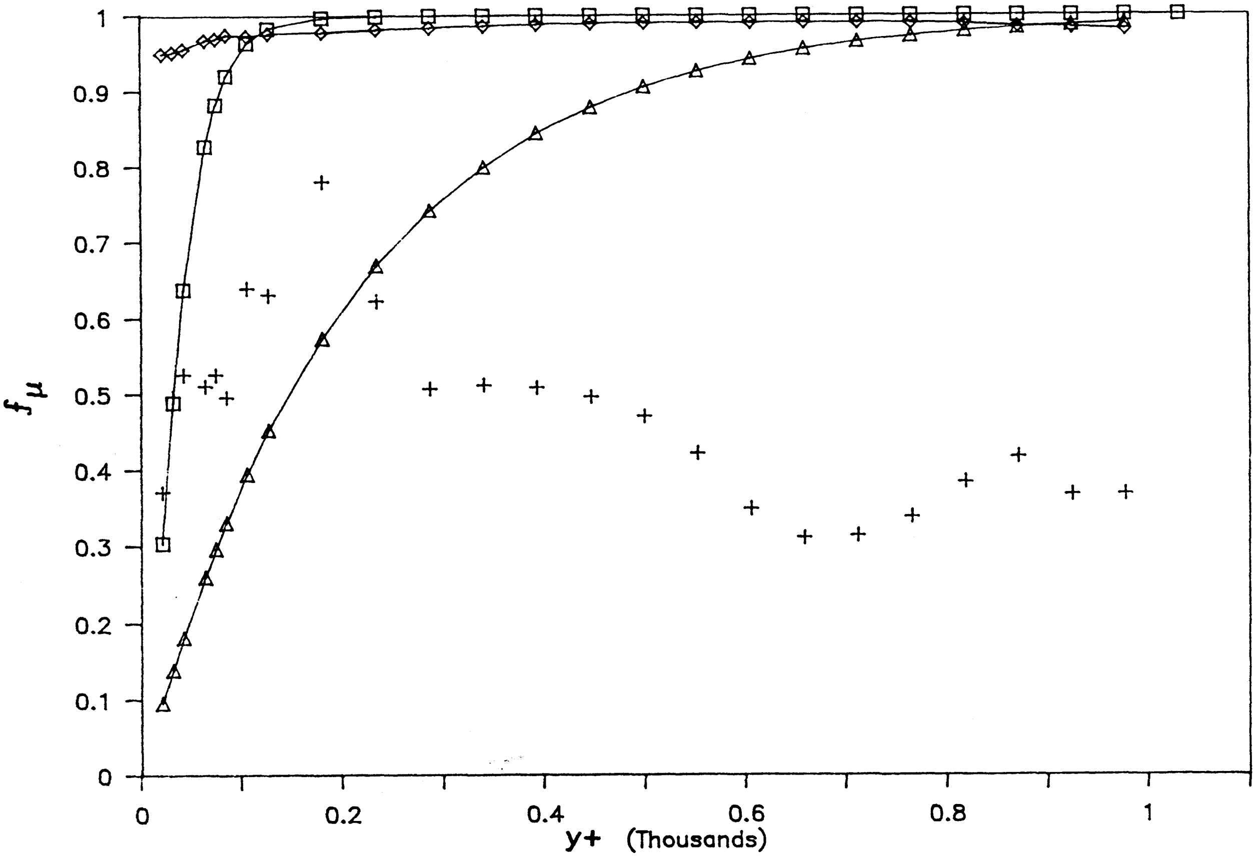

3.10. Comparison with model damping function f_μ with the experimental data at x=66cm: △ LSH, □ NT and Nagano and Hishida, ◇ HOF and Jones and Launder, + experimental (equation (20)).

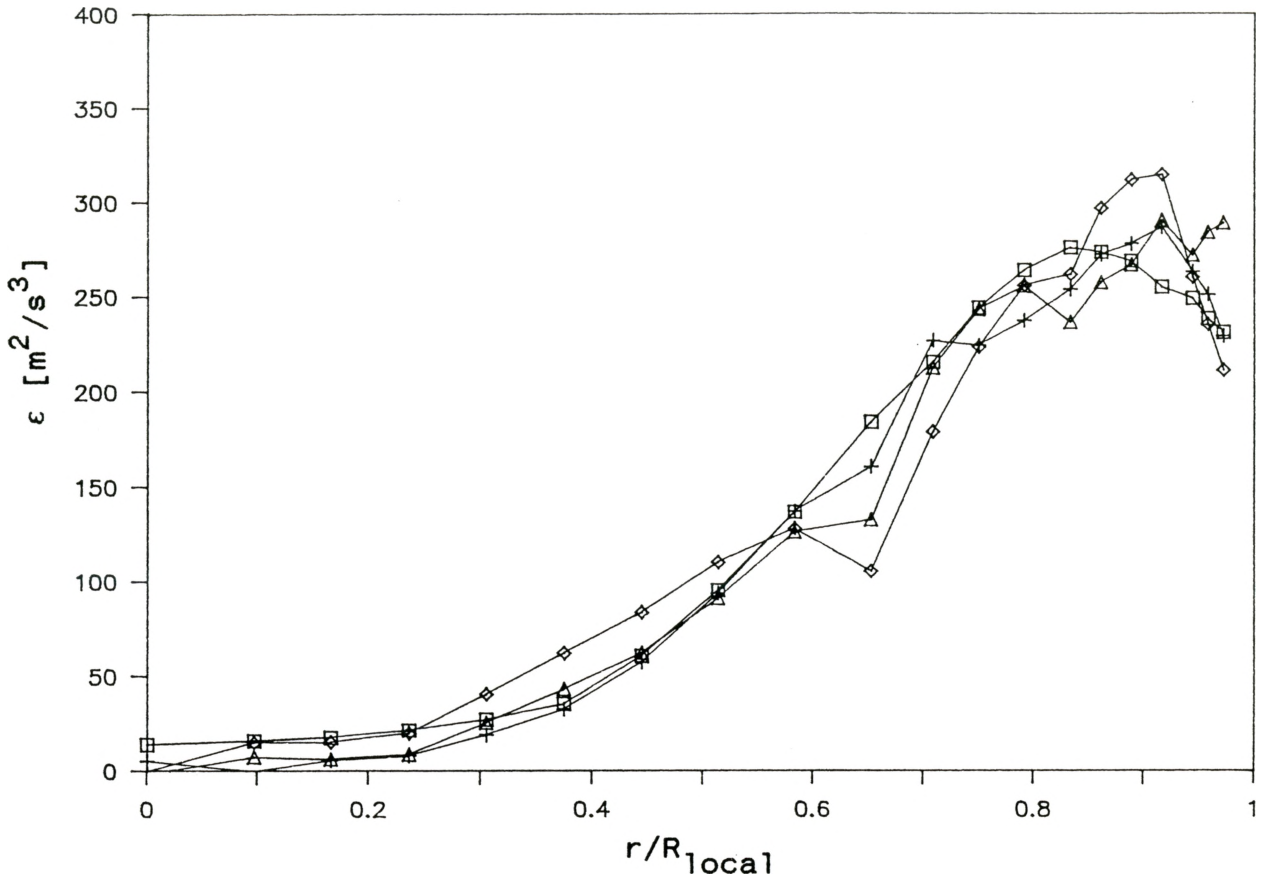

3.11. Comparison of experimental ε with the closing term ε (experimental production is given) at x=30cm: □ experimental, + experimental closing term, △ LSH, ◇ NT.

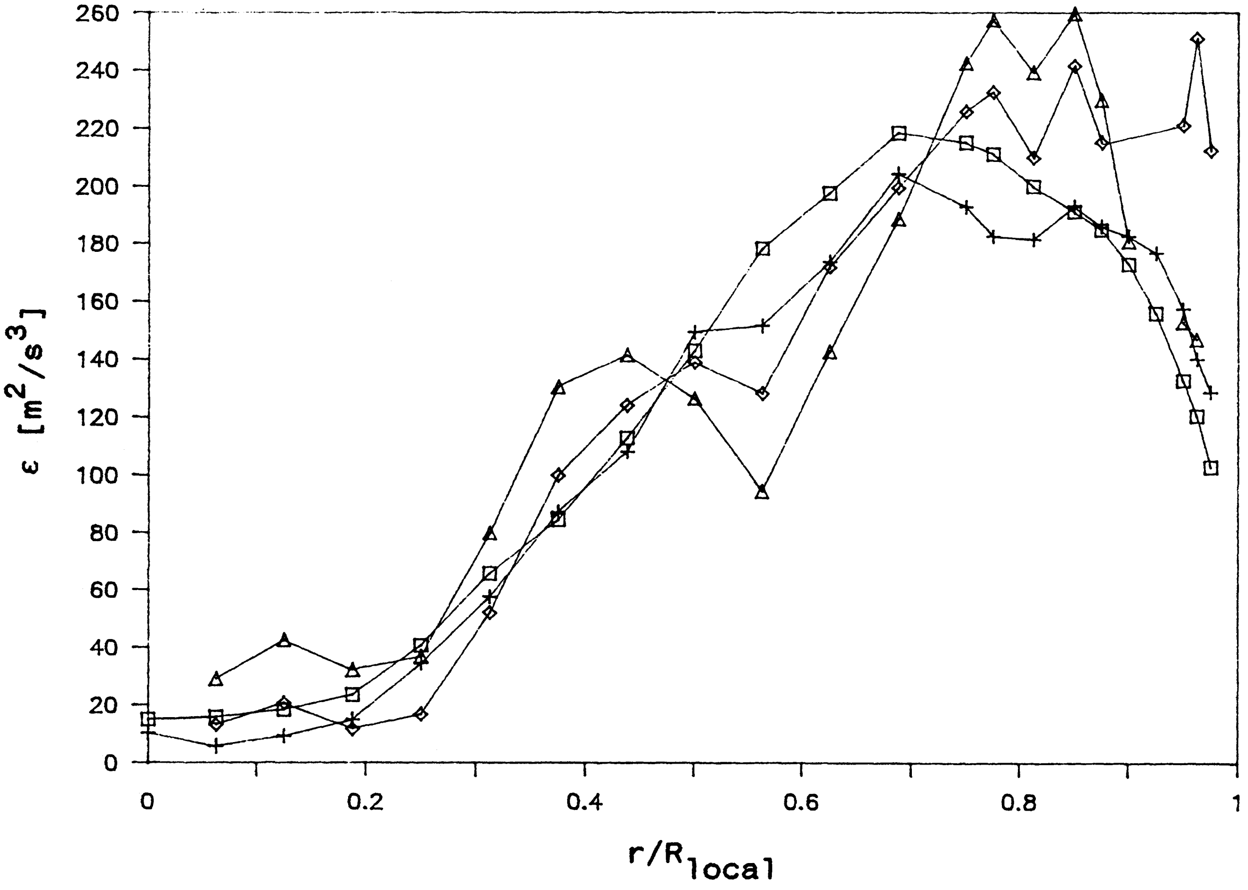

3.12. Comparison of experimental ε with the closing term ε (experimental production is given) at x=42cm: □ experimental, + experimental closing term, △ LSH, ◇ NT.

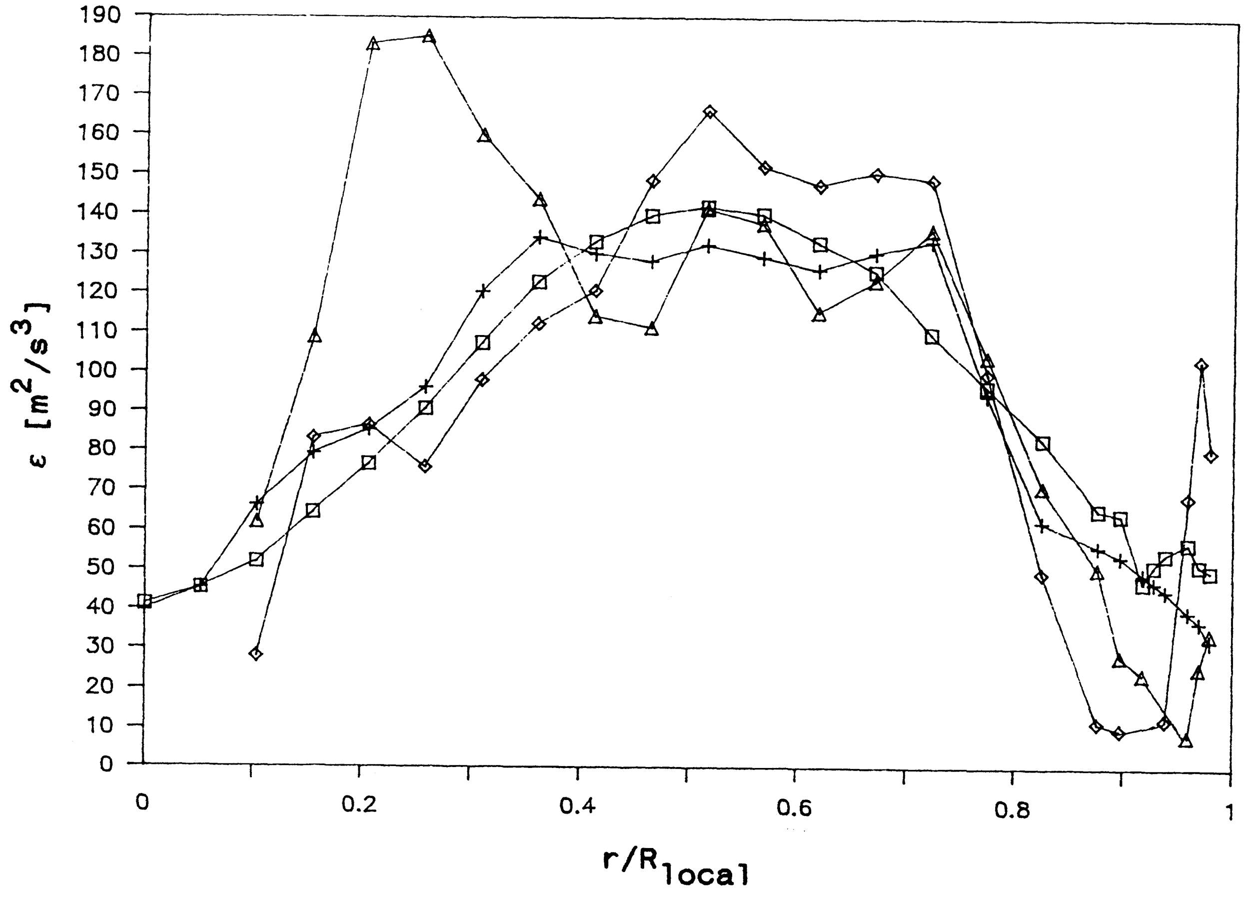

3.13. Comparison of experimental ε with the closing term ε (experimental production is given) at x=66cm: □ experimental, + experimental closing term, △ LSH, ◇ NT.

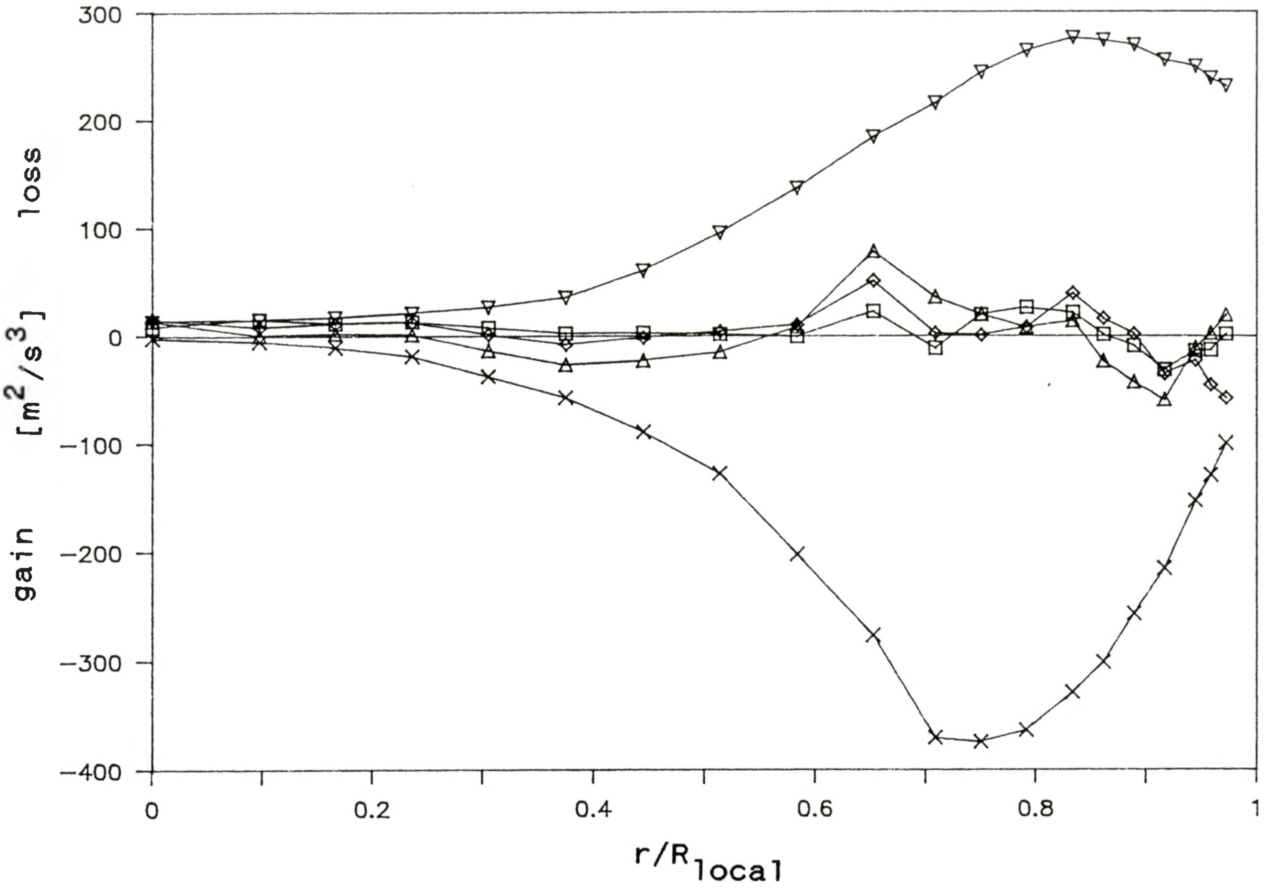

3.14. Remainder of the modeled kinetic energy equation at x=30cm (experimental production is given) at x=30cm: □ experimental remainder, ◇ NT, △ LSH, × production, ▽ dissipation.

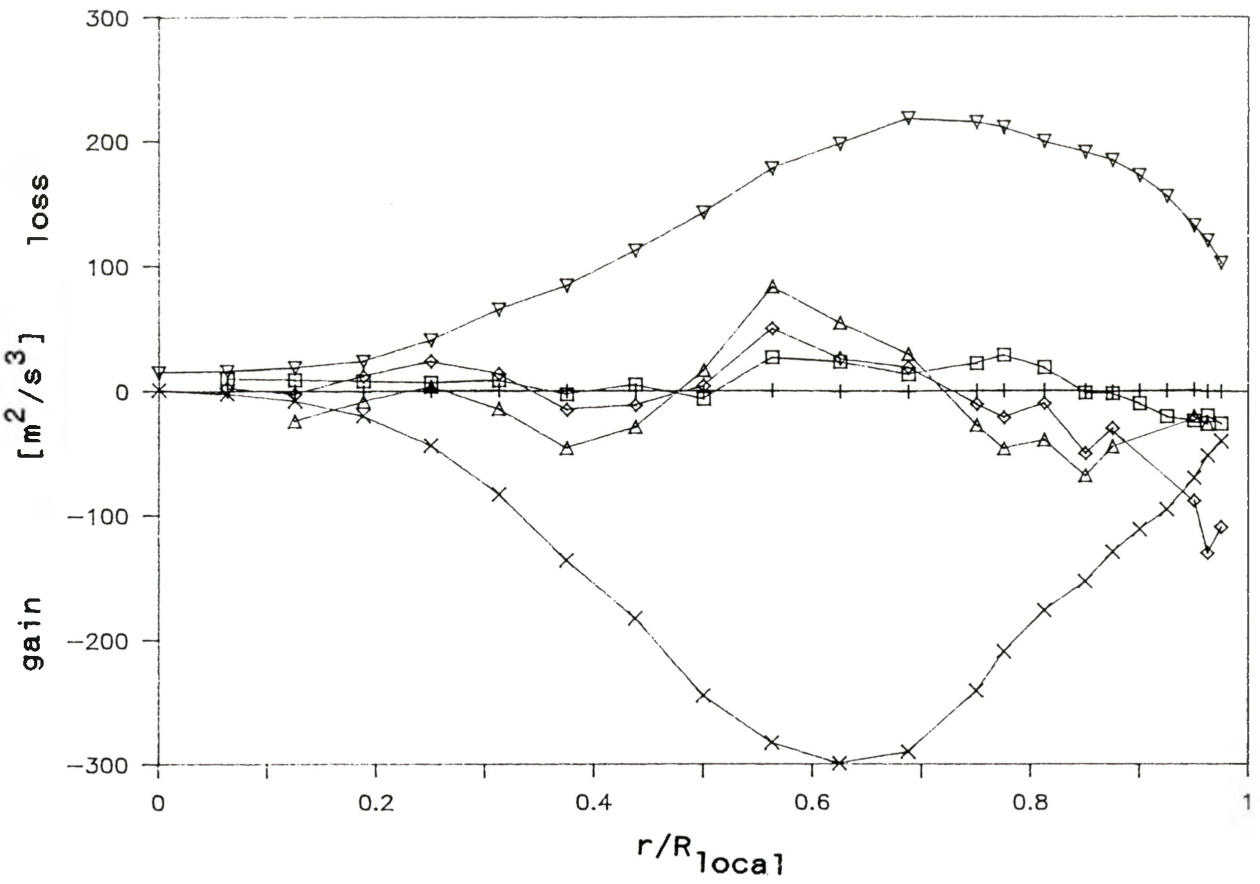

3.15. Remainder of the modeled kinetic energy equation at x=30cm (experimental production is given) at x=42cm: □ experimental remainder, ◇ NT, △ LSH, × production, ▽ dissipation.

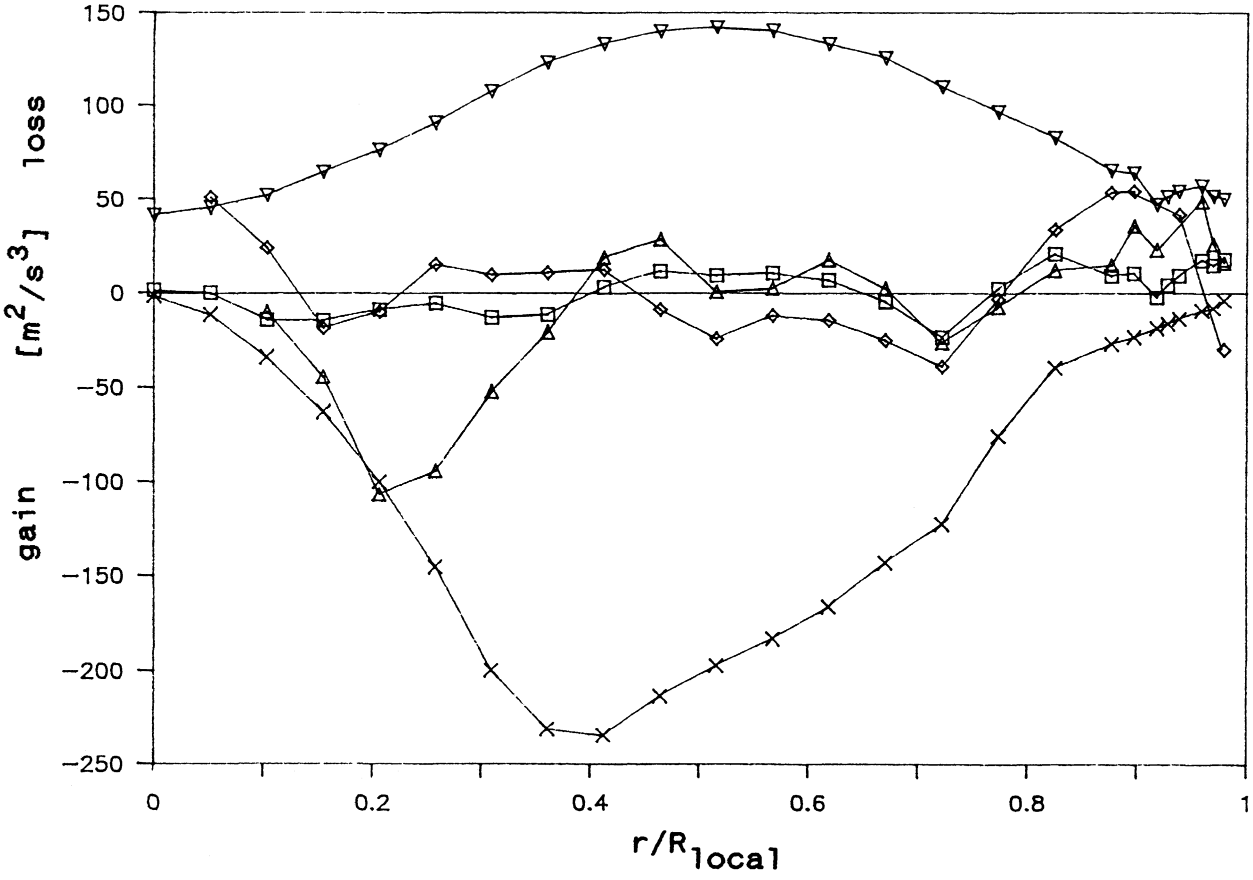

3.16. Remainder of the modeled kinetic energy equation at x=30cm (experimental production is given) at x=66cm: □ experimental remainder, ◇ NT, △ LSH, × production, ▽ dissipation.

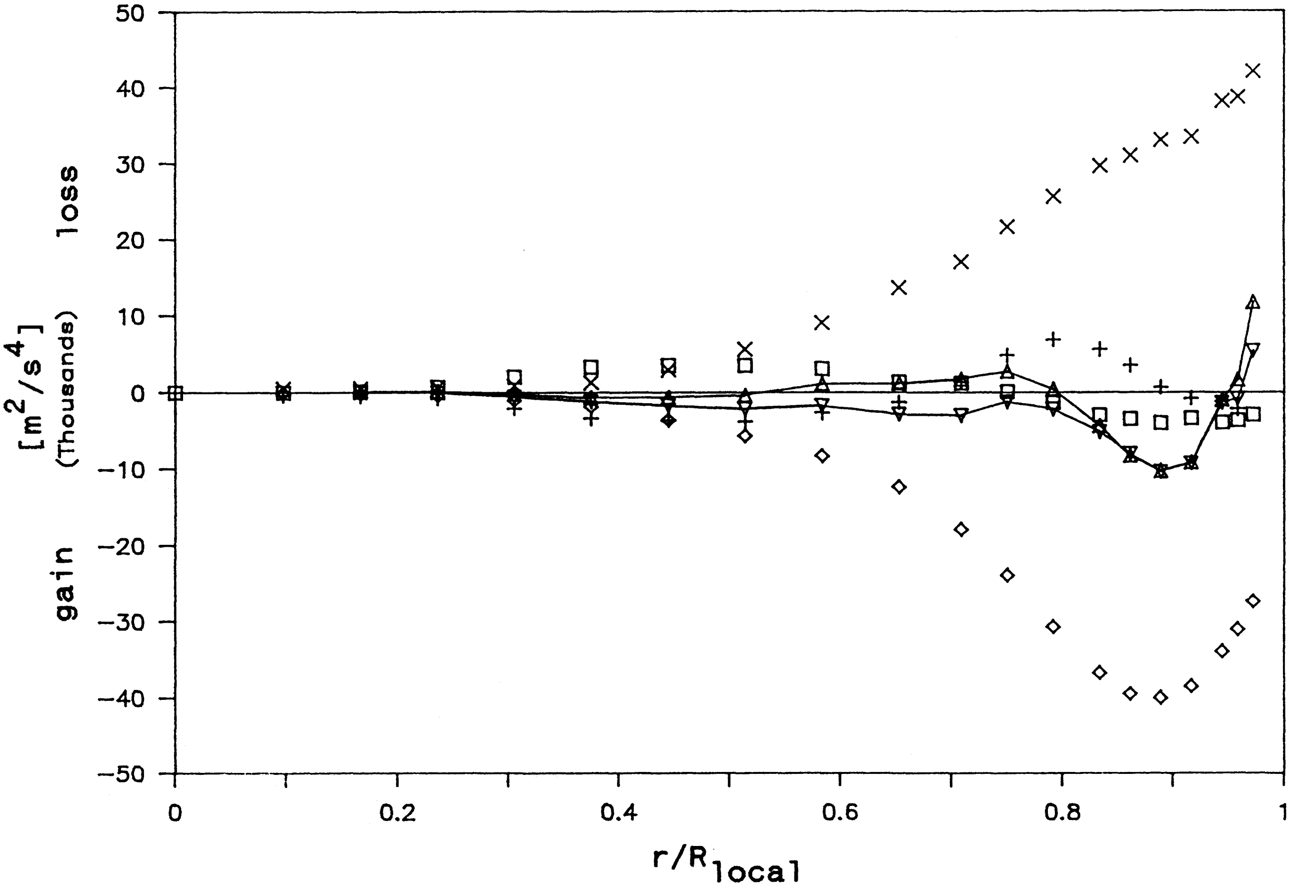

3.17. Remainder of the ε-equation at x=30cm (experimental production is given) and the terms of the LSH ε-balance at x=30cm: × destruction, ◇ production, □ advection, + ε-diffusion, ▽ NT, △ LSH.

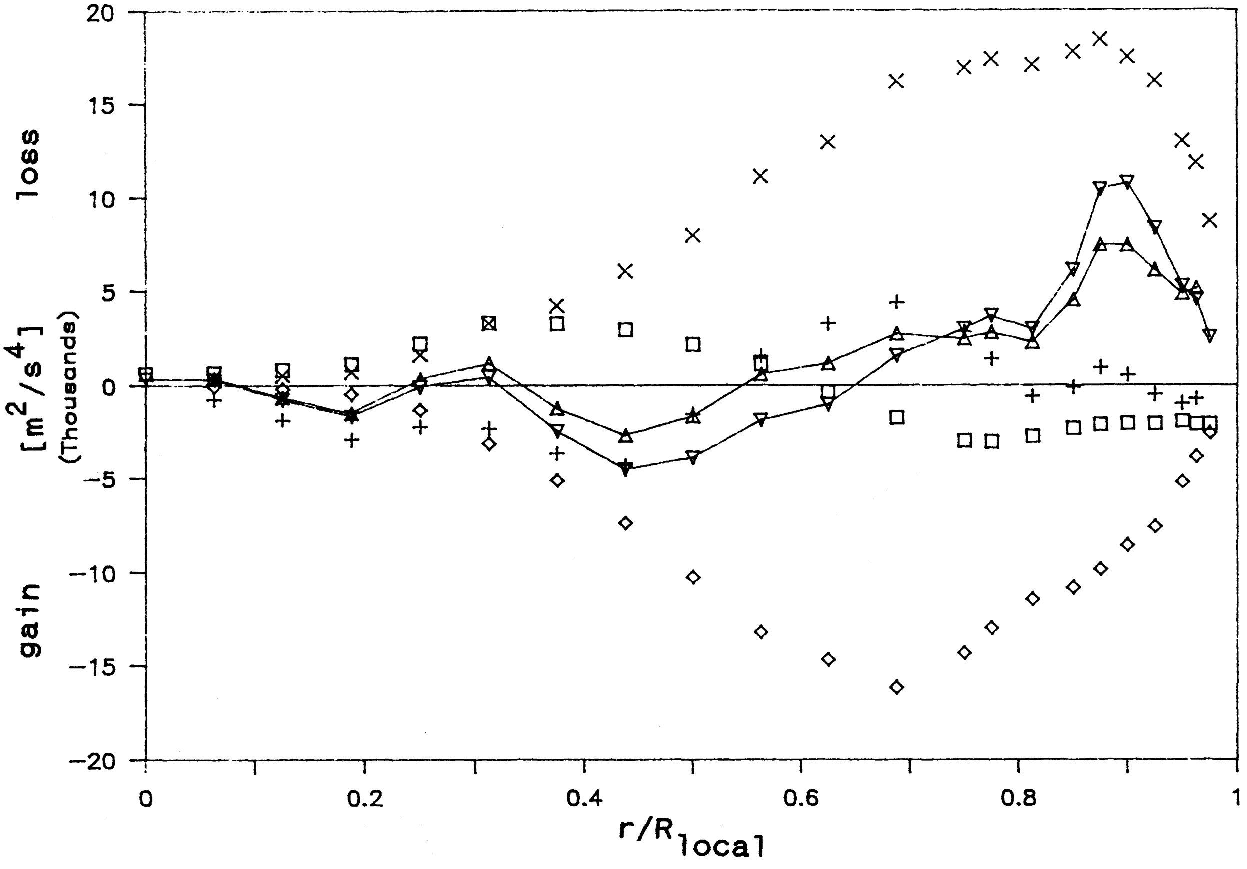

3.18. Remainder of the ε-equation at x=42cm (experimental production is given) and the terms of the LSH ε-balance at x=30cm: × destruction, ◇ production, □ advection, + ε-diffusion, ▽ NT, △ LSH.

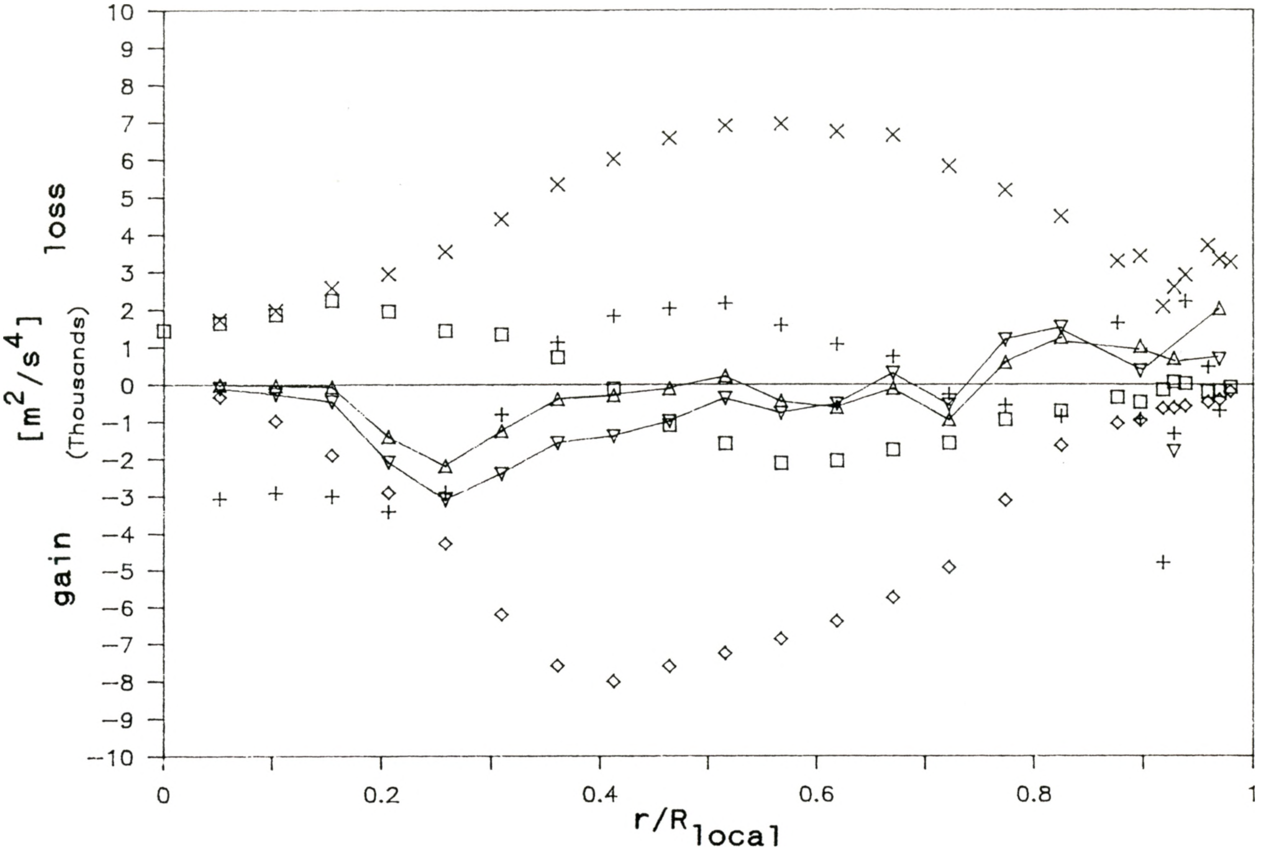

3.19. Remainder of the ε-equation at x=66cm (experimental production is given) and the terms of the LSH ε-balance at x=30cm: × destruction, ◇ production, □ advection, + ε-diffusion, ▽ NT, △ LSH,

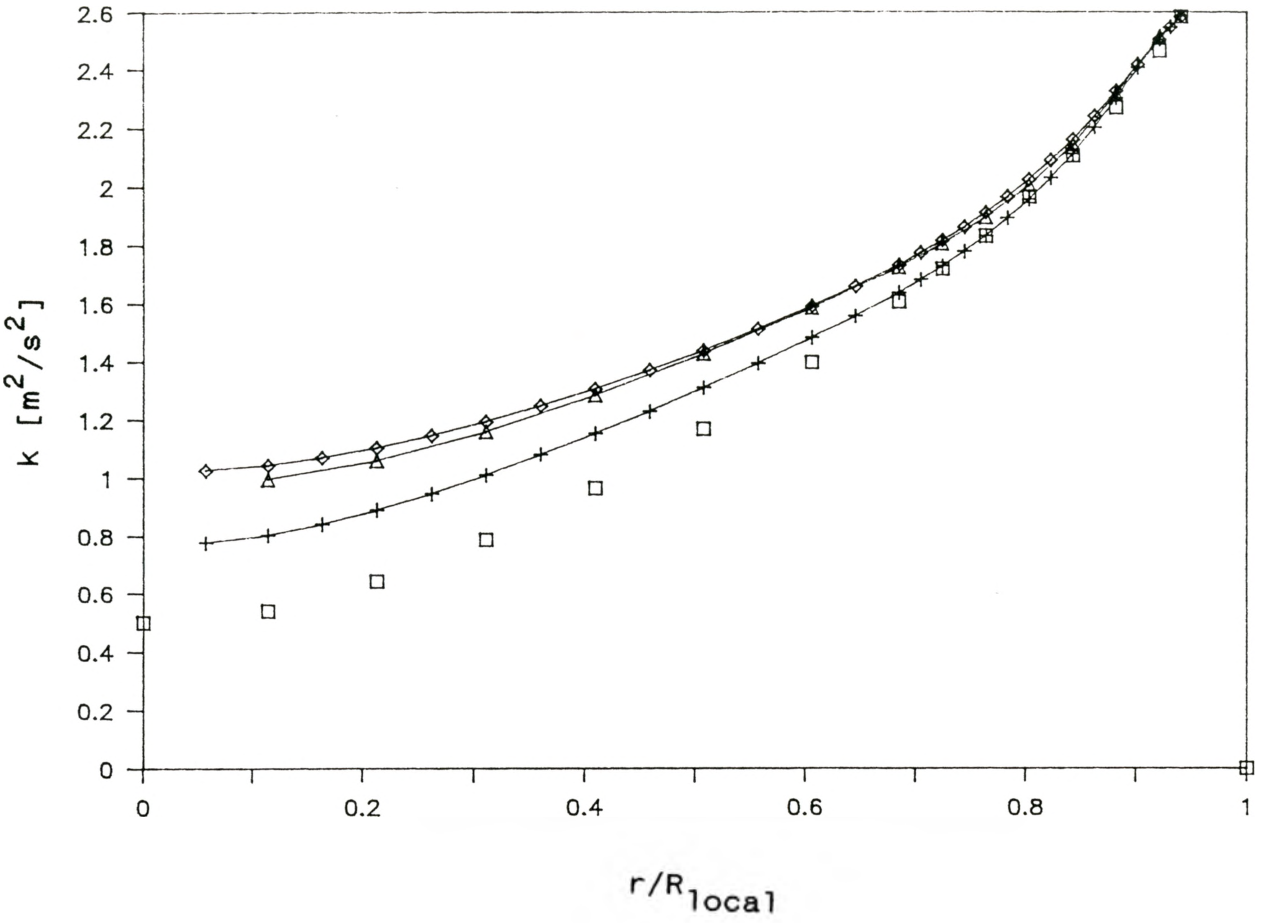

3.20. Comparison of the experimental kinetic energy with the model calculations in the fully-developed pipe flow (one-dimensional; production and mean velocity given): □ experiment, + NT, △ LSH, ◇ HOF.

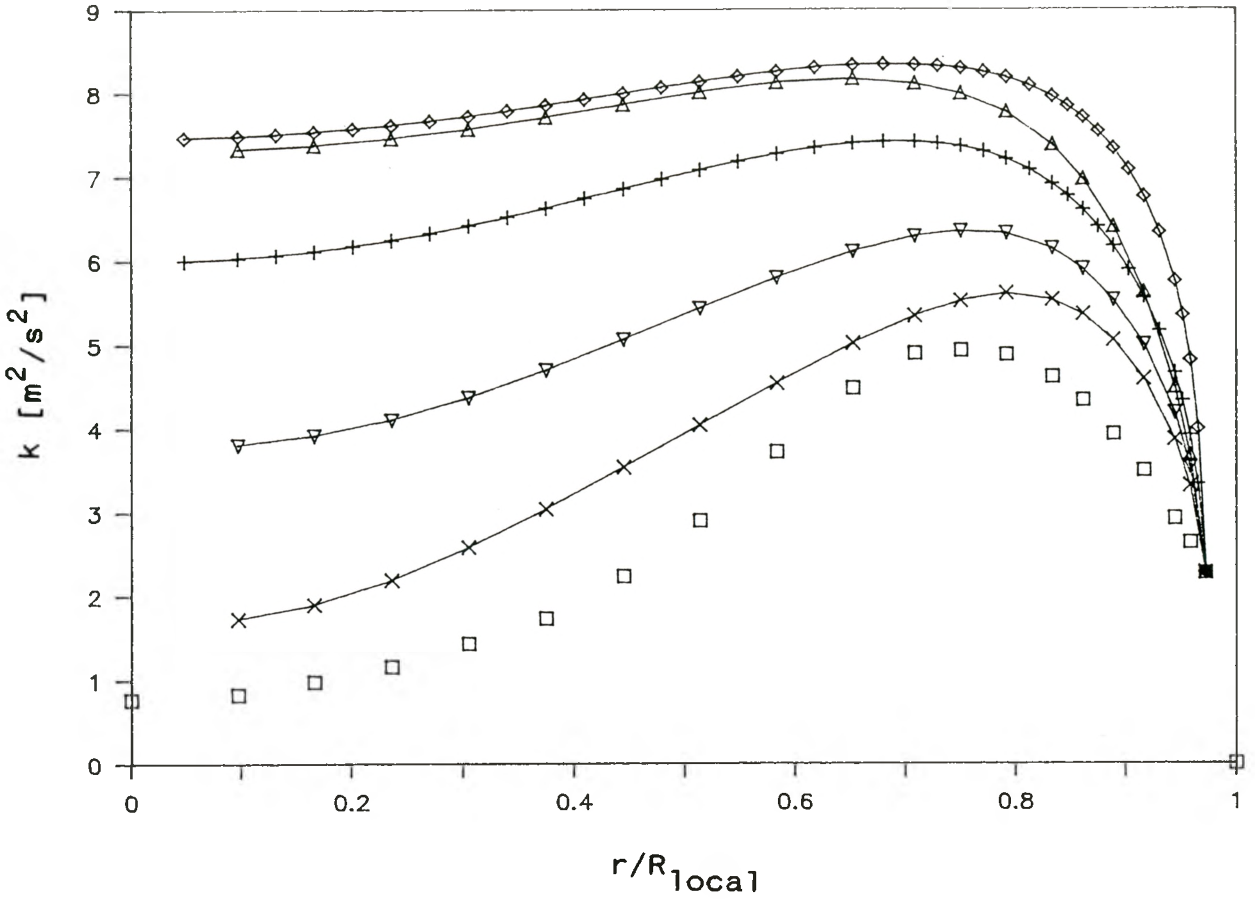

3.21. Comparison of the experimental kinetic energy with the model calculations at x=30cm (one-dimensional; production, axial gradients and mean velocity given): □ experiment, ▽ NT, ◇ LSH, △ HOF, + NT with $C'_{\varepsilon 1}=1.0C_{\varepsilon 1}$, × NT with $C'_{\varepsilon 1}=3.1C_{\varepsilon 1}$.

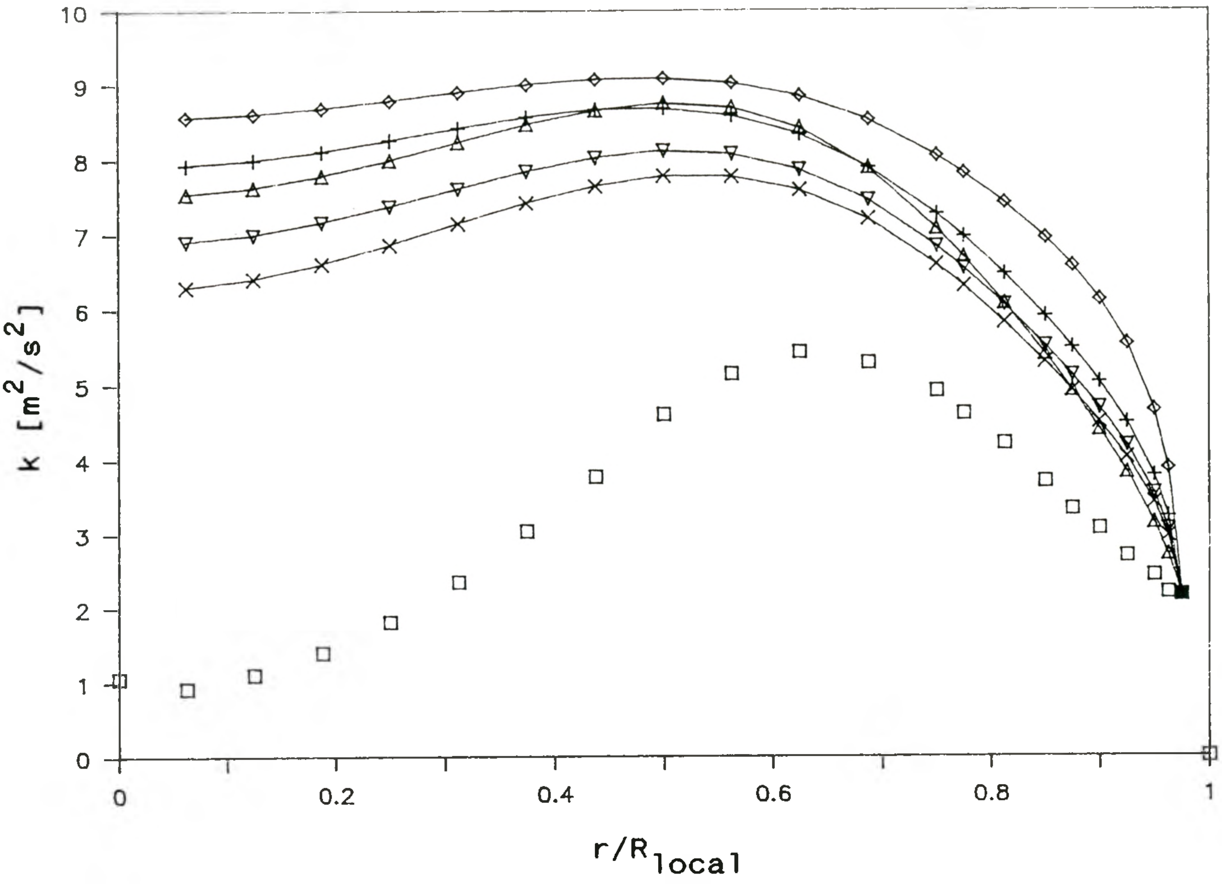

3.22. Comparison of the experimental kinetic energy with the model calculations at x=42cm (one-dimensional; production, axial gradients and mean velocity given): □ experiment, ▽ NT, ◇ LSH, △ HOF, + NT with $C'_{\varepsilon 1}=1.0C_{\varepsilon 1}$, × NT with $C'_{\varepsilon 1}=3.1C_{\varepsilon 1}$.

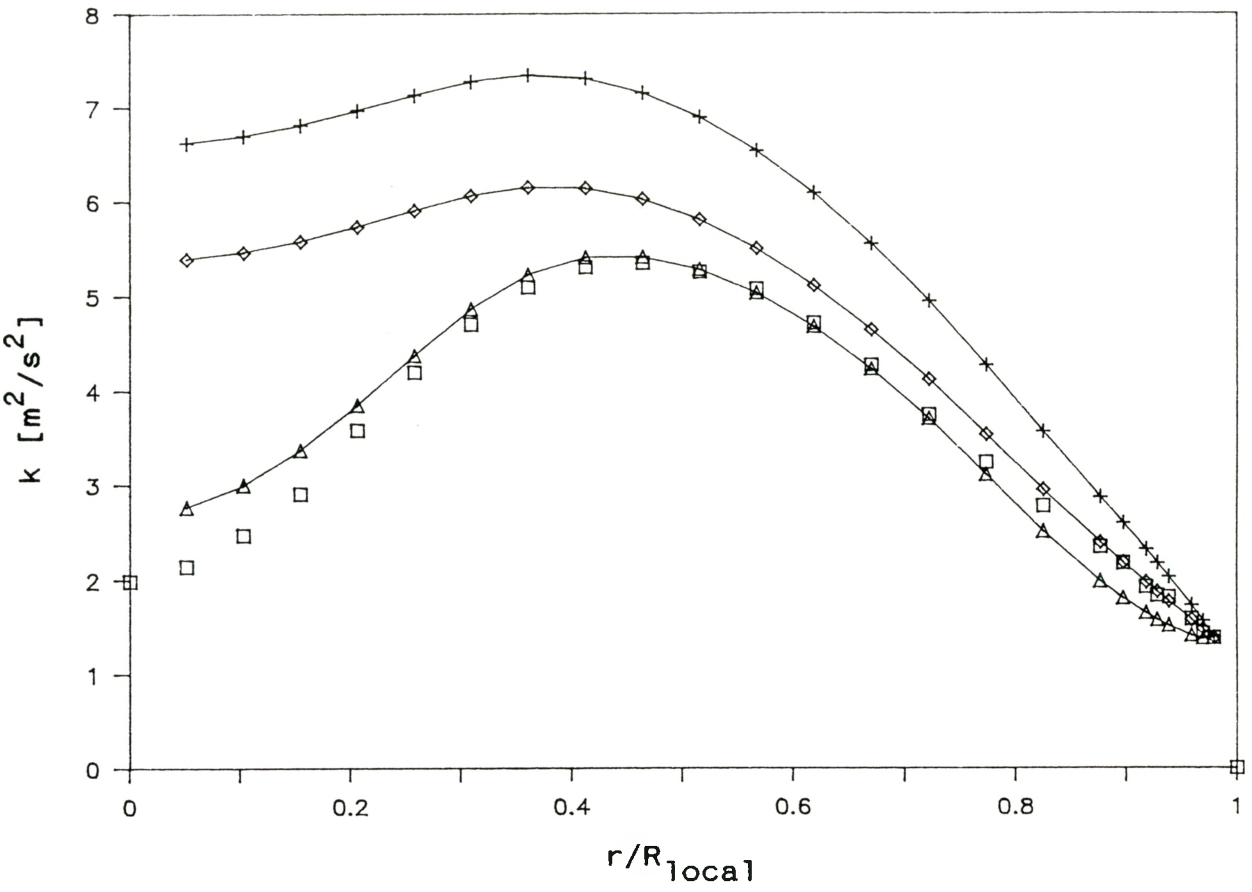

3.23. Comparison of the experimental kinetic energy with the model calculations at x=66cm (one-dimensional; production, axial gradients and mean velocity given): □ experiment, △ NT, ◇ LSH, + NT with $C'_{\varepsilon 1}=1.0C_{\varepsilon 1}$.

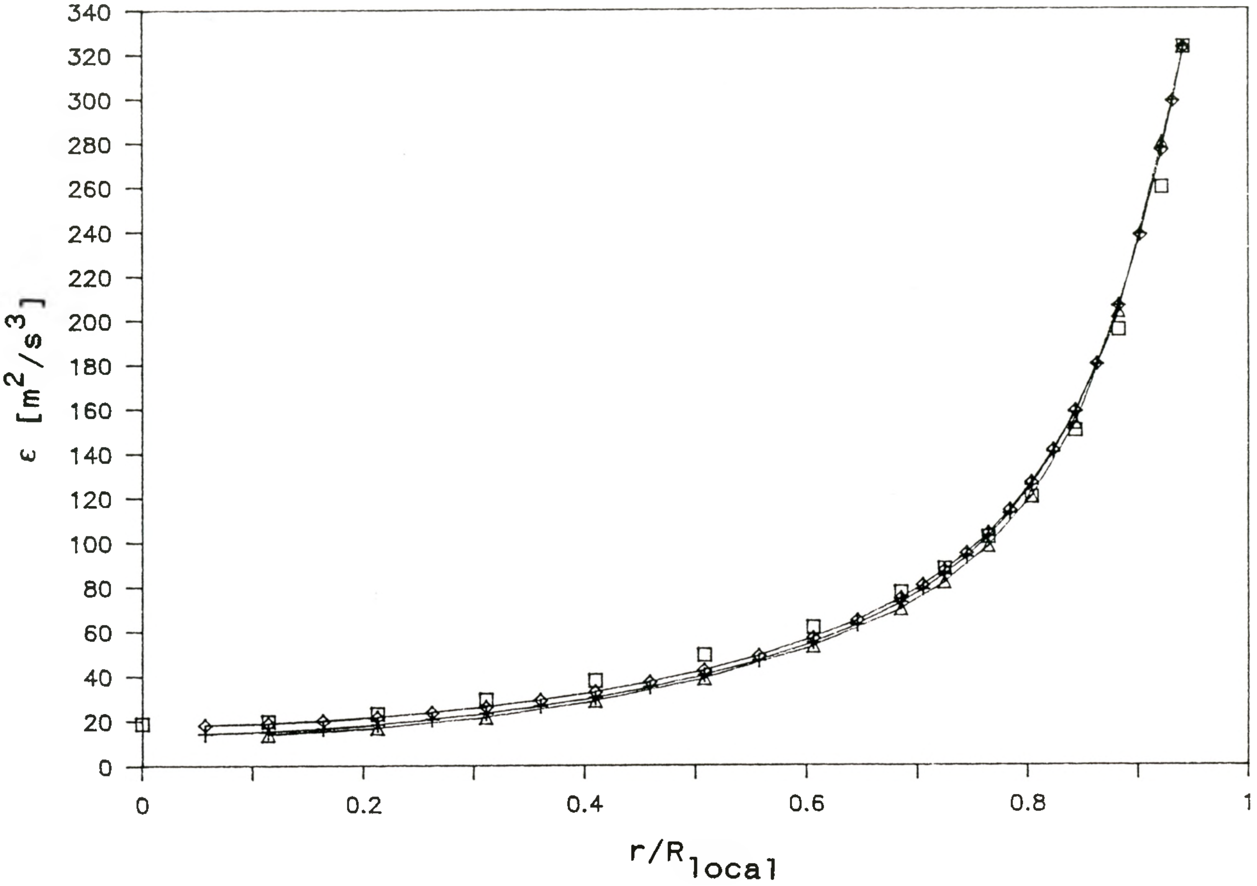

3.24. Comparison of the experimental ε with the model calculations in the fully-developed pipe flow (one-dimensional; production and mean velocity given): □ experiment, + NT, ◇ LSH, △ HOF.

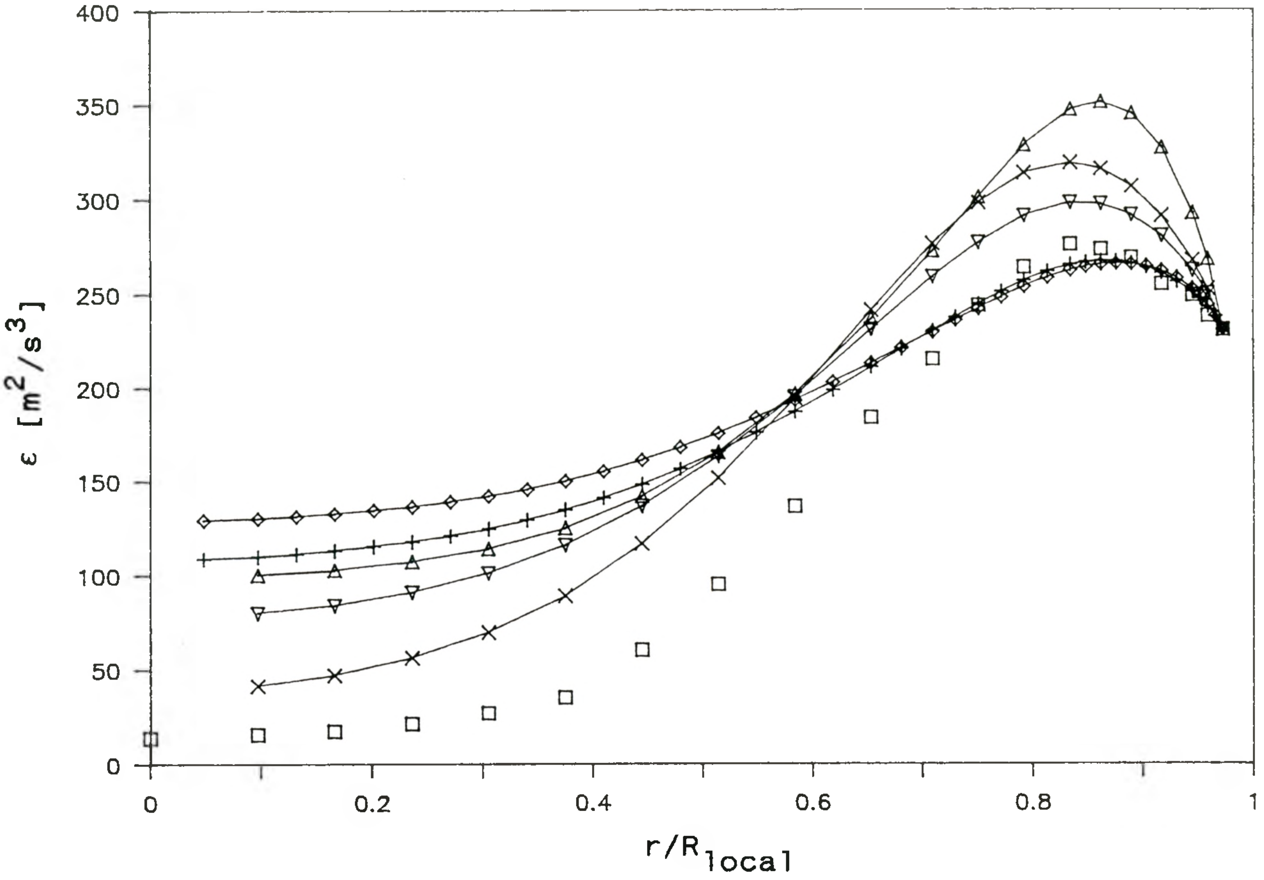

3.25. Comparison of the experimental ε with the model calculations at x=30cm (one-dimensional; production, axial gradients and mean velocity given): □ experiment, ▽ NT, ◇ LSH, △ HOF, + NT with $C'_{\varepsilon 1}=1.0C_{\varepsilon 1}$, × NT with $C'_{\varepsilon 1}=3.1C_{\varepsilon 1}$.

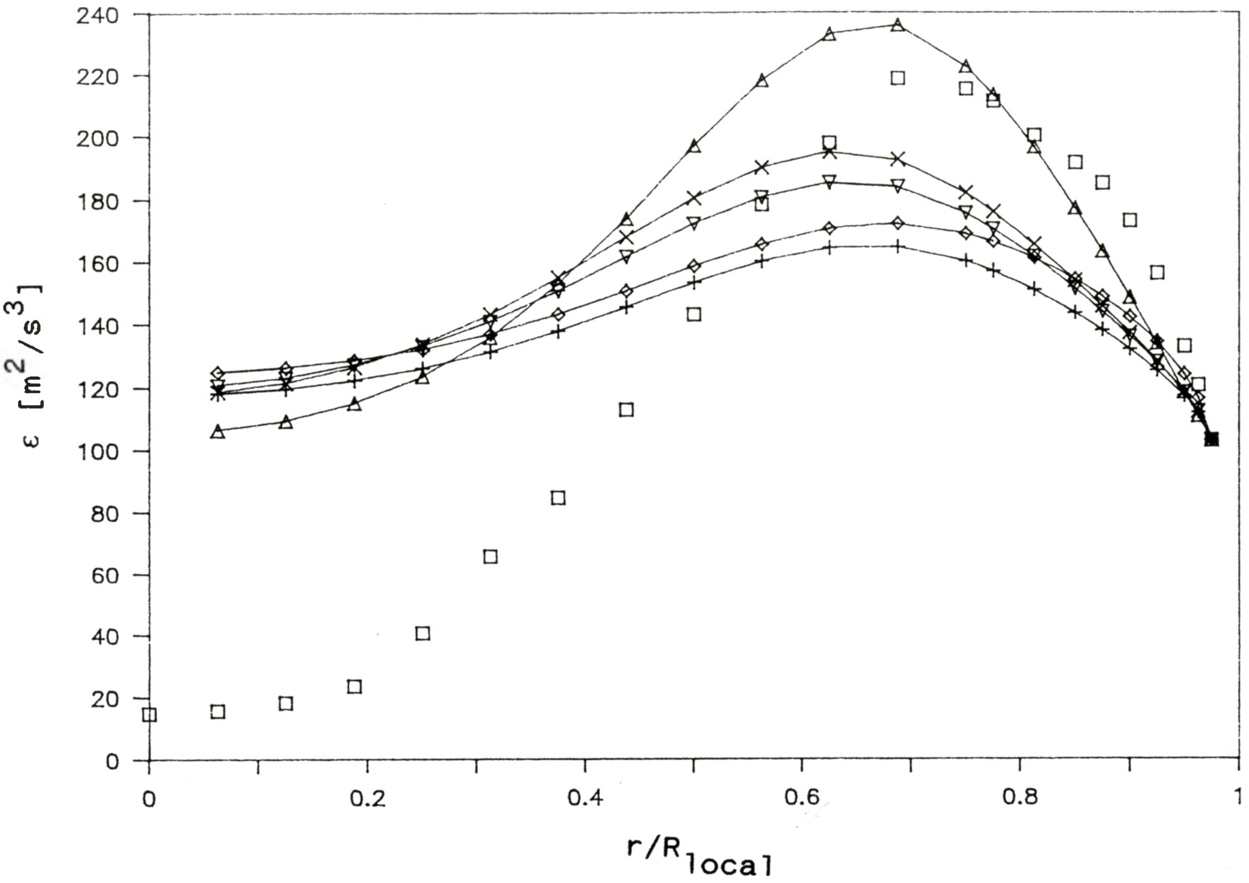

3.26. Comparison of the experimental ε with the model calculations at x=42cm (one-dimensional; production, axial gradients and mean velocity given): □ experiment, ▽ NT, ◇ LSH, △ HOF, + NT with $C'_{\varepsilon 1}=1.0C_{\varepsilon 1}$, × NT with $C'_{\varepsilon 1}=3.1C_{\varepsilon 1}$.

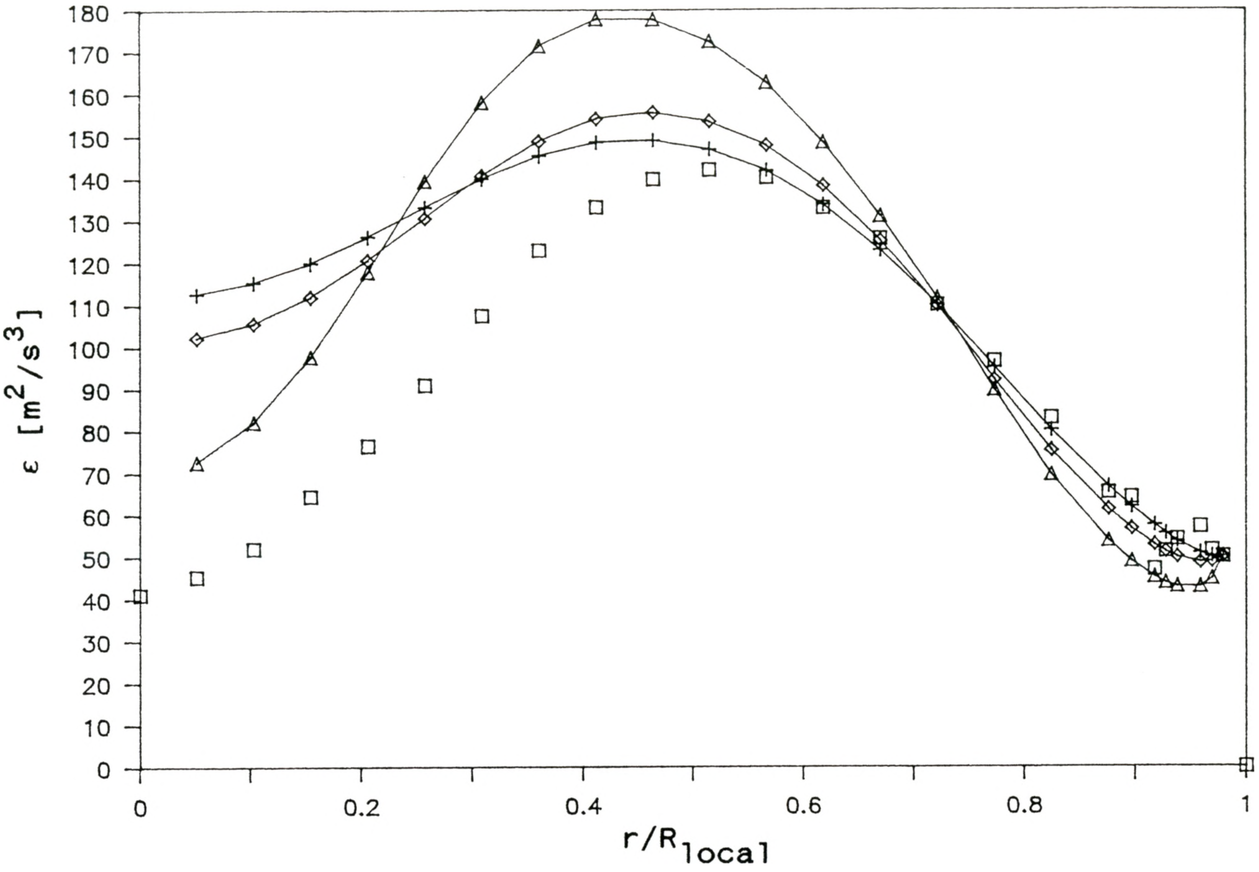

3.27. Comparison of the experimental ε with the model calculations at x=66cm (one-dimensional; production, axial gradients and mean velocity given): □ experiment, △ NT, ◇ LSH, + NT with $C'_{\varepsilon 1}=1.0C_{\varepsilon 1}$.

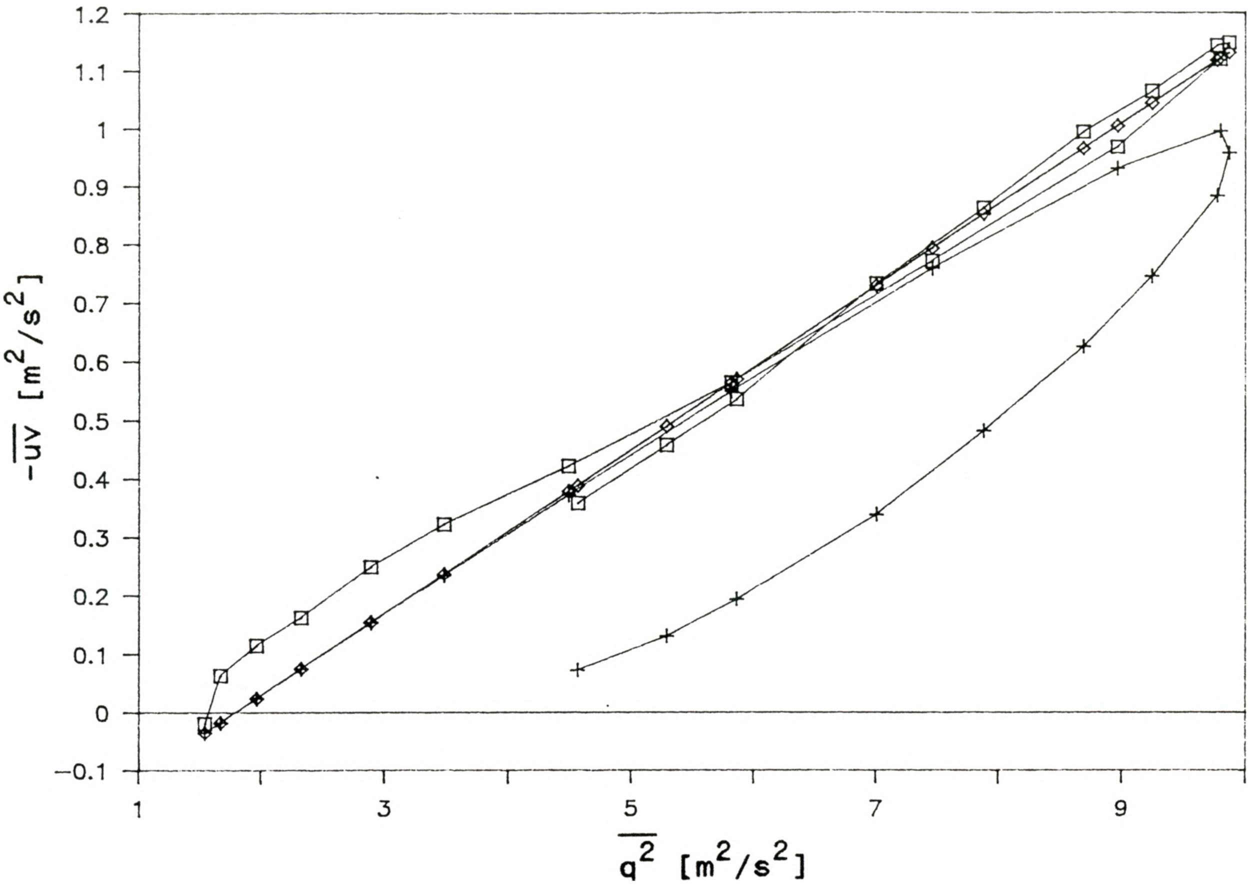

3.28. $-\overline{uv}$ versus $\overline{q^2}$ at x=30cm: □ experimental, ◇ 0.28k-0.25, + f_μ(0.28k-0.25) (LSH f_μ).

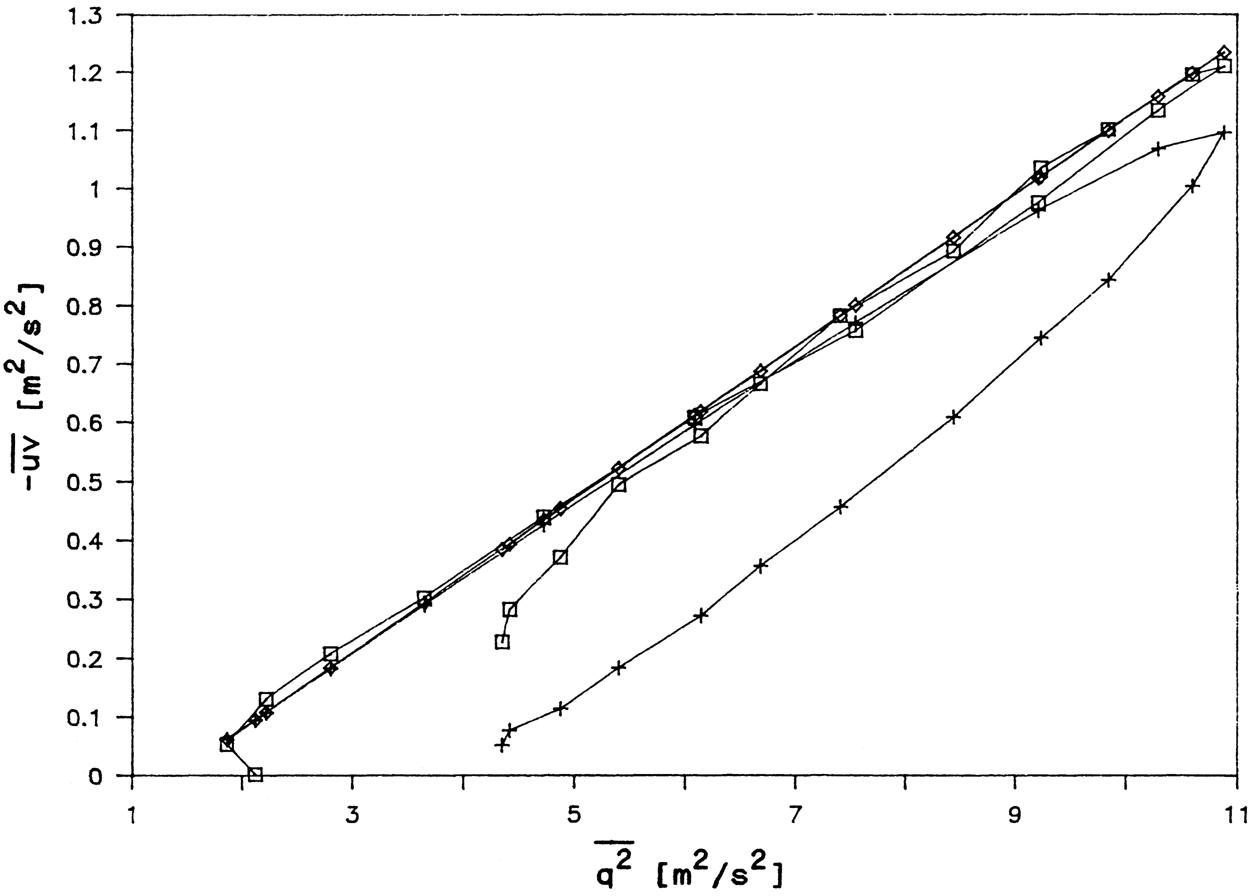

3.29. $-\overline{uv}$ versus $\overline{q^2}$ at x=42cm: □ experimental, ◇ 0.26k-0.18, + f_μ(0.26k-0.18) (LSH f_μ).

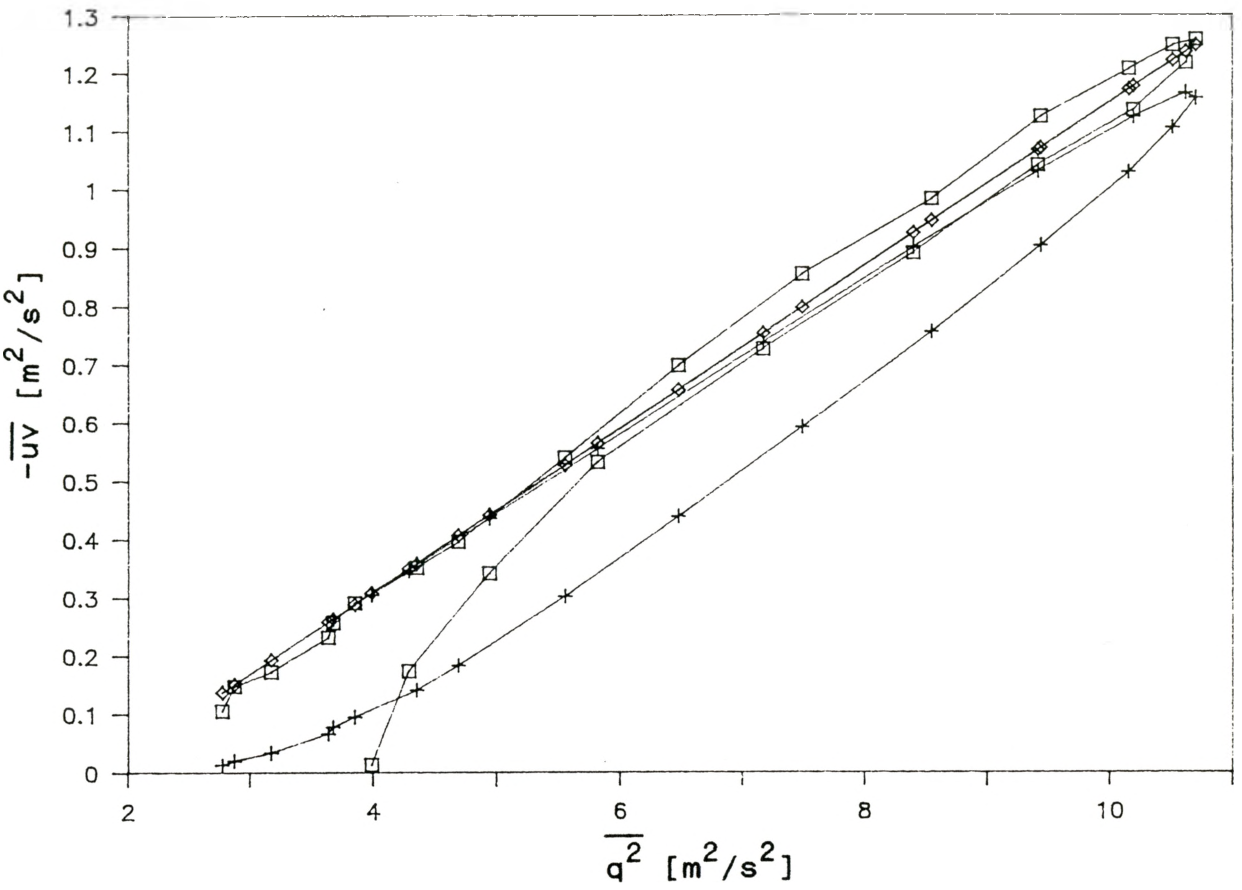

3.30. $-\overline{uv}$ versus $\overline{q^2}$ at x=66cm: □ experimental, ◇ 0.28k-0.25, + f_μ(0.28k-0.25) (LSH f_μ).

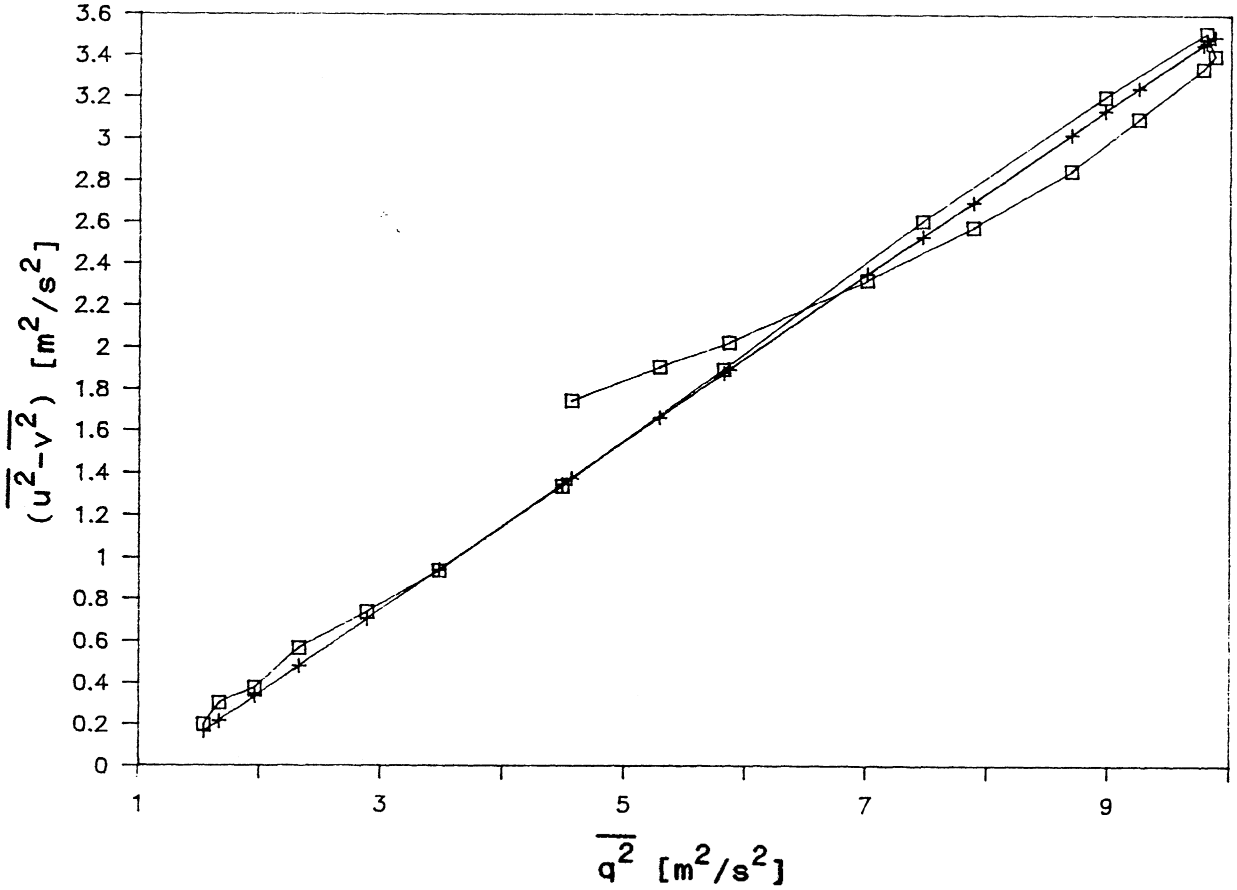

3.31. $(\overline{u^2}-\overline{v^2})$ versus $\overline{q^2}$ at x=30cm: □ experimental, + 0.80k-0.45.

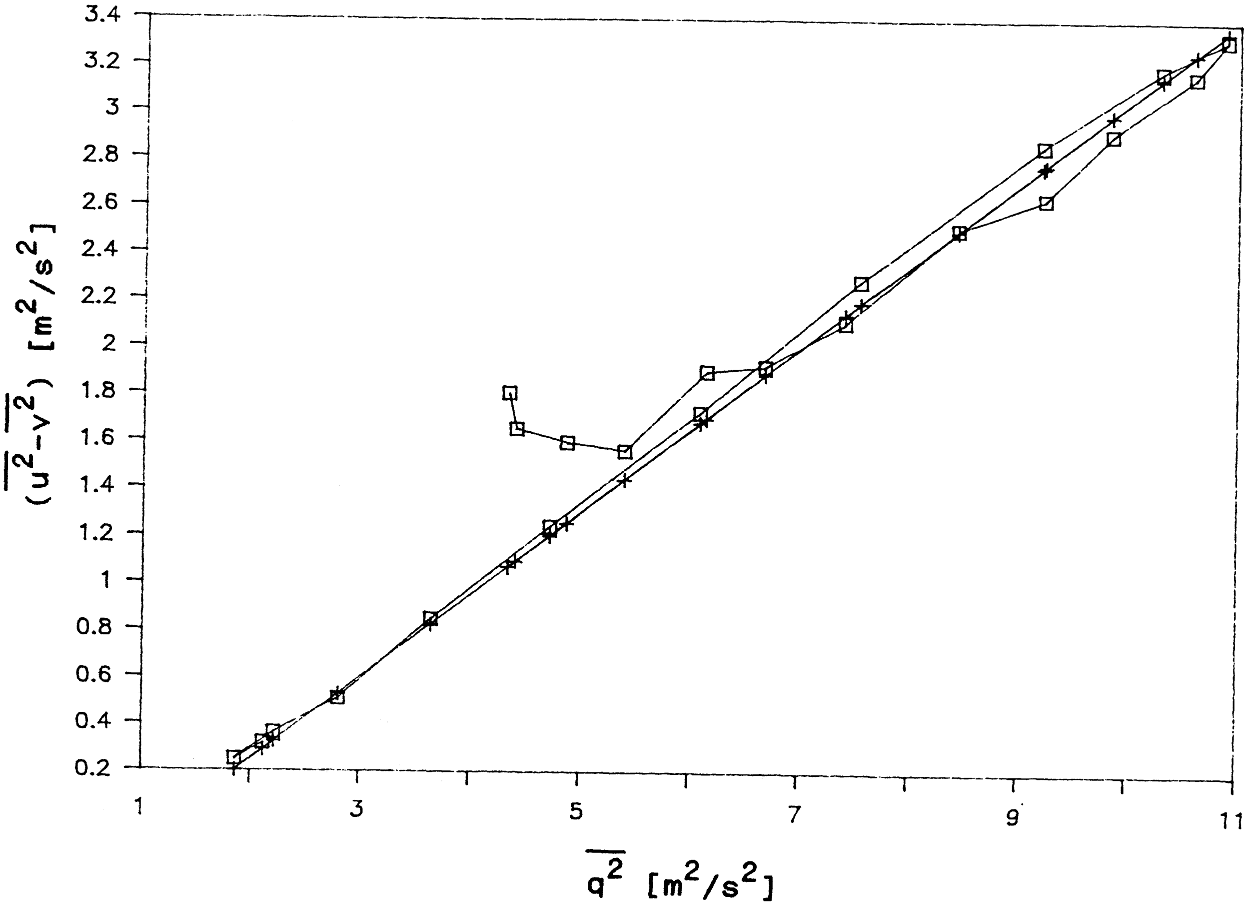

3.32. $(\overline{u^2}-\overline{v^2})$ versus $\overline{q^2}$ at x=42cm: □ experimental, + 0.70k-0.45.

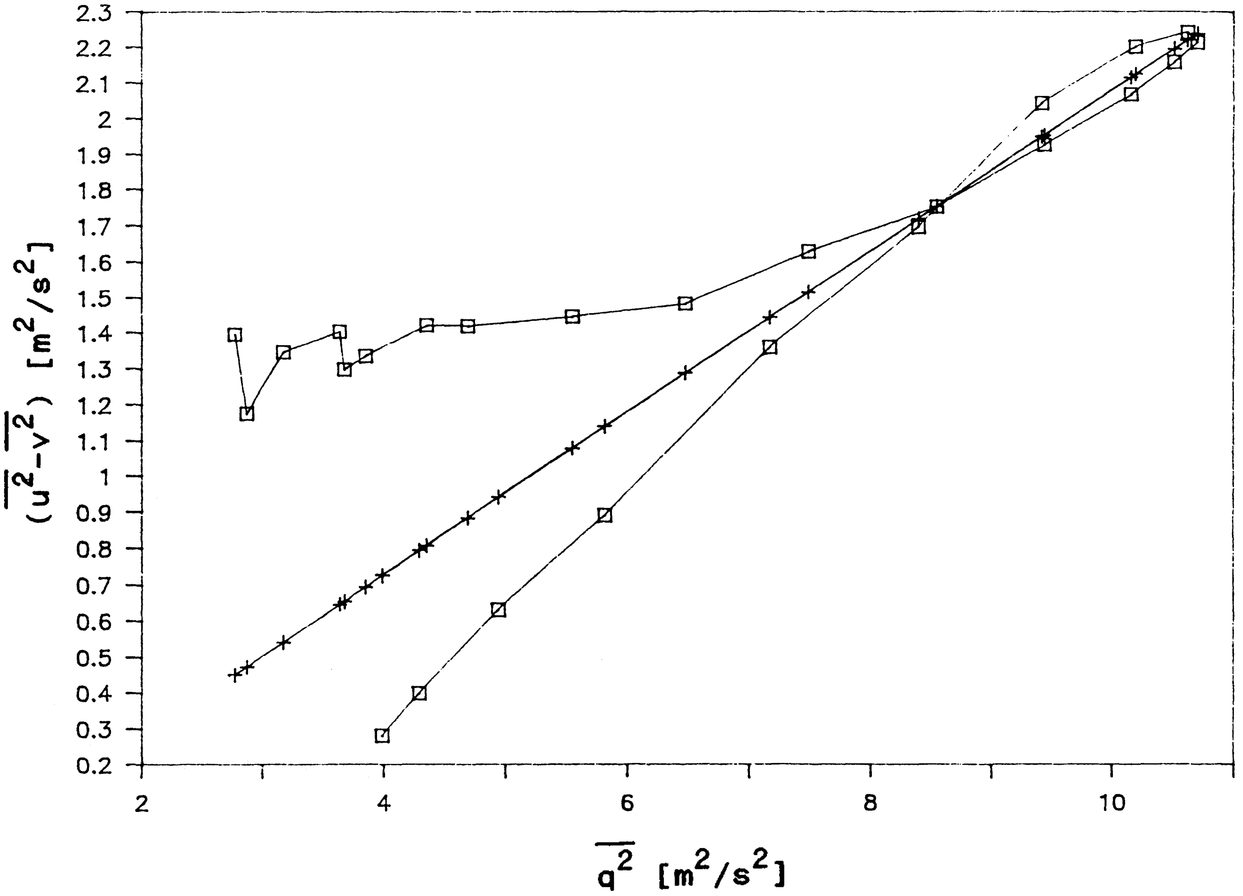

3.33. $(\overline{u^2}-\overline{v^2})$ versus $\overline{q^2}$ at x=66cm: □ experimental, + 0.45k-0.17.

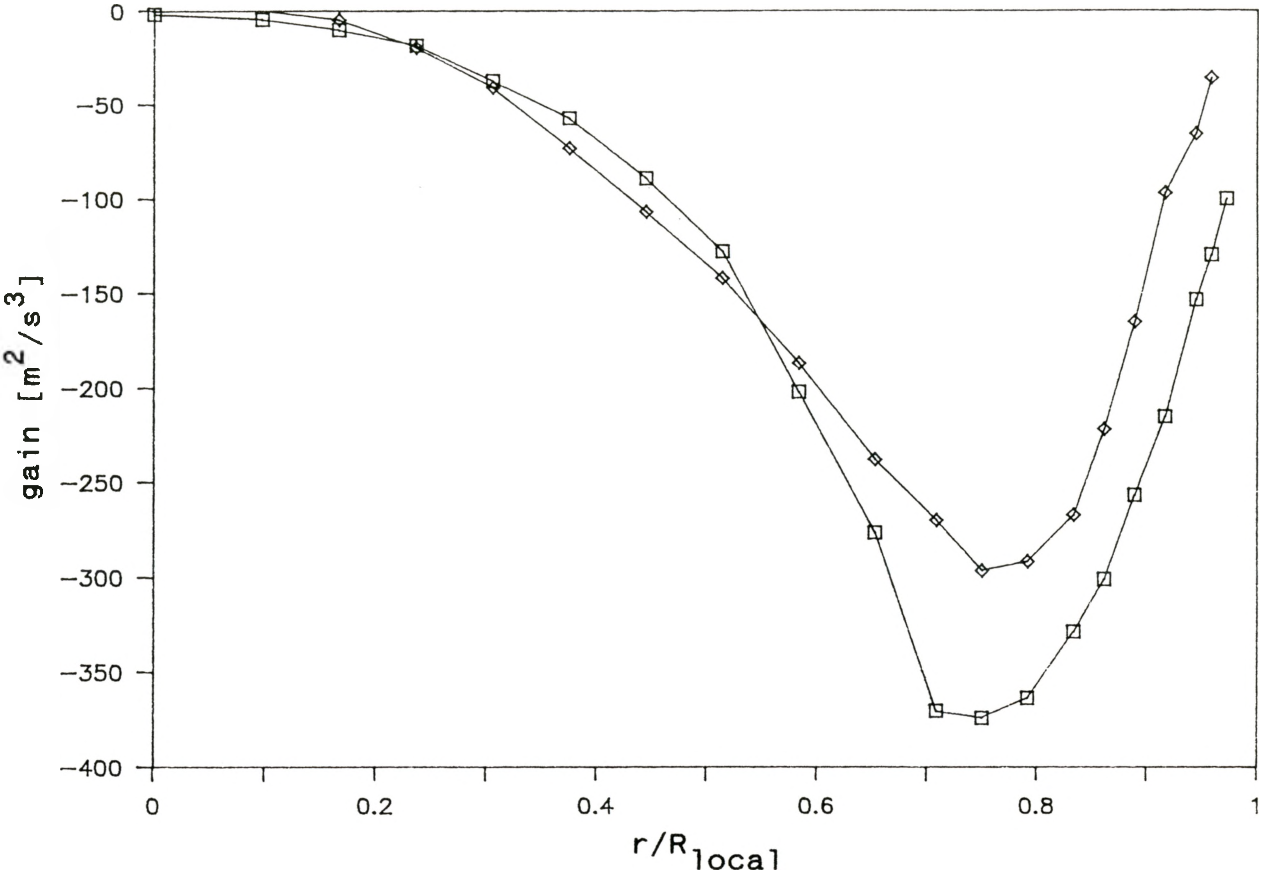

3.34. Comparison of experimental turbulence kinetic energy production with modified k-ε production based on Bradshaw's structural coefficient a_1 at x=30cm: □ experimental, ◇ modified.

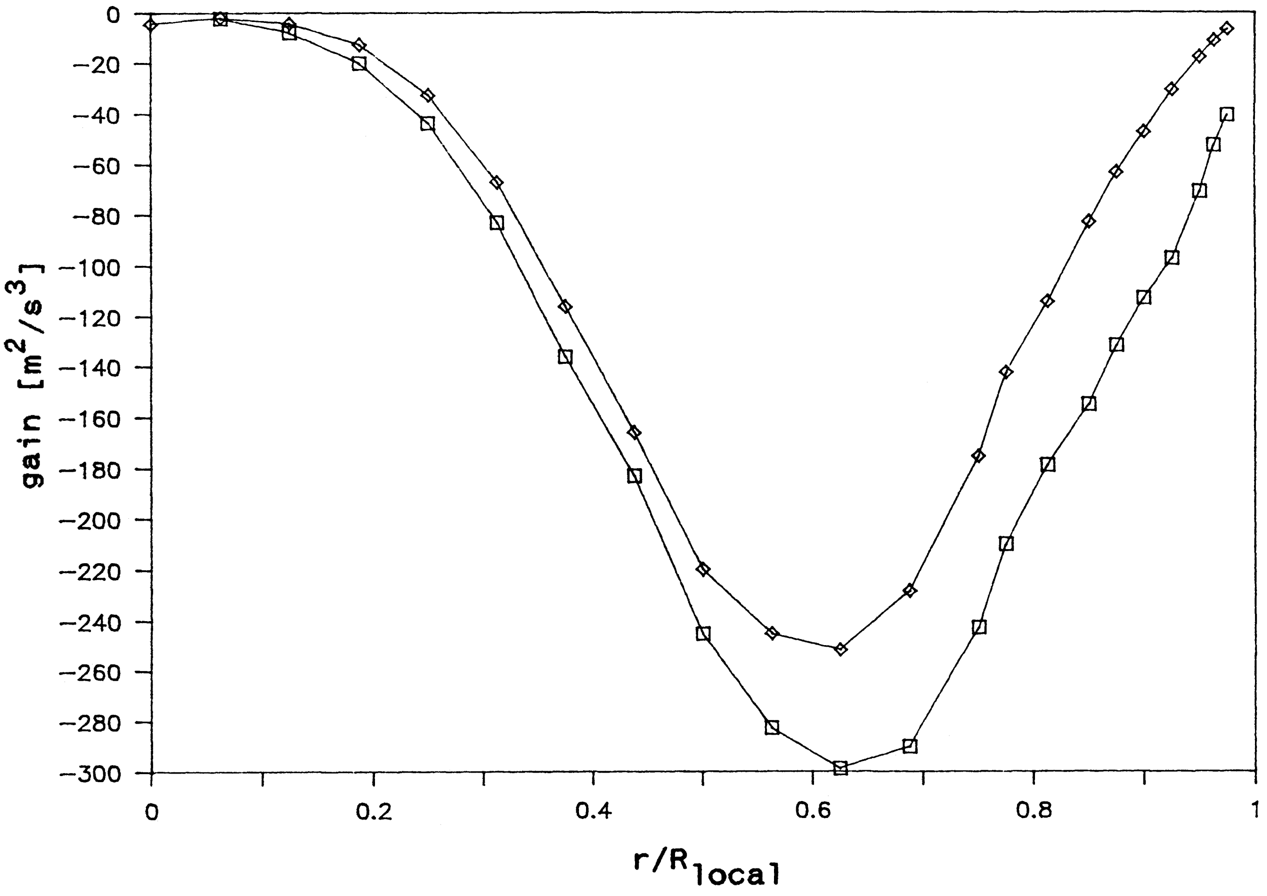

3.35. Comparison of experimental turbulence kinetic energy production with modified k-ε production based on Bradshaw's structural coefficient a_1 at x=42cm: □ experimental, ◇ modified.

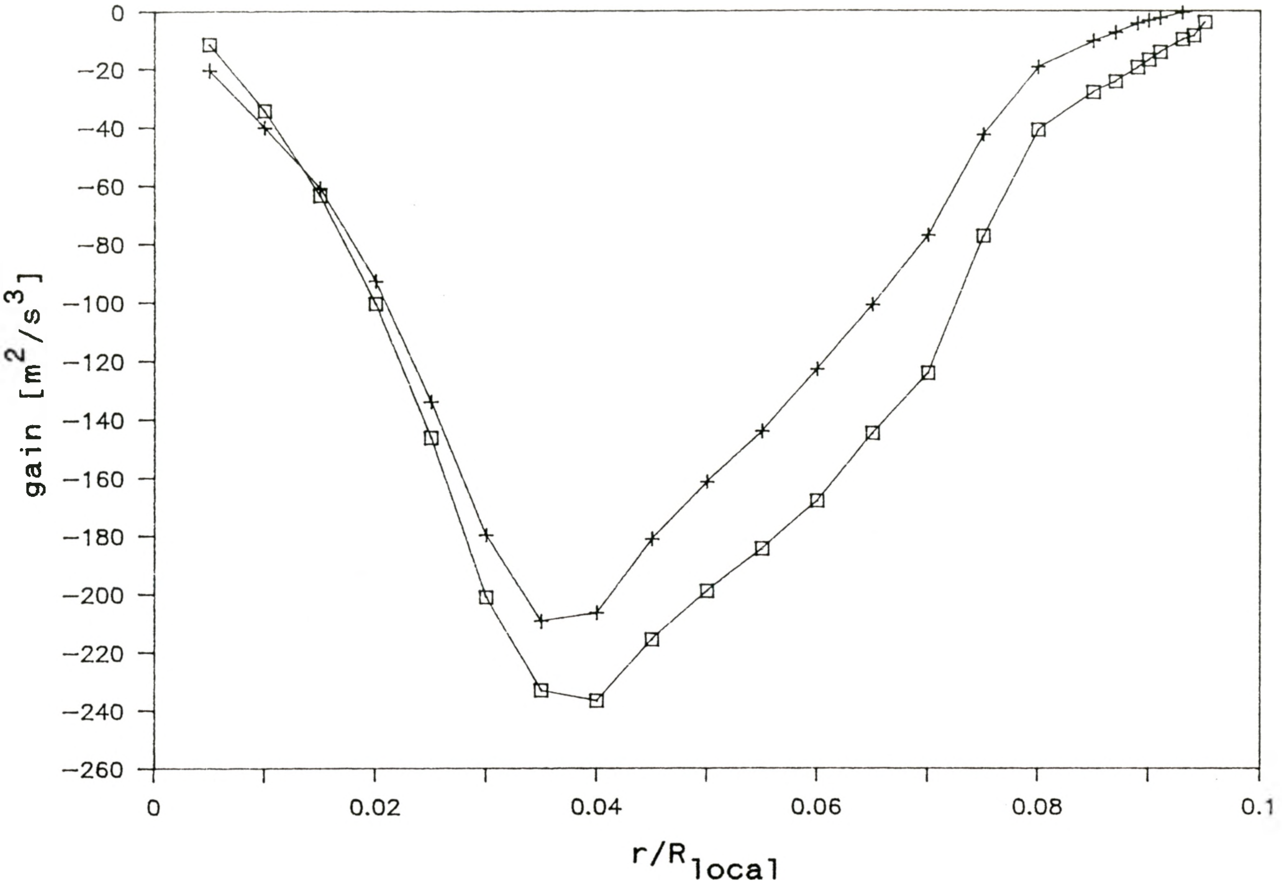

3.36. Comparison of experimental turbulence kinetic energy production with modified k-ε production based on Bradshaw's structural coefficient a_1 at x=66cm: □ experimental, ◇ modified.

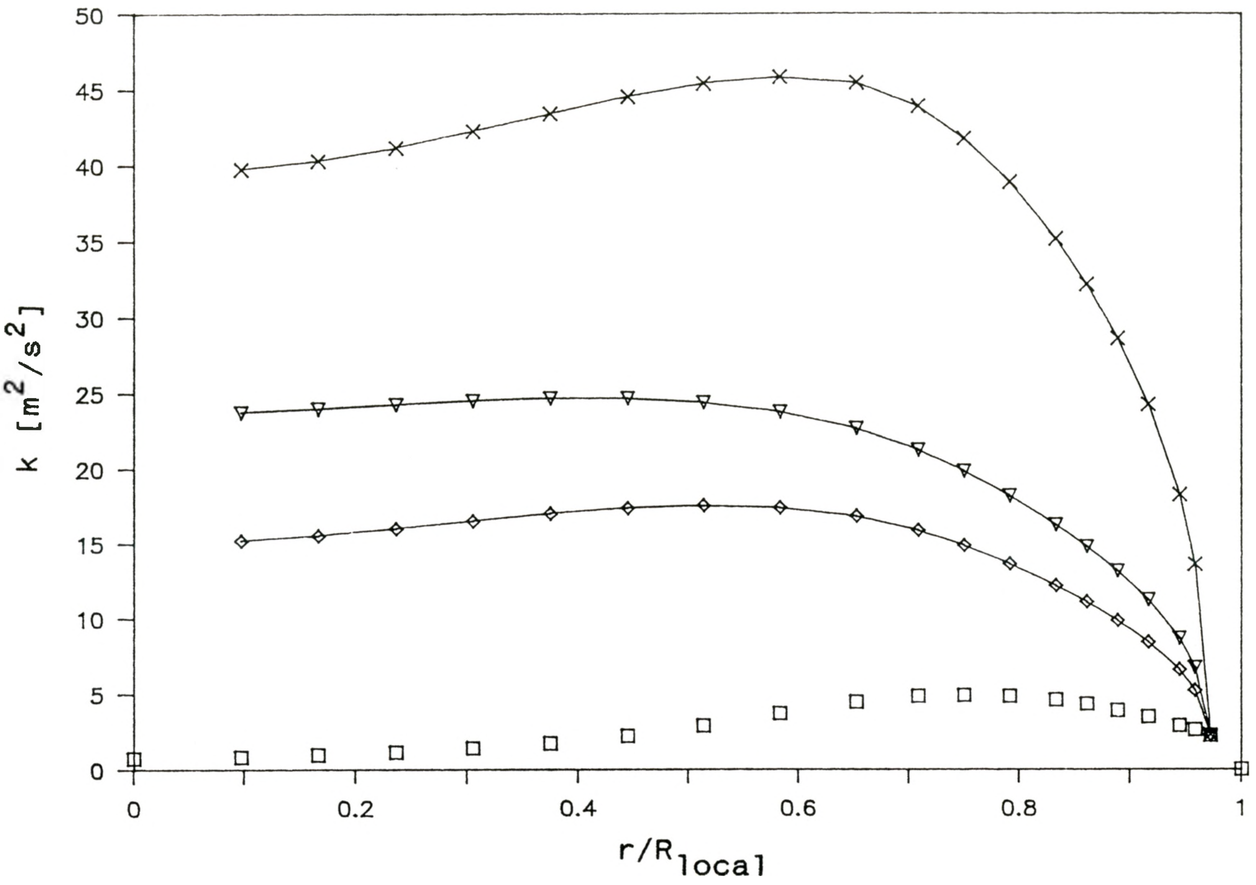

3.37. Comparison of computed values of k versus the experimental values for different Reynolds stresses at x=30cm: □ experimental, × NT model, ▽ NT with modified Reynolds stresses, ◇ NT with modified Reynolds stresses and $C'_{\varepsilon 1} = 3.175 C_{\varepsilon 1}$.

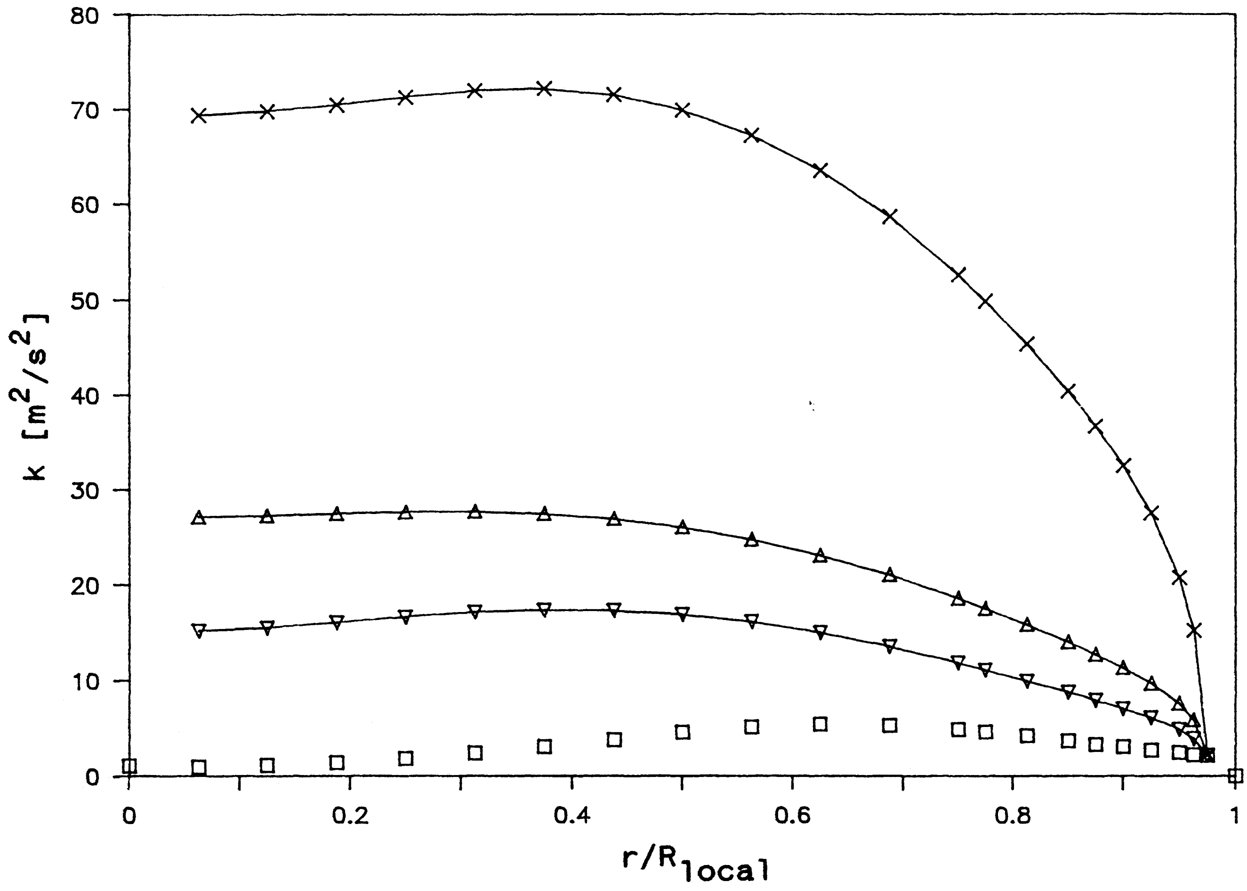

3.38. Comparison of computed values of k versus the experimental values for different Reynolds stresses at x=42cm: □ experimental, × NT model, △ NT with modified Reynolds stresses, ▽ NT with modified Reynolds stresses and $C'_{\varepsilon 1} = 3.88836C_{\varepsilon 1}$.

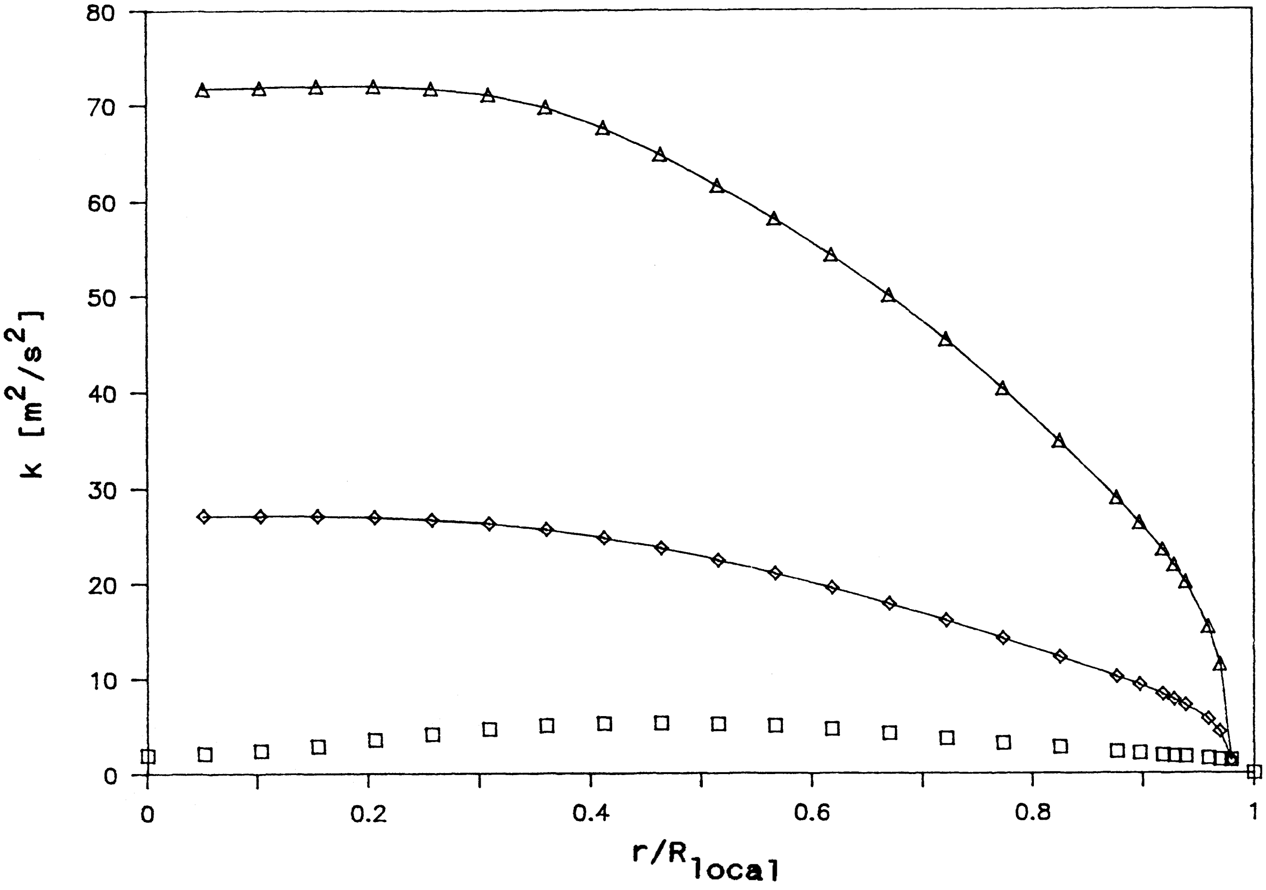

3.39. Comparison of computed values of k versus the experimental values for different Reynolds stresses at x=66cm: □ experimental, △ NT, ◇ NT with modified Reynolds stresses and $C'_{\varepsilon 1} = 2.3C_{\varepsilon 1}$.

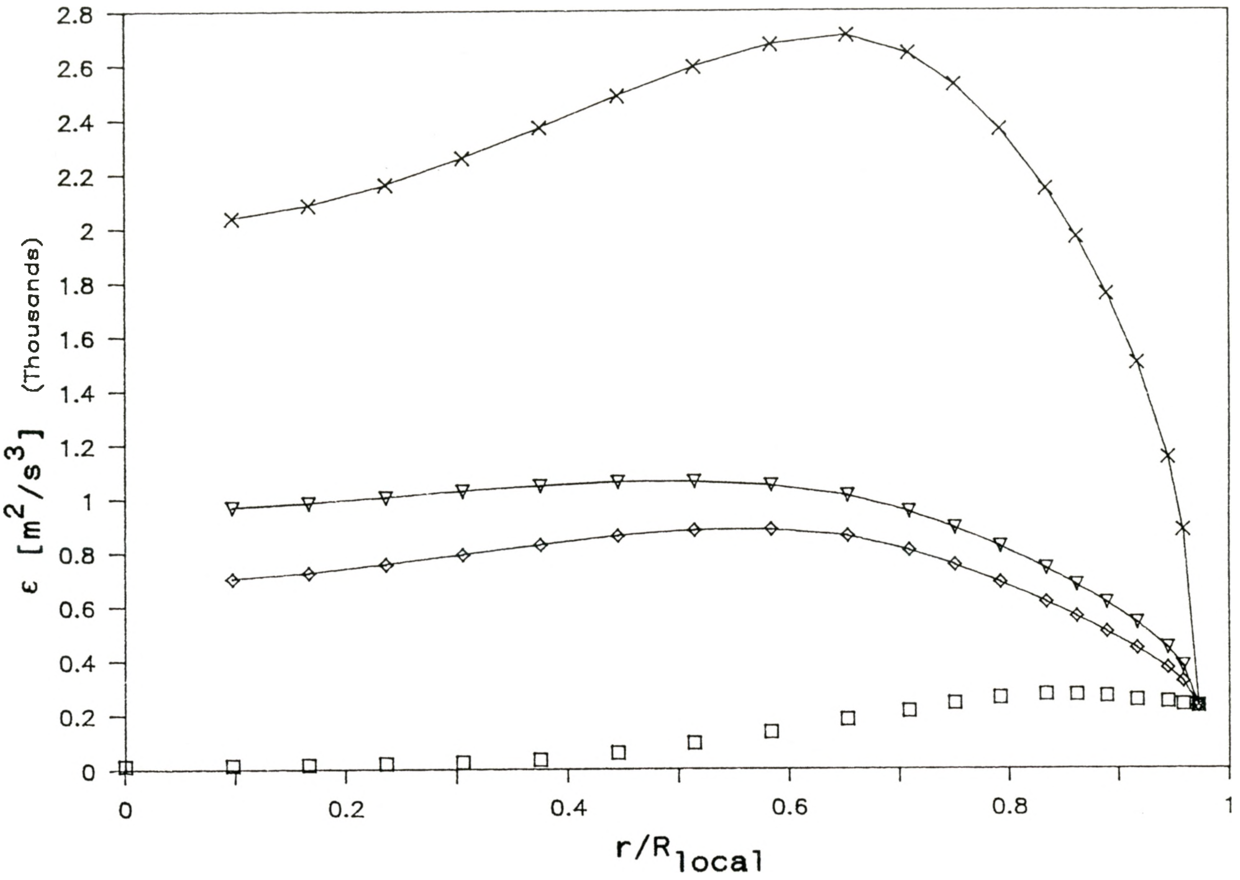

3.40. Comparison of computed values of ε versus the experimental values for different Reynolds stresses at x=30cm: □ experimental, × NT model, ▽ NT with modified Reynolds stresses, ◇ NT with modified Reynolds stresses and $C'_{\varepsilon 1} = 3.175C_{\varepsilon 1}$.

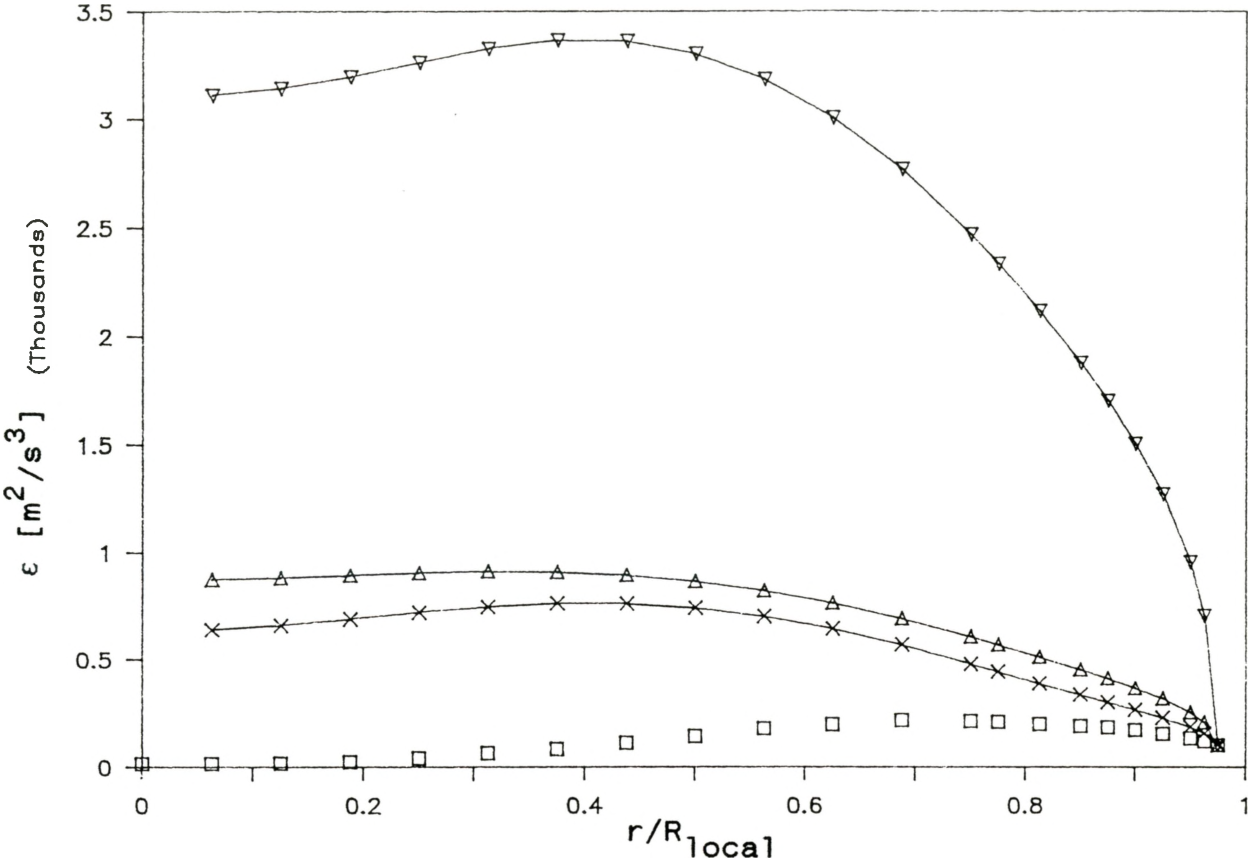

3.41. Comparison of computed values of ε versus the experimental values for different Reynolds stresses at x=42cm: □ experimental, ▽ NT model, △ NT with modified Reynolds stresses, × NT with modified Reynolds stresses and $C'_{\varepsilon 1} = 3.88836 C_{\varepsilon 1}$.

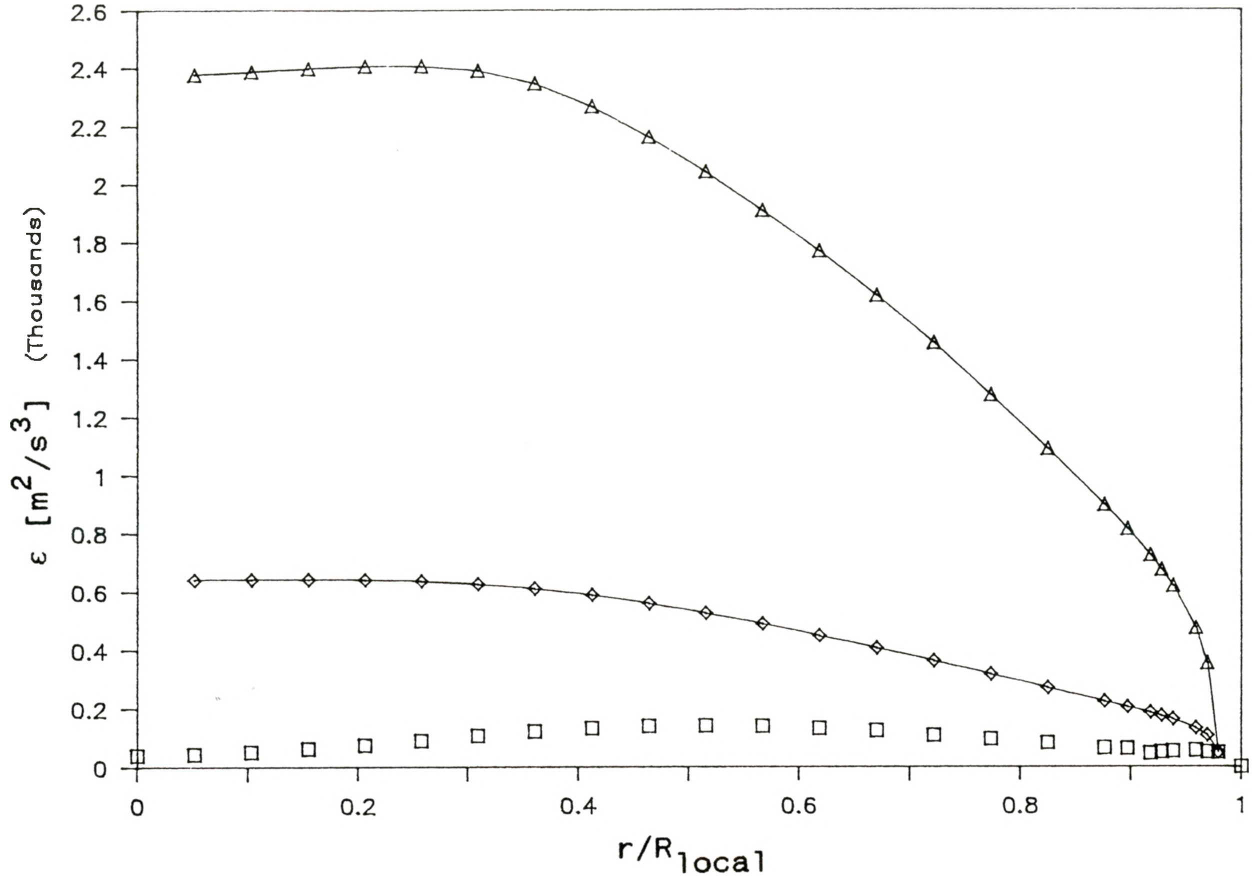

3.42. Comparison of computed values of ε versus the experimental values for different Reynolds stresses at x=66cm: □ experimental, △ NT, ◇ NT with modified Reynolds stresses and $C'_{\varepsilon 1} = 2.3C_{\varepsilon 1}$.

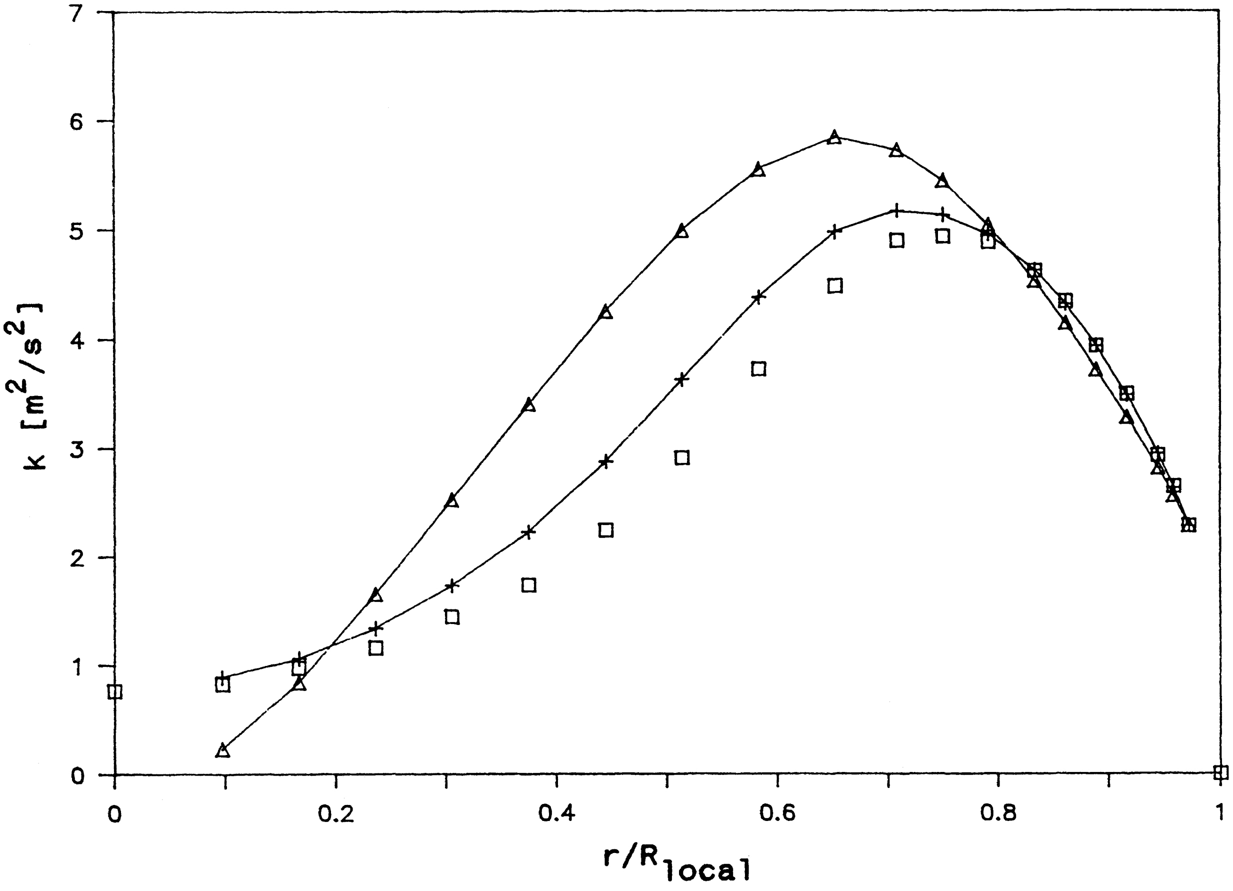

3.43. Comparison of partially converged solutions of k versus the experimental values for different Reynolds stresses at x=30cm: □ experimental, + NT with modified Reynolds stresses (1 iteration), △ NT with modified Reynolds stresses and $C'_{\varepsilon 1} = 3.175C_{\varepsilon 1}$ (8 iterations).

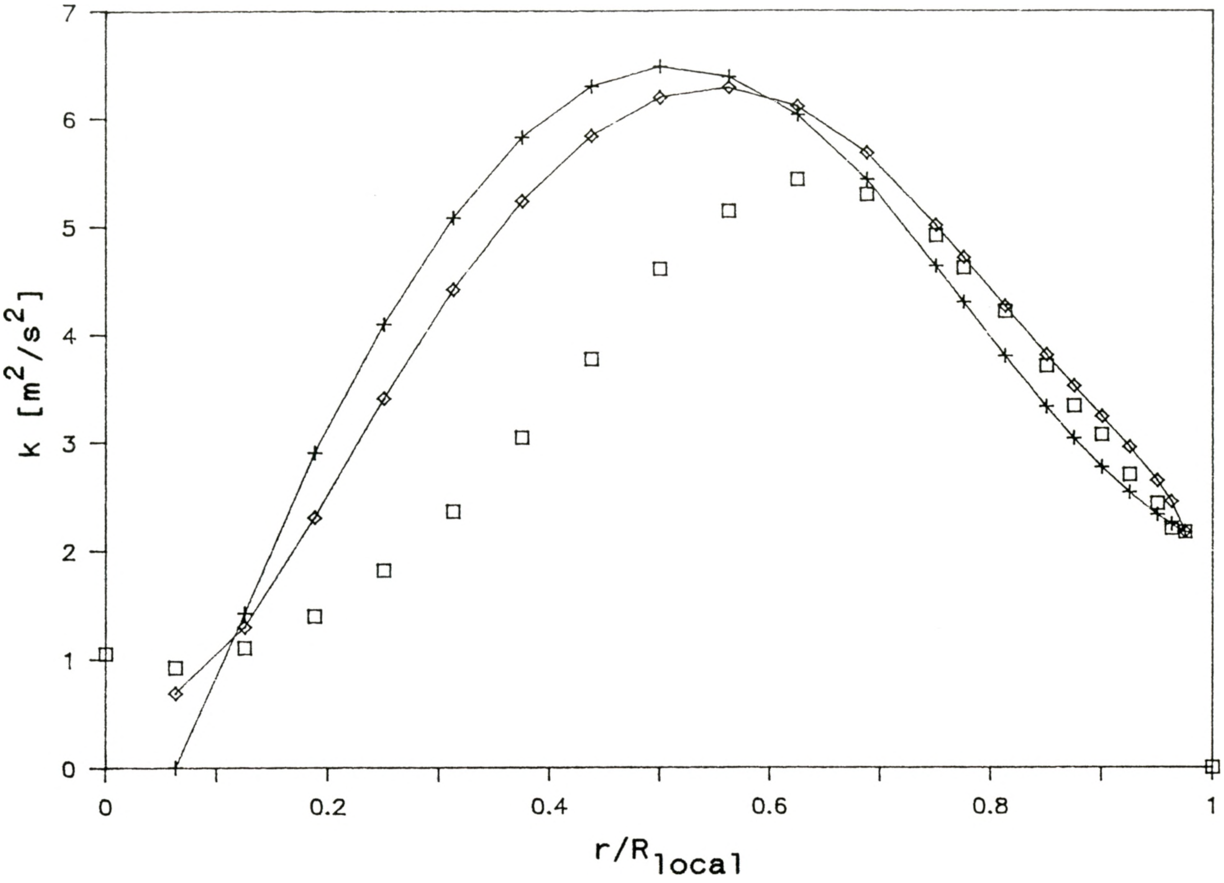

3.44. Comparison of partially converged solutions of k versus the experimental values for different Reynolds stresses at x=42cm: □ experimental, ◇ NT with modified Reynolds stresses (2 iterations), + NT with modified Reynolds stresses and $C'_{\varepsilon 1} = 3.88836 C_{\varepsilon 1}$ (7 iterations).

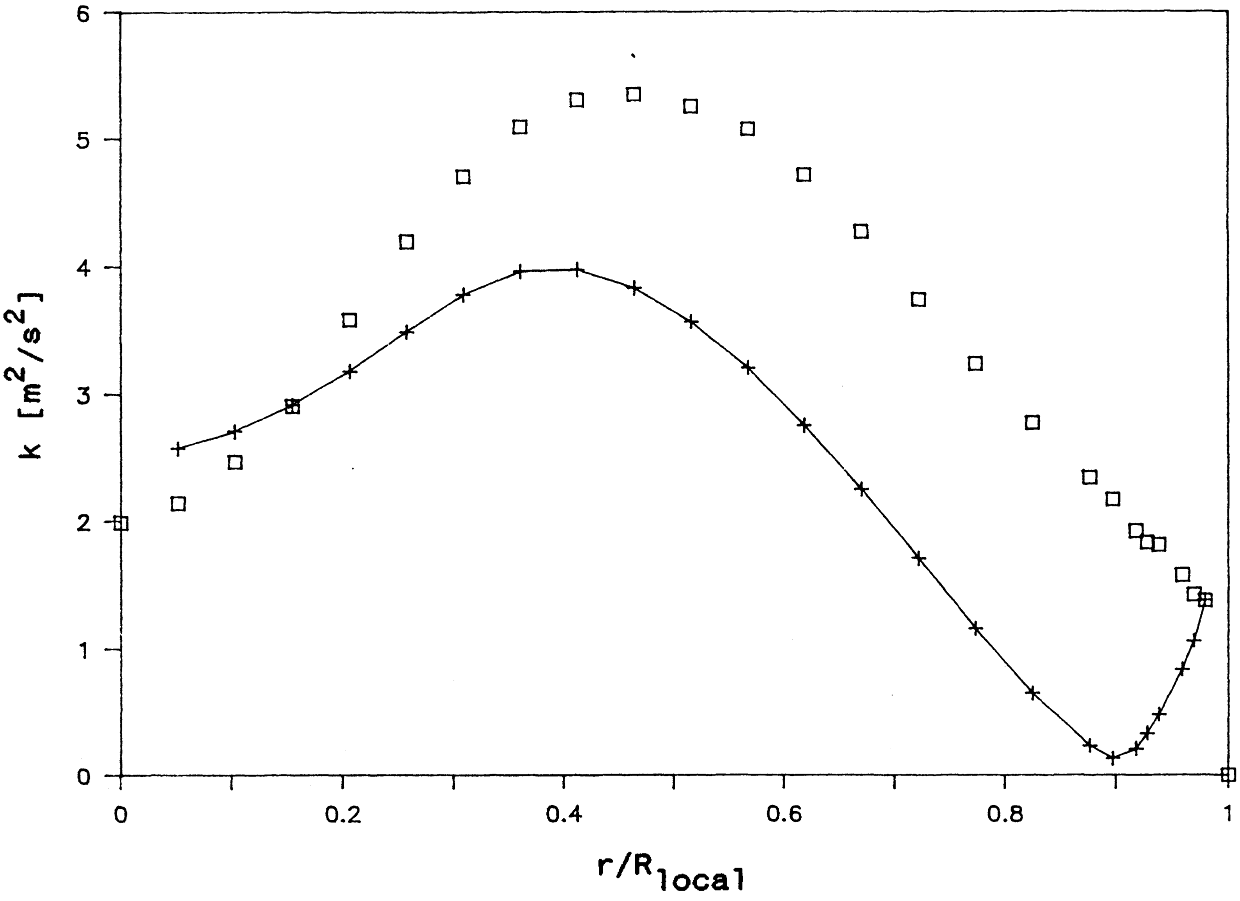

3.45. Comparison of partially converged solutions of k versus the experimental values for different Reynolds stresses at x=66cm: □ experimental, + NT with modified Reynolds stresses and $C'_{\varepsilon 1} = 2.3C_{\varepsilon 1}$ (15 iterations).

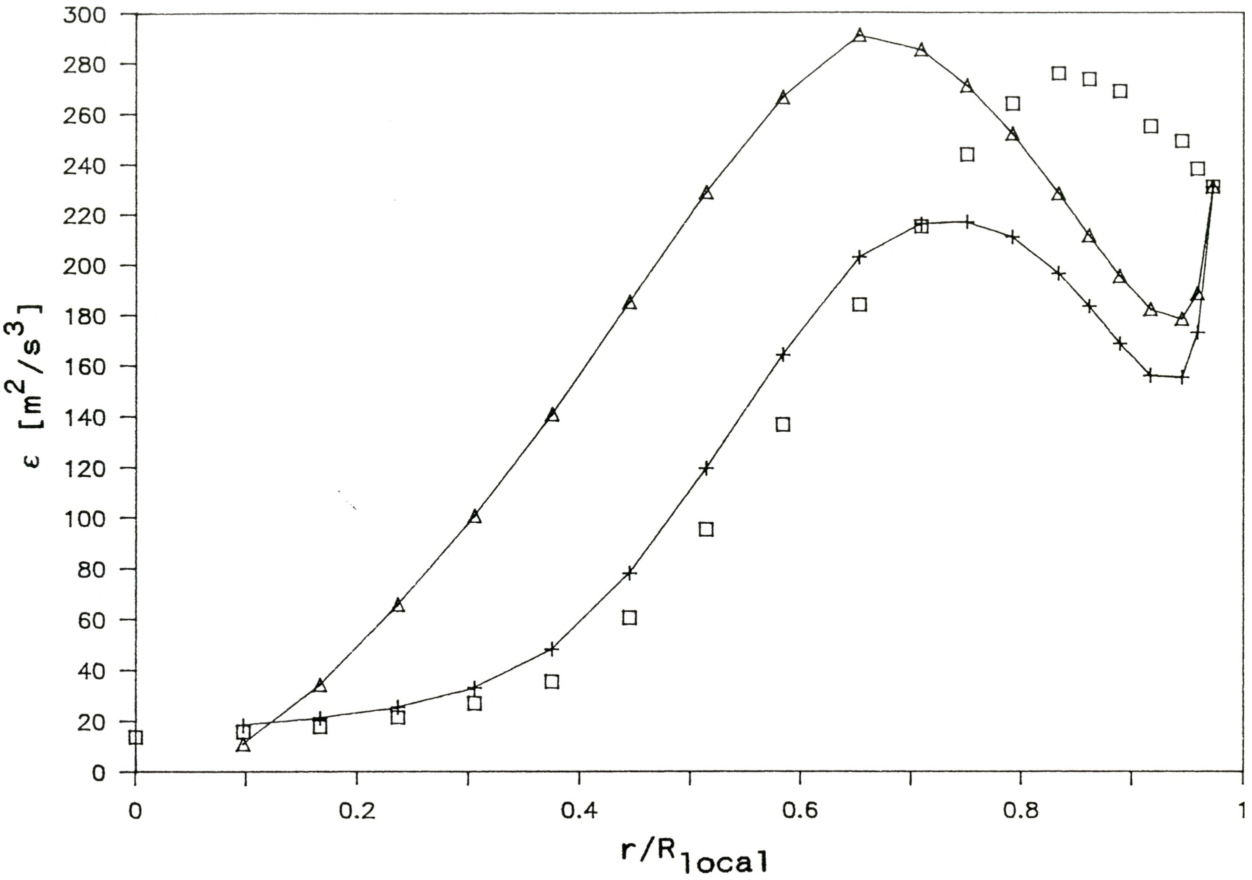

3.46. Comparison of partially converged solutions of ε versus the experimental values for different Reynolds stresses at x=30cm: □ experimental, + NT with modified Reynolds stresses (1 iteration), Δ NT with modified Reynolds stresses and $C'_{\varepsilon 1} = 3.175 C_{\varepsilon 1}$ (8 iterations).

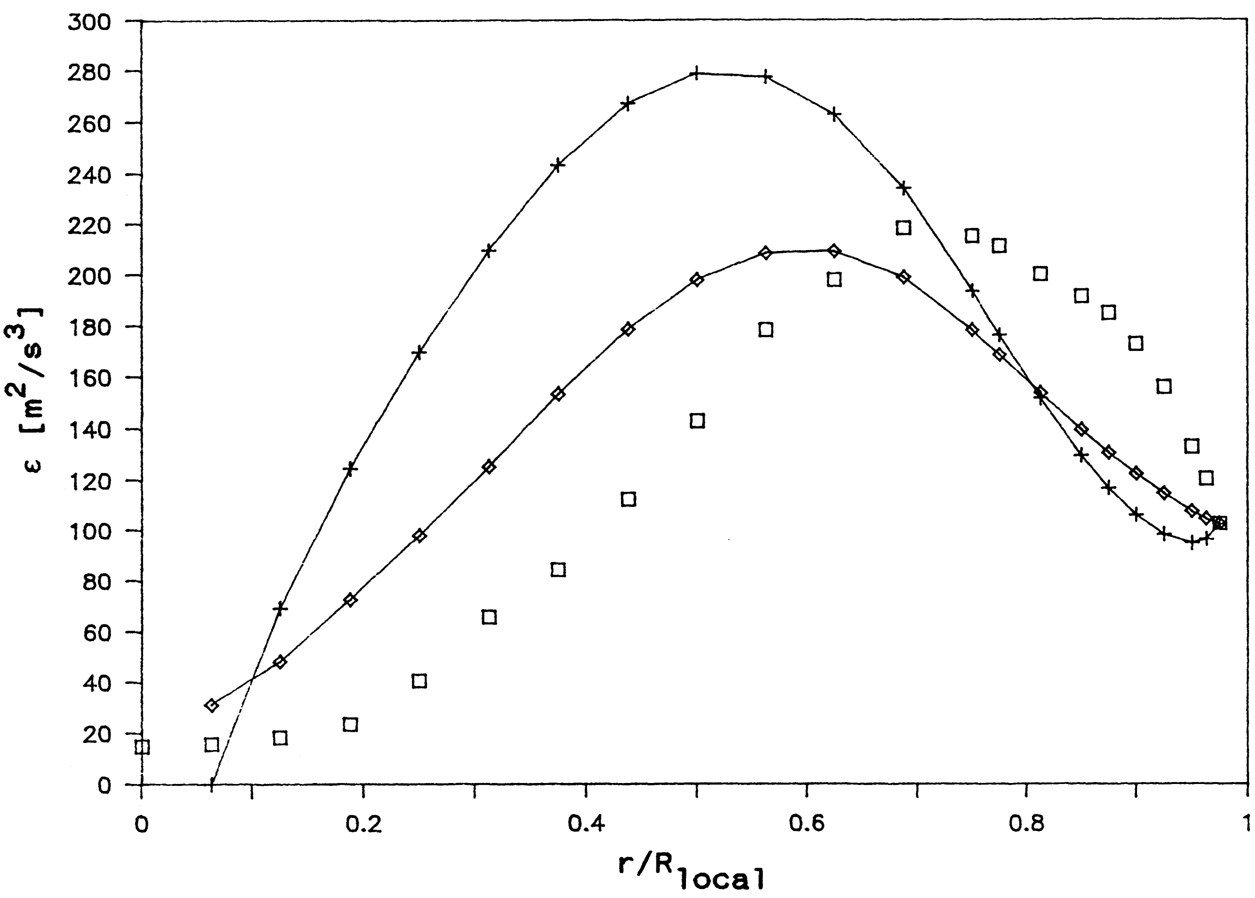

3.47. Comparison of partially converged solutions of ε versus the experimental values for different Reynolds stresses at x=42cm: □ experimental, ◇ NT with modified Reynolds stresses (2 iterations), + NT with modified Reynolds stresses and $C'_{\varepsilon 1} = 3.88836 C_{\varepsilon 1}$ (7 iterations).

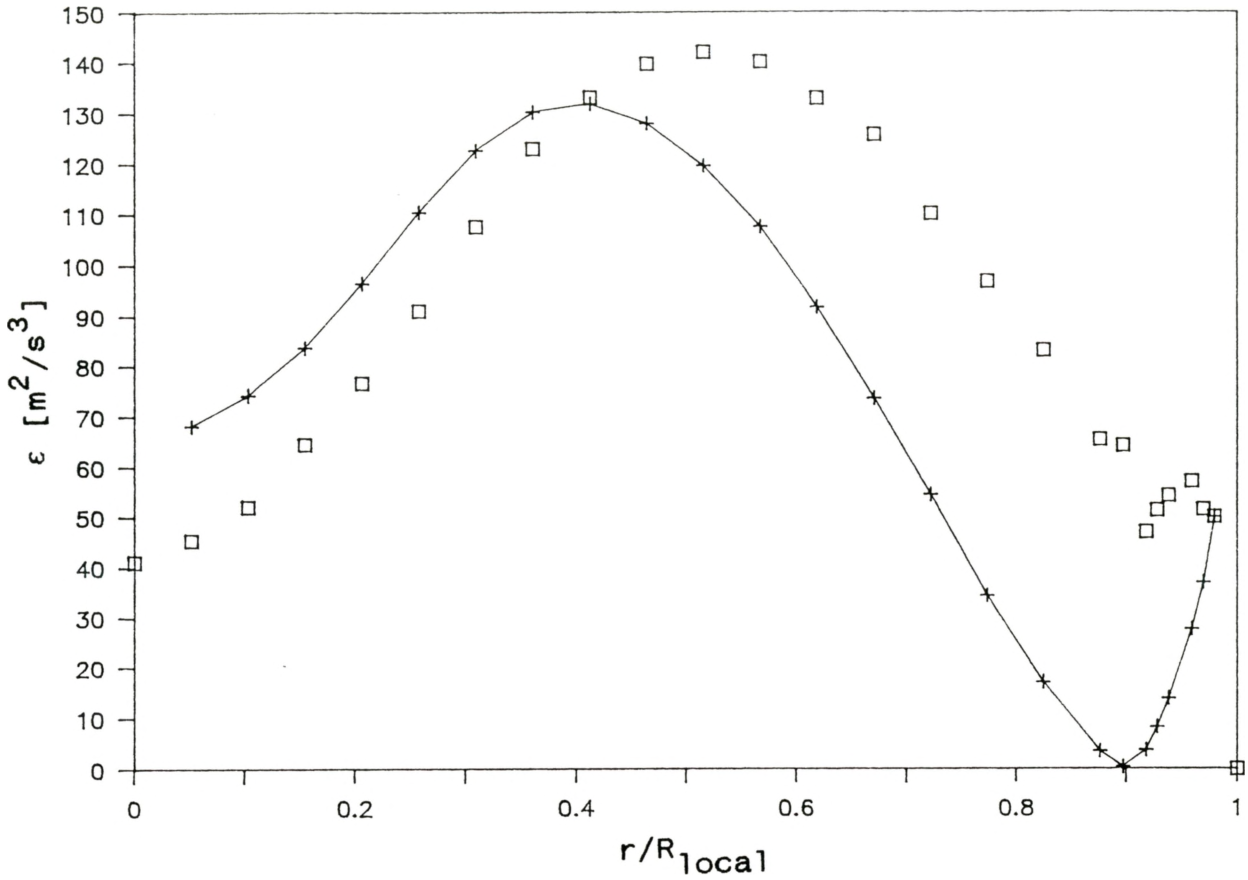

3.48. Comparison of partially converged solutions of ε versus the experimental values for different Reynolds stresses at x=66cm: □ experimental, + NT with modified Reynolds stresses and $C'_{\varepsilon 1} = 2.3C_{\varepsilon 1}$ (15 iterations).

Table 3.1 k-ε Model Constants and Functions

Name	f_μ	f_1	$C_{\varepsilon 1}$	$C_{\varepsilon 2}$	$C'_{\varepsilon 1}$	σ_k	σ_ε
NT	$\{1-\exp(-\frac{y+}{26})\}^2[1+\frac{4.1}{R_t^{3/4}}]$	1.0	1.45	1.90	2.5	1.4	1.3
LSH	$1-\exp[-C_3 y+\lvert 1-C_5\Delta\rvert]$	1.0	1.35	1.80		1.0	1.3
HOF	$\exp[-1.75/(1+R_t/50)]$	1.0	1.81	2.00		2.0	3.0

	C_μ	f_2	C_3	C_5
NT	0.09	$\{1-0.3\exp(-R_t^2/42.25)\}[1-\exp(-y+/6)]^2$		
LSH	0.09	$1-(2/9)\exp[-R_t^2/36]$	0.01113	4.372
HOF	0.09	$1-0.3\exp(-R_t^2)$		

Table 3.2 Curve-fit values for Bradshaw's Structural Coefficents

x(cm)	a_1	b	a_2	c
30	0.28	-0.25	0.80	-0.45
42	0.26	-0.18	0.70	-0.45
66	0.28	-0.25	0.45	-0.17

Table 3.3 Values of $C'_{\varepsilon 1}$ and thier corresponding centreline kinetic energy values.

x=30cm		x=42cm		x=66cm	
$C'_{\varepsilon 1}$	k_{cl}	$C'_{\varepsilon 1}$	k_{cl}	$C'_{\varepsilon 1}$	k_{cl}
2.5	23.76	2.5	27.13	2.5	div.
3.1	16.40	3.5	19.92	2.0	27.56
3.15	15.63	3.8	16.42	2.2	27.32
3.17	15.31	3.85	15.75	2.3	27.17
3.175	15.23	3.888	15.22	2.4	div.
3.176	div.	3.889	div.		

REFERENCES

1. Azad, R.S. and Kassab, *Turbulent Flow in a Conical Diffuser: Overview and Implications*, Physics of Fluids A, vol. 1, 1989, pp.564-573.

2. Bradshaw, P., *The Turbulence Structure of Equilibrium Boundary Layers*, Journal of Fluid Mechanics, vol. 29 part 4, 1967, pp. 625-645.

3. Coles, D.E., *The Law of the Wake in the Turbulent Boundary Layer*, Journal of Fluid Mechanics, vol 1 p2, 1956, pp 191-226.

4. Coles, D.E. and Hirst, E.A., *Computation of Turbulent Boundary Layers - 1968 AFOSR - IFP - Stanford Conference*, 1968.

5. Granville, P.S., *A Modified van Driest Formula for the Mixing Length of Turbulent Boundary Layers in Pressure Gradients*, ASME Journal of Fluids Engineering, vol 111, 1989 pp 94-97.

6. Hanjalic, K. and Launder, B.E., *Sensitizing the Dissipation Equation to Irrotational Strains*, ASME Journal of Fluids Engineering, vol. 102, 1980, pp.34-40.

7. Hinze, J.O., Turbulence, McGraw-Hill Book Co., New York, 1975, ch. 7.

8. Jones, W.P. and Launder, B.E., *The Prediction of Laminarization with a Two-Equation Model of Turbulence*, International Journal of Heat and Mass Transfer, vol. 15, 1972, pp.301-314.

9. Kader, B.A. and Yaglom, A.M., *Similarity Treatment of Moving-Equilibrium Turbulent Boundary Layers in Adverse Pressure Gradients*, Journal of Fluid Mechanics, vol 89 p2, 1978, pp 305-342.

10. Kassab, S.Z., *Turbulence Structure in Axisymmetric Wall-Bounded Shear Flow*, Ph.D. Thesis, University of Manitoba, 1986.

11. Kline, S.J., Cantwell, B.J., and Lilley, G.M., *1980-81 AFOSR - HTTM - Stanford Conference on Complex Turbulent Flows*, 1981.

12. Lai, Y.G., So, R.M.C., and Hwang, B.C., *Calculation of Planar and Conical Diffuser Flows*, AIAA Journal, vol. 27, 1989, pp.542-548.

13. Laufer, J.,*The Structure of Turbulence in Fully Developed Pipe Flow*, NACA Rep. no. 1174, 1954.

14. Mansour, N.N., Kim, J., and Moin, P., *Near-Wall k-ε Turbulence Modeling*, AIAA Journal, vol. 27, 1989, pp.1068-1073.

15. McDonald, H., *The Effect of Pressure Gradient on the Law of the Wall in Turbulent Flow*, Journal of Fluid Mechanics, vol 35 p2, 1969, pp 311-336.

16. Mellor, G.L. and Gibson, D.M., *Equilibrium Turbulent Boundary Layers*, Journal of Fluid Mechanics, vol 24 p2, 1966, pp225-253.

17. Mellor, G.L., *The Effects of Pressure Gradients on Turbulent Flow Near a Smooth Wall*, Journal of Fluid Mechanics, vol 24 p2, 1966, pp 255-274.

18. Nagano, Y. and Hishida, M., *Improved Form of the k-ε Model for Wall Turbulent Shear Flows*, ASME Journal of Fluids Engineering, vol. 109, 1987, pp.156-160.

19. Nagano, Y. and Tagawa, M., *An Improved k-ε Model for Boundary Layer Flows*, ASME Journal of Fluids Engineering, vol. 112, 1990, pp.33-39.

20. Nakayama, A. and Koyama, H., *A Wall Law for Turbulent Boundary Layers in Adverse Pressure Gradients*, AIAA Journal, vol 22, 1984, pp 1386-1389.

21. Ozimek, L.G., *A Comparison of Analog and Digital*

Data for Measurements of Turbulence Parameters, M.Sc. Thesis, University of Manitoba, 1985.

22. Patankar, S.V., Numerical Heat Transfer and Fluid Flow, Hemisphere Publishing Co., New York, 1980.

23. Patel, V.C., Rodi, W., and Scheuerer, G., *Turbulence Models for Near-Wall and Low Reynolds Number Flows: A Review*, AIAA Journal, vol. 23, 1984, pp.1308-1319.

24. Perry, A.E., Bell, J.B., and Joubert, P.N., *Velocity and Temperature Profiles in Adverse Pressure Gradient Turbulent Boundary Layers*, Journal of Fluid Mechanics, vol 25 p2, 1966, pp 299-320.

25. Perry, A.E., *Turbulent Boundary Layers in Decreasing Adverse Pressure Gradients*, Journal of Fluid Mechanics, vol 26 p3, 1966, pp 481-506.

26. Perry, A.E. and Schofield, W.H., *Mean Velocity and Shear Stress Distributions in Turbulent Boundary Layers*, Physics of Fluids, vol 16, 1973, pp 2068-2074.

27. Polak, D.R. and Turan, Ö.F., *Assessment of k-ε Turbulence Models in Predicting Reynolds Stresses in Diffuser Flow*, submitted to ASME Journal of Fluids Engineering, 1991.

28. Rodi, W. and Scheuerer, G., *Scrutinizing the k-ε Turbulence Model Under Adverse Pressure Gradient Conditions*, ASME Journal of Fluids Engineering, vol. 108, 1986, pp.174-179.

29. Samuel, A.E. and Joubert, P.N., *A Boundary Layer Developing in an Increasingly Adverse Pressure Gradient*, Journal of Fluid Mechanics, vol 66 p3, 1974, pp 481-505.

30. Schofield, W.H., *Equilibrium Boundary Layers in Moderate to Strong Adverse Pressure Gradients*, Journal of Fluid Mechanics, vol 113, 1981 pp 91-122.

31. Smith, G.D., Numerical Solution of Partial Differential Equations: Finite Difference Methods, 3rd ed.,

Oxford University Press, New York, 1985.

32. Townsend, A.A., *Equilibrium Layers and Wall Turbulence*, Journal of Fluid Mechanics, vol 11, 1961, pp 97-120.

33. Townsend, A.A., *The Behaviour of a Turbulent Boundary Layer Near Separation*, Journal of Fluid Mechanics, vol 12, 1962, pp 536-554.

34. Trupp, A.C., Azad, R.S., and Kassab, S.Z., *Near-wall Velocity Distributions within a Straight Conical Diffuser*, Experiments in Fluids, vol 4, 1986, pp 319-331.

35. Turan, Ö.F., Azad, R.S., and Atamanchuk, T., *Wall Effect on the Hot-Wire Signal with Flow*, J. Phys. E.: Sci. Instrum. 20, 1987, pp 1278-1280.

36. Turan, Ö.F., *Further Study of a New Method of Evaluating Turbulence Dissipation*, Ph.D. Thesis, University of Manitoba, 1988.

37. van Driest, E.R., *On Turbulent Flow Near A Wall*, Journal of Aeronautical Sciences, vol 23, 1956, pp 1007-1011, 1036.

Appendix A

Samples of Townsend's (chapter 2, equations 11 and 12) and McDonald's (chapter 2, equation 16) formulations in flows #0142 and #0143. The stations shown are listed in their corresponding figure captions, along with the curve-fit coefficients for the linear shear stress approximation (chapter 2, equation 16a). The McDonald slip velocity is given relative to Townsend's.

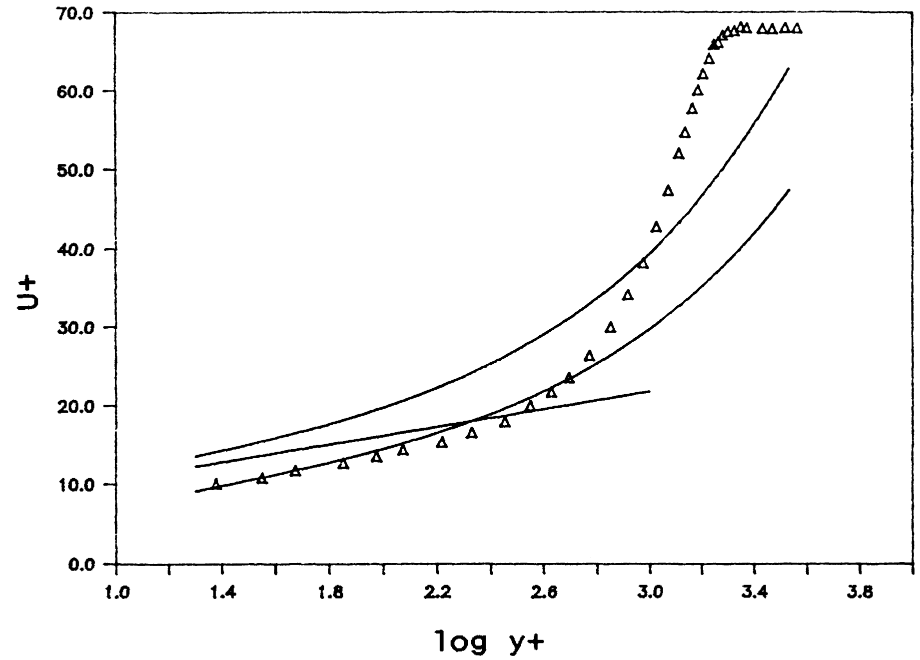

A.1 McDonald (a=0.275, γ=0.559, $U_s=U_s(T)-2.2$), Townsend, and the Log Law at x=1.049m in flow #0142. $U_s(T)$ is Townsend's slip velocity non-dimensionalized with u_*.

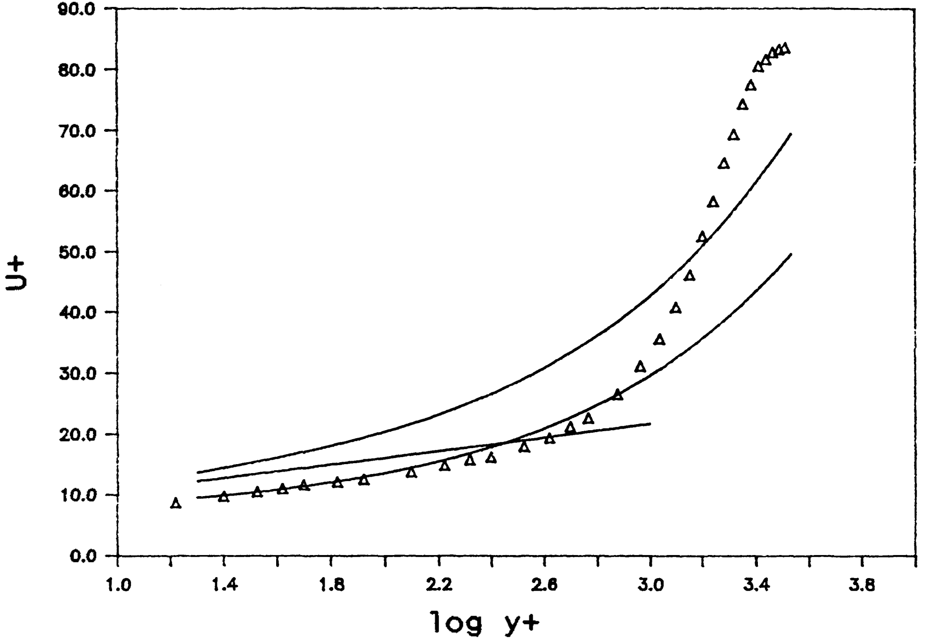

A.2 McDonald (a=0.01, γ=0.50, $U_s=U_s(T)-5.5$), Townsend, and the Log Law at x=1.813m in flow #0142. $U_s(T)$ is Townsend's slip velocity non-dimensionalized with u_*.

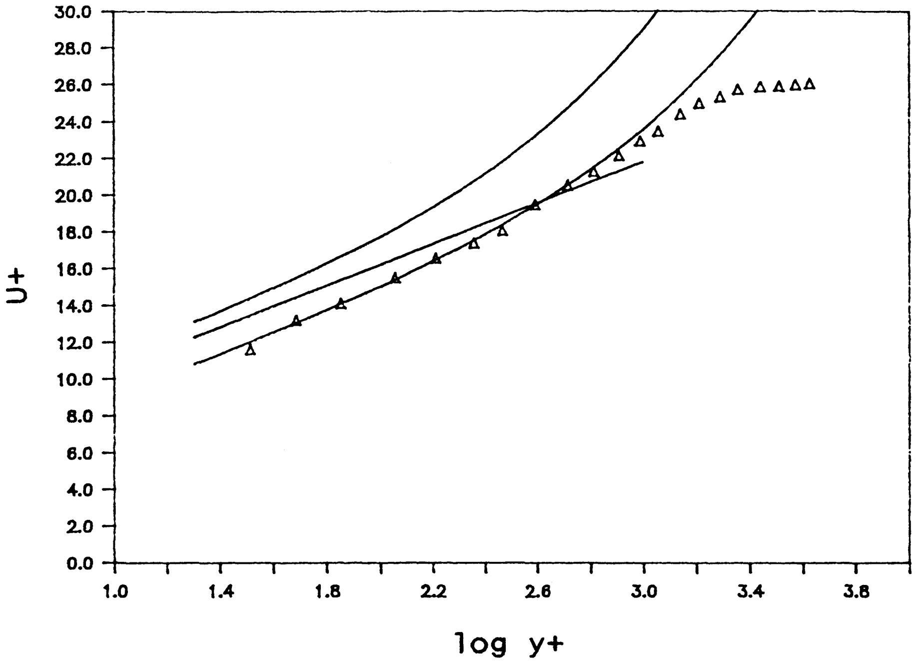

A.3 McDonald (a=0.40, γ=0.424, U_s=U_s(T)-2.4), Townsend, and the Log Law at x=0.573m in flow #0143. U_s(T) is Townsend's slip velocity non-dimensionalized with u_*.

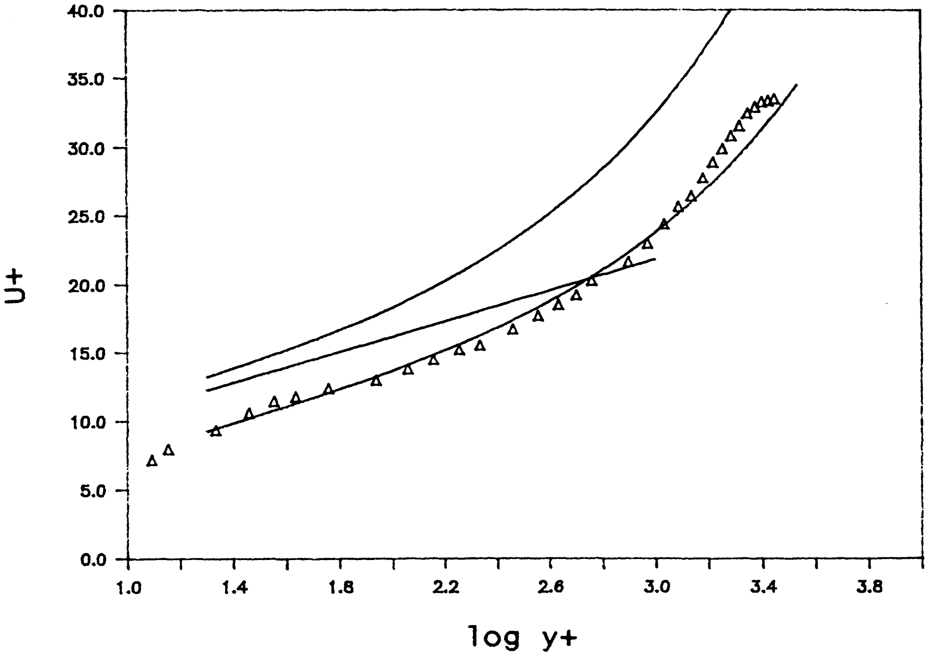

A.4 McDonald (a=0.112, γ=0.146, U_s=U_s(T)-4.0), Townsend, and the Log Law at x=1.813m in flow #0143. U_s(T) is Townsend's slip velocity non-dimensionalized with u_*.

Appendix B

Samples of Perry's and Kader and Yaglom's half-power law and Kader and Yaglom's velocity defect in the eight decreasing adverse pressure gradient flows. For reference, the Log Law (κ=0.41, b=5.0) is shown with only Kader and Yaglom's half-power law and defect at several of the stations. Perry's slip velocity is always larger than Kader and Yaglom's in the flows examined here, and is therefore always above Kader and Yaglom's half-power law.

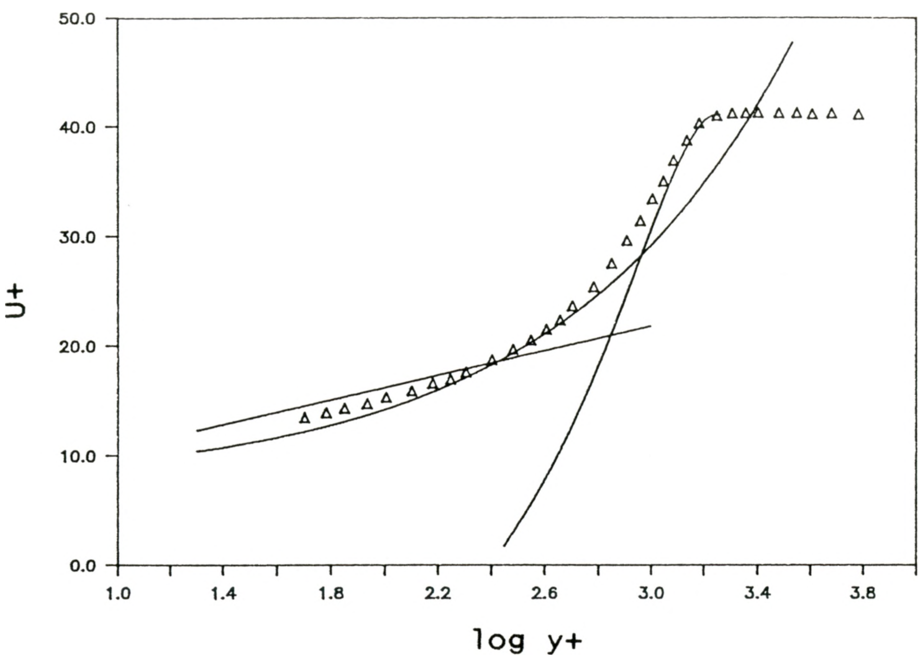

B.1 Kader and Yaglom's half-power law and velocity defect along with the Log Law in flow #0142 at x=0.382m.

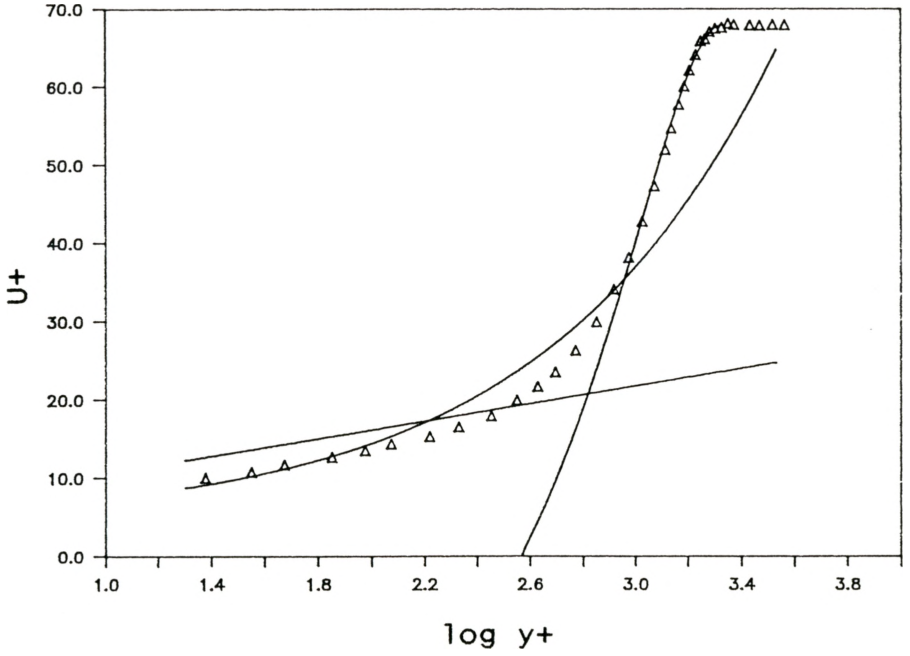

B.2 Kader and Yaglom's half-power law and velocity defect along with the Log Law in flow #0142 at x=1.049m.

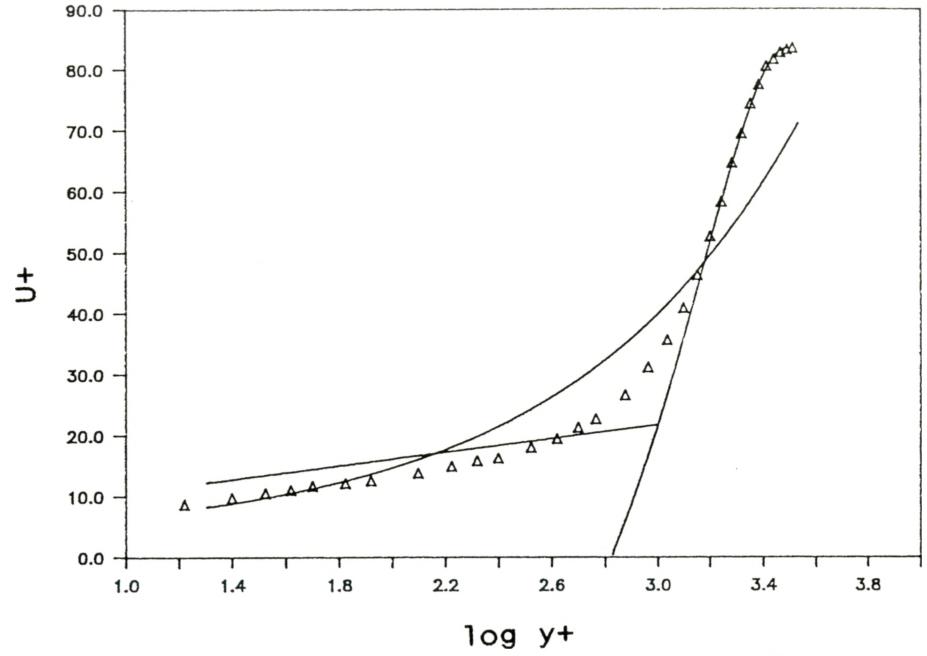

B.3 Kader and Yaglom's half-power law and velocity defect along with the Log Law in flow #0142 at x=1.813m.

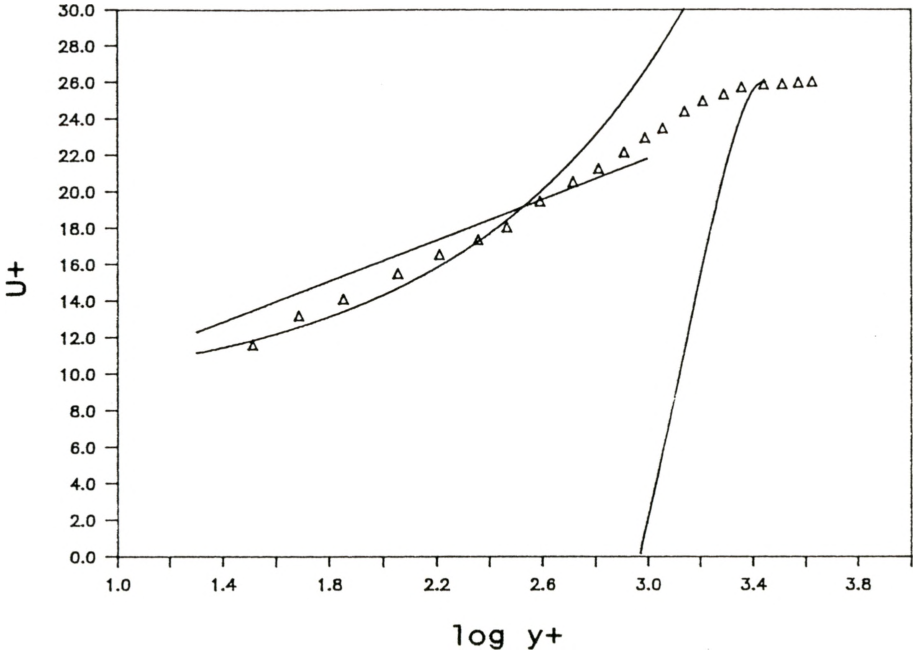

B.4 Kader and Yaglom's half-power law and velocity defect along with the Log Law in flow #0143 at x=0.573m.

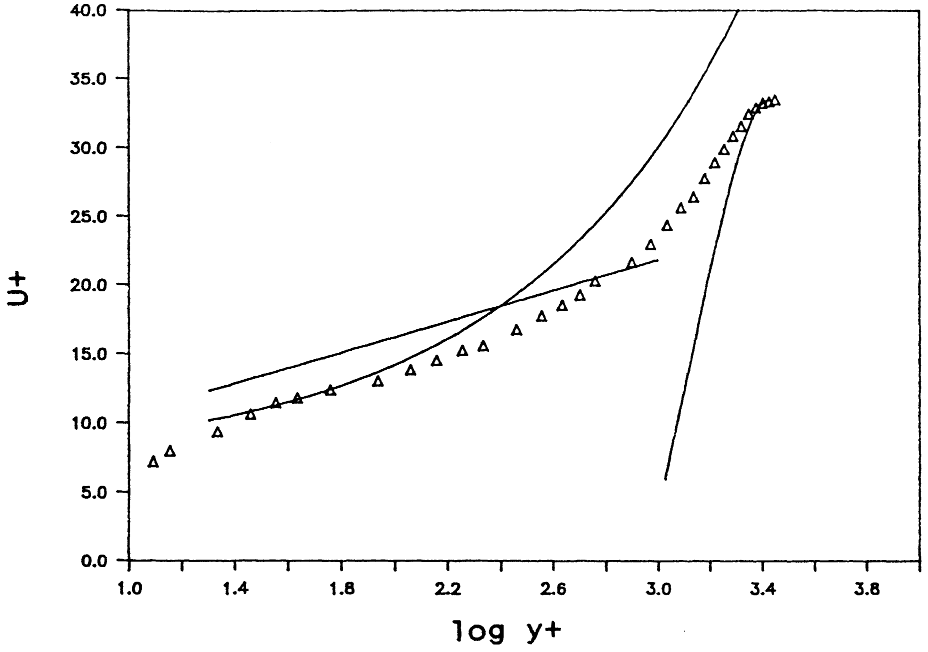

B.5 Kader and Yaglom's half-power law and velocity defect along with the Log Law in flow #0143 at x=1.813m.

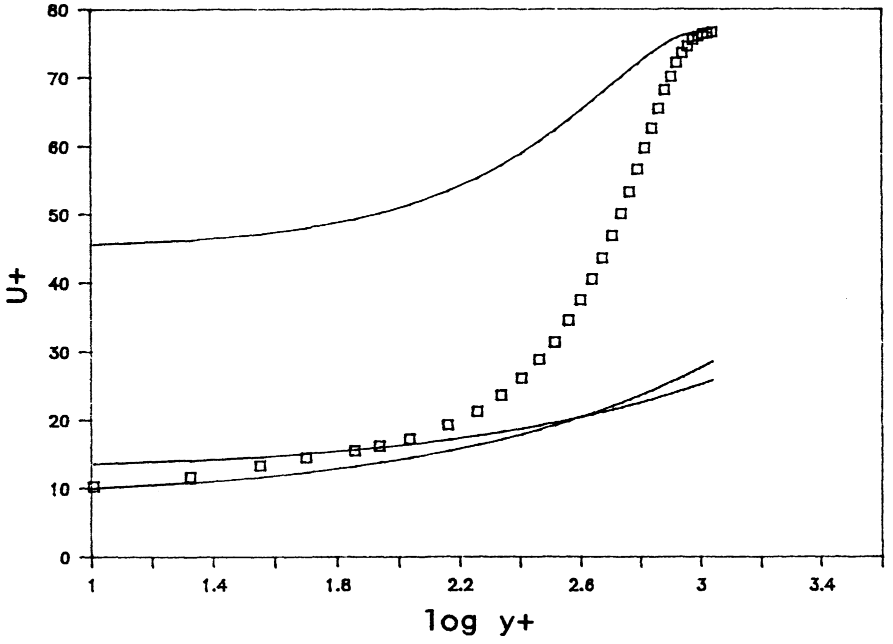

B.6 Perry's and Kader and Yaglom's half-power laws, Kader and Yaglom's velocity defect in flow #5000 at station 9. Perry's half-power law is always above Kader and Yaglom's.

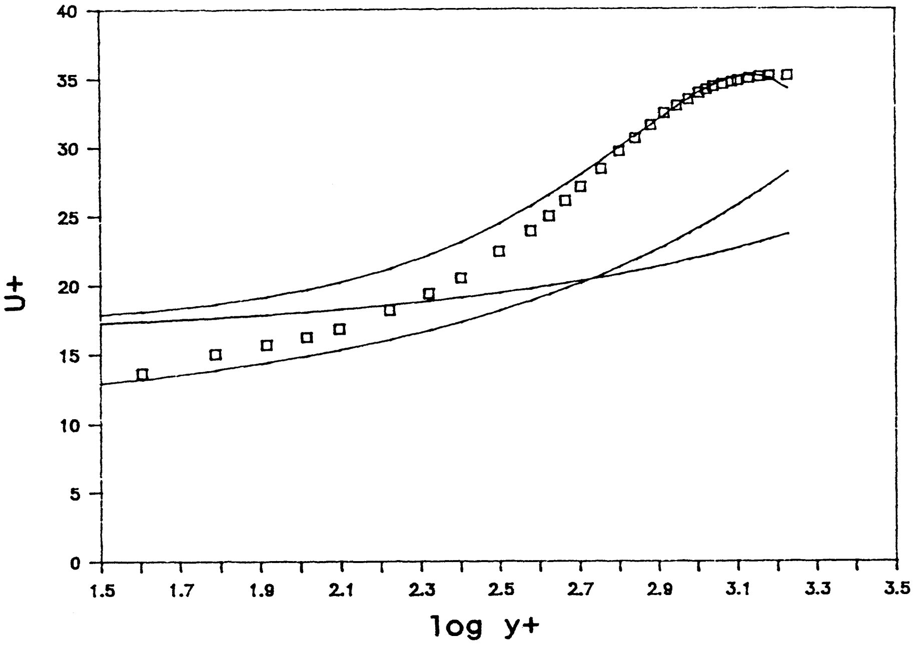

B.7 Perry's and Kader and Yaglom's half-power laws, Kader and Yaglom's velocity defect in flow #5100 at station 5. Perry's half-power law is always above Kader and Yaglom's.

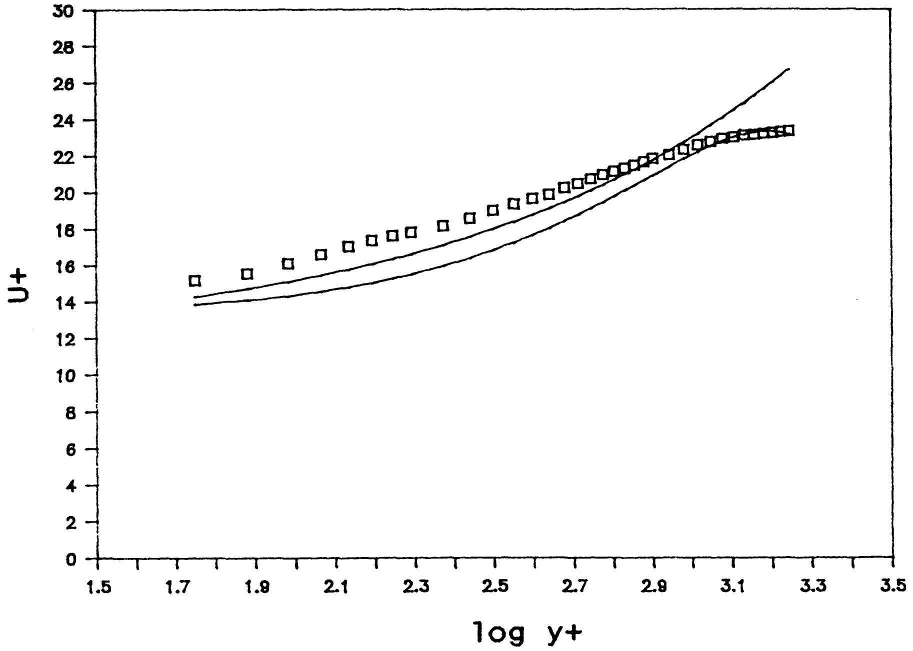

B.8 Kader and Yaglom's half-power law velocity defect in flow #5100 at station 2.

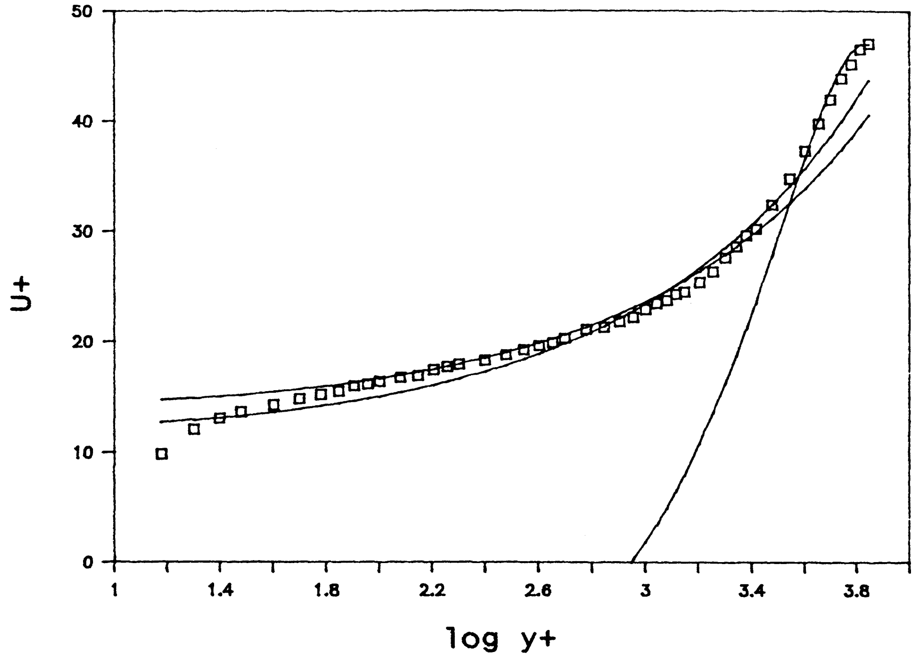

B.9 Perry's and Kader and Yaglom's half-power laws, Kader and Yaglom's velocity defect in flow #2900 at station 5. Perry's half-power law is always above Kader and Yaglom's.

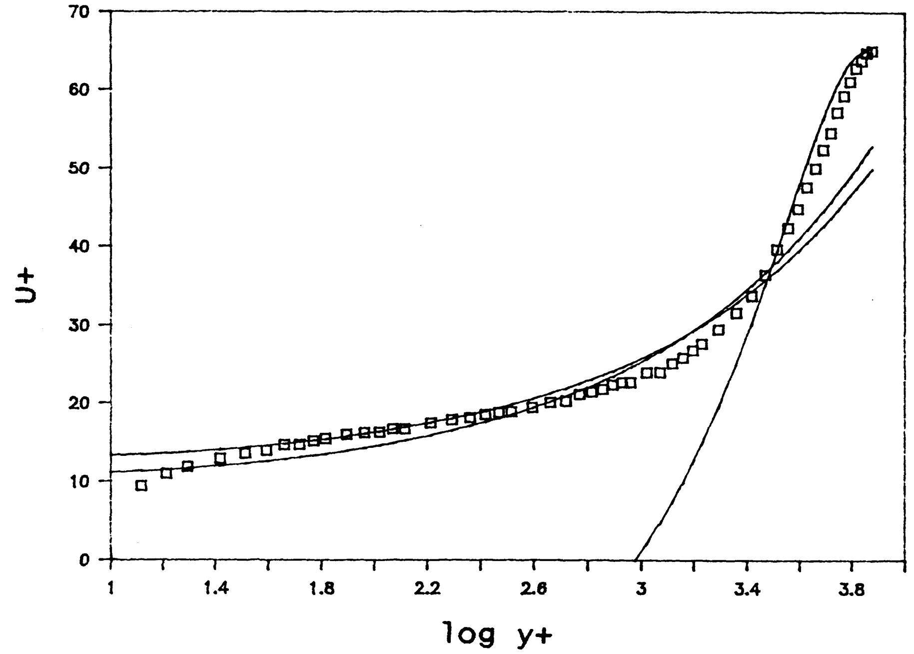

B.10 Perry's and Kader and Yaglom's half-power laws, Kader and Yaglom's velocity defect in flow #2900 at station 8. Perry's half-power law is always above Kader and Yaglom's.

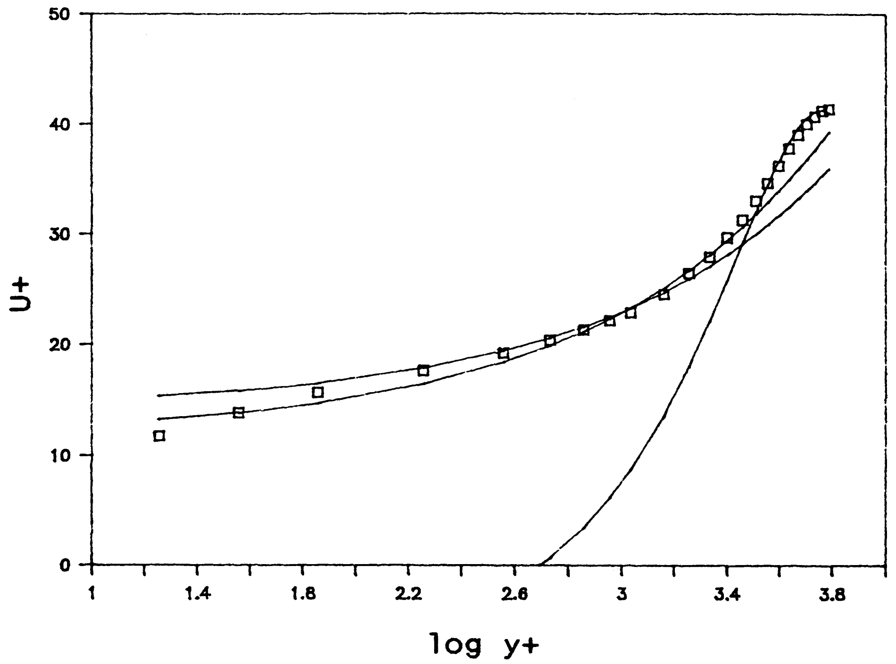

B.11 Perry's and Kader and Yaglom's half-power laws, Kader and Yaglom's velocity defect in flow #1100 at station 12. Perry's half-power law is always above Kader and Yaglom's.

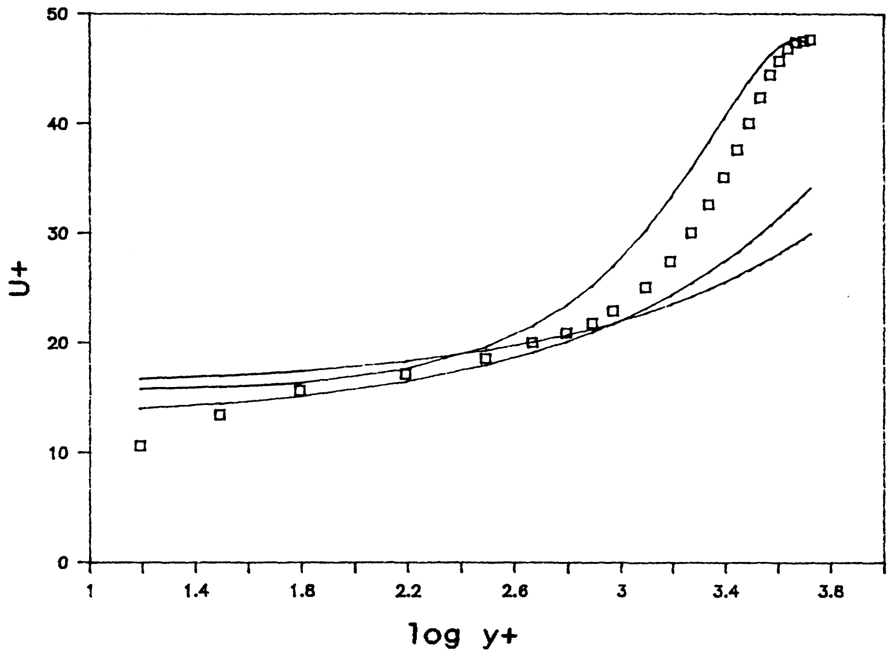

B.12 Perry's and Kader and Yaglom's half-power laws, Kader and Yaglom's velocity defect in flow #1200 at station 9. Perry's half-power law is always above Kader and Yaglom's.

Appendix C

The experimental data for the nine flows examined here are shown on half-power coordinates. For clarity, not all stations are shown.

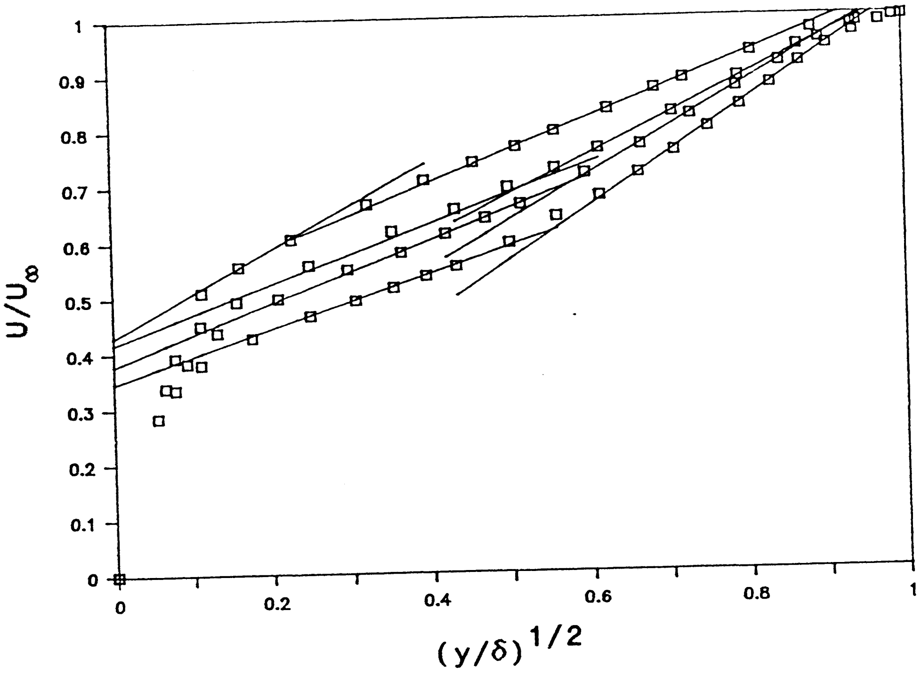

C.1 Half-power flow development in flow #1100.

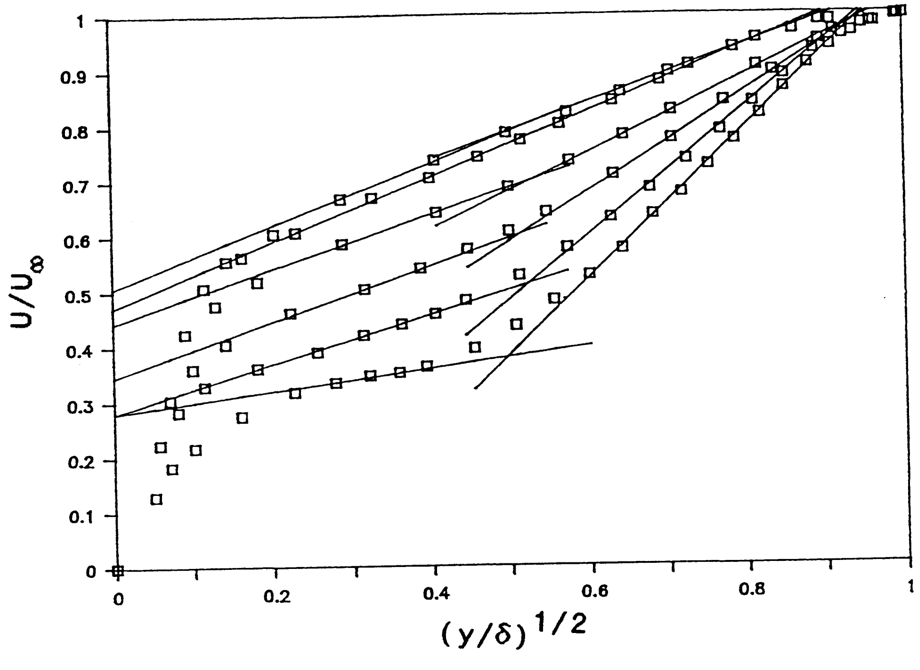

C.2 Half-power flow development in flow #1200.

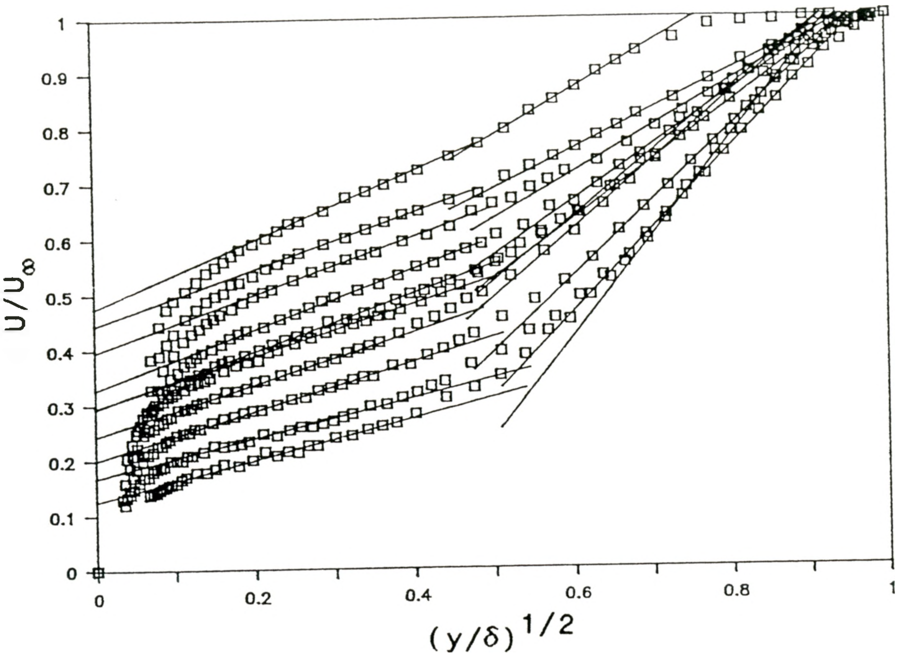

C.3 Half-power flow development in flow #2900.

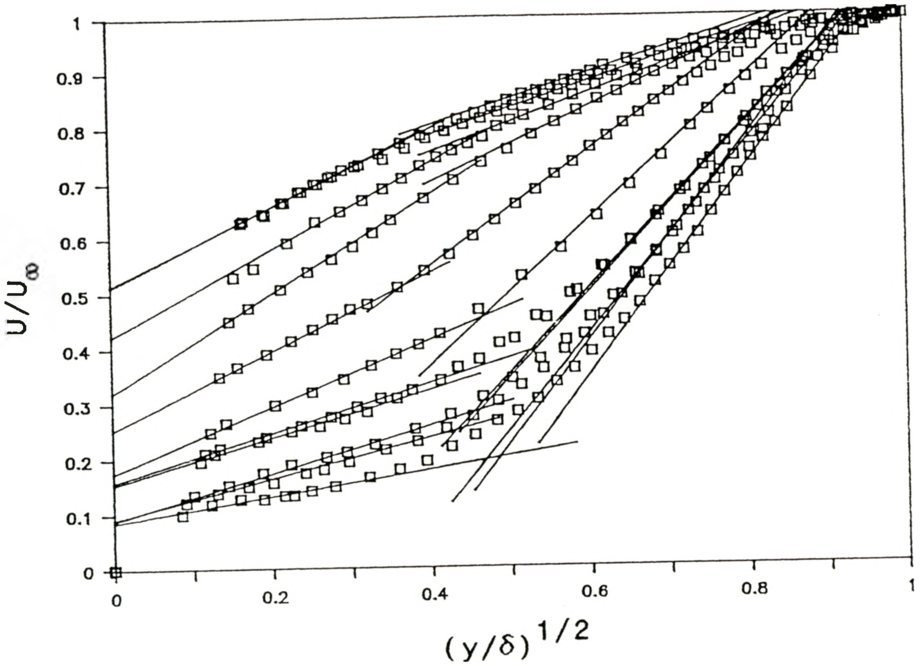

C.4 Half-power flow development in flow #5000.

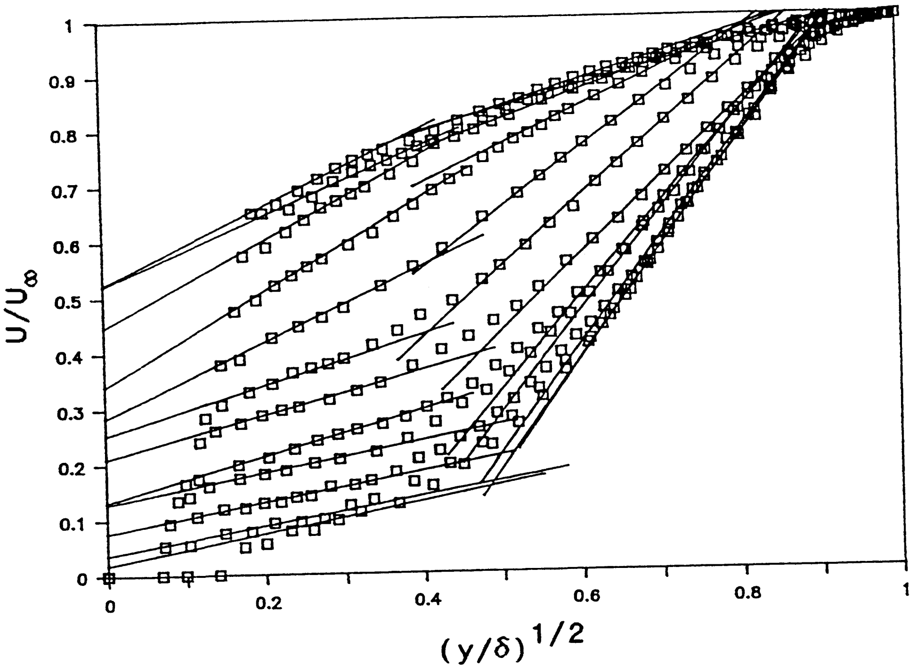

C.5 Half-power flow development in flow #5100.

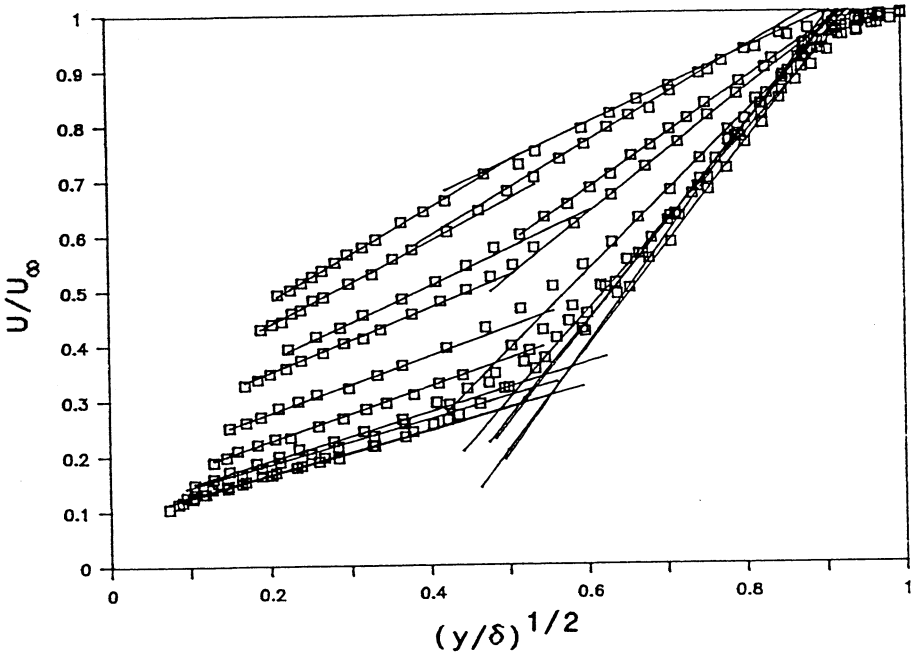

C.6 Half-power flow development in flow #0142.

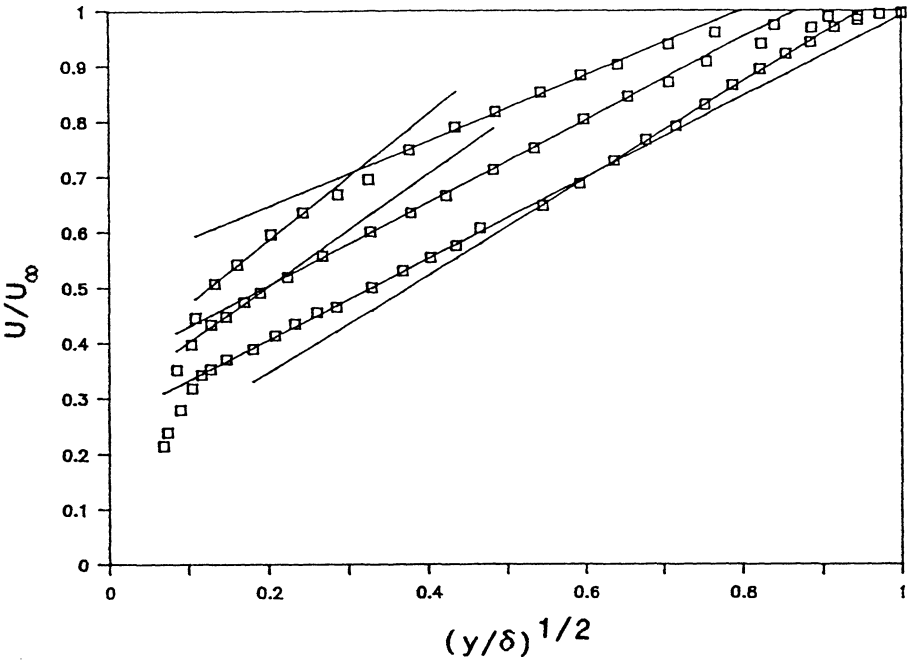

C.7 Half-power flow development in flow #0143.

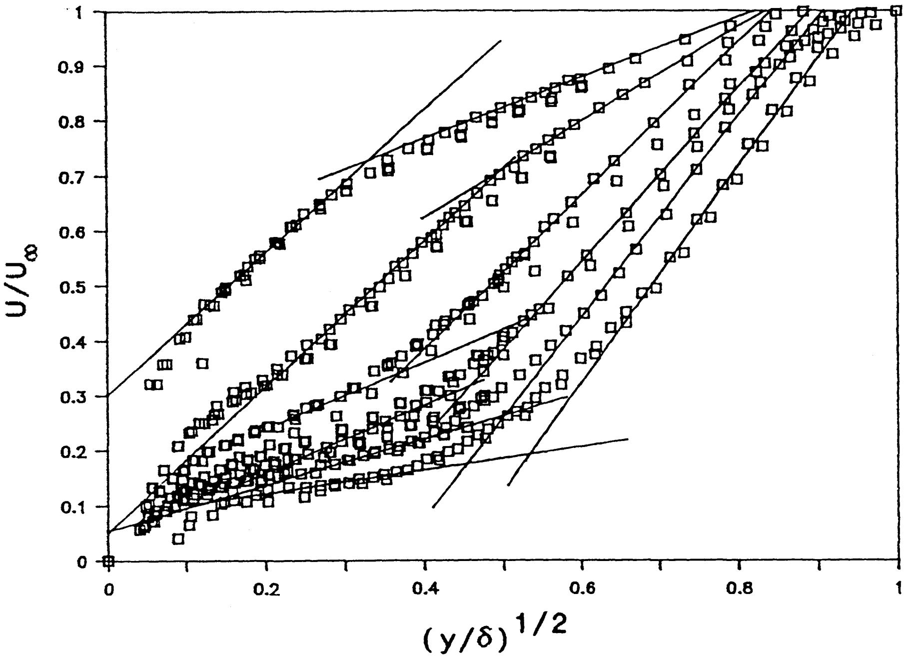

C.8 Half-power flow development in the eight degree conical diffuser flow.

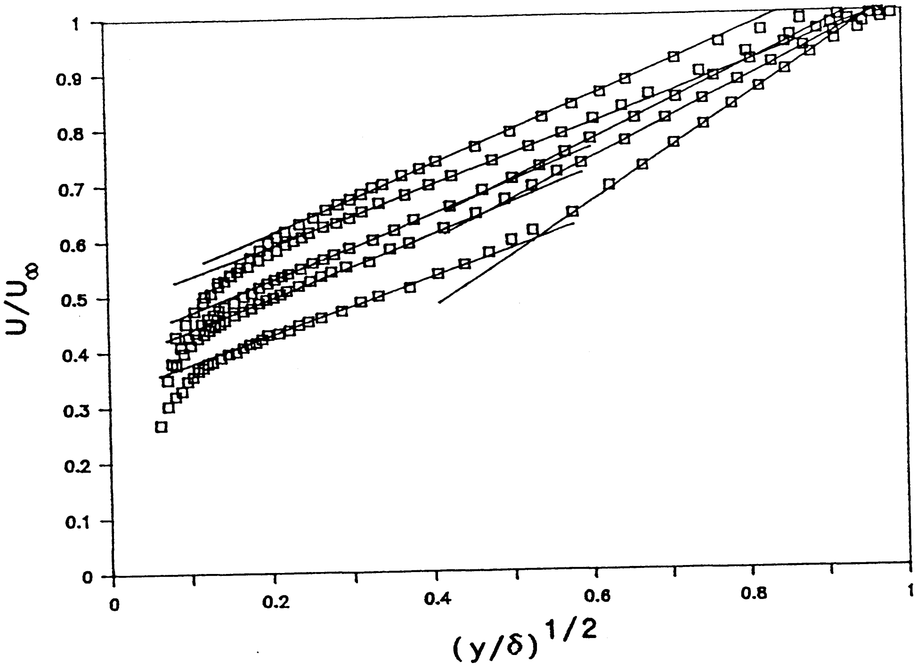

C.9 Half-power flow development in flow #0141.

Appendix D

The modified Nakayama and Koyama (chapter 2, equation 15a) and modified Kader and Yaglom velocity defect (chapter 2, equation 26) constants in the eight degree conical diffuser.

x (cm)	$B_1=b_1(t)^{b_2}$ b1 b2	t_s	C
3	0.70, 0.235	1.00085	1.04
6	1.15, 0.02	1.0014	1.24
9	1.80, 0.05	1.0045	1.50
12	1.10, 0.47	1.0050	1.65
15	0.91, 0.54	1.0041	2.117
18	0.65, 0.93	1.0042	2.30
21	0.41, 1.095	1.0043	3.13
24	0.33, 1.11	1.0038	3.74
27	0.33, 1.15	1.0035	3.85
30	0.31, 1.185	1.0040	4.395
33	0.19, 1.50	1.0044	5.00
36	0.25, 1.267	1.0048	5.50
39	0.14, 1.65	1.0067	6.05
42	0.22, 1.283	1.0053	6.79
45	0.12, 1.647	1.0077	7.15
48	0.18, 1.37	1.0053	7.94
51	0.043,2.148	1.0084	8.65
54	0.057,1.98	1.0088	9.42
57	0.041,2.08	1.0087	10.20
60	0.036,2.21	1.020	11.23
63	0.032,2.31	1.015	12.05
66	0.021,2.50	1.020	13.10
69	0.013,2.81	1.013	13.60

Appendix E

Program Codes to Solve the k and ε Equations with Given Velocity Field

A brief discussion is given below for each of the subroutines in the program codes KEPSILON and GRDVEL, followed by the actual hard copy listing of the two codes and a sample input data file (VELPRD30.DAT).

The program code KEPSILON starts with the input of data, followed by the calculation loop of k, ε, and ν_t. Lastly, k and ε are printed to the file KEPSILON.OUT.

SUBROUTINE MAIN: This is the main body of the program. Its primary functions are to control the flow of the program, input and output data, and to determine when convergence has been obtained.

SUBROUTINE GRID calculates all of the various lengths that are required to define the grid shown in Figure 3.1. A nonuniform mesh is used.

SUBROUTINE CALCKE calculates the coefficients and source terms for the kinetic energy equation using the power-law scheme. Under-relaxation is employed to enhance convergence with the following modification to the difference scheme:

$$a_P = a_P/\alpha \text{ and } b = b + (1 - \alpha)a_P\phi_P^*/\alpha$$

SUBROUTINE CALCDE calculates the coefficients and source terms for the dissipation rate equation using the power-law scheme.

SUBROUTINE PRINTT is used to output any array in the program to the output file.

SUBROUTINE PROPS calculates the eddy viscosity from the Kolmogorov-Prandtl relation.

SUBROUTINE LNSOLV contains the TDMA solver discussed in section 3.2.

SUBROUTINE UVEL calculates the mean streamwise velocity field in the eight degree conical diffuser with the modified Nakayama and Koyama and modified Kader and Yaglom velocity defect. Near the wall, a modified Rannie equation is used.

SUBROUTINE INTERP uses a Lagrangian polynomial to interpolate the experimental data between the experimental stations.

```
      PROGRAM KEPSILON
C
C   CALCULATES K AND EPSILON FOR GIVEN VELOCITY FIELD
C   AND TURBULENCE PRODUCTION
C
C-------declare variables---------
C
      REAL*8 RIN,ROUT,DRNP,DRPS,R,RC,DR,RAD,SNS,ALPHA
      REAL*8 DE,KE,U,V,VSCSTY,DENSTY,EDYVIS,PROD,ADV,
     1    UCL,USTAR,NU,RHO,DUDX,DUDR,DVDX,DVDR,DKDX,DEDX
      REAL*8 SIGMAK,SIGMAE,CMU,CE1,CE2,C3,F1,F2,F3,FMU,C4,C5
      REAL*8 AP,AS,AN,B,SORCE,SC,SP,GREAT,PI
      REAL RESORE,RESORK,SORMAX,URFK,URFD,URFEV,DUM1
      INTEGER NJ,NJP1,NJM1,JSTEP,JSTP1,JSTM1,XY,NUMSTP
      INTEGER MAXNJ,JMON,MAXIT,PRNNUM,NSWPK,NSWPD,NITER
      INTEGER JJ,NJ2,NI
      CHARACTER*18 HEADU,HEADV,HEADK,HEADD
      CHARACTER*80 DUM
      CHARACTER*1 CHCK
      CHARACTER*12 FILENM
      COMMON/PRMTVE/DE(500),KE(500),U(500),V(500),
     1      EDYVIS(500),
     1      VSCSTY,DENSTY,GREAT,PI,USTAR,RHO,UCL,DUDX(500),
     1              DUDR(500),DVDX(500),DVDR(500),DKDX(500),
     1              DEDX(500),
     1      PROD(500),ADV(500),ALPHA
      COMMON/TURB/CMU,CE1,CE2,C3,SIGMAK,SIGMAE,FMU,F1,F2,
     1      F3,C4,C5
      COMMON/PROB/NSWPK,NSWPD,URFK,URFD,URFEV,SORCE,RESORK,
     1      RESORE
      COMMON/GEOM/RIN,RAD,NJ,NJP1,NJM1,NUMSTP,JSTEP,JSTP1,
     1       JSTM1,
     1       SNS(500),DRNP(500),DRPS(500),R(500),RC(500),XY,
     1       MAXNJ,
      COMMON/CVFORM/AS(500),AN(500),AP(500),B(500),SP(500)
C
C-------input grid information
C
      MAXNJ=500
      DO 333 J=1,MAXNJ
        U(J)=0.
        V(J)=0.
        DUDX(J)=0.
        DUDR(J)=0.
        DVDX(J)=0.
        DVDR(J)=0.
  333 CONTINUE
C
C        when changing the size of the arrays (maxni,maxnj)
C       do not
C       forget to change array size in lnsolv subroutine
      GREAT=1.0E+30
      PI=3.141592654
```

```
      OPEN (1,FILE='KE_GRID.DAT',STATUS='OLD')
      READ (1,*) RAD
      WRITE(*,*) RAD
      READ (1,*) MAXIT,SORMAX,PRNNUM,JMON
      WRITE(*,*) MAXIT,SORMAX,PRNNUM,JMON
      READ (1,*) NSWPK,NSWPD,URFK,URFD,URFEV
      WRITE(*,*) NSWPK,NSWPD,URFK,URFD,URFEV
      CLOSE (1,STATUS='KEEP')
C
C-------turbulence model constants-------
C---------NT Model-------
      CMU=0.09
      CE1=1.45
      CE2=1.90
      SIGMAK=1.4
      SIGMAE=1.3
      F1=1.0
C---------LSH Model-------
C      CMU=0.09
C      CE1=1.35
C      CE2=1.8
C      SIGMAK=1.0
C      SIGMAE=1.3
C      F1=1.0
      C3=0.01113
      C4=0.5
      C5=4.372
C---------Hoffmann Model----------
C      CMU=0.09
C      CE1=1.81
C      CE2=2.00
C      SIGMAK=2.0
C      SIGMAE=3.0
C      F1=1.0
C
C-------generate grid-------
C
      OPEN (7,FILE='KEPSILON.OUT',STATUS='UNKNOWN')
      WRITE (7,*)
      WRITE (7,*) '  OUTPUT DATA FILE FOR k-epsilon PROGRAM'
      WRITE (7,*)
C
C-------input velocity fields and initial guesses-------
C
C      OPEN (1,FILE='30GV.OUT',STATUS='OLD')
C      OPEN (1,FILE='VELPRD30.DAT',STATUS='OLD')
C      OPEN (1,FILE='VLPRD303.DAT',STATUS='OLD')
C      OPEN (1,FILE='VLPRD306.DAT',STATUS='OLD')
C      OPEN (1,FILE='VLPRD305.DAT',STATUS='OLD')
C      OPEN (1,FILE='VELPRD42.DAT',STATUS='OLD')
C      OPEN (1,FILE='VLPRD422.DAT',STATUS='OLD')
C      OPEN (1,FILE='VLPRD423.DAT',STATUS='OLD')
      OPEN (1,FILE='VELPRD66.DAT',STATUS='OLD')
```

```
C
      READ (1,*) NJ
      WRITE(*,*) NJ
      DO 5 J=1,NJ
        READ (1,*) JJ,R(JJ),U(JJ),V(JJ),KE(JJ),DE(JJ)
    5 CONTINUE
C
      READ (1,*) NJ
      WRITE(*,*) NJ
      DO 8 J=1,NJ
        READ (1,*) JJ,DUDX(JJ),DUDR(JJ),DVDX(JJ),DVDR(JJ)
C         READ (1,*) JJ,DUDX(JJ),DVDX(JJ),DUDR(JJ),DVDR(JJ)
    8 CONTINUE
C
      READ (1,*) NJ
      WRITE(*,*) NJ
      DO 9 J=1,NJ
        READ (1,*) JJ,PROD(JJ),DKDX(JJ),DEDX(JJ)
    9 CONTINUE
C
      READ (1,*) NJ2
      READ (1,*) UCL,USTAR,NU,DENSTY
      READ (1,*) ALPHA
C
      READ(1,*) NJ
      DO 19 J=1,NJ
        READ(1,*) JJ,ADV(JJ)
   19 CONTINUE
      READ(1,*) NJ
      WRITE(1,*) NJ
C
      CLOSE(1,STATUS='KEEP')
      IF (NJ.EQ.NJ2) WRITE(*,*) 'input complete'
      IF   (NJ.EQ.NJ2)   WRITE(7,*)   'input   complete   -
     1   VELPRD30.DAT'
C
      VSCSTY=NU*DENSTY
      RHO=DENSTY
C
      CALL GRID
C
C
C      DO 891 J=1,NJM1
C        IF (J.NE.NJM1) KE(J)=2.*KE(J)
C        IF (J.NE.NJM1) DE(J)=2.*DE(J)
C 891  CONTINUE
C
      IF (NJ.GT.MAXNJ) STOP
      WRITE(*,*)
      WRITE(*,*) '  NJ ',NJ
C
      EDYVIS(1)=DENSTY*CMU*KE(1)*KE(1)/DE(1)
      EDYVIS(NJ)=0.
```

```
      DO 13 J=2,NJM1
        EDYVIS(J)=DENSTY*CMU*KE(J)*KE(J)/DE(J)
   13 CONTINUE
C
      DO 6 I=1,20
        CALL PROPS
    6 CONTINUE
C
C-------print out initial data and grid information
C
      HEADU=' U-VELOCITY FIELD '
      HEADV=' V-VELOCITY FIELD '
      HEADK='  KINETIC ENERGY  '
      HEADD=' DISSIPATION RATE '
C
C      CALL PRINTT(NJ,MAXNJ,R,U,HEADU)
C      CALL PRINTT(NJ,MAXNJ,R,V,HEADV)
C
C-------main calculation loop---------
C
      RESORE=0.0
      RESORK=0.0
      WRITE (7,1110) JMON
      WRITE (*,1110) JMON
      NITER = 0
      CHCK='Y'
  200 CONTINUE
      NITER=NITER+1
C
      CALL PROPS
      CALL CALCDE
      CALL CALCKE
C
      IF (MOD(NITER,100).EQ.0) WRITE (7,1100) NITER,RESORK,
     1 RESORE,KE(JMON),DE(JMON),EDYVIS(JMON)
      IF (MOD(NITER,1).EQ.0) WRITE (*,1100) NITER,RESORK,
     1 RESORE,KE(JMON),DE(JMON),EDYVIS(JMON)
      IF (MOD(NITER,PRNNUM).NE.0) GO TO 300
      CALL PRINTT(NJ,MAXNJ,R,KE,HEADK)
      CALL PRINTT(NJ,MAXNJ,R,DE,HEADD)
      WRITE (7,1110) JMON
      WRITE (*,1110) JMON
  300 CONTINUE
C-------termination tests-------
      SORCE=AMAX1(RESORK,RESORE)
C      IF (NITER.EQ.75.AND.SORCE.GT.1.0E05*SORMAX) GO TO 400
      IF (NITER.EQ.MAXIT) GO TO 400
      IF (SORCE.GT.SORMAX) GO TO 200
  400 CONTINUE
C-------final operations-------
      WRITE(7,1100) NITER,RESORK,RESORE,KE(JMON)
     1    ,DE(JMON),EDYVIS(JMON)
      CALL PRINTT(NJ,MAXNJ,R,KE,HEADK)
```

```
      CALL PRINTT(NJ,MAXNJ,R,DE,HEADD)
 1110 FORMAT(/,'  The monitoring location is',I3,//
     1,' iteration   Res.Sor.KE    Res.Sor.DE       KE(jmon)
     1  DE(jmon)
     2   EDYVIS')
 1100 FORMAT(2X,I5,4X,5(E11.4,2X))
      CLOSE (7,STATUS='KEEP')
C
      STOP
      END
C
C-------subroutine grid generates the necessary geometric
C       quantities--
C-------for a Practice B type of grid (Patankar chapter 4)--
C
      SUBROUTINE GRID
C
C-------declare variables-------
C
      REAL*8 RIN,ROUT,DRNP,DRPS,R,RC,DR,RAD,SNS,ALPHA
      INTEGER NJ,NJP1,NJM1,JSTEP,JSTP1,JSTM1,XY,NUMSTP
      INTEGER MAXNJ,JMON,MAXIT,PRNNUM,NSWPK,NSWPD,NITER
      COMMON/GEOM/RIN,RAD,NJ,NJP1,NJM1,NUMSTP,JSTEP,
     1      JSTP1,JSTM1,
     1          SNS(500),DRNP(500),DRPS(500),R(500),RC(500),
     1      XY,MAXNJ,
C
C-------calculate geometric quantities-------
C
      IF (NJ.GT.MAXNJ) WRITE(*,*) ' ARRAY OVERFLOW -
     1   INCREASE MAXNJ'
      IF (NJ.GT.MAXNJ) RETURN
C
      NJP1=NJ+1
      NJM1=NJ-1
C
      SNS(1)=(R(2)-R(1))/2
      DO 7 J=2,NJM1
        SNS(J)=(R(J+1)-R(J))/2+(R(J)-R(J-1))/2
    7 CONTINUE
      SNS(NJ)=(R(NJ)-R(NJM1))/2
C
      RC(1)=SNS(1)
      DO 9 J=2,NJM1
        RC(J)=R(J)+(R(J+1)-R(J))/2
    9 CONTINUE
      RC(NJ)=R(NJ)
C
      DRPS(1)=0.0
      DRNP(NJ)=0.0
      DO 20 J=1,NJM1
        DRNP(J)=R(J+1)-R(J)
        DRPS(J+1)=DRNP(J)
```

```
  20  CONTINUE
C
      RETURN
      END
C
C-------subroutine for printing output-------
C
      SUBROUTINE PRINTT(NJ,MAXNJ,R,PHI,HEAD)
C
      REAL*8 R,PHI
      INTEGER START,END,NJ,MAXNJ
      CHARACTER*18 HEAD
      DIMENSION PHI(MAXNJ),R(MAXNJ)
C
      WRITE (7,10)
      WRITE (7,11) HEAD
      START=1
C
C-------main printing loop-------
C
      DO 110 J=NJ,1,-1
        WRITE(7,13) J,PHI(J),R(J)
 110  CONTINUE
C-------format statements-------
  10  FORMAT (' ',///)
  11  FORMAT (1X,30('-'),A18,30('-')/)
  13  FORMAT(1X,I3,1X,1(E12.4,1X),F9.5)
C
      RETURN
      END
C
C-------subroutine calcke calculates the kinetic energy
C-------of turbulence field from the PDE for ke-------
C
      SUBROUTINE CALCKE
C
C-------declare variables-------
C
      REAL*8 PROD2,UV,U2,V2,W2,U2MV2,RT
      REAL*8 ZERO,DIFF,DFN,DFS,EFVISN,EFVISS,FN,FS
      INTEGER NJM2
      REAL*8 RIN,ROUT,DRNP,DRPS,R,RC,DR,RAD,SNS,ALPHA
      REAL*8 DE,KE,U,V,VSCSTY,DENSTY,EDYVIS,PROD,ADV,
     1    UCL,USTAR,NU,RHO,DUDX,DUDR,DVDX,DVDR,DKDX,DEDX
      REAL*8 SIGMAK,SIGMAE,CMU,CE1,CE2,C3,F1,F2,F3,FMU,C4,C5
      REAL*8 AP,AS,AN,B,SORCE,SC,SP,GREAT,PI
      REAL RESORE,RESORK,SORMAX,URFK,URFD,URFEV
      INTEGER NJ,NJP1,NJM1,JSTEP,JSTP1,JSTM1,XY,NUMSTP
      INTEGER MAXNJ,JMON,MAXIT,PRNNUM,NSWPK,NSWPD,NITER
      CHARACTER*18 HEADU,HEADV,HEADK,HEADD
      CHARACTER*80 DUM
      CHARACTER*1 CHCK
      COMMON/PRMTVE/DE(500),KE(500),U(500),V(500),
```

```
     1      EDYVIS(500),
     1   VSCSTY,DENSTY,GREAT,PI,USTAR,RHO,UCL,DUDX(500),
     1   DUDR(500),DVDX(500),DVDR(500),DKDX(500),DEDX(500),
     1   PROD(500),ADV(500),ALPHA
      COMMON/TURB/CMU,CE1,CE2,C3,SIGMAK,SIGMAE,FMU,F1,F2,
     1      F3,C4,C5
      COMMON/PROB/NSWPK,NSWPD,URFK,URFD,URFEV,SORCE,RESORK,
     1      RESORE
      COMMON/GEOM/RIN,RAD,NJ,NJP1,NJM1,NUMSTP,JSTEP,
     1      JSTP1,JSTM1,
     1          SNS(500),DRNP(500),DRPS(500),R(500),RC(500),
     1      XY,MAXNJ,
      COMMON/CVFORM/AS(500),AN(500),AP(500),B(500),SP(500)
C
      NJM2=NJM1-1
      ZERO=0.000000000000000
      DO 2 J=2,NJM1
C
C-------calculation of areas and volume-------
C
      AREAN=RC(J)
      AREAS=RC(J-1)
      VOL=SNS(J)
C
C-------calculation of the convection terms-------
C
      FN=(((R(J+1)-RC(J))*V(J)+(RC(J)-R(J))
     1   *V(J+1))/DRNP(J))*AREAN*DENSTY
      FS=(((R(J)-RC(J-1))*V(J-1)+(RC(J-1)-R(J-1))
     1   *V(J))/DRPS(J))*AREAS*DENSTY
C      FN=0.
C      FS=0.
C
C-------calculation of the diffusion terms-------
C
C  uniform grid in axial direction, non-uniform in radial
      EFVISN=VSCSTY+((R(J+1)-RC(J))*EDYVIS(J)/SIGMAK+
     1   (RC(J)-R(J))
     1   *EDYVIS(J+1)/SIGMAK)/DRNP(J)
      EFVISS=VSCSTY+((R(J)-RC(J-1))*EDYVIS(J-1)/SIGMAK+
     1   (RC(J-1)-R(J-1))
     1   *EDYVIS(J)/SIGMAK)/DRPS(J)
C
      DFN=EFVISN*AREAN/DRNP(J)
      DFS=EFVISS*AREAS/DRPS(J)
C
C-------source term linerarization-------
C
C  NT Model
C        RT=KE(J)*KE(J)/(VSCSTY/DENSTY*DE(J))
C                      FMU=(1.-EXP(-(RAD-R(J))*USTAR*DENSTY/
C       1               VSCSTY/26.))**2
C        FMU=FMU*(1.+4.1/(RT**0.75))
```

```
C  LSH Model
      FMU=1.-EXP(-C3*(RAD-R(J))*USTAR*DENSTY/VSCSTY*
     1   DABS(1.-C5*ALPHA*VSCSTY/DENSTY/(USTAR**3.)))
C  Hoffmann Model
C        FMU=EXP(-1.75/(1.+RT/50.))
C
      UV=-EDYVIS(J)/DENSTY*(DUDR(J)+DVDX(J))
C      U2=2.*EDYVIS(J)/DENSTY*DUDX(J)-2./3.*KE(J)
C      V2=2.*EDYVIS(J)/DENSTY*DVDR(J)-2./3.*KE(J)
C      UV=0.26*KE(J)-0.25
C      FMU=2.*FMU
C      IF (FMU.GT.1.0) FMU=1.0
C      FMU=1.
C      UV=FMU*(0.28*KE(J)-0.25)
C      U2=1.06*KE(J)-0.3
C      V2=0.34*KE(J)-0.18
C      U2=1.06*KE(J)
C      V2=0.34*KE(J)
      U2MV2=0.45*KE(J)-0.
C
C      PROD2=-UV*DUDR(J)-(U2-V2)*DUDX(J)
      PROD2=-UV*(DUDR(J)+DVDX(J))-U2MV2*DUDX(J)
C
      SP(J)=-DENSTY*DE(J)
C      SC=DENSTY*PROD(J)
      SC=PROD2*DENSTY
C
      SP(J)=SP(J)-DMAX1(+DENSTY*(U(J)*DKDX(J)+
     1      KE(J)*DUDX(J)),ZERO)
      SC=SC+DMAX1(-DENSTY*(U(J)*DKDX(J)+
     1      KE(J)*DUDX(J)),ZERO)
C      SP(J)=SP(J)-DENSTY*DMAX1(-ADV(J),ZERO)
C      SC=SC+DENSTY*DMAX1(+ADV(J),ZERO)
C
C-------calculate CV Formulation coefficients-------
C-------using the power-law scheme--------
C
C
      AN(J)=DFN*DMAX1(ZERO,(1.-0.1*DABS(FN/DFN))**5.)+
     1      DMAX1(-FN,ZERO)
      AS(J)=DFS*DMAX1(ZERO,(1.-0.1*DABS(FS/DFS))**5.)+
     1      DMAX1(FS,ZERO)
C
      B(J)=SC*VOL*0.5*(RC(J)+RC(J-1))
      SP(J)=SP(J)*VOL/KE(J)*0.5*(RC(J)+RC(J-1))
C
    2 CONTINUE
C
C-------modify for north and south Dirichlet boundary-------
C
C      AN(2)=0.
      AS(2)=0.
C      B(2)=KE(1)
```

```
C      AP(2)=1.
C
      AN(NJM1)=0.
      AS(NJM1)=0.
      B(NJM1)=KE(NJM1)
      AP(NJM1)=1.
C
      RESORK=0.0
C
C-------source residual calculations-------
C
      DO 40 J=2,NJM2
C
        AP(J)=AN(J)+AS(J)-SP(J)
        RSIDUL=AN(J)*KE(J+1)+AS(J)*KE(J-1)+B(J)-AP(J)*KE(J)
        RESORK=RESORK+ABS(RSIDUL)
C-------under-relaxation--------
        AP(J)=AP(J)/URFK
        B(J)=B(J)+(1.-URFK)*AP(J)*KE(J)
C
   40 CONTINUE
C
C-------call the line solver--------
C
      DO 10 K=1,NSWPK
        CALL LNSOLV(KE)
   10 CONTINUE
C
      RETURN
      END
C
C-------subroutine calcde calculates the dissipation rate of
C-------turbulence kinetic energy from the PDE for epsilon--
C
      SUBROUTINE CALCDE
C
C-------declare variables-------
C
      REAL*8 UV,U2,V2,W2,PROD2,INTMED,U2MV2,RT
      REAL*8 ZERO,DIFF,DFN,DFS,EFVISN,EFVISS,FN,FS
      INTEGER NJM2
      REAL*8 RIN,ROUT,DRNP,DRPS,R,RC,DR,RAD,SNS,ALPHA
      REAL*8 DE,KE,U,V,VSCSTY,DENSTY,EDYVIS,PROD,ADV,
     1    UCL,USTAR,NU,RHO,DUDX,DUDR,DVDX,DVDR,DKDX,DEDX
      REAL*8 SIGMAK,SIGMAE,CMU,CE1,CE2,C3,F1,F2,F3,FMU,C4,C5
      REAL*8 AP,AS,AN,B,SORCE,SC,SP,GREAT,PI
      REAL RESORE,RESORK,SORMAX,URFK,URFD,URFEV
      INTEGER NJ,NJP1,NJM1,JSTEP,JSTP1,JSTM1,XY,NUMSTP
      INTEGER MAXNJ,JMON,MAXIT,PRNNUM,NSWPK,NSWPD,NITER
      CHARACTER*18 HEADU,HEADV,HEADK,HEADD
      CHARACTER*80 DUM
      CHARACTER*1 CHCK
      COMMON/PRMTVE/DE(500),KE(500),U(500),V(500),
```

```
     1      EDYVIS(500),
     1      VSCSTY,DENSTY,GREAT,PI,USTAR,RHO,UCL,DUDX(500),
     1              DUDR(500),DVDX(500),DVDR(500),DKDX(500),
     1      DEDX(500),
     1      PROD(500),ADV(500),ALPHA
      COMMON/TURB/CMU,CE1,CE2,C3,SIGMAK,SIGMAE,FMU,F1,F2,
     1      F3,C4,C5
      COMMON/PROB/NSWPK,NSWPD,URFK,URFD,URFEV,SORCE,RESORK,
     1      RESORE
      COMMON/GEOM/RIN,RAD,NJ,NJP1,NJM1,NUMSTP,JSTEP,JSTP1,
     1      JSTM1,
     1       SNS(500),DRNP(500),DRPS(500),R(500),RC(500),XY,
     1      MAXNJ,
      COMMON/CVFORM/AS(500),AN(500),AP(500),B(500),SP(500)
C
      NJM2=NJM1-1
      ZERO=0.00000000000000
      DO 2 J=2,NJM1
C
C-------calculation of areas and volume-------
C
      AREAN=RC(J)
      AREAS=RC(J-1)
      VOL=SNS(J)
C
C-------calculation of the convection terms-------
C
      FN=(((R(J+1)-RC(J))*V(J)+(RC(J)-R(J))
     1   *V(J+1))/DRNP(J))*AREAN*DENSTY
      FS=(((R(J)-RC(J-1))*V(J-1)+(RC(J-1)-R(J-1))
     1   *V(J))/DRPS(J))*AREAS*DENSTY
C      FN=0.
C      FS=0.
C
C-------calculation of the diffusion terms-------
C
C  uniform grid in axial direction, non-uniform in radial
      EFVISN=VSCSTY+((R(J+1)-RC(J))*EDYVIS(J)/SIGMAE+
     1   (RC(J)-R(J))
     1   *EDYVIS(J+1)/SIGMAE)/DRNP(J)
      EFVISS=VSCSTY+((R(J)-RC(J-1))*EDYVIS(J-1)/SIGMAE+
     1    (RC(J-1)-R(J-1))
     1   *EDYVIS(J)/SIGMAE)/DRPS(J)
C
      DFN=EFVISN*AREAN/DRNP(J)
      DFS=EFVISS*AREAS/DRPS(J)
C
C-------calculate the net source terms-------
C
      INTMED=KE(J)*KE(J)*DENSTY/(VSCSTY*DE(J))
C NT Model
      IF (INTMED.LT.20.) THEN
        F2=1.-0.3*EXP(-INTMED*INTMED/(6.5*6.5))
```

```
        F2=F2*(1.-EXP(-(RAD-R(J))*USTAR*DENSTY
     1     /VSCSTY/6.))**2.
      ELSE
        F2=(1.-EXP(-(RAD-R(J))*USTAR*DENSTY
     1     /VSCSTY/6.))**2
      ENDIF
C LSH Model
C      F2=1.-2./9.*EXP(-INTMED*INTMED/36.)
C Hoffmann Model
C      F2=1.-0.3*EXP(-INTMED*INTMED)
C
C  NT Model
C        RT=KE(J)*KE(J)/(VSCSTY/DENSTY*DE(J))
C       FMU=(1.-EXP(-(RAD-R(J))*USTAR*DENSTY/VSCSTY/26.))**2
C        FMU=FMU*(1.+4.1/(RT**0.75))
C  LSH Model
        FMU=1.-EXP(-C3*(RAD-R(J))*USTAR*DENSTY/VSCSTY*
     1      DABS(1.-C5*ALPHA*VSCSTY/DENSTY/(USTAR**3.)))
C  Hoffmann Model
C        FMU=EXP(-1.75/(1.+RT/50.))
C
      UV=-EDYVIS(J)/DENSTY*(DUDR(J)+DVDX(J))
C      U2=2.*EDYVIS(J)/DENSTY*DUDX(J)-2./3.*KE(J)
C      V2=2.*EDYVIS(J)/DENSTY*DVDR(J)-2./3.*KE(J)
C      UV=0.26*KE(J)-0.25
C      FMU=2.*FMU
C      IF (FMU.GT.1.0) FMU=1.0
C      FMU=1.
C      UV=FMU*(0.28*KE(J)-0.25)
C      U2=1.06*KE(J)-0.3
C      V2=0.34*KE(J)-0.18
C      U2=1.06*KE(J)
C      V2=0.34*KE(J)
      U2MV2=0.45*KE(J)-0.
C
C      PROD2=-UV*DUDR(J)-2.5*(U2-V2)*DUDX(J)
      PROD2=-UV*(DUDR(J)+DVDX(J))-2.30000*U2MV2*DUDX(J)
C      PROD2=-UV*DUDR(J)-U2MV2*DUDX(J)
C
      SP(J)=-DENSTY*CE2*F2*DE(J)*DE(J)/KE(J)
C      SC=+DENSTY*CE1*DE(J)/KE(J)*ADV(J)
C      SC=+DENSTY*CE1*DE(J)/KE(J)*PROD(J)
      SC=+DENSTY*CE1*DE(J)/KE(J)*PROD2
C
      SP(J)=SP(J)-DMAX1(+DENSTY*(U(J)*DEDX(J)+
     1      DE(J)*DUDX(J)),ZERO)
      SC=SC+DMAX1(-DENSTY*(U(J)*DEDX(J)+
     1      DE(J)*DUDX(J)),ZERO)
C
C-------calculate CV Formulation coefficients-------
C-------using the power-law scheme--------
C
      AN(J)=DFN*DMAX1(ZERO,(1.-0.1*DABS(FN/DFN))**5.)+
```

```
     1       DMAX1(-FN,ZERO)
      AS(J)=DFS*DMAX1(ZERO,(1.-0.1*DABS(FS/DFS))**5.)+
     1       DMAX1(FS,ZERO)
C
      B(J)=SC*VOL*0.5*(RC(J)+RC(J-1))
      SP(J)=SP(J)*VOL/DE(J)*0.5*(RC(J)+RC(J-1))
C
    2 CONTINUE
C
C-------modify for north and south Dirichlet boundary-------
C
C      AN(2)=0.
      AS(2)=0.
C      B(2)=DE(1)
C      AP(2)=1.
C
      AN(NJM1)=0.
      AS(NJM1)=0.
      B(NJM1)=DE(NJM1)
      AP(NJM1)=1.
C
      RESORE=0.0
C
C-------source residual calculations-------
C
      DO 40 J=2,NJM2
C
        AP(J)=AN(J)+AS(J)-SP(J)
        RSIDUL=AN(J)*DE(J+1)+AS(J)*DE(J-1)+B(J)-AP(J)*DE(J)
        RESORE=RESORE+ABS(RSIDUL)
C-------under-relaxation--------
        AP(J)=AP(J)/URFD
        B(J)=B(J)+(1.-URFD)*AP(J)*DE(J)
C
   40 CONTINUE
C
C-------call the line solver--------
C
      DO 10 K=1,NSWPD
        CALL LNSOLV(DE)
   10 CONTINUE
C
      RETURN
      END
C
C-------subroutine props calculates the turbulent (or eddy)
C       viscosity
C-------from the Kolmogorov-Prandtl relation-------
C
      SUBROUTINE PROPS
C
C-------declare variables-------
C
```

```
      REAL*8 RT,OLD
      REAL*8 RIN,ROUT,DRNP,DRPS,R,RC,DR,RAD,SNS,ALPHA
      REAL*8 DE,KE,U,V,VSCSTY,DENSTY,EDYVIS,PROD,ADV,
     1    UCL,USTAR,NU,RHO,DUDX,DUDR,DVDX,DVDR,DKDX,DEDX
      REAL*8 SIGMAK,SIGMAE,CMU,CE1,CE2,C3,F1,F2,F3,FMU,C4,C5
      REAL*8 AP,AS,AN,B,SORCE,SC,SP,GREAT,PI
      REAL RESORE,RESORK,SORMAX,URFK,URFD,URFEV
      INTEGER NJ,NJP1,NJM1,JSTEP,JSTP1,JSTM1,XY,NUMSTP
      INTEGER MAXNJ,JMON,MAXIT,PRNNUM,NSWPK,NSWPD,NITER
      CHARACTER*18 HEADU,HEADV,HEADK,HEADD
      CHARACTER*80 DUM
      CHARACTER*1 CHCK
      COMMON/PRMTVE/DE(500),KE(500),U(500),V(500),
     1      EDYVIS(500),
     1      VSCSTY,DENSTY,GREAT,PI,USTAR,RHO,UCL,DUDX(500),
     1              DUDR(500),DVDX(500),DVDR(500),DKDX(500),
     1      DEDX(500),
     1      PROD(500),ADV(500),ALPHA
      COMMON/TURB/CMU,CE1,CE2,C3,SIGMAK,SIGMAE,FMU,F1,F2,
     1      F3,C4,C5
      COMMON/PROB/NSWPK,NSWPD,URFK,URFD,URFEV,SORCE,RESORK,
     1      RESORE
      COMMON/GEOM/RIN,RAD,NJ,NJP1,NJM1,NUMSTP,JSTEP,JSTP1,
     1      JSTM1,
     1       SNS(500),DRNP(500),DRPS(500),R(500),RC(500),XY,
     1      MAXNJ,
C
      DO 20 J=2,NJM1
        OLD=EDYVIS(J)
C
C  NT Model
        RT=KE(J)*KE(J)/(VSCSTY/DENSTY*DE(J))
        FMU=(1.-EXP(-(RAD-R(J))*USTAR*DENSTY/VSCSTY/26.))**2
        FMU=FMU*(1.+4.1/(RT**0.75))
C  LSH Model
C        FMU=1.-EXP(-C3*(RAD-R(J))*USTAR*DENSTY/VSCSTY*
C     1      DABS(1.-C5*ALPHA*VSCSTY/DENSTY/(USTAR**3.)))
C  Hoffmann Model
C        FMU=EXP(-1.75/(1.+RT/50.))
C
C
        EDYVIS(J)=URFEV*DENSTY*CMU*FMU*KE(J)*KE(J)/DE(J)
     1                 +(1.-URFEV)*OLD
C
  20  CONTINUE
C
      RETURN
      END
C
C----this subroutine solves the set of algaebraic equations
C-------using an ADI Routine--------
C
      SUBROUTINE LNSOLV(PHI)
```

```
C
C-------declare variables-------
C
      REAL*8 PHI,Q,M
      REAL*8 RIN,ROUT,DRNP,DRPS,R,RC,DR,RAD,SNS,ALPHA
      REAL*8 AP,AS,AN,B,SORCE,SC,SP,GREAT,PI
      REAL RESORE,RESORK,SORMAX,URFK,URFD,URFEV
      INTEGER NJ,NJP1,NJM1,JSTEP,JSTP1,JSTM1,XY,NUMSTP,NJM2
      INTEGER MAXNJ,JMON,MAXIT,PRNNUM,NSWPK,NSWPD,NITER,NJM3
      COMMON/GEOM/RIN,RAD,NJ,NJP1,NJM1,NUMSTP,JSTEP,JSTP1,
     1      JSTM1,
     1       SNS(500),DRNP(500),DRPS(500),R(500),RC(500),XY,
     1      MAXNJ,
      COMMON/CVFORM/AS(500),AN(500),AP(500),B(500),SP(500)

      DIMENSION PHI(MAXNJ),M(500),Q(500)
C
C-------TDMA south to north-------
C
      NJM2=NJ-2
      M(2)=AN(2)/AP(2)
      Q(2)=B(2)/AP(2)
      DO 20 J=3,NJM1
        M(J)=AN(J)/(AP(J)-AS(J)*M(J-1))
        IF (J.EQ.NJM1) M(J)=0.
        Q(J)=(B(J)+AS(J)*Q(J-1))/(AP(J)-AS(J)*M(J-1))
   20 CONTINUE
      PHI(NJM1)=Q(NJM1)
      DO 30 J=NJM2,2,-1
        PHI(J)=M(J)*PHI(J+1)+Q(J)
   30 CONTINUE
C
C-------TDMA north to south-------
C
      M(NJM1)=AS(NJM1)/AP(NJM1)
      Q(NJM1)=B(NJM1)/AP(NJM1)
      DO 25 J=NJM2,2,-1
        M(J)=AS(J)/(AP(J)-AN(J)*M(J+1))
        IF (J.EQ.2) M(J)=0.
        Q(J)=(B(J)+AN(J)*Q(J+1))/(AP(J)-AN(J)*M(J+1))
   25 CONTINUE
      PHI(2)=Q(2)
      DO 35 J=3,NJM1
        PHI(J)=M(J)*PHI(J-1)+Q(J)
   35 CONTINUE
C
      RETURN
      END
```

```
      PROGRAM GRDVEL
C
C              calculate the grid and velocity field for
C          diffuser
C
      REAL*8 LENGTH,RIN,ROUT,U,V,DX,DR,VSCSTY,DENSTY
     *       ,DUDX,DUDR,DVDX,DVDR,PROD,DKDX,DEDX,KE,DE
      REAL*8 SEW,SNS,DXPW,DXEP,DRNP,DRPS,X,R,RC
     *       ,UCL,USTAR,NU,RAD,RHO,ALPHA,RR(180)
      REAL*8 B1,B2,C,D,TS
      REAL*8 DUM1
      INTEGER NI,NJ,NIP1,NIM1,NJP1,NJM1,JSTEP,NUMSTP
     *        ,JSTP1,JSTM1,MAXNI,MAXNJ,M,NJNJ,NJ2,NJM2
      CHARACTER*20 ENDDAT
      CHARACTER*12 FILENM
      COMMON/VEL/U(180),V(180),DUDX(180),DVDX(180),
     *  DUDR(180),DVDR(180),KE(180),DE(180),
     *  PROD(180),DKDX(180),DEDX(180)
      COMMON/BC/LENGTH,RIN,ROUT,UCL(26),USTAR(26),VSCSTY,NU
     *       ,DENSTY,RHO,ALPHA(26)
      COMMON/GEOM/NI,NIP1,NIM1,NJ,NJP1,NJM1,NUMSTP,
     1      JSTEP,MAXNI,
     * MAXNJ,JSTP1,JSTM1,SEW(26),SNS(180),DXPW(26),DXEP(26),
     * DRNP(180),DRPS(180),X(26),R(180),RC(180)
      COMMON/EMP/B1(26),B2(26),C(26),TS(26),D(26)
C
      MAXNI=26
      MAXNJ=180
C
      DO 667 J=1,MAXNJ
        U(J)=0.
        V(J)=0.
        DUDX(J)=0.
        DVDX(J)=0.
        DUDR(J)=0.
        DVDR(J)=0.
        PROD(J)=0.
        DKDX(J)=0.
        DEDX(J)=0.
        KE(J)=0.
        DE(J)=0.
        RC(J)=0.
        R(J)=0.
  667 CONTINUE
C
C
C----------input all appropriate data----------
C
      OPEN(1,FILE='GRID_VEL.DAT',STATUS='OLD')
      READ(1,*) JSTEP,NUMSTP,LENGTH,RIN,ROUT
      READ(1,*) VSCSTY,NU,DENSTY
      RHO=DENSTY
      NI=NUMSTP+1
```

```
      DO 10 I=1,NI
        READ(1,*) M,UCL(M),USTAR(M),ALPHA(M)
        READ(1,*) M,B1(M),B2(M),C(M),D(M),TS(M)
   10 CONTINUE
      READ(1,*) ENDDAT
      CLOSE(1,STATUS='KEEP')
      WRITE(*,*) ENDDAT
C
      OPEN(1,FILE='VELPRD30.DAT',STATUS='OLD')
      READ (1,*) NJNJ
      WRITE(*,*) NJNJ
      DO 105 J=1,NJNJ
      READ (1,*) JJ,RR(JJ),U(JJ),V(JJ),KE(JJ),DE(JJ)
  105 CONTINUE
C
      READ (1,*) NJNJ
      WRITE(*,*) NJNJ
      DO 106 J=1,NJNJ
        READ (1,*) JJ,DUDX(JJ),DUM1,DVDX(JJ),DVDR(JJ)
  106 CONTINUE
C
      READ (1,*) NJNJ
      WRITE(*,*) NJNJ
      DO 107 J=1,NJNJ
        READ (1,*) JJ,PROD(JJ),DKDX(JJ),DEDX(JJ)
  107 CONTINUE
C
      READ (1,*) NJ2
C
      CLOSE (1,STATUS='KEEP')
      IF (NJNJ.EQ.NJ2) WRITE(*,*) 'input complete'
C
C----------calculate grid for interpolations----------
C
      CALL GRID1(NJNJ,RR)
      WRITE(*,*) ' NJ=',NJ,NJNJ
      DO 443 J=NJNJ,1,-1
        DUDX(2*J-1)=DUDX(J)
        DVDX(2*J-1)=DVDX(J)
        DVDR(2*J-1)=DVDR(J)
        PROD(2*J-1)=PROD(J)
        DKDX(2*J-1)=DKDX(J)
        DEDX(2*J-1)=DEDX(J)
        KE(2*J-1)=KE(J)
        DE(2*J-1)=DE(J)
        V(2*J-1)=V(J)
  443 CONTINUE
C
      CALL INTERP(MAXNI,MAXNJ,NJ,NJNJ,R,RR,V,RC)
      CALL INTERP(MAXNI,MAXNJ,NJ,NJNJ,R,RR,DUDX,RC)
      CALL INTERP(MAXNI,MAXNJ,NJ,NJNJ,R,RR,DVDX,RC)
      CALL INTERP(MAXNI,MAXNJ,NJ,NJNJ,R,RR,DVDR,RC)
      CALL INTERP(MAXNI,MAXNJ,NJ,NJNJ,R,RR,PROD,RC)
```

```
      CALL INTERP(MAXNI,MAXNJ,NJ,NJNJ,R,RR,DKDX,RC)
      CALL INTERP(MAXNI,MAXNJ,NJ,NJNJ,R,RR,DEDX,RC)
      CALL INTERP(MAXNI,MAXNJ,NJ,NJNJ,R,RR,KE,RC)
      CALL INTERP(MAXNI,MAXNJ,NJ,NJNJ,R,RR,DE,RC)
C
C      OPEN(8,FILE='C:\GREG\GV1.PRN',STATUS='UNKNOWN')
C      DO 444 J=1,NJ
C        WRITE(8,*) R(J),KE(J),DE(J)
C  444 CONTINUE
C      CLOSE(8,STATUS='KEEP')
C
C----------calculate U, dU/dr----------
C
      CALL UVEL
        DO 333 J=2,NJM1
          DUDR(J)=(U(J+1)*DRPS(J)**2.+(DRNP(J)**2.-
     1      DRPS(J)**2.)*U(J)-U(J-1)*DRNP(J)**2.)/
     1      (DRPS(J)*DRNP(J)*(DRNP(J)+DRPS(J)))
  333   CONTINUE
C
C
C----------output all appropriate data----------
C
C     FILENAME=Grid_Vel_[numstp][jstep].OUT
      FILENM='30GV.OUT'
      OPEN(7,FILE=FILENM,STATUS='UNKNOWN')
C
      NJM2=NJ-2
      WRITE(7,*) NJM1
      DO 205 J=1,NJM2
        WRITE(7,55) J,R(J),U(J),V(J),KE(J),DE(J)
  205 CONTINUE
        WRITE(7,55) NJM1,R(NJ),U(NJ),V(NJ),KE(NJ),DE(NJ)
C
      WRITE(7,*) NJM1
      DO 206 J=1,NJM2
        WRITE(7,56) J,DUDX(J),DUDR(J),DVDX(J),DVDR(J)
  206 CONTINUE
        WRITE(7,56) NJM1,DUDX(NJ),DUDR(NJ),DVDX(NJ),DVDR(NJ)
C
      WRITE(7,*) NJM1
      DO 207 J=1,NJM2
        WRITE(7,57) J,PROD(J),DKDX(J),DEDX(J)
  207 CONTINUE
        WRITE(7,57) NJM1,PROD(NJ),DKDX(NJ),DEDX(NJ)
C
      WRITE(7,*) NJM1
      WRITE(7,*) UCL(11),USTAR(11),NU,DENSTY
      WRITE(7,*) ALPHA(11)
      WRITE(7,*) NJM1
C
      CLOSE (7,STATUS='KEEP')
C
```

```
  55  FORMAT(' ',I3,5(',',F10.5))
  56  FORMAT(' ',I3,4(',',F10.5))
  57  FORMAT(' ',I3,3(',',F10.5))
      STOP
      END
C
C----------subroutine grid----------
C
      SUBROUTINE GRID1(NJNJ,RR)
C
C-------subroutine grid generates the necessary geometric
C       quantities--
C-------for a Practice A type of grid (Patankar chapter 4)--
C
C-------declare variables-------
C
      REAL*8 LENGTH,RIN,ROUT,U,V,DX,DR,VSCSTY,DENSTY
     *      ,DUDX,DUDR,DVDX,DVDR,PROD,DKDX,DEDX,KE,DE
      REAL*8 SEW,SNS,DXPW,DXEP,DRNP,DRPS,X,R,RC
     *      ,UCL,USTAR,NU,RAD,RHO,ALPHA,RR(180)
      INTEGER NI,NJ,NIP1,NIM1,NJP1,NJM1,JSTEP,NUMSTP
     *       ,JSTP1,JSTM1,MAXNI,MAXNJ,M,NJNJ,NJ2,JJ,JJP1
      COMMON/BC/LENGTH,RIN,ROUT,UCL(26),USTAR(26),VSCSTY,NU
     *      ,DENSTY,RHO,ALPHA(26)
      COMMON/GEOM/NI,NIP1,NIM1,NJ,NJP1,NJM1,NUMSTP,
     1      JSTEP,MAXNI,
     * MAXNJ,JSTP1,JSTM1,SEW(26),SNS(180),DXPW(26),DXEP(26),
     * DRNP(180),DRPS(180),X(26),R(180),RC(180)
C
C-------calculate geometric quantities-------
C
      NJ=2*NJNJ-1
      IF (NI.GT.MAXNI) WRITE(7,*) ' ARRAY OVERFLOW -
     1  INCREASE MAXNI'
      IF (NJ.GT.MAXNJ) WRITE(7,*) ' ARRAY OVERFLOW -
     1  INCREASE MAXNJ'
      IF (NI.GT.MAXNI.OR.NJ.GT.MAXNJ) RETURN
C
      NIP1=NI+1
      NIM1=NI-1
      NIM2=NI-2
      NJP1=NJ+1
      NJM1=NJ-1
      JSTP1=JSTEP+1
      JSTP2=JSTEP+2
      JSTM1=JSTEP-1
      NJNJM1=NJNJ-1
C
      DX=LENGTH/FLOAT(NUMSTP)
      X(1)=0.0
      SEW(1)=DX/2.
      DO 5 I=2,NIM1
        X(I)=X(I-1)+DX
```

```
          SEW(I)=DX
    5   CONTINUE
        X(NI)=X(NIM1)+DX
        SEW(NI)=DX/2.
C
C
        SNS(1)=(RR(2)-RR(1))/2.
        DO 25 J=2,NJNJM1
          SNS(J)=(RR(J+1)-RR(J))/2.+(RR(J)-RR(J-1))/2.
   25   CONTINUE
        SNS(NJNJ)=(RR(NJNJ)-RR(NJNJM1))/2.
C
        RC(1)=SNS(1)
        DO 9 J=2,NJNJM1
          RC(J)=RR(J)+(RR(J+1)-RR(J))/2.
    9   CONTINUE
        RC(NJNJ)=RR(NJNJ)
C
C
        R(1)=RR(1)
        DO 17 J=1,NJNJM1
          JJ=2*J
          JJP1=JJ+1
          R(JJ)=RC(J)
          R(JJP1)=RR(J+1)
    17  CONTINUE
        WRITE(*,*) ' RADIUS=',R(NJ)
C
C
        SNS(1)=(R(2)-R(1))/2.
        DO 26 J=2,NJM1
          SNS(J)=(R(J+1)-R(J))/2.+(R(J)-R(J-1))/2.
   26   CONTINUE
        SNS(NJ)=(R(NJ)-R(NJM1))/2.
C
        RC(1)=SNS(1)
        DO 29 J=2,NJM1
          RC(J)=R(J)+(R(J+1)-R(J))/2.
   29   CONTINUE
        RC(NJ)=R(NJ)
C
        DRPS(1)=0.0
        DRNP(NJ)=0.0
        DO 20 J=1,NJM1
          DRNP(J)=R(J+1)-R(J)
          DRPS(J+1)=DRNP(J)
   20   CONTINUE
C
C
        DXPW(1)=0.0
        DXEP(NI)=0.0
        DO 10 I=1,NIM1
          DXEP(I)=X(I+1)-X(I)
```

```
         DXPW(I+1)=DXEP(I)
   10  CONTINUE
C
       RETURN
       END
C
C
C----------subroutine uvel----------
C
C
       SUBROUTINE UVEL
C
C-------subroutine uvel calculates the velocity field for
C        the conical
C-------diffuser flow using the empirical correlations that
C        fit the
C-------experimental data as closely as possible.--------
C
       REAL*8 LENGTH,RIN,ROUT,U,V,DX,DR,VSCSTY,DENSTY,KE,DE
     *       ,DUDX,DUDR,DVDX,DVDR,DELU,DELUP,PROD,DKDX,DEDX
       REAL*8 SEW,SNS,DXPW,DXEP,DRNP,DRPS,X,R,RC
     *       ,UCL,USTAR,NU,RAD,RHO,ALPHA,RRR
       REAL*8 B1,B2,C,D,TS,T,KSTAR,NKA,TAU,UKY,UNK
       REAL*8 UG(7),XX,DD,FF(7),RD1,RD2,YPLUS
       INTEGER NI,NJ,NIP1,NIM1,NJP1,NJM1,JSTEP,NUMSTP
     *        ,JSTP1,JSTM1,MAXNI,MAXNJ,M,CHECK,NJNJ,NJ2,I
       COMMON/VEL/U(180),V(180),DUDX(180),DVDX(180),
     *  DUDR(180),DVDR(180),KE(180),DE(180),
     *  PROD(180),DKDX(180),DEDX(180)
       COMMON/BC/LENGTH,RIN,ROUT,UCL(26),USTAR(26),VSCSTY,NU
     *       ,DENSTY,RHO,ALPHA(26)
       COMMON/GEOM/NI,NIP1,NIM1,NJ,NJP1,NJM1,NUMSTP,
     1       JSTEP,MAXNI,
     * MAXNJ,JSTP1,JSTM1,SEW(26),SNS(180),DXPW(26),DXEP(26),
     * DRNP(180),DRPS(180),X(26),R(180),RC(180)
       COMMON/EMP/B1(26),B2(26),C(26),TS(26),D(26)
C
C
       I=11
       RAD=0.072
       IF (I.EQ.1) THEN
C
C
         U(1)=UCL(1)
         U(NJ)=0.0
         V(1)=0.0
         V(NJ)=0.0
C
C-------calculate inlet profile (f.d.pipe flow)-------
C
C                          VAN DRIEST
       UG(1)=0.0
       UG(2)=0.2029225757
```

```
      UG(3)=-0.2029225757
      UG(4)=0.3707655928
      UG(5)=-0.3707655928
      UG(6)=0.4745539562
      UG(7)=-0.4745539562
C
      DO 10 J=2,NJM1
        YPLUS=(RAD-R(J))*USTAR(1)/NU
        IF (YPLUS.LE.60.0) THEN
          DO 11 M=1,7
            XX=YPLUS*UG(M)+YPLUS/2.
            DD=(1.-EXP(-XX/26.))
            FF(M)=2./(1.+SQRT(1.+4.*0.40*0.40*XX*XX*DD*DD))
   11     CONTINUE
          U(J)=YPLUS*USTAR(1)*(0.2089795918*FF(1)+
     1        0.1909150253*
     1             (FF(2)+FF(3))+0.1398526957*(FF(4)+FF(5))+
     1        0.06474248308*
     1    (FF(6)+FF(7)))
          U(J)=U(J)*1.03871
        ENDIF
C                                                 LOG LAW
        IF (YPLUS.GT.60.0.AND.YPLUS.LE.128.59) THEN
          U(J)=USTAR(1)*(1./0.41*DLOG(YPLUS)+6.0)
        ENDIF
C                                       COLES WAKE FUNCTION
        IF (YPLUS.GT.128.59) THEN
          RD1=1.-R(J)/RAD
          WAKE=1.+SIN((2.*RD1-1.)*3.141592654/2.)
          U(J)=USTAR(1)*(1./0.41*DLOG(YPLUS)+6.0)+(0.83-
     1           1./0.41*USTAR(1)/UCL(1))*WAKE
        ENDIF
   10 CONTINUE
C
      ELSE
C
C-------calculate U for the diffuser flow-------
C
      U(1)=UCL(I)
      U(NJ)=0.0
      V(1)=0.0
      V(NJ)=0.0
C
      DO 210 J=2,NJM1
        YPLUS=(RAD-R(J))*USTAR(I)/NU
      IF (YPLUS.LE.0.0) THEN
        U(J)=0.0
        V(J)=0.0
      ELSE
C                              KY VISCOUS SUBLAYER AND BUFFER
        IF(YPLUS.LE.30.0) THEN
          U(J)=USTAR(I)*D(I)*TANH(YPLUS/D(I))
        ENDIF
```

```
C
C                                    NAKAYAMA AND KOYAMA
        NKA=NU*ALPHA(I)/(USTAR(I)**3.)
        KSTAR=(0.4+0.6*NKA)/(1.+NKA)
        TAU=1.+NKA*YPLUS
        T=SQRT((1.+2.*TAU)/3.)
        UNK=USTAR(I)/KSTAR*(B1(I)*T**B2(I)*(T-TS(I))
     1  +DLOG((TS(I)+1.)*(T-1.)/((TS(I)-1.)*(T+1.))))
C
C                                     KY VELOCITY DEFECT
        UKY=UCL(I)-USTAR(I)*(C(I)*SQRT(1.+ALPHA(I)
     1  *RAD/(USTAR(I)**2))*((1.-(RAD-R(J))/RAD)**2.))
C
C
          IF(YPLUS.GT.30.0.AND.J.GE.19) U(J)=UNK
          IF(YPLUS.GT.30.0.AND.J.LE.18) U(J)=UKY
      ENDIF
  210 CONTINUE
C
      ENDIF
C
      RETURN
      END
C
C----------subroutine interp----------
C
      SUBROUTINE INTERP(MAXNI,MAXNJ,NJ,NJNJ,R,RR,PHI,RC)
C
      INTEGER MAXNJ,NJ,NJNJ,NJM4,NJNJM1,I,JJJ,K,MAXNI,NJM1
      REAL*8 RR(MAXNJ),R(MAXNJ),PHI(MAXNJ),RC(MAXNJ)
      REAL*8 C2,P2,L,X0,X1,X2,E,F,G,Z1(2)
C
      C2(L,X0,X1,X2) = (L-X1)*(L-X2)/(X0-X1)/(X0-X2)
      P2(L,X0,X1,X2,E,F,G)     =     C2(L,X0,X1,X2)*E     +
     1  C2(L,X1,X2,X0)*F+
     *  C2(L,X2,X0,X1)*G
C
      I=11
      NJM4=NJ-4
      NJM1=NJ-1
C
      DO 101 J=1,NJM4,2
        X0=R(J)
        X1=R(J+2)
        X2=R(J+4)
        E=PHI(J)
        F=PHI(J+2)
        G=PHI(J+4)
        PHI(J+1)=P2(R(J+1),X0,X1,X2,E,F,G)
  101 CONTINUE
        PHI(NJM1)=P2(RC(NJM1),X0,X1,X2,E,F,G)
C
      RETURN
```

Sample Data File: 'VELPRD30.DAT'

```
 21
  21        0.072       0.0000       0.0000    0.0000        0.00
  20        0.070       3.5744       0.1424    2.2811      230.87
  19        0.069       3.9188       0.1795    2.6427      238.20
  18        0.068       4.2275       0.1878    2.9301      249.12
  17        0.066       4.8123       0.2044    3.5020      255.07
  16        0.064       5.3888       0.2119    3.9387      268.86
  15        0.062       5.9696       0.2212    4.3447      273.52
  14        0.060       6.5579       0.2238    4.6224      275.87
  13        0.057       7.4562       0.2313    4.8859      263.85
  12        0.054       8.3729       0.2329    4.9337      243.82
  11        0.051       9.3066       0.2398    4.8984      215.27
  10        0.047      10.5994       0.2219    4.4829      183.98
   9        0.042      11.7533       0.1933    3.7275      136.68
   8        0.037      12.7769       0.1663    2.9076       95.32
   7        0.032      13.6701       0.1408    2.2431       60.60
   6        0.027      14.4330       0.1166    1.7391       35.49
   5        0.022      15.0655       0.0934    1.4433       27.22
   4        0.017      15.5676       0.0711    1.1609       21.64
   3        0.012      15.9394       0.0494    0.9786       17.81
   2        0.007      16.1809       0.0282    0.8315       15.86
   1        0.000      16.3000       0.0000    0.7685       13.88
21
  21      0.0000       0.0000   0.0000     0.0000
  20     63.0825    -825.3481   6.1165   -42.8035
  19     12.8659    -326.5261   5.9300   -22.6820
  18      6.3155    -303.2284   4.2877    -8.2667
  17      2.6843    -290.3393   3.5357    -6.0346
  16      0.7527    -289.3208   3.2914    -4.2018
  15     -0.6091    -292.2716   3.2492    -2.9857
  14     -1.6463    -296.2721   3.0030    -1.7959
  13     -2.7630    -302.4953   2.8324    -1.5105
  12     -2.4212    -308.4030   2.3826    -1.4248
  11     -5.4428    -316.3606   2.0695     0.5994
  10    -10.6513    -282.1216   1.2718     5.0317
   9    -10.1821    -217.7531   0.6962     5.5598
   8     -9.7659    -191.6811   0.3602     5.2479
   7     -9.4027    -165.6092   0.1200     4.9753
   6     -9.0925    -139.5372  -0.0357     4.7430
   5     -8.8353    -113.4652  -0.1224     4.5498
   4     -8.6311     -87.3932  -0.1502     4.3976
   3     -8.4799     -61.3213  -0.1362     4.2833
   2     -8.3818     -35.2493  -0.0885     4.2095
   1      0.0000       0.0000   0.0000     0.0000
21
  21        0.00        0.00        0.00
  20     200.354      3.9262      -382.4
  19     255.202      3.3528      -416.0
  18     295.886      2.8372      -480.1
```

```
  17   391.169     1.8288     -481.4
  16   434.304     1.1199     -541.2
  15   463.712     0.4818     -518.5
  14   455.067     0.3267     -505.0
  13   421.115     0.3237     -388.3
  12   357.929     0.3824     -245.3
  11   301.571     0.4347     -111.2
  10   223.443     0.5931     -59.11
   9   168.072     0.8463     120.03
   8   128.473     1.2857     182.29
   7    98.074     1.8603     203.97
   6    68.018     2.4885     208.27
   5    41.326     2.4320     126.71
   4    18.119     1.8589      42.96
   3     6.583     1.2646       9.32
   2     2.538     0.7918       1.05
   1     0.000     0.3484       0.66
21
  16.3,0.272,0.000016,1.204
  129.
```